*Technical Physics, Vol. 46, No. 10, 2001, pp. 1205–1212. Translated from Zhurnal Tekhnicheskoĭ Fiziki, Vol. 71, No. 10, 2001, pp.1–7.*


**THEORETICAL AND MATHEMATICAL PHYSICS**

# Development Paths of the Instability of a Highly Charged Viscous Droplet

**A. I. Grigor'ev**

*Yaroslavl State University, Sovietskaya ul. 14, Yaroslavl, 150000 Russia*

Received November 17, 2000

**Abstract**—Analysis is presented of the effect on the instability of a droplet of viscous liquid induced by its self-charge of such physical factors as corona discharge initiated in its vicinity and self-sustaining due to photoionization, evaporation of the liquid, and field vaporization of the charge. It has been shown that droplets of micron and submicron size lose their excess charge primarily due to field vaporization. © *2001 MAIK "Nauka/Interperiodica".*

1. In a variety of research setups, technical devices, and technological installations, a problem of great importance is obtaining the size and charge distributions of droplets formed as a result of the instability of the surface of a charged liquid. It is important, for instance, for obtaining insight into physical processes taking place in liquid-metal ion sources and liquid mass-spectrometers; in powerful electrical discharges between metal electrodes, where the electrodes are melted and the molten metal dispersed; and in highly charged droplets dispersing in electrical fields of storm-clouds, etc. (see, for example, [1–5] and the references therein). This problem was analyzed both experimentally and theoretically in a number of studies [1]. Nevertheless, some of its aspects still remain unclear, for example, the observed limits in the distributions of droplets over their sizes (in the range of small sizes) and charges (in the range of large charges), in the case of droplets carrying charges close to the limiting ones in the sense of Rayleigh's stability criterion.

A highly charged droplet in an external electrostatic field (which typically appears in all applications mentioned above) is unstable with respect to its self-charge and polarization charge, and disposes of the excess charge by ejecting fine highly charged daughter droplets, which are unstable and disperse according to the same law [1, 2]. This series of cascade dispersions of the daughter droplets continues until their characteristic size becomes of a submicron range, at which point the effect of viscosity is strong enough to damp the build up of strain in the unstable droplets. Ultimately, the electrostatic instability vanishes when a droplet either splits into two stable daughter droplets of comparable sizes [1, 2], or loses its excess charge through field vaporization [6, 7].

A highly charged droplet in a gas atmosphere may lose its charge due to a corona charge initiated in its vicinity [8, 9].

In connection with the aforesaid, it is interesting to follow the evolution of a highly charged droplet levitating in the electrostatic field of a plane capacitor in air under atmospheric pressure, as in Millikan's experiments on measurement of the electron charge, or in experimental verification of the stability criterion of a droplet with respect to its self-charge [1] (Fig. 1).

2. Consider a small droplet of an incompressible liquid having radius $R$, viscosity $\nu$, density $\rho$, and surface tension $\sigma$ and carrying an electrical charge $q_0$ equal to the limiting one in the sense of Rayleigh's stability criterion, which is placed in an electrostatic field $\mathbf{E}_0$ directed opposite the gravitational acceleration: $\mathbf{E}_0 \parallel -\mathbf{g}$. Since the droplet is unstable with respect to its charge, it will stretch along the field $\mathbf{E}_0$ and take a shape close to a spheroid [1, 2]. Depending on the viscosity, the

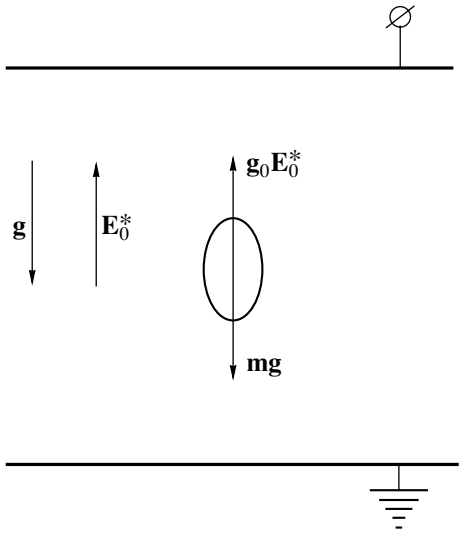


**Fig. 1.** Schematic of a setup for levitation of a charged drop.

1063-7842/01/4610-1205$21.00 

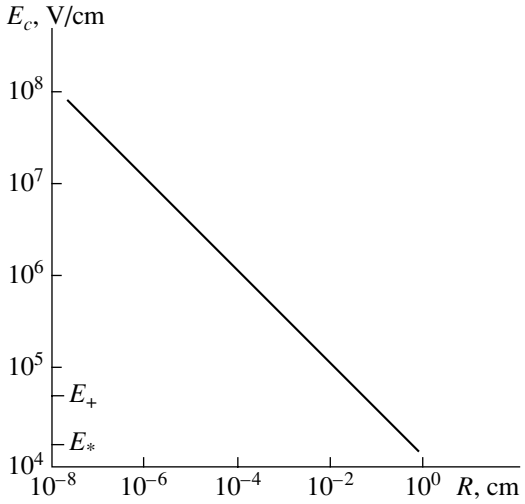


**Fig. 2.** Relation between the droplet radius $R$ and the strength $E_c$ of the electrostatic field induced near the droplet surface by Rayleigh's critical self-charge of the droplet.

droplet will either disperse into a large number of fine highly charged daughter droplets (at $\mu \equiv \nu(\rho/R\sigma)^{1/2} \ll 1$) [1, 2], or split (at $\mu \geq 1$) into two droplets of comparable sizes [10, 11] (the possibility of the charge loss owing to the field vaporization is not considered at this point). In both cases, the characteristic droplet dispersion times are functions of the droplet viscosity (of parameter $\mu$). In the qualitative consideration below we assume that the characteristic droplet dispersion time is determined by the characteristic build up time $\tau_0$ of the spheroidal deformation (i.e., the rise time of the amplitude of the principal unstable mode), and, for both dispersion paths mentioned above, has the same order of magnitude. According to [12], the dependence of $\tau_0$ on $\mu$ (or $\nu$) is a simple linear function

$$\tau_0 = a + b\mu \equiv R^2\left(\frac{\rho}{2\zeta_0\sigma}\right)^{1/2} + \nu\frac{\rho R^{5/2}}{34\zeta_0^{3/2}\sigma}, \qquad (1)$$

where $\zeta_0$ is the amplitude of the initial virtual spheroidal deformation.

If $\zeta_0$ has a thermal nature, then $\zeta_0 \sim 0.1$ nm [12]. Then, it is not difficult to find from (1) that, for a drop with $R = 10$ μm, $\rho = 10^3$ kg/m$^3$, and $\sigma = 0.073$ N/m, the time $\tau_0 \approx 100$ ms, but $\tau_0 \approx 0.4$ ms for a droplet with $R = 1$ μm.

After a time $\tau_0$, in accordance with the above-said, the droplet disperses along one path or the other. However, there arises a question as to whether the droplet may unload its charge before the time $\tau_0$ elapsed by some faster physical mechanism, such as field vaporization of charge or as a result of a corona discharge initiated in the droplet vicinity.

3. Since the droplet is in air containing ions of both signs generated due to natural radiation at a rate of ~10 cm$^{-3}$ s$^{-1}$ [13], then during the time of spheroidal stretching of the droplet $\tau_0$ a free electron or a negative ion can appear in its immediate vicinity (where its electrostatic field is high) initiating a corona discharge that is self-sustaining due to photoionization [14]. The charge of the drop will be neutralized by this corona discharge, and the spheroidal drop will regain the initial spherical shape. Let us find the characteristic initiation time $\tau_*$ of the corona discharge and compare it with $\tau_0$.

The condition for levitation in the electrostatic field $\mathbf{E}_0$ of a plane capacitor of a droplet carrying charge $q_0$ approximately equal to the critical one by Rayleigh's stability criterion imposes a limitation on the magnitude of $E_0$. Rayleigh's criterion of instability with respect to self-charge relates the droplet radius and the self-charge

$$q_0^2/16\pi\sigma R^3 \geq 1. \qquad (2)$$

The condition for levitation of the droplet in the gravitational field and the field $\mathbf{E}_0$ has the form

$$\frac{4}{3}\pi R^3\rho g = q_0 E_0$$

and, taking into account criterion (2), changes to

$$E_0^* = \frac{1}{3}(\pi R^3/\sigma)^{1/2}\rho g. \qquad (3)$$

It is seen from formula (3) that the field strength $E_0^*$ required for levitation depends on the droplet size, and, in the size range of interest ($10^{-4} \leq R \leq 10^{-2}$ cm), is low compared with the field strength $E_c$ due to the self-charge of a spherical droplet near its surface

$$E_c = (q_0/R^2) \geq (16\pi\sigma/R)^{1/2}. \qquad (4)$$

Taking this into account, in our qualitative estimation of the corona discharge initiation conditions we neglect the field $\mathbf{E}_0$ in comparison with the field due to the self-charge of the droplet. Figure 2 demonstrates the dependence of $E_c$ on $R$ for a water droplet.

The critical value of the corona discharge initiation field $E_*$ we take to be equal to the field at which the effective electron multiplication factor in the avalanche produced by the electric field in the droplet vicinity is greater than unity. Since the process takes place at atmospheric pressure, for qualitative estimations we take $E_* \approx 20$ kV/cm [14].

It is seen in Fig. 2 that in the range of droplet sizes $r < 200$ μm the field strength in the vicinity of the droplet exceeds $E_*$ and, consequently, the necessary condition for the corona discharge initiation is satisfied. Nevertheless, one should keep in mind that for discharge initiation at least one free electron is needed in the nearest vicinity of the droplet, where $E \geq E_*$ However, free electrons produced in the near-earth layer of the atmo-

sphere as a result of natural radiation at the low rate of ~10 $cm^{-3}$ $s^{-1}$ [13] are trapped by neutral atoms and molecules in a time of ~$10^{-8}$ s s producing negative ions. Therefore, the probability of a collision between a droplet and a free electron is very low.

It is known [14] that, in high electrical fields, $E_+ > 90P$ V/cm (where $P$ is the pressure in torr), the negative ion decomposes releasing an electron. The concentration of negative ions near the earth's surface under natural conditions is 500–800 $cm^{-3}$ [13]. Therefore, the probability of a collision between a droplet and a negative ion, resulting in the decomposition of the ion and release of an electron is many orders of magnitude higher than the probability of the occurrence of a free electron in the near vicinity of the droplet.

However, it should be kept in mind that, under the conditions of the experiment discussed, the stationary ion concentration between the capacitor plates is substantially less than near the earth's surface because the capacitor field $E_0^*$ drives the ions to the electrodes. The value $E_0^*$ at $R \sim 10$ μm is of an order of a few V/cm. The mobility $\delta$ of the most ions in air at atmospheric pressure does not exceed several $cm^2$/V s [13]. This means that the drift velocity of the ions in the field $\mathbf{E}_0^*$ in a setup with the interelectrode distance of an order of a few centimeters will be several cm/s, while the characteristic time of the ion escape to the electrode does not exceed one second. This means that the ion concentration $n$ in the space between the electrodes will be determined by the rate of ion generation due to natural radiation and will not exceed a value of $n \sim 10$ $cm^{-3}$. Then the density $j$ of the ion flux between the electrodes, defined by the relation

$$j = n\delta E_0,$$

will not be high, and, consequently, the probability of a collision of the levitating droplets with a negative ion and initiation of the corona discharge will also be low.

The characteristic time for collision with a negative ion after insertion of a droplet into the capacitor, i.e., the discharge delay time, is defined by the relation [8, 9]

$$\tau_* \approx (ns\delta E_0^*)^{-1}, \quad (5)$$

where $s$ is the collision cross section.

According to the above, at atmospheric pressure a negative ion decomposes in a field $E_+ \geq 70$ kV/cm. Such a field around the droplet extends to a distance of

$$r \leq \sqrt[4]{E_+^{-2} 16\pi\sigma R^3}$$

from its center. This means that the cross section of an inelastic collision of the droplet with a negative ion has the form

$$s = E_+^{-1}\sqrt{16\pi^3\sigma R^3}.$$

Substituting this relation into expression (5) and taking into account criterion (2) we find that

$$\tau_* = \frac{3E_+}{4\pi^2 n\delta\rho g R^3}.$$

Substituting the values of the physical parameters involved in this expression, it is easy to find that for a drop of $R = 10$ μs under the specified conditions, the time $\tau_*$ amounts to several hours, and to make it shorter $n$ should be increased considerably. Consequently, the initiation of a corona discharge in the vicinity of the droplet that is unstable with respect to its self-charge cannot influence the conditions for droplet dispersion.

4. If the initial radius of a droplet carrying Rayleigh's limiting electrical charge is small enough for the electrical field at the droplet surface due to its charge to be as high as ~ 1–10 V/nm, then field vaporization of the charge from the droplet surface will occur [6]. This process will decrease the charge below the Rayleigh's limit, making the droplet stable. It is seen in Figs. 2 and 4 that such field strengths near the droplet surface are typical for droplets of submicron size ($2R < 0.1$ μm).

According to the existing concepts of the formation of size distribution functions of the daughter droplets emerging as a result of a series of cascade dispersions under electrostatic instability conditions [1–3], the smallness of the droplets capable of further separation is limited due to viscosity; this limit being $R > 1$ μm for water droplets and $R > 0.1$ μm for droplets of liquid metal. For water droplets with $R > 1$ μm the role of the field vaporization, as seen in Fig. 2, appears negligible; nevertheless, under certain conditions it can be appreciable. For instance, analysis of the dispersion pattern of a highly charged drop with $R \approx 1$ μm indicates that, at the final stage of spheroidal stretching where charge redistribution over its surface and the growth of the self-charge field take place near the extreme points or vertices of the droplet, field vaporization can take place. We note that the build up of the spheroidal deformations starts as soon as the droplet's charge exceeds the critical value defined by (2), whatever the viscosity value; however, for viscous drops, the spheroidal stretching, according to (1), will be less. Let us consider this point in more detail.

4.1. The electric field strength $E = 4\pi\kappa$ near the surface of a conductor in a vacuum is determined by the surface charge density $\kappa$ and in the case of an ellipsoid is given by the known expression

$$\kappa = \frac{q_0}{4\pi abc}\left(\frac{x^2}{a^4} + \frac{y^2}{b^4} + \frac{z^2}{c^4}\right)^{-1/2}, \quad (6)$$

where $a$, $b$, and $c$ are the semiaxes of the ellipsoid.

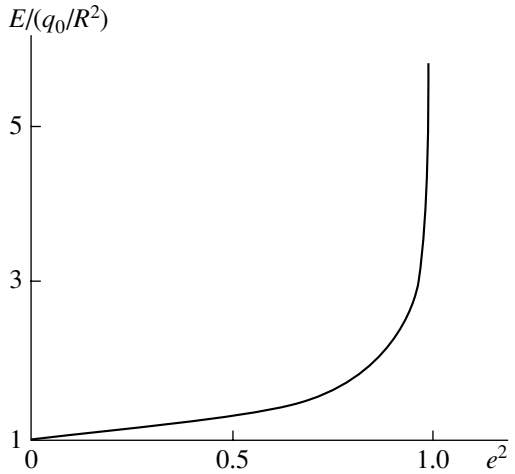


**Fig. 3.** Enhancement factor of the electrostatic field near the vertices of a charged prolate spheroidal droplet as a function of the square of the droplet's eccentricity $e^2$.

The highest surface charge density is found at the point of maximum surface curvature. In the case of a prolate spheroid ($a > b = c$), this takes place at the spheroid vertices ($x = \pm a$, $y = 0$, $z = 1$). Here the field strength is

$$E = q_0/b^2. \quad (7)$$

As follows from Eq. (7), the maximum electrical field strength of a charged droplet in the shape of prolate spheroid depends only on the charge value and the semi-minor axis length $b$ and does not depend on the droplet volume. In Eq. (7) $b$ can be expressed in terms of the eccentricity $e = (1 - b^2/a^2)^{1/2}$ of the prolate spheroidal droplet

$$E = q_0/R^2(1 - e^2)^{1/3}.$$

It is convenient to rewrite the last expression in the form

$$\frac{E}{q_0/R^2} = (1 - e^2)^{-1/3}, \quad (8)$$

where $q_0/R^2$ is the self-charge field strength of initial spherical droplet near its surface.

The plot of function (8) is given in Fig. 3. It is seen that, at sufficiently large eccentricities, the field strength $E$ near the vertices of a spheroidal drop may exceed its value near the surface of a spherical drop by more than an order of magnitude. However, according to the existing concepts [1, 2] a droplet starts to give off the excess charge by ejecting highly charged fine daughter droplets already at $e^2 \approx 0.7$; therefore, the possibility large eccentricity (a large stretching of the droplet) should be verified.

4.2. A charged droplet of an ideal conductive incompressible liquid in a vacuum is unstable, if the following condition is satisfied

$$q_0^2/4(l + 2)\pi\sigma R^3 \geq 1, \quad (9)$$

where $l$ is the mode number of capillary oscillations of the droplet.

If inequality (9) is valid for $l = 2$, the principal mode loses stability, and the droplet will stretch acquiring a shape close to a spheroid. As the eccentricity $e^2$ of the stretching droplet increases redistribution of the self-charge surface density occurs, rising at the droplet's vertices according to formula (6) until the modes higher than the principal one become unstable at the droplet's vertices [15]. The superposition of the unstable higher modes having substantially higher build up rates [16] leads to the formation of protrusions at the vertices of the stretching droplet. The tips of the protrusions eject daughter droplets taking off the excess charge of the parent droplet. In this way the instability of a charged droplet is relieved when $\mu \equiv \nu(\rho/R\sigma)^{1/2} \ll 1$.

When the condition $\mu > 1$ is fulfilled, the instability build up rates of all the modes become lower, but viscosity dampens the buildup rates of higher modes to an especially large degree, so that these rates become lower than the build up rates of the principal mode [16]. Therefore, within the characteristic rise time of the amplitude of the principal mode $\tau_0$ (defined as a reciprocal of the buildup rate), the ejecting protrusions at the vertices of a highly viscous droplet do not form, and the droplet continues to stretch out until it is separated into two droplets of comparable sizes [10], or, according to the above, if the drop is small enough, until the field strength near the droplet's vertices becomes high enough for the field vaporization of ions to be possible.

In estimating the field strength $E$ causing charge vaporization, it should also be taken into account that it is the field in the immediate vicinity of the point at the surface, where the vaporization takes place. This means that small-scale perturbations of the shape of the droplet's vertex (related to the instability of the higher modes that, however slowly, still grow) increase the field strength above that given by formula (8) [15–17]. Figures 4a and 4b illustrate the enhancement of the external field near the tip of a small-scale spheroidal protrusion as a function of the square of eccentricity $e^2$, which was calculated using the expressions defining the field strength of a spheroid in a small vicinity of its vertices for a flattened spheroid

$$\frac{E}{E_0} = \frac{e^3}{(1 + e^2)(e - \arctan e)}, \quad e^2 = \frac{a^2}{b^2} - 1$$

and for a prolate spheroid

$$\frac{E}{E_0} = \frac{e^3}{(1-e^2)(\mathrm{arth}e - e)}, \quad e^2 = 1 - \frac{b^2}{a^2},$$

where $a$ and $b$ are the semi-major and semi-minor axes of the spheroid, and $E_0$ is the uniform field external to the spheroid.

If a small hemispherical protrusion at the vertex of a charged prolate spheroidal droplet is considered, then $E_0$ will be the self-charge field of the droplet, which, as seen in Fig. 4, is further enhanced in the vicinity of the small-scale protrusion at the droplet's vertex.

4.3. An order of magnitude of the characteristic time $\tau_q$ of the charge loss by a droplet, caused by the field vaporization of a single or clustered ion from the droplet's surface, can be estimated using the formula [6, 19, 20]

$$\tau_q \sim \left(\beta\eta\frac{kT}{h}\right)^{-1}, \qquad \beta = \exp\left[-\frac{Q - (z^3|q|^3E)^{1/2}}{kT}\right], \tag{10}$$

where $\beta$ characterizes the probability of the ion vaporization; $\eta$ is the amount of ions at the droplet's surface that can be field-vaporized; $Q$ is the activation energy of the field vaporization of an ion; $zq$ is the ion charge; $z$ is the atomic number; $E$ is the electrical field strength near the droplet's surface; $k$ is Boltzmann's constant; $T$ is the absolute temperature; and $h$ is Planck's constant.

It is seen from expressions (10) that due to large values of $\eta$ and the factor ($kT/h$) the characteristic time $\tau_0$ of the field vaporization of charge may be extremely short, even if $\beta \ll 1$. For instance, as shown in the Appendix to this paper, the activation energy of the field vaporization of a $Na^+$ ion from NaI solution is equal to 1.78 eV, and the exponential factor is $\beta \approx 10^{-10}$ at $E \approx 1$ V/nm. However, a droplet of a 0.1 M NaI solution [19] of a radius in the micron range has on its surface $\eta \geq 10^5$ NaI molecules capable of releasing a $Na^+$ ion via field vaporization. Proceeding on the assumption that only one tenth of the NaI molecules is under the action of the high field at the droplet's vertices, it can easily be found that $\tau_q \leq 1$ μs. For a NaCl molecule under the same conditions $\tau_q \leq 1$ ms. According to [20], for a droplet of $R = 1$ μm, the characteristic field vaporization time of a clustered ion enclosed in a solvate sheath consisting of 6–12 neutral molecules, is of the same order of magnitude. However, the activation energy of this process is much higher than for vaporization of an ion without the solvate sheath (see the Appendix). According to formula (1), for a droplet of radius $R = 1$ μm the time $\tau_0$ of spheroidal stretching preceding the loss of charge as a result of splitting is 0.4 ms or considerably larger than $\tau_q$ for NaI and of the same order of magnitude as $\tau_q$ for NaCl solution.

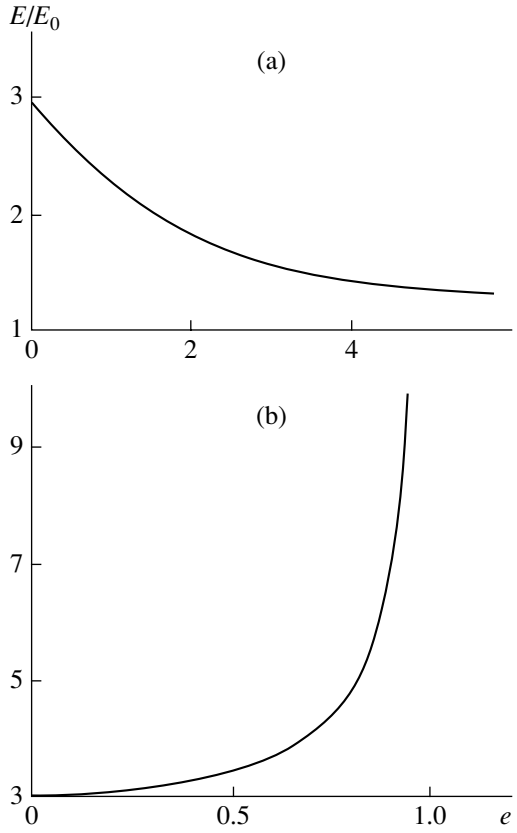


**Fig. 4.** Enhancement factor of the external electrostatic field near the tips of a hemispheroidal protrusion at the surface of a conductive droplet as a function of its eccentricity $e$ for (a) a flattened spheroid, and (b) a prolate spheroid.

Thus, the field vaporization of charge from the surface of viscous droplets of micron and submicron sizes occurring in a very short time can influence their size and charge distribution functions obtained after a series of cascade separations of the parent droplet ejected from the surface of a charged liquid as a result of electrostatic instability [1].

5. One more mechanism, affecting the size distribution of droplets produced as a result of charge-induced dispersion of a liquid, is the thermal evaporation of the liquid with the self-charge remaining unchanged. We note that the probability of thermal vaporization of an ion from the surface of a charged droplet at $E \ll 1$ V/nm is many orders of magnitude less than for a neutral molecule. Such a conclusion can be easily drawn from comparison of amounts of neutral molecules and ions at the surface of a droplet carrying Rayleigh's limiting charge.

Let us estimate the rate of decrease of the droplet radius as a result of evaporation into the ambient gas on the basis of the Hertz–Knudsen equation, on the

assumption that in the course of the evaporation the droplet temperature remains constant and equal to the gas temperature. The following expression for the dependence of the drop radius on time [19] is easily obtainable,

$$R = R_* - \alpha t, \quad \alpha \equiv v\chi m(n_* - n_\infty)/4\rho, \qquad (11)$$

where $R_*$ is the initial drop radius, $v$ is the mean thermal velocity of the vapor molecules, $n_*$ is the concentration of the saturated vapor, $n_\infty$ is the vapor concentration a large distance away from the droplet, $\rho$ is the droplet density, $\chi$ is the evaporation factor, and $m$ is the molecular mass of the evaporating liquid.

The characteristic evaporation time $\tau_e$ (the time it takes for a substantial decrease of the initial drop radius to occur) can be obtained from expressions (11) and has the form

$$\tau_e \approx R_*/\alpha. \qquad (12)$$

For a water droplet at $R_* = 1$ μm; $\rho = 10^3$ kg/m$^3$; $m = 3 \times 10^{-26}$ kg, $v = 590$ m/s; $\chi = 4 \times 10^{-2}$ [19], $n_* = 5.45 \times 10^{23}$ m$^{-3}$; and $n_\infty = 0$, according to [12], we have $\tau_e \approx 8$ ms. This figure indicates that evaporation can play a role in the instability caused by the self-charge of larger droplets, for which the time $\tau_0$ is comparable with the time interval $\tau_e$, in which the droplet size decreases appreciably due to evaporation. For drops with the radius $R \le 1$ μm the role of evaporation is insignificant.

## CONCLUSION

A comparison between the various characteristic times (the instability realization time of a highly charged droplet with respect to its self-charge $\tau_0$; the time $\tau_*$ it takes for a self-sustaining corona discharge to be initiated in the droplet vicinity; the characteristic time $\tau_e$ of the mass loss by a droplet through evaporation; and the characteristic time $\tau_q$ of the charge loss by a droplet due to field vaporization) shows that the droplets of electrolyte solutions of micron and submicron size lose their excess charge predominantly as a result of field vaporization.

## *APPENDIX*

### *On the Field Vaporization of an Ion without a Solvate Sheath from an Electrolyte Solution*

Following a suggestion by Iribarne and Thomson [20], the field vaporization ions and charged clusters from electrolyte solutions is assumed to be governed by the same physical mechanism as the field vaporization of ions from a metal surface considered theoretically for the cases of field ion microscopy [6] and liquid-metal ion sources [21]. In particular, the vaporization rate constant $K$ of metal ions under an electrical field due to thermal activation to energies above the Schottky barrier (arising due to the electrical field $E$ near the metal surface) is described by the Arrhenius law [6]

$$K = \omega \exp\left[-\frac{Q - (z^3|q|^3E)^{1/2}}{kT}\right], \qquad (1A)$$
$$Q \equiv \Lambda + J - \varphi,$$

where $k$ is Boltzmann's constant; $\omega$ is the oscillation frequency of an atom; $T$ is the absolute temperature; $q$ is the ion charge; and $z$ is the atomic number.

The activation energy $Q$ of the ion vaporization in a virtual thermoionic cycle in expression (1A) is determined taking into account the following contributions [6]: (i) the sublimation energy $\Lambda$ absorbed by a neutral atom vaporized from the metal surface; (ii) the ionization energy $J$ of an atom; and (iii) the energy $\varphi$ given away by the electron returned to the metal, which is equal to the electronic work function of the metal. The second term in the numerator of the exponent index describes lowering of the activation energy because of the Schottky effect.

According to the above consideration, the field vaporization of ions or ion clusters from an electrolyte solution, can also be described using an expression of the form (1A) [20, 22], where $kT/h$ is substituted for $\omega$ ($h$ is Planck's constant), and the activation energy of the ion vaporization from the metal surface $Q$ is replaced by the change of enthalpy $\Delta H_+$ accompanying the transition of an ion or an ion cluster from the solution into a vacuum, which is taken to be equal in absolute value to the enthalpy change for solvation of an ion (or finalizing the solvation of a clustered ion) in the solution. As shown in [20], for clustered ions $\Delta H_*$ as a function of the number $n$ of neutral atoms in a cluster is a nonmonotonous function, and at a certain value of $n = n_*$ has a minimum, where $\Delta H_* = 2.32 - 2.73$ eV. This value of the activation energy of field vaporization of clustered ions provides good agreement between the theory and the experiment at $E = 1$ V/nm. However, for single ions the vaporization activation energy $\Delta H_*$ calculated by the solvation energy is two or three times higher than the above values [22, 23]. This means that for the theory to agree with experiment the electrostatic field strength near the solution surface should be an order of magnitude higher or as high as is necessary for the field vaporization of metal ions ($E \ge 10$ V/nm) [17, 22, 24]. However, this conclusion appears somewhat premature because, in practice, the field strength $E \ge 10$ V/nm required for the field vaporization of ions from the surface of solid or liquid metal can only be achieved with specially prepared ion emitting tips having the apex radius of ~1 μm. Attainment of the field strength ~10 V/nm in mass spectrometers with an electrohydrodynamic injection of substances to be analyzed into the discharge chamber through a capillary tube ~100 μm in

diameter is hardly possible (the theory of these mass spectrometers was developed in [19, 20, 22]). Besides, not all possible ways of the field vaporization of ions from solutions were considered in [19, 22, 24].

In real (nonideal) solutions, not all the solute molecules are dissociated; a fraction of dissociated molecules are dependent on the concentration of solution components, solution temperature, and the peculiarities of intermolecular interaction [23]. In this connection, consider, by way of example, the likelihood of field vaporization of a positive ion $Na^+$ from an aqueous solutions of Na–NaI and NaCl salts. The activation energy of the field vaporization of a $Na^+$ ion from the solution is calculated according to the virtual thermoionic cycle based on neutral molecules of NaI and NaCl in the same way as it is done in the case of the field vaporization of ions from a metal surface [6]. However, in distinction from [6], we shall consider not the extraction by the field of an ion from the surface of a solid metal, but the process of breakup by the field of the neutral molecule of NaI or NaCl salt found at the surface of the electrolyte solution in the region of a high electric field into $Na^+$ and $I^-$ ($Cl^-$) ions, with transfer of the $Na^+$ ion into the gaseous phase. If $\Lambda$ is the sublimation energy of a molecule; $D$ is the energy of dissociation of a molecule into two neutral atoms, Na and I (Cl); $J$ is the ionization energy of a Na atom; $L$ is the electron affinity for I or Cl atom; and $\varphi$ is the electronic work function for water; then the activation energy of the field vaporization of a $Na^+$ ion from the electrolyte solution has the form

$$Q = \Lambda + D + J - \varphi - L. \quad (2A)$$

In other words, the salt molecule sublimated from the solution dissociates into two neutral atoms, the Na atom is then ionized and its electron and the I (Cl) neutral atom return to the solution, where the electron associates with an I (Cl) atom to form a negative ion. It should be remembered that the whole thermochemical process described is virtual, while occurs in reality is the breakup by the field of the salt molecule into a $Na^+$ ion and a negative $I^-$ ($Cl^-$) ion directly at the solution surface. According to [25], for a NaI molecule $\Lambda$ = 2.08 eV and $D$ = 3.76 eV, and for a NaCl molecule $\Lambda$ = 2.39 eV and $D$ = 4.22 eV. Besides, according to the data in [25, 26], the ionization potential of Na atom is $J$ = 5.14 eV, the electron affinity for I and Cl atoms is $L$ = 3.06 and 3.61 eV, respectively. The electronic work function for water is given in [27] as $\varphi$ = 6.13 eV. Substituting these values into formula (2A) we find that the activation energies of the field vaporization of the $Na^+$ ion from the electrolytes based on aqueous solutions NaI and NaCl are $Q_{NaI}$ = 1.78 eV and $Q_{NaCl}$ = 2.01 eV. It can be seen that in both cases the energy $Q$ calculated using (2A) is less than the vaporization energy of a single (unsolvated) $Na^+$ ion calculated with the use of its hydration (solvation) energy according to the concepts developed in [19, 20], which is equal to 4.18 eV [22, 23]. It is also seen that the calculated $Q$ values are close to the activation energies of the field vaporization from the solution of clustered ions, obtained according to the Iribarne–Thomson concept, which are in a range of 2.32–2.73 eV [28].

To obtain the vaporization rate $V$ of $Na^+$ ions from the solution surface using the reaction rate constant defined by formulas (1A) and (2A), it is necessary to multiply the reaction rate constant by the number of nondissociated salt molecules found at the solution surface under the action of a high electrical field (nonuniform over the solution surface). In this case, the dimension of $V$ is $s^{-1}$, giving the number of vaporized ions per second. If $V$ is multiplied by the ion charge, then an expression for the ion current $I$ due to field vaporization is obtained. The reciprocal of $V$ represents the characteristic time $\tau_q$ of the field vaporization of ions from the solution surface.

## REFERENCES


1. A. I. Grigor'ev and S. O. Shiryaeva, Izv. Akad. Nauk, Mekh. Zhidk. Gaza, No. 3, 3 (1994).
2. A. I. Grigor'ev and S. O. Shiryaeva, Zh. Tekh. Fiz. **61** (3), 19 (1991) [Sov. Phys. Tech. Phys. **36**, 258 (1991)].
3. A. I. Grigor'ev and S. O. Shiryaeva, J. Aerosol Sci. **25**, 1079 (1994).
4. A. I. Grigor'ev and S. O. Shiryaeva, Phys. Scr. (1996).
5. A. I. Grigor'ev, Zh. Tekh. Fiz. **70** (5), 22 (2000) [Tech. Phys. **45**, 543 (2000)].
6. E. W. Muller and T. T. Tsong, *Field Ion Microscopy: An Introduction to Principles, Experiments, and Applications* (American Elsevier, New York, 1969; Metallurgiya, Moscow, 1972).
7. A. I. Grigor'ev and S. O. Shiryaeva, Zh. Tekh. Fiz. **62** (12), 9 (1992) [Sov. Phys. Tech. Phys. **37**, 1136 (1992)].
8. A. I. Grigor'ev and O. A. Sinkevich, Zh. Tekh. Fiz. **54** (7), 1276 (1984) [Sov. Phys. Tech. Phys. **29**, 735 (1984)].
9. A. I. Grigor'ev, I. D. Grigor'eva, and S. O. Shiryaeva, J. Sci. Expl. **5**, 163 (1991).
10. V. A. Koromyslov, A. I. Grigor'ev, and S. O. Shiryaeva, Zh. Tekh. Fiz. **68** (8), 31 (1998) [Tech. Phys. **43**, 904 (1998)].
11. S. I. Shchukin and A. I. Grigor'ev, Zh. Tekh. Fiz. **70** (4), 1 (2000) [Tech. Phys. **45**, 381 (2000)].
12. S. O. Shiryaeva, Zh. Tekh. Fiz. **70** (9), 30 (2000) [Tech. Phys. **45**, 1128 (2000)].
13. S. C. Brown, *Basic Data of Plasma Physics* (MIT Press, Cambridge, 1959; Gosatomizdat, Moscow, 1961).
14. É. D. Lozanskiĭ and O. B. Firsov, *Theory of Spark* (Atomizdat, Moscow, 1975).
15. A. I. Grigor'ev, Zh. Tekh. Fiz. **55** (7), 1272 (1985) [Sov. Phys. Tech. Phys. **30**, 736 (1985)].
16. S. O. Shiryaeva, Zh. Tekh. Fiz. **68** (4), 20 (1998) [Tech. Phys. **43**, 366 (1998)].
17. S. O. Shiryaeva, A. I. Grigor'ev, and D. F. Belonozhko, Zh. Tekh. Fiz. **69** (7), 15 (1999) [Tech. Phys. **44**, 750 (1999)].

18. L. D. Landau and E. M. Lifshitz, *Course of Theoretical Physics*, Vol. 8: *Electrodynamics of Continuous Media* (Nauka, Moscow, 1982; Pergamon, New York, 1984).
19. N. B. Zolotoĭ, G. V. Karpov, and V. E. Skurat, Zh. Tekh. Fiz. **58** (2), 315 (1988) [Sov. Phys. Tech. Phys. **33**, 193 (1988)].
20. J. V. Iribarne and B. A. Thomson, J. Chem. Phys. **64** (6), 2287 (1976).
21. R. Comer, Appl. Phys. **19**, 365 (1979).
22. N. B. Zolotoĭ, Zh. Tekh. Fiz. **65** (11), 159 (1995) [Tech. Phys. **40**, 1175 (1995)].
23. N. A. Izmaĭlov, *Electrochemistry of Solutions* (Khimiya, Moscow, 1976).
24. N. B. Zolotoĭ and G. V. Karpov, Dokl. Akad. Nauk **348**, 336 (1996).
25. *Thermodynamic Properties of Individual Substances. Reference Edition*, Ed. by L. V. Gurvich, I. V. Veĭts, V. A. Medvedev, *et al.* (Nauka, Moscow, 1982), Vol. 4, Part 1.
26. *Thermodynamic Properties of Individual Substances. Reference Edition*, Ed. by L. V. Gurvich, I. V. Veĭts, V. A. Medvedev, *et al.* (Nauka, Moscow, 1978), Vol. 1, Part 1.
27. V. S. Fomenko, *Emission Properties of Materials. Handbook* (Naukova Dumka, Kiev, 1981).
28. F. W. Rollgen, E. Bramer-Weger, and L. Buttfering, J. Phys. (Paris) **48**, C6-253 (1987).

*Translated by N. Mende*

*Technical Physics, Vol. 46, No. 10, 2001, pp. 1213–1217. Translated from Zhurnal Tekhnicheskoĭ Fiziki, Vol. 71, No. 10, 2001, pp. 8–12.*


**THEORETICAL AND MATHEMATICAL PHYSICS**

# An Analytic Representation for the Potential of a Uniform Elliptic Cone

**V. A. Antonov and A. S. Baranov**

*Pulkovo Observatory, Russian Academy of Sciences, Pulkovskoe sh. 65, St. Petersburg, 196140 Russia*

*e-mail: baranov@gao.spb.ru*

Received December 21, 2000

**Abstract**—In view of the fact that various gravitating and charged bodies may have singular points on their surface, the problem of the effect of these singularities in the mass distribution on the behavior of potential arises. The analytic representation for gravitational and electrostatic potentials of a uniform elliptic cone in terms of ordinary integrals is derived. Generally, these integrals are somewhat more complicated than the elliptic ones; however, they reduce to elementary functions in the case of a circular cone. The arbitrariness in the way of truncating a cone manifests itself in the possibility of adding various harmonic polynomials. However, the singularity of potential in the vicinity of the vertex of a cone is of an objective and unique character. © *2001 MAIK "Nauka/Interperiodica"*.

## INTRODUCTION

The practical significance of calculations of the gravitational and electrostatic potentials for various bodies is well known. In some cases, potentials may be represented in an elementary form or even in terms of well-known functions. This may be exemplified by the figures of equilibrium for celestial bodies [1–3], nonuniformities of the Earth crust in gravimetry and geodesy, asteroids of an irregular shape, and various pointed contacts in electrostatics [4]. Another example in which the potential is expressed in an elementary form is a rectangular prism [5].

We consider a somewhat more complicated example, specifically, a uniform elliptic cone. In comparison with the case of a rectangular prism, the complication is the fundamental uncertainty of the potential for an infinitely extended gravitating or charged body. Indeed, the divergence of the potential in this case can be compensated by adding a quadratic function in Cartesian coordinates in contrast to the constant additive for prismatic bodies. The aforementioned fundamental uncertainty manifests itself in the arbitrary choice of the coefficients of the quadratic function. However, as a result of this uncertainty, the problem of determination of the potential does not lose its significance, since the local conditions in the vicinity of the vertex are defined by the Laplace and Poisson equations and are independent of the manner of truncation of a body at large distances.

In mathematical physics, little attention has been given to the field behavior in the neighborhood of the singular points of the body surface. One of the few papers, [6], is devoted to studying the field singularity in the vicinity of the vertex of a pyramid (various cones may be considered as limiting cases of pyramids). However, in [6], the Dirichlet problem is formulated and solved; i.e., in contrast to our case of a uniformly charged insulator, the field of a conductor is considered.

## BASIC FORMULAS

To be specific, we assume that gravitating or charged matter fills the region

$$\frac{x^2}{a^2}+\frac{y^2}{b^2}-\frac{z^2}{c^2}<0, \quad z>0, \tag{1}$$

where $x$, $y$, and $z$ are the Cartesian coordinates; $a$, $b$, and $c$ are some positive parameters (we assume $a \geq b$); and, henceforth, the matter density as well as the gravitational interaction constant are taken to be equal to unity.

Let us first select the functions satisfying the Laplace and Poisson equations in the upper half-space only. This is done similarly to the well-known formulas for the potential of a uniform ellipsoid. We introduce one of the so-called sphero-conical coordinates $\lambda$ as a root of the equation

$$\frac{x^2}{a^2+\lambda}+\frac{y^2}{b^2+\lambda}-\frac{z^2}{c^2-\lambda}=0, \tag{2}$$

the value of this root lies in the interval $(-b^2, c^2)$ [2]. Topological considerations show that $\lambda$ is defined uniquely and continuously in all space. The extreme values of the above-mentioned interval are attained only in two cases. The value $\lambda = -b^2$ is attained in the sector

$$y=0, \quad \left(\frac{x}{z}\right)^2<\frac{a^2-b^2}{c^2+b^2}. \tag{3}$$

1063-7842/01/4610-1213$21.00 

The largest value $\lambda = c^2$ is attained asymptotically in the plane $z = 0$; i.e.,

$$\lim_{z\to 0}\frac{\sqrt{c^2-\lambda}}{|z|} = \left(\frac{x^2}{a^2+c^2}+\frac{y^2}{b^2+c^2}\right)^{-1/2}. \quad (4)$$

Generally, $\lambda$ is an even function with respect to each of the coordinates $x$, $y$, and $z$. Let us introduce the quantities

$$J_a(\lambda) = \pi abc\int_{-b^2}^{\lambda}\frac{ds}{(a^2+s)D(s)},$$

$$J_c(\lambda) = \pi abc\int_{-b^2}^{\lambda}\frac{ds}{(s-c^2)D(s)}, \quad (5)$$

$$J_b(\lambda) = -\frac{2\pi abc}{D(\lambda)} - J_a(\lambda) - J_c(\lambda),$$

where $D_s = \sqrt{(a^2+s)(b^2+s)(c^2-s)}$, and define the function

$$U = [J_a(0)x^2 + J_b(0)y^2 + J_c(0)z^2] \quad (6)$$

inside the cone and

$$U = [J_a(\lambda)x^2 + J_b(\lambda)y^2 + J_c(\lambda)z^2] \quad (7)$$

outside it.

It may be easily verified that the function $U(x, y, z)$ and its first derivatives are continuous in all the exterior half-space. After implicit differentiation of $\lambda(x, y, z)$, we verify that the Laplace equation $\Delta U = 0$ and Poisson equation $\Delta U = -4\pi$ are satisfied inside the cone.

In the lower half-space, we can easily define the harmonic function

$$W = J_a(c^2)(x^2-z^2) + J_b(c^2)(y^2-z^2), \quad (8)$$

which coincides with $U$ at $z = 0$. However, the only incorrectness, namely, the difference between normal derivatives, still takes place. Indeed, in view of (4), we obtain at $z = 0$

$$\frac{\partial U}{\partial z} = -\frac{4\pi abc}{AB}\sqrt{\frac{x^2}{A^2}+\frac{y^2}{B^2}}, \quad (9)$$

where $A = \sqrt{a^2+c^2}$ and $B = \sqrt{b^2+c^2}$, and $\partial W/\partial z = 0$ at the same points.

In order to correct this, we have to add to $U$ and $W$ the potential corresponding to a simple layer in the plane $z = 0$ with the surface density

$$\sigma = \frac{1}{4\pi}\frac{\partial U}{\partial z}, \quad (10)$$

where $\partial U/\partial z$ is given by (9).

In order to simplify the calculations, we first find the potential of the layer with the density

$$\nu = \frac{2}{\pi}\left(\frac{x^2}{A^2}+\frac{y^2}{B^2}\right)\left(1-\frac{x^2}{A^2}-\frac{y^2}{B^2}\right)^{-1/2}, \quad (11)$$

defined inside the ellipse $x^2/A^2 + y^2/B^2 = 1$ in the same plane.

The corresponding potential has the form

$$\Phi = AB\int_l^{\infty}\left(1+\frac{x^2}{A^2+s}+\frac{y^2}{B^2+s}+\frac{z^2}{s}\right) \times\frac{ds}{\sqrt{(A^2+s)(B^2+s)s}}, \quad (12)$$

where $l$ is the positive root of the equation $x^2/(A^2 + l) + y^2/(B^2 + l) + z^2/l = 1$.

This potential is a combination of well-known potentials of a uniform triaxial ellipsoid and ellipsoidal homothetic layer in the case of their ultimate oblateness.

Along with $\Phi$, we consider the potential $\Phi(q)$ that differs from the former in replacement of $A$ and $B$ by $Aq$ and $Bq$, where $q$ is an arbitrary similarity factor. After simultaneous integration of the corresponding density $\sigma(q)$ and the potential with respect to $q$, we first arrive at

$$\int_0^{\infty}\sigma(q)dq = \sqrt{\frac{x^2}{A^2}+\frac{y^2}{B^2}}, \quad (13)$$

which differs from Eq. (10) only in a constant factor. We perform the corresponding integration for the potential up to some finite $Q$ in order to avoid formal divergence. The integral with respect to $q$, specifically,

$$\int_0^{Q}\Phi(q)dq = AB\int q^2dq \times\int_{l(q)}^{\infty}\left(1+\frac{x^2}{A^2q+s}+\frac{y^2}{B^2q+s}+\frac{z^2}{s}\right)\frac{ds}{\sqrt{(A^2q+s)(B^2q+s)s}} \quad (14)$$

is transformed by the substitution of variable $s = q^2$ with the corresponding substitution in the lower integration limit. Then, the lower integration limit $\Lambda$ is defined as the root of the equation

$$\frac{x^2}{A^2+\Lambda}+\frac{y^2}{B^2+\Lambda}+\frac{z^2}{\Lambda} = q^2. \quad (15)$$

After integration with respect to $q$, we obtain

$$\int_0^Q \Phi(q)dq = AB \times \int_\nu^\infty \frac{(Q^2 - q^2(u))/2 + (x^2/(A^2+u) + y^2/(B^2+u) + z^2/u)\ln Q/q(u)}{\sqrt{(A^2+u)(B^2+u)u}}du, \tag{16}$$

where $q(u) = \sqrt{x^2/(A^2+u) + y^2/(B^2+u) + z^2/u}$ and $\nu$ is the root of the equation resulting from (15) by substitution of $q$ by $Q$.

The asymptotic behavior at large $Q$, specifically,

$$\nu = z^2Q^{-2} + z^2\left(\frac{x^2}{A^2} + \frac{y^2}{B^2}\right)Q^{-4} + \ldots \tag{17}$$

is important for us.

From (17), it follows particularly that

$$\int_\nu^\infty \frac{du}{\sqrt{(A^2+u)(B^2+u)u}} = \int_0^\infty \frac{du}{\sqrt{(A^2+u)(B^2+u)u}} - \frac{2z}{ABQ} + O(Q^{-3}) \tag{18}$$

and

$$\int_\nu^\infty \frac{q^2du}{\sqrt{(A^2+u)(B^2+u)u}} = \int_0^\infty \left(\frac{x^2-z^2}{A^2+u} + \frac{y^2-z^2}{B^2+u}\right) \times \frac{du}{\sqrt{(A^2+u)(B^2+u)u}} + \frac{2zQ}{AB} + O(Q^{-1}). \tag{19}$$

The logarithmic factor in combination with $u^{-3/2}$ [see formula (16)] is somewhat more inconvenient. We can get rid of the logarithm using the integration by parts; i.e.,

$$\left(\int_\nu^0 \left(\frac{1}{u} + \frac{1}{A^2+u} + \frac{1}{B^2+u}\right)\ln\frac{Q}{q(u)}\right) \times ((A^2+u)(B^2+u)u)^{-1/2}du = \frac{2}{D(u)} - \int_\nu^\infty \left[\frac{1}{A^2+u} + \frac{1}{B^2+u} + \frac{1}{q^2(u)} \times \left(\frac{A^2x^2}{u(A^2+u)^2} + \frac{B^2y^2}{u(B^2+u)^2}\right)\right]\frac{du}{D(u)}. \tag{20}$$

Thus, we obtain the asymptotic representation

$$\frac{1}{AB}\int_0^\infty \Phi(q)dq = -\int_0^\infty \left[\frac{x^2+z^2}{(A^2+u)u} + \frac{y^2+z^2}{(B^2+u)u} + \frac{x^2+y^2}{(A^2+u)(B^2+u)u}\right]\frac{du}{q^2(u)D(u)} + \ldots, \tag{21}$$

where the omitted terms, besides the corrections vanishing at $Q \longrightarrow \infty$, are the functions that are harmonic in the entire space, and, hence, may be disregarded.

Thus, the potential of a cone is given by

$$\begin{aligned} U(x, y, z) &= abcH(x, y, z) \ (z \geq 0), \\ W(x, y, z) &= abcH(x, y, z) \ (z \leq 0), \end{aligned} \tag{22}$$

where $H$ is the right-hand side of (21).

## INTEGRAL REPRESENTATION IN COMPLEX PLANE

The formulas obtained take a more compact form after complex integration with respect to variables $s$ or $u$.

We will take all the integrals with respect to $u$ along the loop $L$ enclosing the origin from the left with both branches extending to $\infty$. The $\sqrt{u}$ sign changes to the opposite on the lower branch. Then, repeating the aforementioned integration by parts, we obtain

$$H = -\frac{1}{2}\int_L \frac{q^2(u)[\ln q(u) + \pi i]}{D_1(u)}du, \tag{23}$$

where $D_1(u) = \sqrt{(A^2+u)(B^2+u)u}$.

We note that the additive $\pi i$ to the logarithm in the right-hand side of (23) is required to compensate for the imaginary terms that would appear otherwise as a result of extending this logarithm to the lower half-plane in tracing the path around the point $u = 0$, which is a singular point for the function $q(u)$.

The formulas take a more symmetric form if we use the substitution $u = s - c^2$ in Eq. (23) and perform complex integration in (6)–(8). Finally, (22) yields the fol-

lowing expression for the total potential outside a cone at $z > 0$:

$$V = \frac{\pi abc}{2}\int_{-b^2}^{\lambda}\left(\frac{x^2}{a^2+s}+\frac{y^2}{b^2+s}+\frac{z^2}{s-c^2}\right)\frac{ds}{D(s)}$$

$$+\frac{abc}{4}\int_L \frac{S\ln S}{\sqrt{(a^2+c^2+u)(b^2+c^2+u)u}}du$$

$$= \frac{\pi abc}{2}\int_{T(\lambda)}\left(\frac{x^2}{a^2+s}+\frac{y^2}{b^2+s}+\frac{z^2}{s-c^2}\right)\frac{ds}{D(s)} \qquad (24)$$

$$+\frac{\pi abc}{2}\int_{T_1(\lambda)}\left(\frac{x^2}{a^2+s}+\frac{y^2}{b^2+s}+\frac{z^2}{s-c^2}\right)$$

$$\times\ln\left(\frac{x^2}{a^2+s}+\frac{y^2}{b^2+s}+\frac{z^2}{s-c^2}\right)\frac{ds}{D(s)}.$$

Here, $S = x^2/(a^2 + c^2 + u) + y^2/(b^2 + c^2 + u) + z^2/u$, where $T(\lambda)$ is the integration path enclosing the point $b^2$ from the left with both branches extending to $s = \lambda$; $T_1(\lambda)$ similarly encloses the point $c^2$ from the left with both branches extending to $-\infty$.

Expression (8) for $W$ has a rather simple form, but we do not present it here.

Inside the cone, the only difference in comparison with (24) is that $\lambda$ is substituted by zero.

Using formula (24), we can easily verify that the Laplace's equation is satisfied. The continuity of $\partial V/\partial z$ at $z = 0$ can also be easily verified by means of the substitution $s = c^2 + z^2\xi^2$.

We emphasize that a statement similar to the Maclaurin–Laplace theorem for ellipsoids [7] follows from expression (24), since in the exterior region, the result depends, besides constant factors, only on the combination of $A^2$ and $B^2$. We note also that the same results may be obtained by separation of the variables in the sphero-conical coordinates. The variables $r = \sqrt{x^2+y^2+z^2}$ and $\mu$ can serve as these coordinates. Indeed, expression (24) decomposes into the finite sum of pairs of functions of $\lambda$ with the factors $r^2$ and $r^2 \ln r$. This may be easily verified using the formulas

$$x^2 = \frac{(a^2+\lambda)(a^2+\mu)r^2}{(a^2-b^2)(a^2+c^2)},\quad y^2 = \frac{(b^2+\lambda)(b^2+\mu)r^2}{(a^2-b^2)(b^2+c^2)},$$

$$z^2 = \frac{(c^2-\lambda)(c^2-\mu)r^2}{(a^2+c^2)(b^2+c^2)}$$

and

$$\frac{x^2}{a^2+s}+\frac{y^2}{b^2+s}+\frac{z^2}{s-c^2} = \frac{(s-\lambda)(s-\mu)r^2}{(a^2+s)(b^2+s)(s-c^2)}.$$

## THE CASE OF THE CIRCULAR CONE

The case in which $b \longrightarrow a$ is of a particular interest. Since, in our formulation of the problem, any harmonic polynomial can be added to the potential in the entire space, we can change the form of (7) by adding a closed integration path enclosing the points $s = -a_2$ and $s = -b_2$. Indeed, the Laplacian of the additional polynomial with respect to $x$, $y$, and $z$ is reduced to the integral of a total derivative of a single-valued function over a closed path, and, hence, is equal to zero. As a result of this modification, the integration path passes now just above the real semiaxis from $-\infty$ to $\lambda$ and just below the real semiaxis when passed in the opposite direction, which yields doubling of the integral. There is also a method for simplifying the evaluations of integral (23) at $a = b$. Using the substitution $s = c^2 - t^2$, we obtain the integration path passing somewhat higher than the entire real axis. This path may be lifted to perform integration over both sides of the imaginary axis $t$ as far as singular points allow. The singular points are $i\sqrt{\lambda}$ and $i\sqrt{a^2+c^2}$. The contributions to the integral over the paths on either side of the imaginary axis higher than the latter point cancel each other. Hence, the integration path is virtually closed. Then, we use the well-known rule for the changing of the logarithm value when changing the singular point. The upper singular point should be passed around along a circle of a small radius $\varepsilon$ in order to take into account the singularity resulting from the denominator $a^2 + c^2 + t^2$ (it is convenient to reduce the degree of the denominator in one of the terms by integration by parts). Finally, the exterior potential of a cone takes the form

$$V_e = \frac{\pi r^2 \sin^2\theta_0\cos\theta_0}{2}$$

$$\times\left[(3\cos^2\theta_0-1)\left(\ln a-\ln\sin\theta_0-\ln r-2\ln\sin\frac{\theta}{2}\right)\right. \qquad (25)$$

$$\left.-3\cos^2\theta_0-3\cos\theta+\frac{\sin^2\theta_0}{2}\right]$$

and the interior one,

$$V_i = \frac{\pi r^2\sin^2\theta_0\cos\theta_0}{2}\left[(3\cos^2\theta_0-1)\left(\ln a-\ln\sin\theta_0\right.\right.$$

$$\left.\left.-\ln r-2\ln\cos\frac{\theta}{2}\right)-3\cos^2\theta_0-3\cos\theta+\frac{\sin^2\theta}{2}\right] \qquad (26)$$

$$-\pi r^2 3\cos^2\theta_0\left[\sin^2\theta_0+\sin^2\theta_0\cos\theta_0\tan\frac{\theta_0}{2}\right]-\pi r^2\sin^2\theta,$$

where the polar coordinates $r$ and $\theta$ are used, and the constant $\theta_0$ is the apex angle of a cone.

We also note that the terms proportional to $r^2(2\cos^2\theta - \sin^2\theta)$ in expressions (25) and (26) can be added or subtracted with an arbitrary constant factor. However, expressions (25) and (26) apparently can be easily derived using the theory of spherical functions [7]. For instance, one can easily verify that the Laplace and Poisson equations in the polar coordinates as well as the matching conditions at the boundary $\theta = \theta_0$ are satisfied.

## CONCLUSION

The potential of a real cone truncated at a certain finite distance naturally differs from those described by our formulas. However, inside the remaining part of a cone, the difference between the functions (with its first derivatives) is continuous, satisfies the Laplace's equation, and is bounded at the vertex of a cone. Therefore, the difference is a harmonic function and can be expanded in the ordinary series of spherical functions. In particular, the truncation can be considered as a self-similar process of increasing the retained part to an infinite size. As follows from the consideration of dimensionalities, such a way of determining the potential yields a single-valued result accurate to a harmonic polynomial of the second degree. The resulting limiting function increases at large distances no faster than $r^2 \ln r$. Therefore, this function has to coincide with our expressions (25) and (26) to the additive harmonic polynomial of second degree.

The formulas in this paper can yield a meaningful result only for the calculations in some volume rather than on individual surfaces. The only exception is the singularity in the vicinity of the vertex of a cone. Specifically, except for an arbitrary linear function of coordinates, the principal part of the potential should have the form $f(\theta, \varphi)$, where $f$ is a function of the angular coordinates $\theta$ and $\varphi$.

The expressions obtained have a rather compact form and may be used in various problems of mathematical physics, in particular, in the theory of figures of equilibrium of celestial bodies.

## REFERENCES

1. P. Appell, *Figure d'equilibre d'une masse liquide homogene en rotation* (Gauthier-Villar, Paris, 1932; ONTI, Moscow, 1936).
2. S. Chandrasekhar, *Ellipsoidal Figures of Equilibrium* (Yale Univ. Press, New Haven, 1969; Mir, Moscow, 1973).
3. V. A. Antonov, E. I. Timoshkova, and K. V. Kholshevnikov, *An Introduction to the Theory of Newtonian Potential* (Nauka, Moscow, 1988).
4. M. P. Galanini and Yu. P. Popov, *Quasi-stationary Electromagnetic Fields in Inhomogeneous Media* (Nauka, Moscow, 1995).
5. V. V. Brovar, V. A. Magnitskiĭ, and B. L. Shimbirev, *Theory of the Figure of Earth* (Geodezizdat, Moscow, 1961).
6. G. Fikera, Usp. Mat. Nauk **30** (3), 105 (1975).
7. E. W. Hobson, *The Theory of Spherical and Ellipsoidal Harmonics* (Cambridge Univ. Press, Cambridge, 1931; Inostrannaya Literatura, Moscow, 1952).

*Translated by M. Fofanov*

*Technical Physics, Vol. 46, No. 10, 2001, pp. 1218–1224. Translated from Zhurnal Tekhnicheskoĭ Fiziki, Vol. 71, No. 10, 2001, pp. 13–19.*


**THEORETICAL AND MATHEMATICAL PHYSICS**

# The Propagation of Magnetostatic Surface Waves in Ferrite/Superconductor Structures

**A. A. Semenov*, S. F. Karmanenko*, A. A. Melkov*, A. V. Bobyl'**, R. A. Suris**, Yu. M. Gal'perin***, and T. H. Johansen*****

** St. Petersburg State University of Electrical Engineering, St. Petersburg, 197376 Russia*

*** Ioffe Physicotechnical Institute, Russian Academy of Sciences, Politekhnicheskaya ul. 26, St. Petersburg, 194021 Russia*

**** University of Oslo, P. O. Box 1048 Blindern, 0316 Oslo, Norway*

Received January 31, 2001

**Abstract**—An electrodynamic model that describes the dispersion of magnetostatic surface waves in ferrite/superconductor structures is suggested. On its basis, a new approach to determining the microwave sheet resistance $R_S$ of superconducting films in a magnetic field is elaborated. The values calculated ($R_S$ = 0.20–0.96 mΩ) agree with results obtained by the Tauber method. For YIG/YBCO structures, the controllable phase shift is about 1.5π when the depth of magnetostatic wave penetration into the YBCO film varies from 2.0 to 0.8 μm. © *2001 MAIK "Nauka/Interperiodica".*

## INTRODUCTION

The propagation of electromagnetic waves in ferrite/superconductor films is of particular interest for both fundamental research and applications. Specifically, the films can be used in microwave devices that are capable of controlling the phase and the propagation velocity of a signal [1, 2]. As ferromagnetic materials, yttrium iron garnet (YIG, $Y_3Fe_5O_{12}$) films are usually used. In these films, excited magnetostatic surface waves (MSSWs) propagate with low microwave loss [3]. The combination of YIG films and high-temperature superconductors (HTSCs) makes it possible to considerably improve the performance of microwave devices and provides an additional means for controlling microwave propagation [4].

It is the aim of this work to study the effect of the depth of magnetostatic wave (MSW) penetration into the superconducting film on the MSW phase shift in the YIG/YBCO structure, to set a correlation between the penetration depth and the HTSC critical current, and to analyze the results of the microwave experiment on the magnetooptic visualization of the HTSC field profile.

To investigate MSW propagation in ferrite/superconductor structures, one must (1) analytically characterize the interaction of electromagnetic waves with the layered YIG/VBCO system, (2) derive expressions that fit experimental data, and (3) carefully study the properties of the HTSC films using appropriate local diagnostic tools (i.e., take the spatial distribution of superconductor parameters).

In this work, we use a complex approach to studying the behavior of HTSC films in a magnetic field. Our approach combines the electrodynamic simulation and experimental observation of the MSW dispersion in the layered ferrite/superconductor structure. Also, we measured the parameters of the as-deposited films using magnetooptic imaging. It is shown that the microwave sheet resistance of the YBCO films subjected to an external magnetic field can be determined by comparing MSW theoretical and experimental dispersion characteristics.

## PHYSICAL MODEL OF MSW PROPAGATION AT THE FERRITE/SUPERCONDUCTOR INTERFACE

Consider an MSW propagating in a layered superconductor–insulator–ferromagnetic (SIF) structure shown in Fig. 1, where $B$ and $g$ are the constant magnetic field and the MSW vectors, respectively. Let the crystallographic $c$ axis of the YBCO lattice coincide with the $x$ direction and the axes $a$ and $b$, with the $y$ and $z$ directions, respectively. Thus, the axis $c$ runs normally to the substrate surface.

When considering wave processes in a superconductor, one should remember that the London penetration depth $\lambda_L$ of the magnetic field is a tensor (for detail, see [5]):

$$\lambda_L = \begin{vmatrix} 0 & \lambda_c & \lambda_c \\ \lambda_{ab} & 0 & \lambda_c \\ \lambda_{ab} & \lambda_c & 0 \end{vmatrix}. \quad (1)$$

The penetration depth is a highly anisotropic parameter and depends on a variety of factors, such as the cationic and oxygen composition of the film, structure ordering, the presence of weak links, etc. In [5, 6], the

penetration depths $\lambda_c$ and $\lambda_{ab}$ were studied as a function of the YBCO film composition. The spread of these values is significant; the most reliable value of the ratio $\lambda_{ab}/\lambda_c$ for good YBCO films varies from 4 to 6.6. As a result, the diagonal elements of the conductivity tensor

$$\sigma_S = \frac{1}{\lambda_T^2 i\omega\mu_0} \tag{2}$$

(where $\omega$ is the circular frequency and $\mu_0$ is the permeability of a vacuum) turn out to exceed off-diagonal elements by about six orders of magnitude. Hereafter, the latter are set equal to zero.

The ferromagnetic medium will be described by the permeability tensor [7]

$$\mu = \begin{pmatrix} \mu & i\mu_a & 0 \\ -i\mu_a & \mu & 0 \\ 0 & 0 & 1 \end{pmatrix}, \tag{3}$$

where

$$\mu = \frac{\omega_H(\omega_H + \omega_M) - \omega^2}{\omega_H^2 - \omega^2}, \quad \mu_a = \frac{\omega\omega_M}{\omega_H^2 - \omega^2},$$

$$\omega_H = \gamma H_0, \quad \omega_M = 4\pi\gamma M_0,$$

$\gamma$ is the gyromagnetic ratio, $H_0$ is the internal magnetic field, and $M_0$ is the saturation magnetization.

A solution to the wave process at the ferromagnetic–superconductor interface is found from the first two Maxwell equations

$$\mathrm{curl}\mathbf{E} = -i\omega\mu_0 H, \quad \mathrm{curl}\mathbf{H} = i\omega\varepsilon_0 + \mathbf{J}. \tag{4}$$

In terms of the two-fluid model, the total current density in a superconductor is the sum of the current densities in the superconducting and normal phases: $\mathbf{J} = \mathbf{J}_S + \mathbf{J}_N$. Represent the respective current densities as

$$\mathbf{J}_S = \sigma_S\mathbf{E}, \quad \mathbf{J}_N = \sigma_N\mathbf{E}, \tag{5}$$

where $\sigma_S$ and $\sigma_N$ are the conductivities of the superconducting and normal phases.

With the mutual arrangement of the magnetizing field and the wave vector in Fig. 1, a so-called magnetostatic surface wave (MSSW) appears in the structure [7]. In the coordinate system adopted, the condition $\partial/\partial z = 0$ is valid for MSSWs. A solution can then be obtained in the form of two, *TE* ($E_x$, $H_x$, $H_y$) and *TM* ($H_z$, $E_x$, $E_y$), independent modes.

Consider the transverse electric (*TE*) mode, since just this mode corresponds to the MSSW. Expressing the magnetic field components $H_x$ and $H_y$ through the electric field component $E_z$, we come to the equation for the superconductor

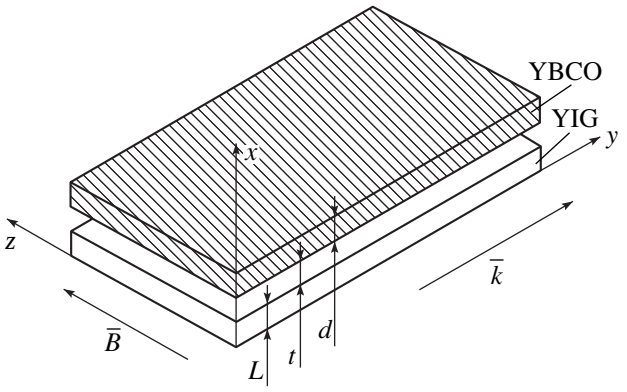


**Fig. 1.** CIF layered structure.

$$\frac{\partial^2 E_z}{\partial x^2} + \frac{\partial^2 E_z}{\partial y^2} - (-\omega^2\varepsilon_0 - \mu_0 + i\omega\mu_0\sigma_n + i\omega\mu_0\sigma_{33})E_z = 0. \tag{6}$$

Similarly, for the ferromagnetic film and for free space, we obtain

$$\frac{\partial^2 E_z}{\partial x^2} + \frac{\partial^2 E_z}{\partial y^2} + \omega^2\varepsilon_0\mu_0\varepsilon\mu E_z = 0, \tag{7}$$

$$\frac{\partial^2 E_z}{\partial x^2} + \frac{\partial^2 E_z}{\partial y^2} + \omega^2\varepsilon_0\mu_0 E_z = 0. \tag{8}$$

The partial solution for each of the media are written as follows:

$$E_z = (A\exp(k_f(x-L)) + (B\exp(-k_f x))\exp(-iky), \quad k_f = \sqrt{k^2 - \omega^2\varepsilon_0\mu_0\varepsilon\mu} \tag{9}$$

for the ferromagnetic film ($0 < x < L$),

$$E_z = (C\exp(k_x(x-L-t)) + D\exp(-k_x(x-L)))\exp(-iky), \quad k_x = \sqrt{k^2 - \omega^2\varepsilon_0\mu_0} \tag{10}$$

for the air gap ($L < x < (L + t)$),

$$E_z = (E\exp(k_s(x-L-t-d)) + F\exp(-k_s(x-L-t)))\exp(-iky), \tag{11}$$

$$k_s = \sqrt{k^2 - \omega^2\varepsilon_0\mu + i\omega\mu_0\sigma_n + i\omega\mu_0\sigma_{33}}$$

for the superconducting film [$(L = t) < x < (L + t + d)$],

$$E_z = G\exp(-k_x(x-L-t-d))\exp(-iky) \tag{12}$$

for the free space $x > (L + t + d)$, and

$$E_z = H\exp(k_x x)\exp(-iky) \tag{13}$$

for the free space $x < 0$.

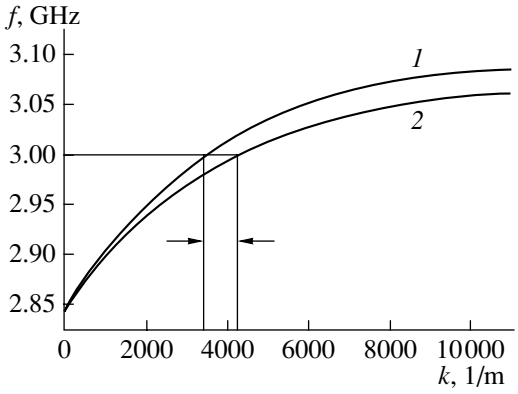


**Fig. 2.** Theoretical dispersion properties of MSSWs in the HTSC/YIG layered structure. $j_c$ = (*1*) $3 \times 10^9$ and (*2*) $7 \times 10^9$ A/m$^2$.

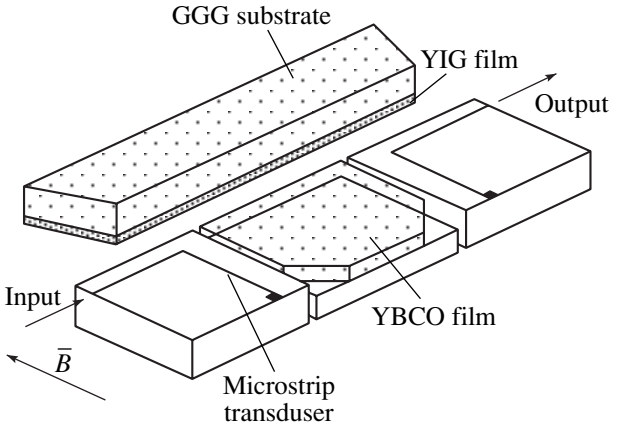


**Fig. 3.** Measuring mockup for studying the MSW dispersion.

Using the usual boundary electromagnetic conditions—the equality of the tangential components of the vectors $E$ and $H$ at the interfaces—we can obtain the dispersion relation. It is transcendental and rather complicated, so that the ω vs. $k$ dependence cannot be represented in the explicit form:

$$\exp(-2kL) = \frac{\left(s\mu_e + 1 + s\frac{\mu}{\mu_a}\right)\left(s\mu_e - \frac{k}{k_s}\left(1 - s\frac{\mu}{\mu_a}\right)\right)}{\left(s\mu_e + 1 - s\frac{\mu}{\mu_a}\right)\left(s\mu_e - \frac{k}{k_s}\left(1 + s\frac{\mu}{\mu_a}\right)\right)}, \quad (14)$$

where

$$\mu_e = \frac{\mu^2 - \mu_a^2}{\mu_a}$$

and $s = \pm 1$ defines the direction of wave propagation.

Formula (14) is the dispersion relation for the specific case $t = 0$, $d \longrightarrow \infty$ (see Fig. 1). In going to the limit cases of a free ferromagnetic film ($\sigma_s = 0$, $\sigma_n = 0$) and a film screened by a perfect metal ($\sigma_s = 0$, $\sigma_n \longrightarrow \infty$), expression (14) transform into the Damon–Eshbach [8] and Sashadri [9] equation, respectively.

The equations were solved numerically. The graphs for the MSSW spectrum are shown in Fig. 2. They are constructed for two penetration depths taken from the range where the possibility of their variation is the highest. As follows from Fig. 2, the change in the penetration depth from 2.0 to 0.8 μm (which corresponds to the change in the critical current density $j_c$ from $3 \times 10^9$ to $7 \times 10^9$ A/cm$^2$ in an external magnetic field of 570 Oe) gives an MSSW phase shift of 20% at a frequency of 3 GHz. The fact that the MSSW dispersion relations are sensitive to the field penetration depth allows the sheet resistance and the penetration depth to be measured from the phase shift under an applied magnetic field. In addition, this effect seems to be promising for microwave devices that control the phase shift and the propagation rate of a signal.

## EXPERIMENTAL STUDY OF MSW DISPERSION

We conducted a series of experiments on measuring the dispersion properties to check the validity of the model results for MSSW propagation. Figure 3 shows the waveguide part of a special measuring mockup. The mockup consists of the input and output microstrip microwave transducers, an epitaxial YIG film grown on a GGG substrate (so-called spin-wave guide), and an HTSC film. The YIG film waveguide is placed on the transducers and the HTSC film. In the experiments, the YIG film was magnetized by a uniform constant magnetic field tangent to the ferromagnetic film surface and normal to the MSW propagation direction. To perform cryogenic measurements, the mockup was placed into a liquid-nitrogen vessel. Three HTSC films were stud-

Parameters of the YBCO films under study

| Film no. | $j_c$, A/m$^2$ | | $T_C$, K | $d$, nm | $\sigma_N$, $\Omega^{-1}$ | $\lambda_L$, nm | $R_S$, mΩ |
|---|---|---|---|---|---|---|---|
| | $T$ = 15 K | $T$ = 77 K | | | | | |
| 1 | $2.7 \times 10^{10}$ | $7.2 \times 10^9$ | 89 | 500 | $6.5 \times 10^6$ | 670 | 1.26 |
| 2 | $1.2 \times 10^{10}$ | $3 \times 10^9$ | 89 | 500 | $6.5 \times 10^6$ | 930 | 2.95 |
| 3 | $9.8 \times 10^{10}$ | $2.6 \times 10^{10}$ | 94 | 500 | $6.5 \times 10^6$ | 370 | 0.20 |

ied (see table). The measurements were carried out in three stages. First, using the cryogenic measuring mockup, we studied the dispersion properties of the MSSWs in several $Y_3Fe_5O_{12}/YBa_2Cu_3O_7$ (YIG/YBCO) layered structures. Then, microbridges were patterned by lithography on the YBCO films and examined by magnetooptic (MO) imaging. The numerical processing of the MO images makes it possible to obtain the current density distribution and to determine the critical current density $j_c$ of the microbridges. Finally, the London penetration depth was determined by an independent technique from the values obtained.

After the microwave measurements, we plotted the dispersion properties of the MSSW propagating in the YIG/YBCO structure (Fig. 4). Here, the theoretical dependences $\omega(k)$ are depicted by the continuous curves. When calculating the theoretical dependences, we used the values of $\lambda_L$ and $\sigma_N$ for the HTSC films, as well as their thickness. One of these parameters can be used as an adjustable parameter. In our experiments, the field penetration depth in the superconducting film served as an adjustable parameter. For the conduction $\sigma_N$ of the normal phase, we took the literature value $6.5 \times 10^6\ \Omega^{-1}$. Note that the numerical values used are typical of superconducting films with different superconducting properties. Using the value of $\lambda_L$ obtained by fitting, we calculated the other parameters of the superconducting films. The sheet resistance of the superconducting films was estimated by the formula

$$R_S(d) = (\omega\mu_0)^2\frac{\lambda_L^4}{d}\sigma_N, \qquad (15)$$

which is valid for $d \le 2\lambda_L$ [10].

At a frequency of 3 GHz and for a tangent magnetic field $H = 570$ Oe, $R_S$ for the different YBCO films was found to vary between 0.2 and 1.6 mΩ.

Thus, the experiments performed allowed us to determine the parameters of the HTSC films under the magnetic field (see table). Their values are consistent with experimental data obtained by other techniques [11, 12].

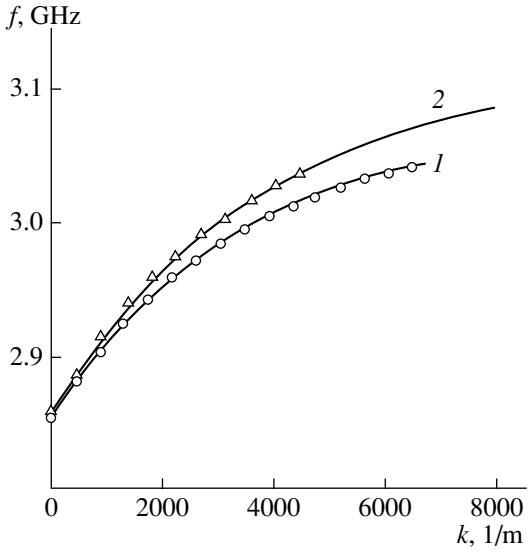


**Fig. 4.** Experimental dispersion characteristics. Curve number corresponds to film number.

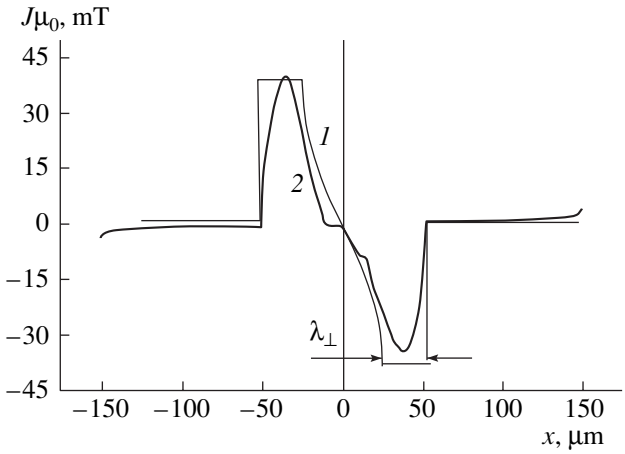


**Fig. 5.** Theoretical and experimental distributions of the current density over the cross section of the superconducting bridge.

## MAGNETOOPTIC INVESTIGATION INTO THE ELECTROPHYSICAL PARAMETERS OF THE YBCO FILMS

We determined the magnetic field penetration depth as follows. The basic parameters of the superconducting film that define the penetration depth are critical current density and current density distribution over the cross section of the film. The latter in the microbridge was studied with the MO technique described in detail in [13–15]. In the superconductor, the current density distribution was simulated with the Been model [16, 17]. Figure 5 shows the current density distribution, where curve *1* depicts the Been model distribution. The actual current density distribution (curve *2*) taken from one of the YBCO microbridges was obtained by numerically processing the MO images of the bridge when the current induced by the external magnetic field passed through it. Figure 5 shows also the microbridge region that corresponds to the vortex lattice penetrating toward the bridge center. In this case, the penetration depth is given by

$$\lambda_\perp = \frac{B_0}{\mu_0 j_c}, \qquad (16)$$

where $B_0$ is the external magnetic induction.

At $d < 2\lambda_L$, the London equation yields, along with formula (16), the expression

$$\lambda_\perp = \frac{2\lambda_L^2}{d}. \qquad (17)$$

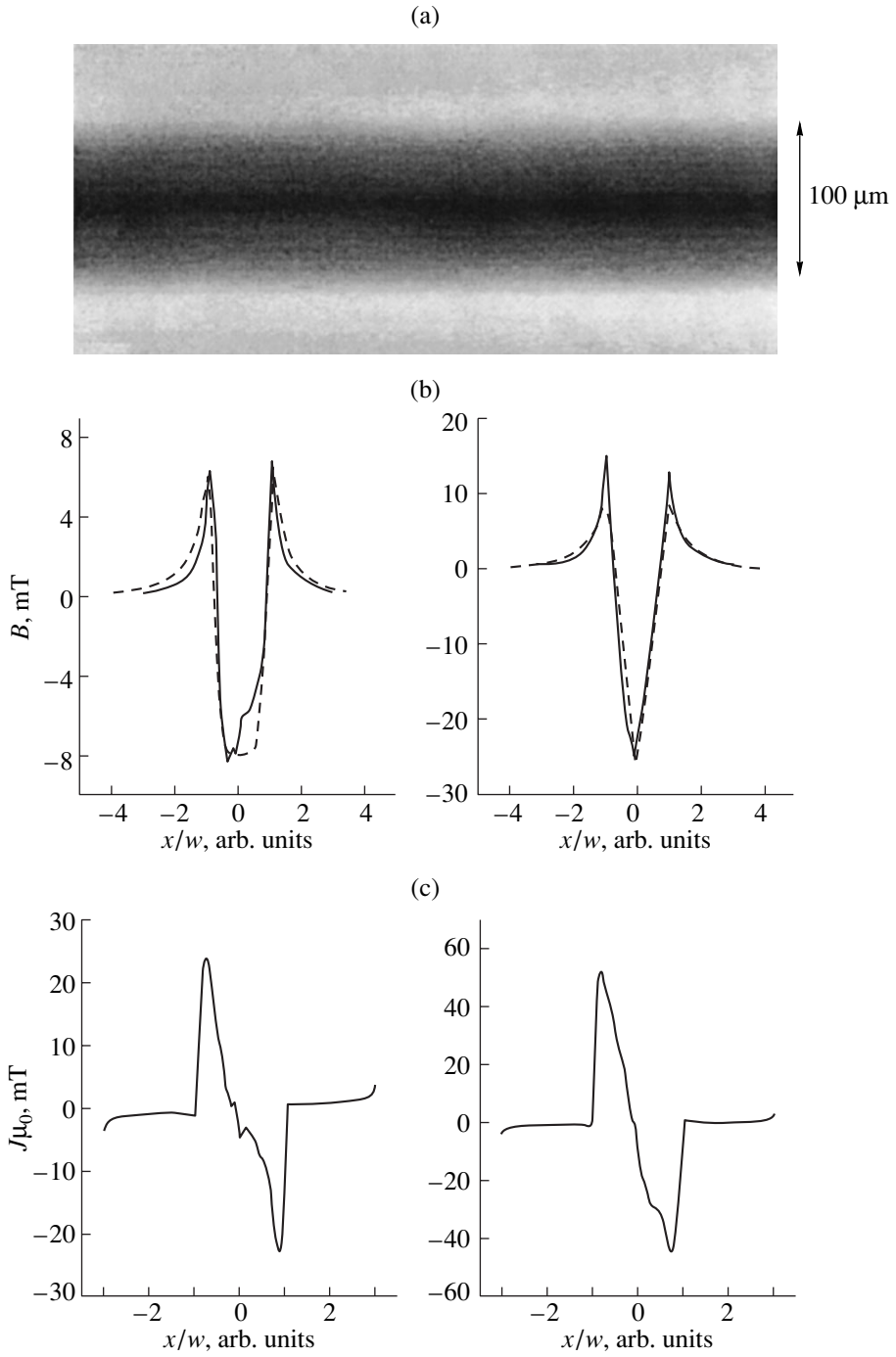


**Fig. 6.** Results of the MO imaging of the HTSC bridges.

Expression (17) was analyzed in [18].

Thus, the critical current density and the London penetration depth turn out to be interrelated. One can determine the field penetration depth, knowing the critical current density and the current density distribution in the film. The joint use of expressions (16) and (17) is consistent with the physical nature of the vortex structure in a superconductor, and the procedures to derive these expressions are not in conflict.

With such an approach, we studied a series of the films that were previously incorporated into the SIF layered structure on which the dispersion characteristics were measured.

Figure 6a demonstrates the MO image from a part of microbridge *1*. This sample is homogeneous and does not contain visible defects. Using the MO images and calibration measurements, we obtained the spatial distributions of the magnetic field and current density in

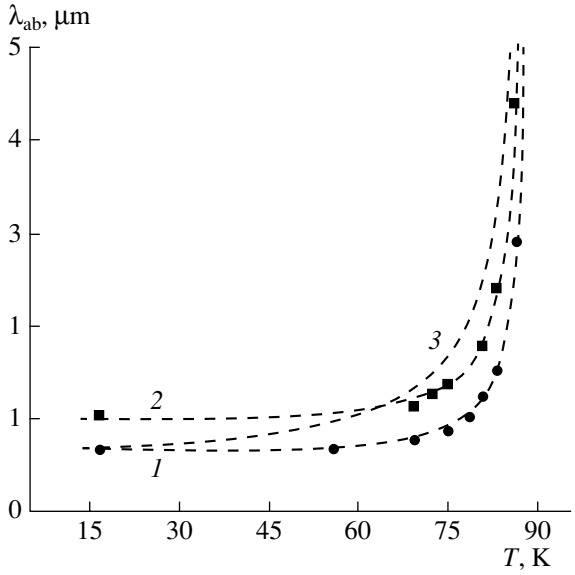


**Fig. 7.** Theoretical and experimental temperature dependences of the London penetration depth for microbridges *1* and *2*. Dashed curve *3* corresponds to formula (18) at $\gamma = 2$.

the bridge (see Figs. 6b and 6c; the curves on the right and on the left were taken at magnetic fields of 20 and 60 Oe, respectively), as well as the temperature dependences of the critical current density in the films studied. The dashed lines refer to the theoretical dependences for $j_c$ that were constructed with the Been model. The continuous lines demonstrate the experimental dependences obtained by the numerical analysis of the MO images. From the experimental data on the current density distribution in the microbridges and the numerical simulation, we determined the penetration depths for the films considered and constructed their temperature dependences.

The theoretical and experimental temperature dependences of the penetration depth for the microbridges are shown in Fig. 7. They can be described by the relationship [10]

$$\lambda_L(T) \sim \left[1 - \left(\frac{T}{T_c}\right)^{\gamma}\right]^{-3/4}, \qquad (18)$$

where $T_c$ is the critical temperature. The literature values for the parameter $\gamma$, which governs the run of the temperature dependence, vary from 1.5 to 2.0. It depends on the presence of weak links (SNS, SIS, etc.) in a superconductor [19, 20].

Our results are best approximated with $\gamma = 6$. A reason for such a large discrepancy between our data and those cited in the literature may be associated with the fact that the films investigated have an ordered structure and a small concentration of weak links identified previously in [5, 19, 20]. Such highly oriented defect-free epitaxial films exhibit a slight temperature dependence of $\lambda_L$ in the low-temperature region and a drastic jump near the critical temperature. For these films, the parameter $\gamma$ is relatively large.

## CONCLUSIONS

The table lists several physical parameters of the films that were obtained by MO imaging and by measuring the MSSW dispersion in the CIF structure. From these results, the following conclusion can be made.

(1) The temperature dependence of the critical current density, as well as their analysis, indicate that the YIG/YBCO films grow epitaxially or have a highly ordered structure. At the same time, the films offering high superconducting properties (film *3* in the table) exhibit a relatively large magnetic field penetration depth (≈930 nm). A possible explanation for this fact is that the YBCO films have a mosaic structure with differently oriented blocks (along with the basic (001) phase, the YBCO films contain (100)-oriented blocks). Another reason may be the presence of superconducting inclusions of another cationic composition that increase the effective penetration depth.

(2) The difference between the superconducting parameters in the HTSC films is the reason for the significant modification of the MSW dispersion when the waves cross the ferrite/superconductor interface. The decline in the critical current density in the HTSC film from $7 \times 10^9$ to $3 \times 10^9$ A/m$^2$ (which corresponds to the change in the field penetration depth from 0.8 to 2.0 μm under an applied field of 570 Oe) causes a phase shift of about 20% for the MSW at the YIG/YBCO interface. In the measuring mockup used in this work (Fig. 3), the phase shift was about $1.5\pi$ at a spacing between the microstrip transducers of 7.25 mm.

(3) Among the YBCO films studied, film *3* (see the table), which offers the high superconducting parameters, is of special interest. Its cationic composition deviates from the stoichiometric 1 : 2 : 3 proportion and is close to 2 : 3 : 5. The fact that $Y_2BaO_3Cu_5O_z$ HTSC films have high superconducting properties has been reported previously (see, e.g., [12]). This work supports the assumption that $Y_{Ba}$ substitutional cation defects present in the lattice stabilize the HTSC phase and improves the superconducting parameters of the YBCO films.

Thus, we performed the MO and microwave investigation of the electrophysical parameters and the structure of the HTSC films. The results obtained by these methods are shown to correlate. It has also been demonstrated that the propagation of MSWs at the YIG/YBCO interface can be controlled both electrically and magnetically. The use of HTSC films and their thermostatic control at cryogenic temperatures reduce microwave loss during MSSW propagation and open up possibilities for MSW-based devices with unique parameters.

## ACKNOWLEDGMENTS

The authors thank B.A. Kalinikos for the encouragement and the participation in the physical simulation.

This work was supported by the Russian Foundation for Basic Research (grant no. 99-02-16370) and by the State Program "Topical Problems of Condensed Matter Physics: Superconductivity" (projects "Interfeĭs-2" and "Porog-3").

## REFERENCES

1. L. V. Lutsev and S. V. Yakovlev, J. Appl. Phys. **83**, 7330 (1998).
2. G. F. Dionne, D. E. Oates, D. H. Temme, and J. A. Weiss, IEEE Trans. Microwave Theory Tech. **44**, 1361 (1996).
3. Yu. V. Gulyaev and P. E. Zil'berman, *Spin Wave Electronics. Radio Electronics and Communication* (Znanie, Moscow, 1988), No. 6.
4. S. F. Karmanenko and A. A. Semenov, Pis'ma Zh. Tekh. Fiz. **26** (3), 12 (2000) [Tech. Phys. Lett. **26**, 96 (2000)].
5. Yu. M. Gufan, I. G. Levchenko, and E. G. Rudashevskiĭ, Fiz. Tverd. Tela (St. Petersburg) **41** (9), 1552 (1999) [Phys. Solid State **41**, 1422 (1999)].
6. C. Panagopoulos, J. R. Cooper, N. Athanassopoulou, *et al.*, Phys. Rev. B **54** (18), 12721 (1996).
7. A. G. Gurevich and G. A. Melkov, *Magnetic Oscillations and Waves* (Nauka, Moscow, 1994).
8. R. W. Damon and J. R. Eshbach, J. Phys. Chem. Solids **19** (3–4), 104 (1961).
9. S. R. Sashadri, Proc. IEEE **58**, 508 (1970).
10. I. B. Vendik and O. G. Vendik, *High-Temperature Superconductor Devices for Microwave Signal Processing*, Part 1.
11. H. Jiang, T. Yvan, H. How, *et al.*, Phys. Rev. B **49**, 9924 (1994).
12. S. F. Karmanenko, A. A. Semenov, A. A. Svishchev, *et al.*, Pis'ma Zh. Tekh. Fiz. **25** (15), 79 (1999) [Tech. Phys. Lett. **25**, 626 (1999)].
13. M. E. Gaevski, A. V. Bobyl, Y. M. Galperin, *et al.*, Phys. Rev. B **59** (14), 9655 (1999).
14. M. E. Gaevski, T. H. Johansen, A. V. Bobyl, *et al.*, Appl. Phys. Lett. **71**, 3147 (1997).
15. T. H. Johansen, M. Bazilevich, M. E. Gaevski, *et al.*, in *High-Temperature Superconuctors* (The Minerals, Metals and Materials Society, Warrendale, 1997), pp. 99–108.
16. C. P. Been, Phys. Rev. Lett. **8**, 250 (1962).
17. E. Zeldov, J. R. Clem, M. McElfresh, *et al.*, Phys. Rev. B **49**, 9802 (1994).
18. J. Pearl, Appl. Phys. Lett. **5** (4), 65 (1964).
19. S. V. Gaponov, G. G. Kaminskiĭ, E. B. Klyuenkov, *et al.*, Zh. Éksp. Teor. Fiz. **95**, 2191 (1989) [Sov. Phys. JETP **68**, 1266 (1989)].
20. V. V. Nemoshkalenko, M. A. Vasil'ev, and A. S. Filippov, Metallofizika **13** (2), 3 (1991).

*Translated by V. Isaakyan*

*Technical Physics, Vol. 46, No. 10, 2001, pp. 1225–1234. Translated from Zhurnal Tekhnicheskoĭ Fiziki, Vol. 71, No. 10, 2001, pp. 20–28.*


**ATOMS, SPECTRA, RADIATION**

# Charge Exchange in Collisions between Heavy Low-Charged Ions

**V. P. Shevel'ko**

*Lebedev Institute of Physics, Russian Academy of Sciences, Leninskiĭ pr. 53, Moscow, 119991 Russia*

*e-mail: shev@sci.lebedev.ru*

Received June 15, 2000; in final form, November 20, 2000

**Abstract**—The probabilities and the effective cross sections of collision-induced one-electron charge exchange between singly charged and four-charged heavy Xe, Cs, Ba, Pb, Bi, and U ions at energies $E > 0.1$ keV/u are calculated by a method of multichannel normalization in the impact parameter representation. The cross sections are rather large with a maximum $\sigma_m \approx 10^{-15}$ cm$^2$ at relative energies $E_m \approx 10$–30 keV/u. For collision energies $E < 10$ keV/u, the cross sections sharply decrease with growing resonance defect of the reaction. At high energies $E > 1$ MeV/u, the charge exchange proceeds largely by the capture of inner shell electrons of the ionic targets. The charge exchange cross sections calculated for low-charged Xe, Cs, Ba, Pb, Bi, and U ions are compared with available theoretical and experimental data. © *2001 MAIK "Nauka/Interperiodica".*

## INTRODUCTION

Charge exchange and ionization that occur when heavy low-charged ions like $Bi^+$, $U^{4+}$, etc. collide with atoms and ions are of great interest for the production of long-lived ion beams in accelerators, ion thermonuclear fusion, and other applications [1–3]. Processes that change the charge state of the ions when they collide with atoms and molecules of a residual gas at energies $E = 1$–100 MeV/u define the lifetime of ion beams in accelerators, and ion–ion Coulomb interaction taking place in the beam at energies $E = 1$–10 keV/u specifies the beam quality (i.e., the ion loss). Available experimental and theoretical data for the effective cross sections of charge exchange and ionization that occur when heavy low-charged ions collide with each other are very scarce [1, 3]; therefore, relevant calculations are of great interest.

For heavy atoms or ions with a charge $q < 10$ and a number of electrons of about 50–100, the interaction cross section is most convenient to calculate using the Thomas–Fermi statistical method [4] or Monte Carlo method of classical trajectories [5]. As far as we know, however, such calculations have not been performed for the systems under study. Estimations carried out by other techniques are known only for a few reactions [3].

In this article, we consider one-electron charge exchange during a collision of heavy low-charged ions,

$$X^{A+} + Y^{B+} \longrightarrow X^{(A-1)+} + Y^{(B+1)+}, \qquad (1)$$

at relative energies $E \geq 1$ keV/u. Charge exchange is known to be a complex process involving particle redistribution, as a result of which the ionic and atomic compositions before and after the collision differ. Therefore, these reactions are more difficult to study theoretically than electron–atom collisions. For example, the parameters of electron–atom collision can today be estimated with an accuracy of 10–30%. At the same time, to calculate the cross sections of ion–atom collision even up to a factor of 2 is a challenge, especially if the collision involves particle redistribution. This is associated with a number of fundamental difficulties arising in describing such processes: the nonorthogonality of the wave functions of the initial and final states of the entire system, different interaction potentials before and after the collision (so-called post–prior discrepancy), the presence of Coulomb interaction between resulting ions in the final channel and its absence in the initial channel upon ion–neutral collision, etc. (see, e.g., [1]).

In this work, we suggest a method of multichannel normalization in the impact parameter representation to calculate the probabilities and the effective cross sections of one-electron charge exchange (1). The method uses the relationship between the quasi-classical and the quantum-mechanical charge exchange amplitudes that was obtained in [6, 7] and adequately describes charge exchange between light atoms and ions [7, 8]; therefore, it seems to be promising for the characterization of charge exchange processes during heavy ion collisions.

In what follows, we report preliminary results for the cross sections of charge exchange between singly charged and four-charged ions in the relative energy range $E \gtrsim 1$ keV/u for the reactions

$$X^{1+} + X^{1+} \longrightarrow X^{0+} + X^{2+}, \qquad (2)$$

$$X^{4+} + X^{4+} \longrightarrow X^{3+} + X^{5+}, \qquad (3)$$

where $X$ = Xe, Cs, Ba, Pb, Bi, or U.

1063-7842/01/4610-1225$21.00 

Low-charged ions of these atoms are today of great interest for ion thermonuclear fusion [2]. Unless otherwise stated, we use the atomic unit system $e = m_e = \hbar = 1$.

## RELATIONSHIP BETWEEN THE QUASI-CLASSICAL AND QUANTUM-MECHANICAL AMPLITUDES OF CHARGE EXCHANGE

In [6–8], the charge exchange between the *nlm* components of a target and a resulting ion has been considered:

$$X^q + A(n_0 l_0 m_0) \longrightarrow X^{(q-1)+}(n_1 l_1 m_1) + A^+, \qquad (4)$$

where $n$, $l$, and $m$ are the principal, orbital, and magnetic quantum numbers, respectively, and the relationship

$$a(\boldsymbol{\rho}, v) = \frac{1}{v(2\pi)^2}\int_P f(\mathbf{k}, v) e^{i\mathbf{k}\boldsymbol{\rho}} d^2\mathbf{k} \qquad (5)$$

between the quasi-classical, $a(\boldsymbol{\rho}, v)$, and the quantum-mechanical, $f(\mathbf{k}, v)$, exchange amplitudes has been derived in the Brinkman–Kramers approximation (the first-order modification of the perturbation theory [1, 9]). (Here, $v$ is the relative velocity of the colliding particles and $p$ is the impact parameter.)

In (5), integration is over the plane $P$, given by

$$\mathbf{kv} - \omega - \frac{v^2}{2} = 0, \qquad (6)$$

where $\mathbf{kv}$ is the scalar product of the vectors and $\omega$ is the resonance defect, i.e., the difference between the binding energies of an optical (captured) electron in the initial, 0, and final, 1, state:

$$\omega = I_0 - I_1. \qquad (7)$$

The resonance defect can be both positive and negative. The vector $\mathbf{k}$ in Eqs. (5) and (6) is related to the momentum transfer vector $\mathbf{Q}$ as

$$\mathbf{k} = \mathbf{Q} + \frac{\mathbf{v}}{v}\left(\frac{\omega}{v} + \frac{v}{2}\right). \qquad (8)$$

Expression (5) has been obtained under the assumption that the trajectory of the incident ion is straight and takes into account the translational factor $\exp(i\mathbf{vr})$ of the electron being captured. According to (5), the radial part of the exchange amplitude for the $n_0 l_0 m_0 - n_1 l_1 m_1$ transition has the form

$$a(\rho, v) = \frac{4}{v}\int_0^\infty k dk C_{l_0 m_0} C_{l_1 m_1} P_{l_0}^{m_0}(\cos\Theta_0) P_{l_1}^{m_1}(\cos\Theta_1)$$
$$\times J_{\Delta m}(k\rho) F_{n_0 l_0}\left(\sqrt{k^2 + (\omega/v - v/2)^2}\right) \qquad (9)$$
$$\times F_{n_1 l_1}\left(\sqrt{k^2 + (\omega/v + v/2)^2}\right),$$

where

$$C_{lm} = \left(\frac{(2l+1)(l-m)!}{(l+m)!}\right)^{1/2}, \quad \Delta m = |m_0 - m_1|, \qquad (10)$$

$$\cos\Theta_1 = \frac{\frac{v}{2} + \frac{\omega}{v}}{\sqrt{k^2 + \left(\frac{\omega}{v} + \frac{v}{2}\right)^2}},$$
$$\cos\Theta_0 = \frac{\frac{v}{2} - \frac{\omega}{v}}{\sqrt{k^2 + \left(\frac{\omega}{v} - \frac{v}{2}\right)^2}}, \qquad (11)$$

$P_l^m$ is the Legendre polynomial, and $J_m(x)$ is the Bessel function.

The functions $F$ for the initial and final states are defined by the radial integrals

$$F_{n_0 l_0}(y) = \int_0^\infty P_{n_0 l_0}(r) j_{l_0}(ry) r dr, \qquad (12)$$

$$F_{n_1 l_1}(x) = \int_0^\infty P_{n_1 l_1}(r) j_{l_1}(rx) V(r) r dr, \quad x^2 - y^2 = 2\omega, \qquad (13)$$

where $j_l(x)$ is the spherical Bessel function and $V(r)$ characterizes the interaction of the resulting ion $X^{(q-1)+}$ with an optical electron whose radial functions $P(r)$ are normalized as

$$\int_0^\infty P_{nl}^2(r) dr = 1. \qquad (14)$$

In the impact parameter representation, the exchange cross section is given by

$$\sigma(v) = 2\pi\int_0^\infty W(\rho, v)\rho d\rho, \qquad (15)$$

where $W(\rho, v) = |a(\rho, v)|^2$ is the exchange probability.

## HYDROGEN-LIKE APPROXIMATION

For the charge exchange of nuclei on hydrogen-like systems,

$$Z_1 + Z_0(n_0 l_0 m_0) \longrightarrow Z_1(n_1 l_1 m_1) + Z_0 \qquad (16)$$

expressions for the probabilities and the cross sections can be obtained in the closed analytical form by using

the H-like wave functions of an optical electron in the initial and final states:

$$P^z_{nl}(r) = Z^{1/2}P^H_{nl}(Zr), \tag{17}$$

where $P^H_{nl}(r)$ is the radial wave function of a hydrogen atom and the Coulomb interaction potential has the form $V(r) = -Z_1/r$.

For the exchange from the ground $1s_0$ state,

$$Z_1 + Z_0(1s_0) \longrightarrow Z_1(nlm) + Z_0, \tag{18}$$

to the final state $1s \le nl \le 3d$, the exchange amplitudes $a(\rho, v)$ are

$$a(1s_0 - 1s_0) = \frac{2\rho^2(Z_0Z_1)^{5/2}}{vD^2}K_2(\rho D),$$

$$a(1s_0 - 2s_0) = \frac{\rho^2(Z_0Z_1)^{5/2}}{\sqrt{2}vD^2}\left(K_2(\rho D) - \frac{\rho Z_1^2 K_3(\rho D)}{12D}\right),$$

$$a(1s_0 - 2p_0) = \frac{\sqrt{2}\rho^3(Z_0Z_1)^{5/2}Z_1}{12vD^3}\left(\frac{\omega}{v} + \frac{v}{2}\right)K_3(\rho D),$$

$$a(1s_0 - 2p_{\pm1}) = \frac{\rho^3(Z_0Z_1)^{5/2}Z_1}{12vD^2}K_2(\rho D),$$

$$a(1s_0 - 3s_0) = \frac{2}{3\sqrt{3}}\frac{(Z_0Z_1)^{5/2}\rho^2}{vD^2} \tag{19}$$

$$\times\left(K_2(\rho D) - \frac{8Z_1^2\rho}{3^4D}K_3(\rho D) + \frac{Z_1^4\rho^2}{3^6D^2}K_4(\rho D)\right),$$

$$a(1s_0 - 3p_{\pm1}) = \frac{2^2}{3^4}\frac{(Z_0Z_1)^{5/2}Z_1\rho^3}{vD^2}$$

$$\times\left(K_2(\rho D) - \frac{Z_1^2\rho}{36D}K_3(\rho D)\right),$$

$$a(1s_0 - 3d_0) = \frac{2^3(Z_0Z_1)^{5/2}Z_1^2\rho^3}{3^5\sqrt{6}vD^3}$$

$$\times\left(\left[2\left(\frac{\omega}{v} + \frac{v}{2}\right)^2 + D^2\right]\frac{\rho}{2^3D}K_4(\rho D) - K_3(\rho D)\right),$$

$$a(1s_0 - 3d_{\pm1}) = \frac{(Z_0Z_1^2)^{5/2}Z_1^2\rho^4}{3^5vD^3}\left(\frac{\omega}{v} + \frac{v}{2}\right)K_3(\rho D), \tag{20}$$

$$a(1s_0 - 3d_{\pm2}) = \frac{(Z_0Z_1^2)^{5/2}Z_1^2\rho^4}{2\times3^5vD^2}K_2(\rho D),$$

$$D^2 = \left(\frac{\omega}{v} + \frac{v}{2}\right)^2 + \frac{Z_1^2}{n_1^2}, \quad \omega = \frac{Z_0^2}{2n_0^2} - \frac{Z_1^2}{2n_1^2}.$$

Here, $K_n(r)$ are the Macdonald functions with the asymptotics

$$K_n(r) \cong \begin{cases} (n-1)!2^{n-1}r^{-n}, & n \neq 0, \quad r \longrightarrow 0 \\ \ln\dfrac{2}{\gamma r} = \ln\dfrac{2}{r} - 0.577, & n = 0, \ r \longrightarrow 0, \ \gamma = 1.78 \\ \sqrt{\dfrac{\pi}{2r}}e^{-r}, & r \longrightarrow \infty. \end{cases} \tag{21}$$

Formula (19) for the resonance exchange probability (the resonance defect $\omega = 0$) coincides with that obtained in [9] for the charge exchange of protons on hydrogen atoms in the ground state, as well as with the formula [10] (up to a factor of $\sqrt{\pi}/2$) obtained by the strong coupling method for two levels. The above analytic formulas for the probability amplitudes can be used for estimating the probability distribution and exchange cross sections over the quantum numbers $l$ and $m$. They can also be applied for estimating the multielectron capture probability when multiply charged ions collide with atomic and ionic targets.

For $n_0 - n_1$ transitions,

$$Z_1 + Z_0(n_0) \longrightarrow Z_1(n_1) + Z_0 \tag{22}$$

(that is, for those averaged over the quantum numbers $l$ and $m$), the summation of the exchange probabilities is impossible even in the hydrogen-like approximation. In this case, however, one can take advantage of the properties of the quantum amplitude for the $n_0 - n_1$ transitions. The radial part of this amplitude has the form [8]

$$\left|f_{n_0n_1}(k, v)\right|^2 = \frac{1}{n_0^2}\sum_{l_0m_0l_1m_1}\left|f_{n_0l_0m_0, n_1l_1m_1}(k, v)\right|^2$$

$$= \frac{2^6(Z_0Z_1)^5}{n_0^5n_1^3\left[k^2 + \left(\dfrac{\omega}{v} + \dfrac{v}{2}\right)^2 + \dfrac{Z_1^2}{n_1^2}\right]^6} \tag{23}$$

[$k$ is given by (8)].

Using relationship (5) with the amplitude $f_{n_0n_1}(k, v)$ and also the fact that the resonance defect for reaction (22) depends on the quantum numbers $l$ and $m$ only slightly, one obtains for the exchange probability aver-

aged over $l$ and $m$[1]

$$|a_{n_0 n_1}(\rho, v)|^2 = \frac{4(Z_0 Z_1)^5 \rho^4}{n_0^5 n_1^3 v^2 \left[\left(\frac{\omega}{v} + \frac{v}{2}\right)^2 + \frac{Z_1^2}{n_1^2}\right]^2} K_2^2\left(\rho \sqrt{\left(\frac{\omega}{v} + \frac{v}{2}\right)^2 + \frac{Z_1^2}{n_1^2}}\right). \quad (24)$$

The exchange cross section for the $n_0 - n_1$ transition calculated with the quantum [expression (23)] or quasiclassical [expression (24)] amplitude coincides with the result obtained in [12]:

$$\begin{aligned}\sigma(n_0 - n_1) &= \frac{8\pi a_0^2}{v^2} \int_{\left|\frac{\omega}{v} + \frac{v}{2}\right|}^{\infty} |f_{n_0 n_1}(k, v)|^2 k dk \\ &= 2\pi \int_0^{\infty} |a_{n_0 n_1}(\rho, v)|^2 \rho d\rho \\ &= \pi a_0^2 \frac{2^8 (Z_0 Z_1)^5}{5 n_0^5 n_1^3 v^2} \left[\left(\frac{\omega}{v} + \frac{v}{2}\right)^2 + \frac{Z_1^2}{n_1^2}\right]^{-5}, \\ \omega &= I_0 - I_1 = \frac{Z_0^2}{2n_0^2} - \frac{Z_1^2}{2n_1^2}.\end{aligned} \quad (25)$$

Formula (25) is the Brinkman–Kramers approximation and is applied for estimating the charge exchange cross sections at high collision energies $E > 25$ keV/u ($v > 1$ a.u.).

## EXCHANGE PROBABILITY NORMALIZATION IN THE IMPACT PARAMETER REPRESENTATION

The exchange probabilities and cross sections calculated by formulas (9)–(15) are often one order of magnitude higher than those found experimentally. This is especially true when the relative velocities are low, $v < \sqrt{2|\omega|}$. The reason is that relationship (5) has been obtained in the first order of the perturbation theory. Therefore, it can violate the condition of flux conservation for incident and scattered particles. In other words, the unitarity of the scattering matrix is violated, hence, larger (greater than unity) transition probabilities. This weakness is usually removed by applying more accurate computing procedures, such as the method of strong coupling between atomic states or the method of charge exchange probability normalization in the impact parameter representation (see, e.g., [1, 10]).

[1] Such a procedure of calculating the amplitudes averaged over the magnetic and orbital quantum numbers is common in the theory of atomic collisions. For example, it was used in [11] to calculate the probabilities of the transitions between highly excited atomic levels.

In this work, we use a method of multichannel normalization of the exchange probability for the 0–1 transition in the form

$$W_{01}^N(\rho, v) = \frac{W_{01}(\rho, v)}{1 + \sum_j W_{0j}(\rho, v)}, \quad (26)$$

where the summation in the denominator is over all possible final exchange channels $j$ for the resulting ion $X^{(q-1)+}$, including the exchange into the state 1 under study.

The physical meaning of formula (26) is straightforward: if the probabilities $W_{01}$ are small, the normalized probability is also small, $W_{01}^N \approx W_{01}$. Even if the unnormalized probabilities $W_{01}$ are large ($W_{01} \gg 1$), the normalized value remains small, $W_{01}^N \leq 1$. Generally speaking, the sum in the denominator of (26) should be complemented by the probabilities of ionization channels occurring. These channels arise upon colliding heavy particles. However, in the low-energy region, where the effect of normalization is essential, the ionization is negligible in comparison with the charge exchange (see, e.g., [1]) and is not considered in the article.

The total cross sections of charge exchange for multielectron systems are difficult to calculate with formulas (9)–(15) and (26) even in a narrow energy range. It is necessary to estimate the wave functions and matrix elements of many excited $nl$ states of the $X^{(q-1)+}(nl)$ ion, whose contributions to the total cross section may be of the same order. In addition, one should take into account the possibility of inner shell electrons of the target being captured [13]. Note also that the energies of the excited levels in heavy ions are unknown in most cases. At the same time, for a number of applications, it is necessary to estimate the total exchange cross sections without resort to the numerical evaluations of the energy levels and the radial wave functions. This can be accomplished with the multichannel normalization method suggested and using hydrogen-like wave functions for electrons captured.

The wisdom of using H-like functions is the following. First, it is known [1] that the electron capture in the highly excited (hydrogen-like) states of a resulting ion makes a great contribution to the total cross section of charge exchange. At large collision energies, the exchange cross sections depend largely on the capture of inner shell electrons of the target, which are located near the unscreened nucleus and are also hydrogen-like. Second, the use of the hydrogen-like functions considerably simplify the calculation of the exchange total cross sections, i.e., those averaged over the quantum numbers $m$ and $l$. This is associated with the special form of exchange matrix elements, which are the Fourier components of the wave functions of an optical electron [12]. In this article, the problem of normalizing

the probabilities and cross sections in the impact parameter representation with H-like wave functions is solved by using the CAPTURE program, described in the next section.

## NUMERICAL CALCULATION OF EXCHANGE PROBABILITIES AND CROSS SECTIONS

The probabilities and the cross sections of charge exchange were calculated with the CAPTURE program by using formulas (9)–(15) and (26) and hydrogen-like functions (17) with the effective charge

$$Z^* = n\sqrt{2I_{nl}}, \quad (27)$$

where $I_{nl}$ is the binding energy of an electron in the initial or in the final state and $n$ is the principal quantum number.

Generally speaking, one can use H-like wave functions with an integer charge $Z$ (as a rule, this charge corresponds to the spectroscopic symbol of an atom or an ion) and the effective quantum number

$$n^* = (2I_{nl}/Z^2)^{-1/2}. \quad (28)$$

Functions with the effective (noninteger) quantum numbers $n^*$ were used, for example, to calculate the dipole and quadrupole matrix elements in the Bates–Damgaard tables [14]. For the charge exchange problem, approximations (17) and (27) with the integer $n$ are necessary, since they allow the analytical averaging over the orbital and magnetic quantum numbers $l$ and $m$, thereby greatly simplifying the procedure of calculating the probabilities and the cross sections.

In (13), the interaction potential $V(r)$ is taken in the form of Coulomb potential $V(r) = -Z^*/r$, where $Z^*$ is the effective charge (27) of the resulting ion $X^{(q-1)+}$. The program allows the normalization over an arbitrary number of the channels; in practice, however, $j < 50$ final states with the principal quantum numbers $n$ will suffice. Both total and partial (with respect to the principal quantum number $n$) probabilities and cross sections (i.e., those averaged over the orbital, $l$, and magnetic, $m$, quantum numbers of the initial and final states) can be calculated.

In the CAPTURE program, the unnormalized probabilities $W_{01}$ (26) of one-electron charge exchange [are multiplied by the factor $0.295N$, where $N$ is the number of equivalent electrons in the capturing target shell and the numerical coefficient 0.295 provides the correct asymptotics of the cross section at large energies [1].

In Figs. 1–10, the exchange probabilities and cross sections calculated with the CAPTURE program by formulas (9)–(15), (17), (26), and (27) are compared with experimental data and with results obtained by other techniques. Figures 1–3 show the probabilities (more exactly, the values of $\rho W(\rho)$) of charge exchange for protons and $\alpha$ on hydrogen and lithium atoms. In the case of hydrogen atoms H(1$s$) (Figs. 1, 2), the electron capture probabilities calculated by the multichannel normalization method agree well with those obtained by the method of strong coupling of molecular states and by the classical approach.

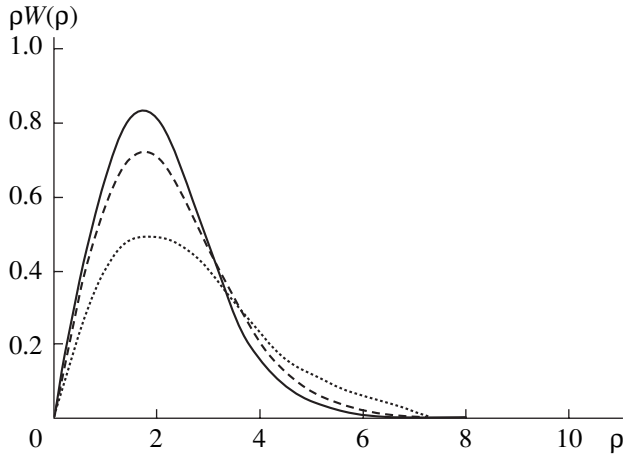


**Fig. 1.** Calculated probabilities $\rho W(\rho)$ of the 1$s$ electron of a hydrogen atom being captured by a proton ($H^+ + H(1s) \longrightarrow H + H^+$) in all final states of the resulting H atom as a function of impact parameter $\rho$. The relative velocity $v = 1$ a.u. Dotted curve, classical calculation [15]; dashed curve, method of strong coupling between molecular states [16]; and continuous curve, multichannel normalization method (this work).

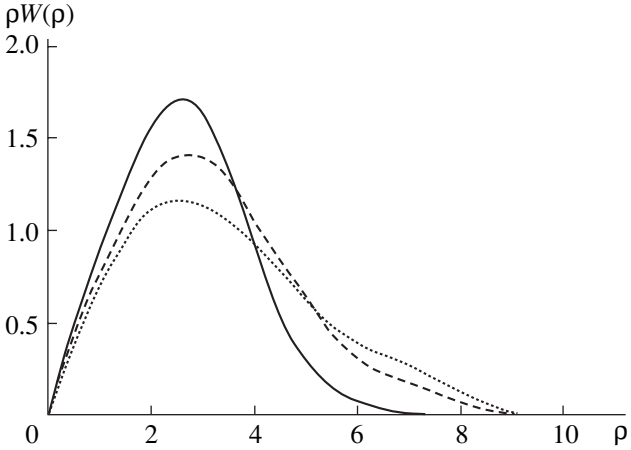


**Fig. 2.** The same as in Fig. 1 for $He^{2+} + H(1s) \longrightarrow He^+ + H^+$ reaction.

The variation of the capture probabilities for electrons from different target shells when the $\alpha$ particles collide with the Li atoms is demonstrated in Fig. 3 for the velocities $v = 0.8$, 1.3, and 2.0 atomic units (a.u.) (1 a.u. $\cong 2.2 \times 10^8$ cm/s). For $v = 0.8$ a.u., the 2$s$ outer shell electron is captured most probably at $v = 1.3$ a.u., the capture probabilities for the 2$s$ and 1$s$ electrons are nearly the same; and at $v > 2.0$ a.u., the 1$s$ inner shell electrons are captured most probably. For the reaction $He^{2+} + Li(1s^2 2s)$, the total cross section of the exchange

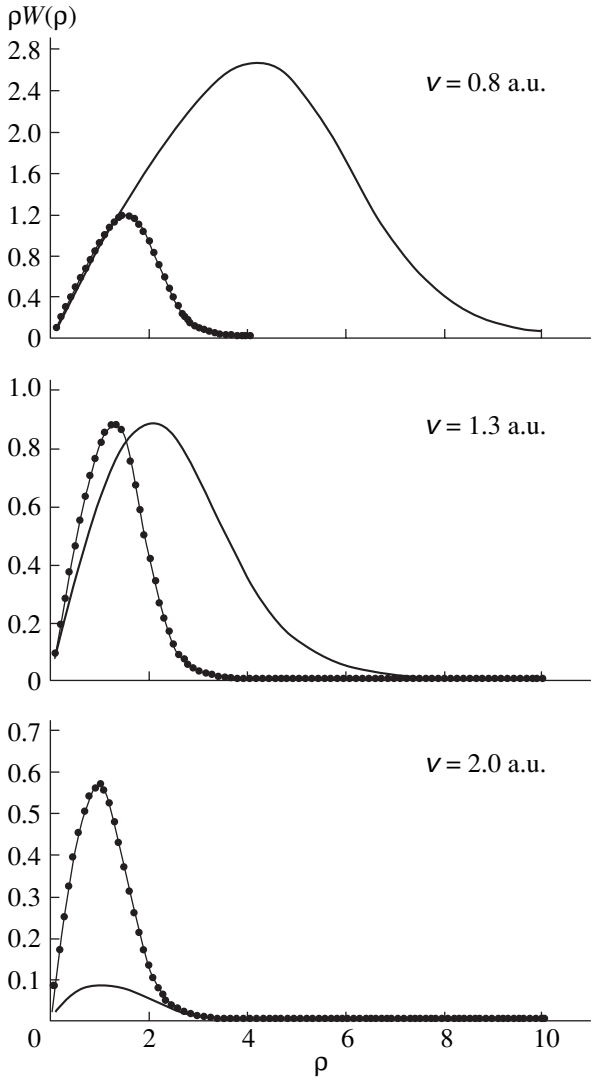


**Fig. 3.** Variation of the probabilities of capturing the outer shell, 2*s*, and the inner shell, 1*s*, electrons of a lithium atom Li($1s^2 2s$) upon collision with $He^{2+}$ ions. Continuous curves, capture of the 2*s* electron; dotted curves, capture of the 1*s* electron (this work).

calculated from formulas (9)–(15), (17), (26), and (27) is in satisfactory agreement with experimental data [17, 18] and other calculations.

Figure 4 depicts the probabilities of outer shell electrons being captured in all states of resulting $Bi^{0+}$ and $U^{3+}$ ions upon $Bi^{1+} + Bi^{1+}$ and $U^{4+} + U^{4+}$ collisions at the relative velocity $v = 1$ a.u. In these figures, the values of $\rho W(\rho)$ correspond to the integrand in (15) and have a maximum at the impact parameters $\rho \approx 2.2a_0$ and $3.8a_0$, where $a_0$ is the Bohr radius. As for the normalized exchange probabilities, $W(\rho) \longrightarrow$ const at $\rho \longrightarrow 0$: $W(\rho = 0) = 0.87$ and 0.97 for the $Bi^{1+}$ and $U^{4+}$ ions, respectively. At $\rho \longrightarrow \infty$, they exponentially drop according to the asymptotic behavior of Macdonald functions (21).

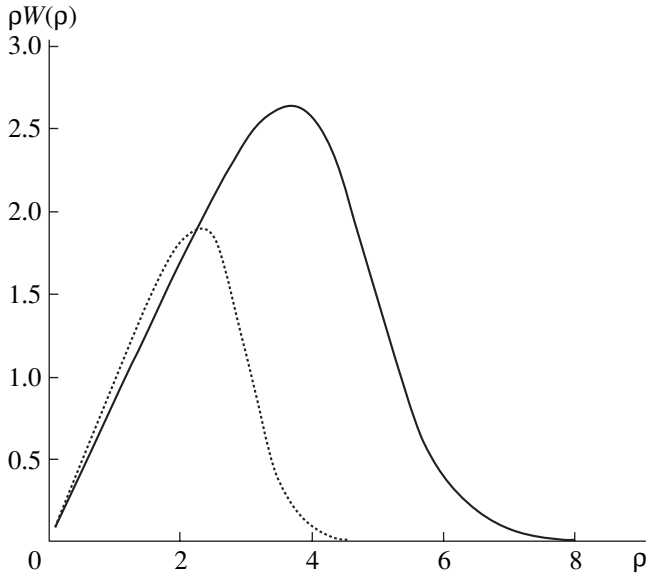


**Fig. 4.** Probabilities $\rho W(\rho)$ of capturing the inner shell electron for the reactions $Bi^+ + Bi^+(6p^2) \longrightarrow Bi^{0+} + Bi^{2+}$ and $U^{4+} + U^{4+}(5f^2) \longrightarrow U^{3+} + U^{5+}$ in all final states of the resulting $Bi^{0+}$ and $U^{3+}$ ions as a function of impact parameter ρ. The relative velocity $v = 1$ a.u. Continuous curve, bismuth ion collision; dotted curve, uranium ion collision (this work).

The charge exchange total cross sections for the singly charged and four-charged ions are given in Figs. 5 and 6, respectively, and the table lists their values as a function of relative energy $E$ [keV/u] $\cong 25v^2$ [a.u.]. The table also shows the resonance defects ω for the charge exchange reactions considered. From Figs. 5 and 6, it follows that the cross sections are rather large, despite the Coulomb character of the interaction between the colliding ions, and peak at $E \cong 10$–30 keV/u, that is, at $v \cong 1$ a.u. For the $X^{1+} + X^{1+} \longrightarrow X^{0+} + X^{2+}$ collisions, the maximal cross sections are $\sigma_m \approx 0.5$–$3.0 \times 10^{-15}$ cm$^2$, while for the $X^{4+} + X^{4+} \longrightarrow X^{3+} + X^{5+}$ collisions, $\sigma_m \approx 5$–$8 \times 10^{-16}$ cm$^2$. At $E < 10$ keV/u, the cross sections rapidly decrease with increasing resonance defect ω and become dependent on the electron shell configuration in the colliding ions.

For the four-charged ions (Fig. 6), the exchange cross sections were calculated in a wider energy range. Unlike Fig. 5, where the cross sections were calculated under the assumption that only the outer shell electron of the target is captured, the sections in Fig. 6 were estimated with regard for all inner shell electrons, which contribute significantly at high collision energies. The cross section of charge exchange on neutral uranium atoms is also given for comparison (Fig. 6, curve *1*). As was expected, the section is large ($\approx 1.1 \times 10^{-14}$ cm$^2$) at low energies and is nearly independent of the collision energy. This value is well fitted by the conventional expression for cross section when multiply charged

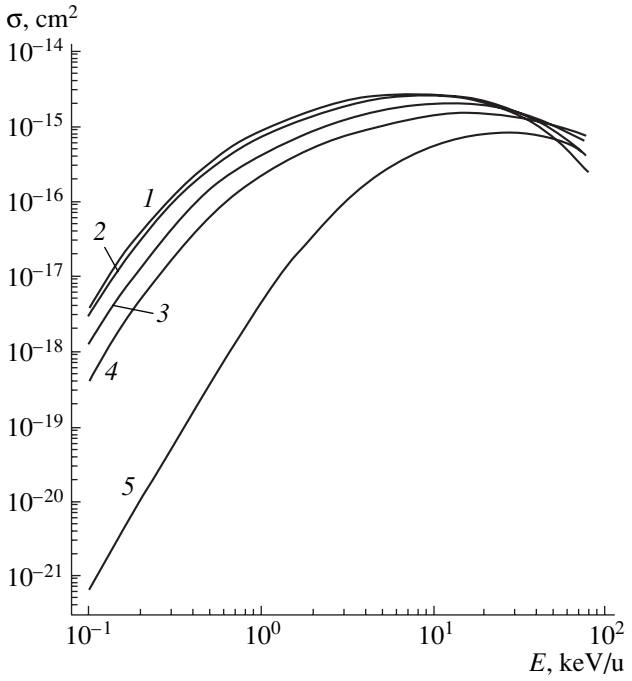


**Fig. 5.** Cross section of charge exchange between heavy singly charged ions vs. relative collision energy $E$. (*1*) $Ba^{1+}$ + $Ba^{1+}$, (*2*) $U^{1+}$ + $U^{1+}$, (*3*) $Bi^{1+}$ + $Bi^{1+}$, (*4*) $Xe^{1+}$ + $Xe^{1+}$, and (*5*) $Cs^{1+}$ + $Cs^{1+}$ (this work).

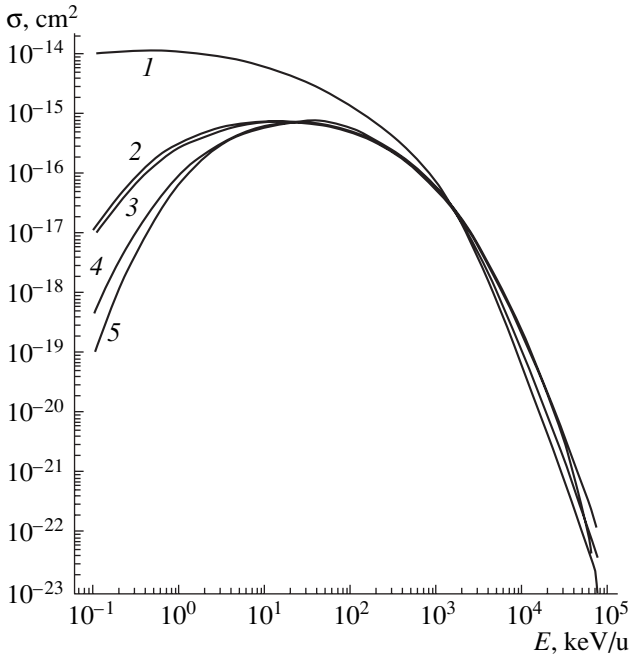


**Fig. 6.** Cross section of charge exchange between heavy four-charged ions vs. relative collision energy $E$. (*1*) $U^{4+}$ + $U^{0+}$, (*2*) $Bi^{4+}$ + $Bi^{4+}$, (*3*) $Xe^{4+}$ + $Xe^{4+}$, (*4*) $Pb^{4+}$ + $Pb^{4+}$, and (5) $U^{4+}$ + $U^{4+}$ (this work).

ions exchange charge with neutral atoms at low energies [1]:

$$\sigma \approx \text{const} = 10^{-15} cm^2 \frac{q}{(I_A/Ry)^{3/2}}; \qquad E/q^{1/2} < 10 \text{ keV/u}, \tag{29}$$

where $I_A$ is the ionization potential of a neutral target atom, 1 Ry = 13.606 eV. For the $U^{4+} + U^{0+} \longrightarrow U^{3+} + U^{1+}$ collisions, estimate (29) yields $\sigma \approx 1.4 \times 10^{-14}$ cm$^2$.

In the method suggested, the exchange cross sections severely depend on the resonance defect ω. At relatively low energies, $E < 20$ keV/u, the sections sharply

Calculated cross sections (cm$^2$) of ion–ion collisions (2) and (3) vs. relative energy $E$

| $E$, keV/u | Colliding ions | | | | | | | | |
|---|---|---|---|---|---|---|---|---|---|
| | $Xe^+ + Xe^+$ | $Cs^+ + Cs^+$ | $Ba^+ + Ba^+$ | $Bi^+ + Bi^+$ | $U^+ + U^+$ | $Xe^{4+} + Xe^{4+}$ | $Pb^{4+} + Pb^{4+}$ | $Bi^{4+} + Bi^{4+}$ | $U^{4+} + U^{4+}$ |
| | ω = 11.6 | ω = 19.3 | ω = 4.79 | ω = 9.40 | ω = 5.44 | ω = 13.0 | ω = 26.5 | ω = 12.1 | ω = 19.0 |
| 0.1 | 3.7–19 | 6.4–22 | 3.5–18 | 2.1–18 | 2.7–18 | 8.7–18 | 4.8–19 | 1.1–17 | 1.2–19 |
| 0.2 | 4.6–18 | 1.0–20 | 3.5–17 | 1.3–17 | 2.7–17 | 3.7–17 | 4.2–18 | 4.4–17 | 5.1–18 |
| 0.4 | 3.4–17 | 1.5–19 | 1.9–16 | 8.0–17 | 1.5–16 | 1.1–16 | 2.1–17 | 1.3–16 | 1.2–17 |
| 0.8 | 1.4–16 | 2.0–18 | 6.2–16 | 2.9–16 | 5.0–16 | 2.5–16 | 6.9–17 | 2.8–16 | 5.3–17 |
| 1.0 | 2.0–16 | 4.3–18 | 8.3–16 | 4.0–16 | 6.8–16 | 3.1–16 | 9.6–17 | 3.4–16 | 7.8–17 |
| 2.0 | 5.0–16 | 3.6–17 | 1.6–15 | 8.8–16 | 1.4–15 | 5.1–16 | 2.2–16 | 5.3–16 | 2.0–16 |
| 4.0 | 9.0–16 | 1.6–16 | 2.4–15 | 1.5–15 | 2.1–15 | 6.7–16 | 4.3–16 | 6.8–16 | 3.9–16 |
| 8.0 | 1.3–15 | 4.3-16 | 2.7–15 | 1.9–15 | 2.6–15 | 7.4–16 | 6.3–16 | 7.3–16 | 5.8–16 |
| 10 | 1.4–15 | 5.4–16 | 2.7–15 | 2.0–15 | 2.6–15 | 7.5–16 | 6.9–16 | 7.6–16 | 6.2–16 |
| 20 | 1.5–15 | 8.1–16 | 2.1–15 | 1.9–15 | 2.2–15 | 7.5–16 | 8.0–16 | 7.3–16 | 7.3–16 |
| 40 | 1.2–15 | 7.8–16 | 1.1–15 | 1.4–15 | 1.3–15 | 6.9–16 | 8.0–16 | 6.8–16 | 6.9–16 |
| 80 | 7.4–16 | 4.3–16 | 2.5–16 | 6.7–16 | 4.2–16 | 5.7–16 | 6.1–16 | 5.9–16 | 6.1–16 |

Note: Resonance defect ω is given in eV; 3.7–19 means $3.7 \times 10^{-19}$.

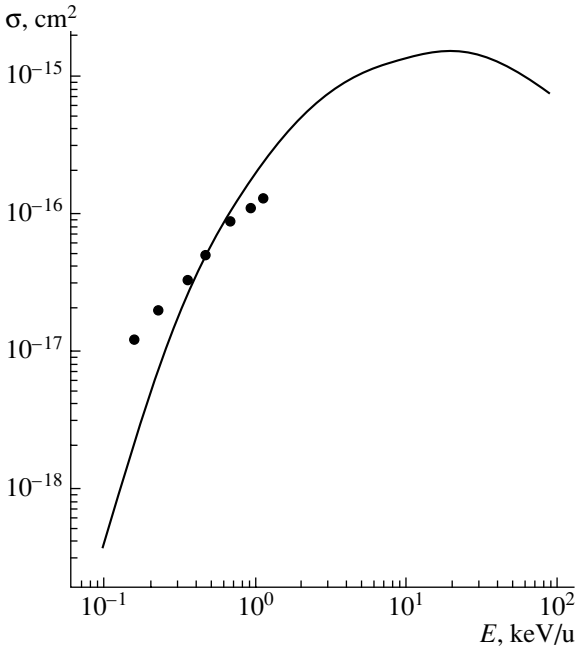


**Fig. 7.** Cross section of charge exchange upon $Xe^{1+} + Xe^{1+}$ collision vs. relative collision energy *E*. Circles, experiment [3]; continuous curve, this work.

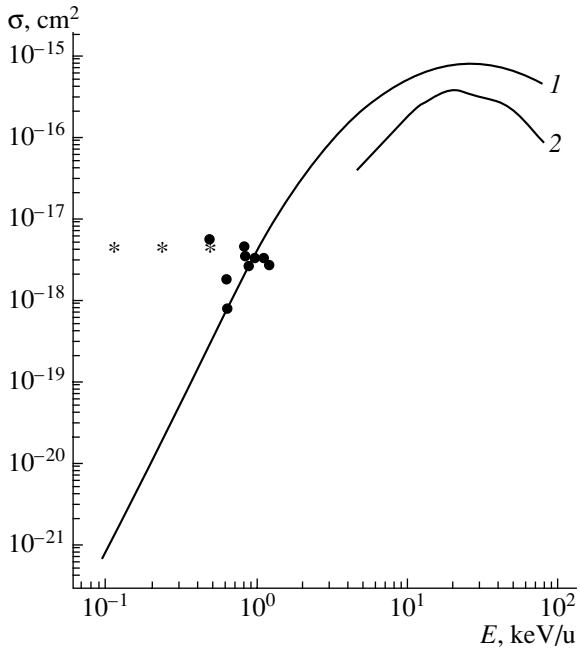


**Fig. 8.** Cross section of charge exchange upon $Cs^{1+} + Cs^{1+}$ collision vs. relative collision energy *E*. Circles, experiment [19]; stars, experiment [3]; (*1*) this work and (*2*) calculation by the method of atomic orbitals [20].

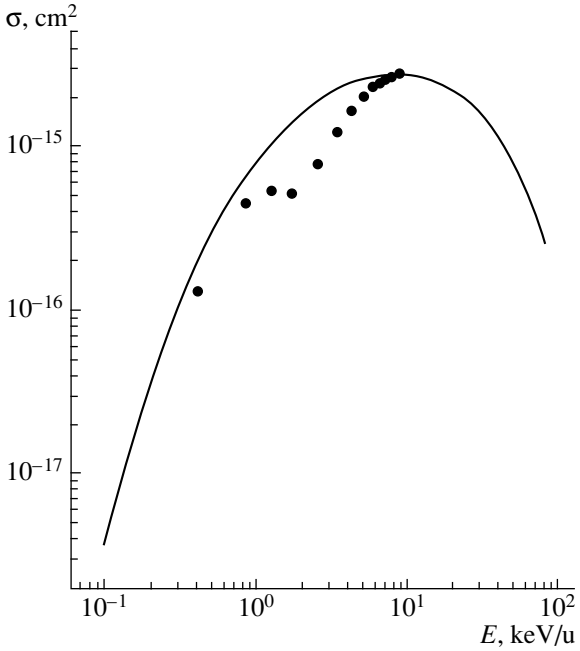


**Fig. 9.** Cross section of charge exchange upon $Ba^{1+} + Ba^{1+}$ collision vs. relative collision energy *E*. Circles, classical trajectory method [21]; continuous curve, this work.

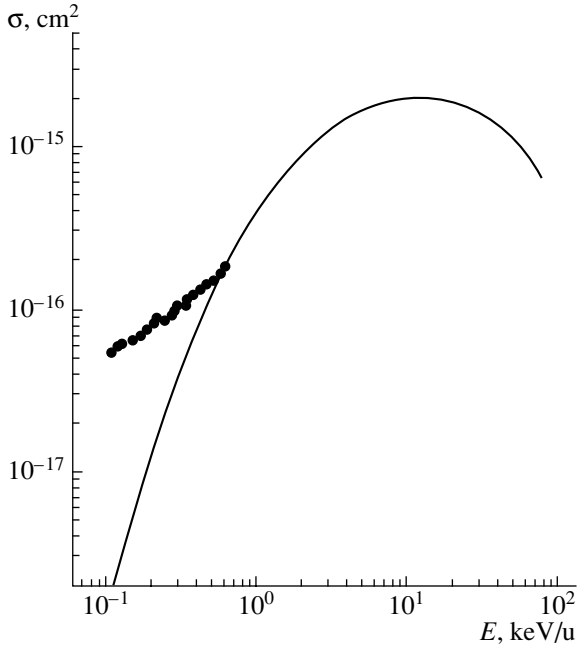


**Fig. 10.** Cross section of charge exchange upon $Bi^{1+} + Bi^{1+}$ collision vs. relative collision energy *E*. Circles, experiment [22]; continuous curve, this work.

decrease with increasing ω (Figs. 5, 6). They are the smallest for reactions with the greatest ω (such as $Cs^{1+} + Cs^{1+}$, $Pb^{4+} + Pb^{4+}$, or $U^{4+} + U^{4+}$ with ω = 19.3, 26.5, and 19.0 eV, respectively), while for reactions with the same resonance defects, they are roughly equal (Fig. 5, curves *1* and *2*; Fig. 6, curves *4* and *5*). At high collision energies, the exchange cross sections are almost independent of ω and depend largely on the electron shell configuration in the target atom. At $E >$ 1 MeV/u, where the capture of inner shell electrons of the target prevails, the exchange cross sections for the reactions $U^{4+} + U^{4+} \longrightarrow U^{3+} + U^{5+}$ and $U^{4+} + U^{0+} \longrightarrow$

$U^{3+} + U^{1+}$(i.e., for ion–ion and ion–atom collisions) virtually coincide (curves *1* and *5*), although the targets have the different number of electrons. The equality of the charge exchange cross sections in ion–ion and ion–atom collisions at high energies follows from the theory of charge exchange on multielectron systems [1, 13] and is essential to the understanding of the process.

A more detailed comparison of the cross sections calculated with available experimental and analytical data is given in Figs. 7–10. In Figs. 7 and 8, the sections calculated for the $Xe^{1+} + Xe^{1+}$ and $Cs^{1+} + Cs^{1+}$ reactions are compared with experimental data from [3]. Note the large cross sections of ion–ion charge exchange and their quasi-constant values at low energies (data obtained by the team headed by Prof. E. Salzborn in the University of Gissen, Germany) for the collision $Cs^{1+} + Cs^{1+}$ (stars in Fig. 8) and also the large values of the recently measured cross sections for the $Xe^{4+} + Xe^{4+}$ and $Bi^{4+} + Bi^{4+}$ collisions. These data for the cross sections of ion–ion charge exchange have not yet been properly explained. Possibly, such behavior is associated with the presence of metastable ions in the beams. The cross sections of charge exchange between unexcited and excited cesium ions,

$$Cs^{1+} + [Cs^{1+}(5p^5 6s)]^* \longrightarrow Cs^{0+} + Cs^{2+}$$
$$(\omega = 7.8 \text{ eV})$$

at $E = 0.25$ keV/u was estimated at $\sigma \approx 3.8 \times 10^{-18}$ cm$^2$, which is several orders of magnitude higher than the cross section of charge exchange on cesium ions in the ground state,

$$Cs^{1+} + Cs^{1+}(5p^6) \longrightarrow Cs^{0+} + Cs^{2+}$$
$$(\omega = 19.3 \text{ eV})$$

at the same energy (Fig. 8).

This point invites further investigation and is omitted in this article.

The exchange cross sections for the $Ba^{1+} + Ba^{1+}$ and $Bi^{1+} + Bi^{1+}$ collisions are shown in Figs. 9 and 10. At $E > 1$ keV, our results agree with experimental data and calculations made by the method of molecular orbitals (Fig. 9) and by the classical method (Fig. 10). It should be noted that, unlike the method used in [21], our procedure cannot calculate the cross section of charge exchange for a particular value of the spin of a target atom or a resulting ion. It yields only cross sections averaged over all (except principal) quantum numbers.

Thus, the cross sections of charge exchange between heavy low-charged ions calculated by the probability normalization method in the impact parameter representation are in fairly good agreement with available experimental data and other calculations. Our method provides relatively accurate (up to a factor of 2 or 3) values of the sections at energies $E > 1$–10 keV/u. More comprehensive conclusions are difficult to make, since data on the cross sections for the systems under study are very scarce. However, it has been demonstrated that the cross sections of charge exchange in ion–ion collisions may be large because of a great number of electrons in the colliding systems and also because of small resonance defects. New experiments and detailed calculations of the cross sections of charge exchange and stripping are necessary in order to gain full information on the collision parameters of low-charged multielectron ions.

## CONCLUSION

Using the method of multichannel normalization in the impact parameter representation, we made preliminary calculations of the cross sections of charge exchange between heavy low-charged ions. In the energy range $E > 1$–10 keV/u, the cross sections are in qualitative agreement with some experimental data and calculations performed by other authors. At lower energies, the normalization method proves to be inaccurate, since it ignores Coulomb repulsion of colliding ions, resonance defect vs. internuclear spacing dependence, and other effects. One advantage of the method is that the total cross sections of charge exchange between heavy multielectron atoms and ions can be calculated with regard for the capture of inner shell electrons of the target and the capture into excited states. Definite conclusions on the applicability of the probability normalization method can be drawn after further detailed calculations have been made and compared with new experimental data and results obtained by other methods.

## ACKNOWLEDGMENTS

The author is indebted to I.L. Beĭgman for the valuable comments and I.Yu. Tolstikhina for the assistance in the developing the CAPTURE program.

This work was supported by the Russian Foundation for Basic Research (grant no. 01-02-16139).

## REFERENCES

1. L. P. Presnyakov, V. P. Shevel'ko, and R. K. Yanev, *Elementary Processes with the Participation of Multiply Charged Ions* (Énergoatomizdat, Moscow, 1986).
2. *The HIDIF-Study*, Ed. by I. Hofmann and G. Plass (GSI, Darmstadt, 1998), Report GSI-98-06.
3. F. Melchert, in *Atomic Physics with Heavy Ions*, Ed. by H. Beyer and V. P. Shevelko (Springer-Verlag, Berlin, 1999), p. 323.
4. P. Gombäs, *Die Statistuche Theorie des Atoms und Ihre Anwendungen* (Springer-Verlag, Vienna, 1949; Inostrannaya Literatura, Moscow, 1951).
5. R. E. Olson, Phys. Rev. A **24**, 1726 (1981).
6. V. P. Shevelko, J. Phys. B **13**, L319 (1980).
7. V. P. Shevel'ko, Kratk. Soobshch. Fiz. **5**, 36 (1981).
8. V. P. Shevelko, Fizika (Zagreb) **13**, 185 (1981).

9. H. C. Brinkman and H. A. Kramers, Proc. R. Acad. Sci. Amsterdam **33**, 973 (1930).
10. L. P. Presnyakov, Tr. Fiz. Inst. Akad. Nauk **119**, 52 (1980).
11. I. L. Beĭgman, L. A. Vaĭnshteĭn, and I. I. Sobel'man, Zh. Éksp. Teor. Fiz. **57**, 1703 (1969) [Sov. Phys. JETP **39**, 920 (1970)].
12. R. M. May, Phys. Rev. A **136**, 669 (1964).
13. A. V. Vinogradov and V. P. Shevel'ko, Zh. Éksp. Teor. Fiz. **59**, 593 (1970) [Sov. Phys. JETP **32**, 323 (1971)].
14. L. P. Vaĭnshteĭn, I. I. Sobel'man, and E. A. Yukov, *Excitation Cross Sections of Atoms and Ions by Electrons* (Nauka, Moscow, 1973).
15. L. F. Errea, C. Harel, and C. Illescas, J. Phys. B **31**, 3199 (1998).
16. C. Illescas, I. Rabadan, and A. Riera, Phys. Rev. A **57**, 1809 (1998).
17. G. A. Murray, J. Stone, M. Mayo, and T. J. Morgan, Phys. Rev. A **25**, 1805 (1982).
18. K. Kadota, D. Dijkkamp, and R. L. van der Woude, J. Phys. B **15**, 3275 (1982).
19. B. Peart, R. A. Forrest, and K. T. Dolder, J. Phys. B **14**, L383 (1981).
20. A. M. Ermolaev, C. J. Noble, and B. H. Bransden, J. Phys. B **15**, 457 (1982).
21. S. J. Sramek, J. H. Macek, and G. A. Gallup, Phys. Rev. A **22**, 1467 (1980).
22. F. Melchert, E. Salzborn, I. Hofmann, *et al.*, Nucl. Instrum. Methods Phys. Res. A **278**, 65 (1989).

*Translated by V. Isaakyan*

*Technical Physics, Vol. 46, No. 10, 2001, pp. 1235–1241. Translated from Zhurnal Tekhnicheskoĭ Fiziki, Vol. 71, No. 10, 2001, pp. 29–35.*


**ATOMS, SPECTRA, RADIATION**

# The Effect of Inelastic Loss on the Development of Interatomic Collision Cascades

**V. V. Marinyuk and V. S. Remizovich**

*Moscow State Engineering Physics Institute (Technical University), Kashirskoe sh. 31, Moscow, 115409 Russia*

*e-mail: remixa@online.ru*

Received July 12, 2000; in final form, December 26, 2000

**Abstract**—A theory of interatomic collision cascades in an infinite medium subject to inelastic energy loss (ionization slowdown) of particles is developed. Emphasis is on the angular and energy distributions of primary ions and cascade atoms upon slowdown. Analysis is performed under the assumption that single scattering of the particles follows the hard ball law, and the electronic stopping power of the medium is determined by the Lindhard formula. It is shown that the inclusion of slowdown directly in solving the Boltzmann transport equation radically changes the angular and energy spectra of the ions and cascade atoms obtained when the slowdown is ignored. Moreover, slowdown is the factor responsible for the anisotropy of the angular distributions of low-energy primary ions and cascade atoms. © *2001 MAIK "Nauka/Interperiodica".*

## INTRODUCTION

The available theories of sputtering amorphous materials under linear cascade conditions are based on solving the Boltzmann transport equation [1–4]. Sputtering analysis usually ignores inelastic loss of the atom energy [5–12]. One can distinguish three basic mechanisms of inelastic energy loss. First, energy loss due to collisions with atomic electrons (ionization slowdown). For atomic particles, this loss can be considered almost continuous. Second, the energy is lost when the atoms cross the target boundary because of the surface potential barrier. Third, discrete energy loss when the atom is knocked out.

Sigmund [5, 6] has suggested the procedure that approximately takes into consideration the ionization slowdown of the atoms. Its essence is that the energy distribution of sputtered atoms (obtained when a solution of the Boltzmann transport equation ignores slowdown) is refined by multiplying by the factor $\nu(T_0)/T_0$. This factor is the fraction of the initial energy $T_0$ of the atom that is spent on interatomic collision cascades. In other words, according to Sigmund, taking account of ionization slowdown is reduced to multiplying the final result by a constant factor that depends neither on the energy nor on the sputtered atom direction. Later, Williams suggested the way to accurately take into consideration ionization slowdown upon calculating the amount of displaced atoms [13, 14]. He showed that the total number of the displaced atoms turns out to be finite if ionization slowdown is considered directly in solving the transport equation (when this phenomena is not considered, the total number of the displaced atoms becomes infinite). As for the second and third mechanisms of inelastic loss, they also can accurately be taken into consideration (see, e.g., [1]). However, none of the present-day theories uses these accurate procedures [5–12].

Interatomic collision cascades can be described most simply in the case of an infinite medium with a uniform distribution of ion sources. The problem thus stated has been solved to theoretically derive the angular and energy spectra of sputtered atoms [6–8] (the so-called steady-state spectra [1]). For inverse-power interatomic potentials ($V(r) \propto r^{-1/m}$) in the absence of slowdown, the steady-state spectrum of sputtered atoms is proportional to $1/T^{2-2m}$ (at $T \longrightarrow 0$) [1, 2, 6] and is nonintegrable at $m \le 1/2$. Under such conditions, the total sputtering coefficient becomes infinitely large; therefore, the steady-state spectrum approximation without considering inelastic energy loss is inapplicable to the sputtering problem thus stated. Usually, the divergence of the atom energy distribution is removed by introducing a phenomenological surface potential barrier into the final result (obtained by solving the transport equation without considering the surface barrier) [15]. It can however be expected that the problem of energy spectrum divergence for the recoil atoms will not arise if inelastic energy loss is properly taken into consideration. Moreover, of great interest is the anisotropy of the angular distribution of the recoil atoms. It is known that the angular distribution of cascade atoms isotropizes as the particle energy diminishes. This circumstance is behind the isotropic cascade approximation in Sigmund's theory of sputtering [2].

Thus, the effect of inelastic energy loss on the energy and angular distributions of the recoil atoms still remains unclear. In this work, we try at least partially to bridge the gap by correctly taking into account the ion-

1063-7842/01/4610-1235$21.00 © 2001 MAIK "Nauka/Interperiodica"

ization slowdown of the atoms directly while solving the Boltzmann transport equation.

## STATEMENT OF THE PROBLEM

According to the Sigmund–Roosendaal–Sanders model [6–8], we assume that an ion source is uniformly distributed over an infinite target so that one particle of energy $T_0$ is emitted in the direction $\mathbf{\Omega}_0$ per unit time in a unit volume. Then, the differential flux densities of both sputtered ions, $N_{\text{ion}}(\mathbf{\Omega}, T)$, and recoil atoms, $N_{\text{rec}}(\mathbf{\Omega}, T)$, depend on the particle motion direction $\mathbf{\Omega}$ and their energy $T$ and are independent of the space coordinates (steady-state spectrum [1]). The unit vector $\mathbf{\Omega}$ of the particle velocity is reckoned from the direction $\mathbf{\Omega}_0$ of primary ion emission. Then, the angular dependences of $N_{\text{ion}}(\mathbf{\Omega}, T)$ and $N_{\text{rec}}(\mathbf{\Omega}, T)$ are characterized by the cosine of the angle $\Theta$ between the vectors $\mathbf{\Omega}$ and $\mathbf{\Omega}_0$ ($0 < \Theta < \pi$):

$$N_{\text{ion}}(\mathbf{\Omega}, T) \equiv N_{\text{ion}}(\mu, T), \quad N_{\text{rec}}(\mathbf{\Omega}, T) \equiv N_{\text{rec}}(\mu, T), \quad \mu = \cos\Theta = \mathbf{\Omega}_0\mathbf{\Omega}, \tag{1}$$

where $\mathbf{\Omega}_0\mathbf{\Omega}$ is the scalar product of the unit vectors.

Inelastic energy loss for the ions and the atoms will be described in terms of the well-known continuous slowdown model [16]. Assuming also that the recoil atoms interact only with target atoms at rest (linear cascade conditions [1–4]), we can write for $N_{\text{ion}}(\mu, T)$ and $N_{\text{rec}}(\mu, T)$ the set of Boltzmann transport equations [1]

$$\begin{aligned} w_{el}^{ia}(T)N_{\text{ion}} &= \iiint d\mathbf{\Omega}'dT'w_1^{ia}(\mathbf{\Omega}', T' \longrightarrow \mathbf{\Omega}, T)N_{\text{ion}}(\mu', T') \\ &+ \frac{\partial}{\partial T}\{\bar{\varepsilon}_{\text{ion}}(T)N_{\text{ion}}(\mu, T)\} + \frac{\delta(1-\mu)}{2\pi}\delta(T - T_0), \end{aligned} \tag{2}$$

$$\begin{aligned} w_{el}^{aa}(T)N_{\text{rec}} &= \iiint d\mathbf{\Omega}'dT'\{w_1^{aa}(\mathbf{\Omega}', T' \longrightarrow \mathbf{\Omega}, T) \\ &+ w_2^{aa}(\mathbf{\Omega}', T' \longrightarrow \mathbf{\Omega}, T)\}N_{\text{rec}}(\mu', T') \\ &+ \frac{\partial}{\partial T}\{\bar{\varepsilon}_{\text{at}}(T)N_{\text{rec}}(\mu, T)\} \\ &+ \iiint d\mathbf{\Omega}'dT'w_2^{ia}(\mathbf{\Omega}', T' \longrightarrow \mathbf{\Omega}, T)N_{\text{ion}}(\mu', T'). \end{aligned} \tag{3}$$

Here, $w_{el}^{aa}$ ($w_{el}^{ia}$) is the total probability of a moving atom (ion) of energy $T$ being elastically scattered by an atom at rest per unit path length, $w_1^{aa(ia)}(\mathbf{\Omega}', T' \longrightarrow \mathbf{\Omega}, T)$ is the probability of a moving atom (ion) being elastically scattered from the state ($\mathbf{\Omega}'$, $T'$) to the state ($\mathbf{\Omega}$, $T$) per unit path length, $w_2^{aa(ia)}(\mathbf{\Omega}', T' \longrightarrow \mathbf{\Omega}, T)$ is the probability that an atom (ion) of energy $T'$ moving in the direction $\mathbf{\Omega}'$ knocks out an atom of energy $T$ in the direction $\mathbf{\Omega}$ per unit path length, and $\bar{\varepsilon}_{\text{ion(at)}}(T)$ is the electronic stopping power of the medium for an ion (atom) of energy $T$. The parameters $N_{\text{ion}}(\mu, T)$ and $N_{\text{rec}}(\mu, T)$ define the angular and energy distributions of the primary ions and recoil atoms, respectively. Note that the atoms can be both knocked out by the primary ions and generated in atomic collisions. The probability of atomic collisions is specified by the parameter $w_2^{aa}$ in (3).

As follows from Eq. (2), calculating the primary ion flux density $N_{\text{ion}}(\mu, T)$ is an independent problem that in no way is related to solving the equation for the recoil atoms. On the contrary, in order to find $N_{\text{rec}}(\mu, T)$, it is necessary to calculate $N_{\text{ion}}(\mathbf{\Omega}, T)$, which is involved in the inhomogeneity term in Eq. (3). The situation is somewhat simplified if the primary ions are of the same sort as target atoms (self-sputtering). In this case, along with Eq. (2) for $N_{\text{ion}}(\mu, T)$, we can also obtain the closed equation for the flux density of all the atoms (of both emitted by the source and cascade-generated):

$$N_{\text{at}}(\mu, T) = N_{\text{ion}}(\mu, T) + N_{\text{rec}}(\mu, T). \tag{4}$$

Hereafter, we consider only self-sputtering. In this case, the stopping powers $\bar{\varepsilon}_{\text{ion}}(T)$ and $\bar{\varepsilon}_{\text{at}}(T)$, entering into Eqs. (2) and (3), as well as the scattering probabilities of the ions and atoms, coincide:

$$\bar{\varepsilon}_{\text{ion}}(T) = \bar{\varepsilon}_{\text{at}}(T) = \bar{\varepsilon}(T), \tag{5a}$$

$$\begin{aligned} w_{1(2)}^{ia}(\ldots) &= w_{1(2)}^{aa}(\ldots) \\ &= n_0\frac{d\sigma_{1(2)}}{d\mathbf{\Omega}}(\mathbf{\Omega}'\mathbf{\Omega}; T')\delta(T - T'(\mathbf{\Omega}'\mathbf{\Omega})^2), \end{aligned} \tag{5b}$$

$$w_{el}^{ia}(T) = w_{el}^{aa}(T) = n_0\sigma_{el}(T). \tag{5c}$$

Here, $n_0$ is the concentration of the atoms of the medium, $\sigma_{el}(T)$ is the total cross section of atom elastic scattering, $d\sigma_1/d\mathbf{\Omega}$ is the differential cross section of atom elastic scattering, and $d\sigma_2/d\mathbf{\Omega}$ is the differential cross section of recoil atom scattering. The presence of the $\delta$ function in Eq. (5b) is a consequence of the energy and momentum conservation laws under elastic collision of particles [17].

Adding Eqs. (2) and (3) termwise in view of (5a)–(5c), we arrive at the equation for $N_{\text{at}}(\mu, T)$:

$$\begin{aligned} n_0\sigma_{el}(T)N_{\text{at}}(\mu, T) &= n_0\int_T^{T_0} dT'\iint d\mathbf{\Omega}'\left\{\frac{d\sigma_1}{d\mathbf{\Omega}}(\mathbf{\Omega}\mathbf{\Omega}'; T')\right. \\ &\left. + \frac{d\sigma_2}{d\mathbf{\Omega}}(\mathbf{\Omega}\mathbf{\Omega}'; T')\right\}\delta(T - T'(\mathbf{\Omega}\mathbf{\Omega}')^2)N_{\text{at}}(\mu', T') \\ &+ \frac{\partial}{\partial T}\{\bar{\varepsilon}(T)N_{\text{at}}(\mu, T)\} + \frac{\delta(1-\mu)}{2\pi}\delta(T - T_0). \end{aligned} \tag{6}$$

It is important that it is the quantity $N_{\text{at}}(\mu, T)$, given by (4), that should be used in describing atomic colli-

sion cascades upon self-sputtering, since the recoil atoms of the target and the primary particles emitted by the source are indistinguishable. As for the primary ion flux density $N_{\text{ion}}(\mu, T)$, it, as is seen from (2) and (5a)–(5c), satisfies the equation

$$n_0\sigma_{el}(T)N_{\text{ion}}(\mu, T) = n_0\int_T^{T_0} dT'\iint d\boldsymbol{\Omega}'\frac{d\sigma_1}{d\boldsymbol{\Omega}}(\boldsymbol{\Omega}\boldsymbol{\Omega}'; T')$$
$$+ \delta(T - T'(\boldsymbol{\Omega}\boldsymbol{\Omega}')^2)N_{\text{ion}}(\mu', T') \quad (7)$$
$$+ \frac{\partial}{\partial T}\{\bar{\varepsilon}(T)N_{\text{ion}}(\mu, T)\} + \frac{\delta(1-\mu)}{2\pi}\delta(T - T_0).$$

As before, the parameter $N_{\text{ion}}(\mu, T)$ defines the angular and energy spectra of only the primary ions emitted by the source when the masses of the ion and the target atom equal each other (cascade processes are ignored). The difference between $N_{\text{ion}}(\mu, T)$ and $N_{\text{at}}(\mu, T)$ shows how the slowdown affects the rate of atom multiplication in the cascades.

## SOLUTION TO THE BASIC INTEGRO-DIFFERENTIAL EQUATIONS

Before proceeding to solve Eqs. (6) and (7), it is necessary to determine the form of the elastic scattering cross sections $d\sigma_1$ and $d\sigma_2$, as well as of the electronic stopping power $\bar{\varepsilon}(T)$ of the medium. Usually, two kinds of elastic scattering cross section are used for theoretically describing atom scattering and knockout. The first is the Lindhard scattering cross section for inverse-power interatomic potentials ($V(r) \propto r^{-1/m}$) [18]. No doubt, these cross sections most adequately characterize single scattering of atoms, but sometimes they greatly complicate the solution of the transport equation. For example, one fails to obtain an analytic solution of the Boltzmann transport equation with Lindhard cross sections if ionization slowdown is taken into consideration. The second type is the cross section of hard ball scattering. While this kind of cross section ignores the fact that the single scattering of atoms is highly anisotropic, it considerable widens the scope of analytically solvable problems [1, 9, 11]. In what follows we assume the single scattering of the atoms follows the hard ball law; that is,

$$\frac{d\sigma_1}{d\boldsymbol{\Omega}}(\boldsymbol{\Omega}'\boldsymbol{\Omega}; T) = \frac{d\sigma_2}{d\boldsymbol{\Omega}}(\boldsymbol{\Omega}'\boldsymbol{\Omega}; T) = \frac{\sigma}{\pi}(\boldsymbol{\Omega}'\boldsymbol{\Omega})\eta(\boldsymbol{\Omega}'\boldsymbol{\Omega});$$
$$\sigma_{el}(T) = \sigma \quad (8)$$

($\eta(x) = 1$ or 0 at $x > 0$ or $< 0$, respectively).

As follows from (8), the hard ball cross section is energy-independent. As for the electronic stopping power of the medium, its value $\bar{\varepsilon}(T)$ for moderate-energy atoms is found from the Lindhard formula [19]

$$\bar{\varepsilon}(T) = \frac{2\sqrt{T_0 T}}{R_0}, \quad R_0 \equiv R(T_0) = \int_0^{T_0}\frac{dT}{\bar{\varepsilon}(T)}. \quad (9)$$

Here, $R_0$ is the total inelastic range of an atom with an energy $T_0$. The solutions of Eqs. (6) and (7) are routinely sought in the form of the expansion in Legendre polynomials $P_l(\mu)$ [20]:

$$N_{\text{ion}}(\mu, T) = \sum_{l=0}^{\infty}\frac{2l+1}{4\pi}N_{\text{ion}}^{(l)}(T)P_i(\mu);$$
$$N_{\text{at}}(\mu, T) = \sum_{l=0}^{\infty}\frac{2l+1}{4\pi}N_{\text{at}}^{(l)}(T)P_l(\mu). \quad (10)$$

The angular moments $N_{\text{ion}}^{(l)}(T)$ and $N_{\text{at}}^{(l)}(T)$ are related to $N_{\text{ion}}(\mu, T)$ and $N_{\text{at}}(\mu, T)$ as

$$N_{\text{ion}}^{(l)}(T) = 2\pi\int_{-1}^{1} d\mu P_l(\mu)N_{\text{ion}}(\mu, T);$$
$$N_{\text{at}}^{(l)}(T) = 2\pi\int_{-1}^{1} d\mu P_l(\mu)N_{\text{at}}(\mu, T). \quad (11)$$

As follows from (15), the zero moments $N_{\text{ion}}^{(0)}(T)$ and $N_{\text{at}}^{(0)}(T)$ specify the energy spectra of the scattered ions and the recoil atoms, respectively, regardless of the direction of particle motion. Substituting expansions (10) into Eqs. (6) and (7), one easily obtains the integro-differential equations for the angular moments $N_{\text{ion}}^{(l)}(T)$ and $N_{\text{at}}^{(l)}(T)$:

$$n_0\sigma N_{\text{ion}}^{(l)}(T) = n_0\sigma\int_T^{T_0}\frac{dT'}{T'}P_l(\sqrt{T/T'})N_{\text{ion}}^{(l)}(T')$$
$$+ \frac{d}{dT}\{\bar{\varepsilon}(T)N_{\text{ion}}^{(l)}(T)\} + \delta(T - T_0), \quad (12)$$

$$n_0\sigma N_{\text{at}}^{(l)}(T) = 2n_0\sigma\int_T^{T_0}\frac{dT'}{T'}P_l(\sqrt{T/T'})N_{\text{at}}^{(l)}(T')$$
$$+ \frac{d}{dT}\{\bar{\varepsilon}(T)N_{\text{at}}^{(l)}(T)\} + \delta(T - T_0), \quad (13)$$

where $\bar{\varepsilon}(T)$ is given by (9).

Basically, Eqs. (12) and (13) allow the calculation of all the angular moments $N_{\text{ion}}^{(l)}(T)$ and $N_{\text{at}}^{(l)}(T)$. We will restrict our analysis by finding only the first two angular moments ($l = 0, 1$). This will suffice to visualize the

energy spectra of the ions and atoms [$N_{\text{ion}}^{(0)}(T)$ and $N_{\text{at}}^{(0)}(T)$], as well as the anisotropy of the angular distribution of the particles. In fact, it is seen from (10) that the mean cosine of the angle of multiple scattering of the ions and atoms depends on these two angular moments of the functions $N_{\text{ion}}(\mu, T)$ and $N_{\text{at}}(\mu, T)$:

$$\langle \cos\Theta \rangle_T^{(\text{ion})} = \frac{N_{\text{ion}}^{(1)}(T)}{N_{\text{ion}}^{(0)}(T)}, \quad \langle \cos\Theta \rangle_T^{(\text{at})} = \frac{N_{\text{at}}^{(1)}(T)}{N_{\text{at}}^{(0)}(T)}. \quad (14)$$

Obviously, if $\langle\cos\Theta\rangle_T$ is close to unity, the angular distribution of the particles is highly anisotropic and many terms must be left in expansions (10). On the contrary, if $\langle\cos\Theta\rangle_T$ is much less than unity, the distribution is almost isotropic and the functions $N_{\text{ion}}(\mu, T)$ and $N_{\text{at}}(\mu, T)$ depend largely on their zero angular moments.

Let us replace the angular moments $N_{\text{ion}}^{(l)}(T)$ and $N_{\text{at}}^{(l)}(T)$ by new unknown functions $F_l(\xi)$ and $\Phi_l(\xi)$ as follows:

$$N_{\text{ion}}^{(l)}(T) = \frac{R_0}{2\sqrt{T_0 T}} F_l(\xi), \quad N_{\text{at}}^{(l)}(T) = \frac{R_0}{2\sqrt{T_0 T}} \Phi_l(\xi), \quad (15)$$
$$\xi = \sqrt{T/T_0} \le 1.$$

Substituting (15) into Eqs. (12) and (13) and taking into account the explicit form of stopping power (9) yields the integro-differential equations for $F_l(\xi)$ and $\Phi_l(\xi)$:

$$F_l(\xi) = 2\xi \int_\xi^1 \frac{d\xi'}{\xi'^2} P_l(\xi/\xi') F_l(\xi') + (n_0\sigma R_0)^{-1} \frac{dF_l(\xi)}{d\xi}, \quad (16)$$

$$\Phi_l(\xi) = 4\xi \int_\xi^1 \frac{d\xi'}{\xi'^2} P_l(\xi/\xi') \Phi_l(\xi') + (n_0\sigma R_0)^{-1} \frac{d\Phi_l(\xi)}{d\xi}. \quad (17)$$

Here, the singular terms $\delta(1-\xi)$ on the right of Eqs. (16) and (17) [these terms correspond to the terms $\delta(T-T_0)$ in Eqs. (12) and (13)] are replaced by the equivalent boundary conditions

$$F_l(\xi = 1) = 1, \quad \Phi_l(\xi = 1) = 1. \quad (18)$$

Now we divide the equations for $F_0(\xi)$ and $\Phi_0(\xi)$ by $\xi$ and those for $F_1(\xi)$ and $\Phi_1(\xi)$ by $\xi^2$ and differentiate the results with respect to $\xi$. In this way, we reduce integro-differential equations (16) and (17) to ordinary differential equations of second order, which are easy to solve [21]. Eventually, we find for $F_l(\xi)$ and $\Phi_l(\xi)$ ($l$ = 0, 1)

$$F_0(\xi) = 1 - \lambda\xi^2 J^{(2)}(\xi; \lambda), \quad (19a)$$

$$F_1(\xi) = \frac{2(\lambda-1)}{\lambda^2} + \frac{\lambda^2\xi^2 - 2\lambda\xi + 2}{\lambda^2} \exp\{-\lambda(1-\xi)\}, \quad (19b)$$

$$\Phi_0(\xi) = \frac{1}{12}(\lambda^2 + 6\lambda + 6)(\lambda^2\xi^2 + 6\lambda\xi + 2) - \frac{\lambda}{12}\xi^2(\lambda^2\xi^2 + 8\lambda\xi + 12)[(\lambda+4)\exp\{-\lambda(1-\xi)\} + (\lambda^2 + 6\lambda + 6)J^{(2)}(\xi; \lambda)], \quad (20a)$$

$$\Phi_1(\xi) = \frac{1}{3}(\lambda+3)(\lambda\xi+1) - \frac{\lambda}{3}\xi^3(\lambda\xi+4) \times [\exp\{-\lambda(1-\xi)\} + (\lambda+3)J^{(3)}(\xi; \lambda)]. \quad (20b)$$

Here,

$$\lambda = n_0\sigma R_0, \quad (21)$$

$$J^{(n)}(\xi; \lambda) = \int_\xi^1 \frac{dt}{t^n} \exp\{-\lambda(t-\xi)\} = \lambda^{n-1} e^{\lambda\xi} [\Gamma(1-n; \lambda\xi) - \Gamma(1-n; \lambda)], \quad (22)$$

and $\Gamma(a; y)$ is the incomplete gamma function [22].

The dimensionless parameter $\lambda$ characterizes the relative contributions of the slowdown and scattering processes to the angular and energy distributions of the particles. For $\lambda \ll 1$, the slowdown prevails and the atoms are deflected by small angles up to their stop. As a result, knocking-out is absent ($F_l \approx \Phi_l \approx 1$ and $\lambda \ll 1$). Conversely, at $\lambda \gg 1$ (weak slowdown), the atoms are scattered by large angles and, hence, can effectively produce atomic collision cascades.

## THE EFFECT OF SLOWDOWN ON THE ANGULAR AND ENERGY DISTRIBUTIONS OF PRIMARY IONS AND CASCADE ATOMS

Let us analyze first the angular and energy distributions of the particles in the absence of slowdown ($\bar{\varepsilon}(T) = 0$). To do this, it is necessary to proceed to the limit $R_0 \longrightarrow \infty$ ($\lambda \longrightarrow \infty$) in expressions (19), (23), and (24), as follows from Eq. (9):

$$N_{\text{ion}}(\mu, T < T_0; R_0 \longrightarrow \infty) = \frac{1}{4\pi n_0\sigma}\left(\frac{1}{T} + 3\mu\frac{1}{\sqrt{T_0 T}} + \ldots\right), \quad (23a)$$

$$N_{\text{at}}(\mu, T < T_0; R_0 \longrightarrow \infty) = \frac{1}{4\pi n_0\sigma}\left(\frac{2T_0}{T^2} + 3\mu\frac{2\sqrt{T_0}}{T^{3/2}} + \ldots\right). \quad (23b)$$

Formula (23b) coincides (up to a factor) with the result obtained by Roosendaal and Sanders for low-energy ions and the energy-independent Lindhard cross section ($m = 0$) [7, 8]. From (23a) and (23b), it follows that the energy spectra $N_{\text{ion}}^{(0)}(T)$ of the scattered ions and $N_{\text{at}}^{(0)}(T)$ of the recoil atoms are nonintegrable (they diverge as $1/T$ and $1/T^2$, respectively) in the absence of slowdown. In addition, expressions (23a) and (23b) imply that the anisotropy of the angular distributions of both the scattered ions and recoil atoms disappears if the particle energy is low (that is, at $T \longrightarrow 0$). In fact, in the absence of slowdown, the mean cosine of the multiple scattering angle for both the ions and atoms is given by [in view of (14)]

$$\langle \cos\Theta \rangle_T^{\text{ion}} = \langle \cos\Theta \rangle_T^{\text{at}} = \sqrt{\frac{T}{T_0}} \quad (R_0 \longrightarrow \infty). \qquad (24)$$

The perfect isotropy of the ions and atoms at $T \longrightarrow 0$ is explained by the fact that, in the absence of slowdown, the particles may have the energy $T = 0$ only if they undergo an infinite number of collisions.

Here, the following circumstance is noteworthy. In the absence of slowdown, the energy spectra (23a) of the scattered ions ($\propto 1/T$) and the energy spectra (23b) of the recoil atoms ($\propto 1/T^2$) were derived under the assumption that the cross sections are energy-independent. For the energy-dependent Lindhard cross sections ($m \neq 0$) in the absence of slowdown, the energy spectra are $N_{\text{ion}}^{(0)}(T; m) \propto 1/T^{1-2m}$ and $N_{\text{at}}^{(0)}(T; m) \propto 1/T^{2-2m}$ [1, 2, 6, 7]. As for the anisotropy of the angular distributions in the absence of slowing down, it disappears with decreasing energy for any value of $m$ in the Lindhard cross section ($0 \le m \le 1$) [7, 8]. Hence, it is because of the neglect of the ionization slowdown of the atoms that the low-energy atom distribution perfectly isotropizes and does not depend on the cross section kind.

Now let us turn to expressions (15), (19), and (20) to see how the inclusion of slowdown affects the angular and energy distributions of the scattered ions and recoil atoms. These expressions are valid in the entire interval $0 < T < T_0$. Figures 1 and 2 show the energy spectra of the recoil atoms, $N_{\text{ion}}^{(0)}(T)$, and scattered ions, $N_{\text{at}}^{(0)}(T)$, that were calculated according to (15), (19), and (20), as well as the energy dependences of the mean cosines, $\langle \cos\Theta \rangle_T^{(\text{at})}$ and $\langle \cos\Theta \rangle_T^{(\text{ion})}$, calculated from (18), (19), (23), and (24) for several $\lambda$. For comparison, the same curves for purely elastic scattering ($\lambda \longrightarrow \infty$) are also depicted. It is seen that the effect of the slowdown is most pronounced when the particle energy is low. The smaller $\lambda$ (the stronger slowdown), the slower the rise in the curves $N_{\text{at}}^{(0)}(T)$ and $N_{\text{ion}}^{(0)}(T)$. In addition, the slowdown noticeably affects the anisotropy of the angular distributions of the particles in the entire energy range $0 < T < T_0$. Note that, in the case of purely elastic scattering, the angular and energy distributions of the scattered ions and recoil atoms tend to their ultimate values rather slowly (cf. curves for $\lambda = 10$ and $\lambda = \infty$).

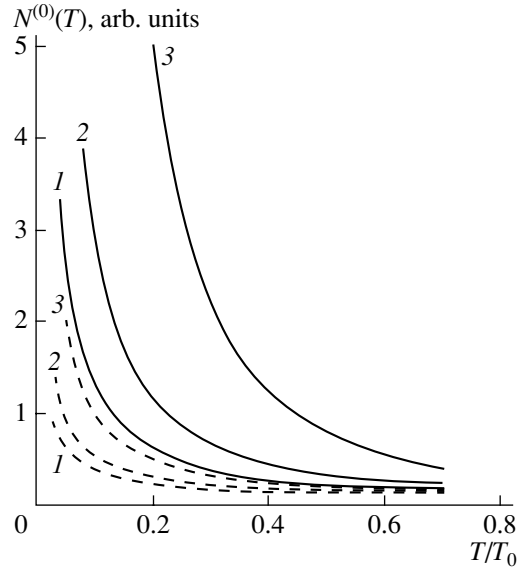


**Fig. 1.** Energy spectra of scattered ions, $N_{\text{ion}}^{(0)}(T)$ (dashed curves), and recoil atoms, $N_{\text{at}}^{(0)}(T)$ (continuous curves) calculated from (15), (19), and (20). The energy is given in units of $T_0$. $\lambda$ = (*1*) 5 and (*2*) 10. Curve *3* shows the absence of slowdown ($\lambda = \infty$, $N_{\text{ion}}^{(0)}(T) \sim 1/T$, and $N_{\text{at}}^{(0)}(T) \sim 1/T^2$).

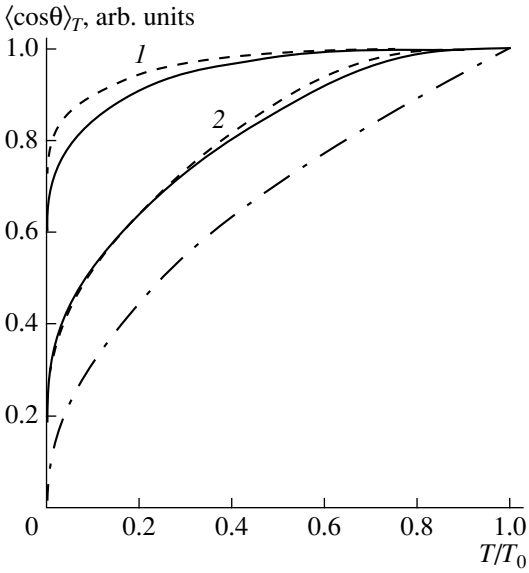


**Fig. 2.** Mean cosines of the multiple scattering angles for the ions $\langle \cos\Theta \rangle_T^{(\text{ion})}$ (dashed curves) and recoil atoms $\langle \cos\Theta \rangle_T^{(\text{at})}$ (continuous curves) [calculated from (18), (19), (23), and (24)] vs. reduced energy $T/T_0$. $\lambda$ = (*1*) 1 and (*2*) 10. The dash-and-dot curve shows the absence of slowdown ($\lambda = \infty$, $\langle \cos\Theta \rangle_T^{(\text{ion})} = \langle \cos\Theta \rangle_T^{(\text{at})} = \sqrt{T/T_0}$).

Of primary importance is, however, the low-energy range, since the energy spectra of the atoms diverge and the anisotropy of the angular distributions disappears just at low energies of the particles. For $T/T_0 \longrightarrow 0$, we obtain from expressions (15), (19), and (20)

$$N_{\text{ion}}(\mu;\ T \ll T_0) \approx \frac{R_0}{2\sqrt{T_0 T}}\left(1 + 3\mu\frac{2(\lambda + e^{-\lambda} - 1)}{\lambda^2} + \ldots\right), \quad (25)$$

$$N_{\text{at}}(\mu;\ T \ll T_0) \approx \frac{R_0}{2\sqrt{T_0 T}}\left(\frac{\lambda^2 + 6\lambda + 6}{6} + 3\mu\frac{\lambda + 3}{3} + \ldots\right). \quad (26)$$

As follows from (25) and (26), ionization slowdown radically changes the energy and angular spectra of both primary ions and recoil atoms. With slowdown taken into consideration, the low-energy spectra become convergent; that is, nonintegrable energy spectra (23a) and (23b) transform into integrable spectra (25) and (26). The $N_{\text{ion}}(\mu, T \ll T_0)$ and $N_{\text{at}}(\mu, T \ll T_0)$ vs. energy curves vary as $1/\sqrt{T}$. Moreover, when slowdown is ignored, the inclusion of cascading changes the proportionality of the low-energy spectrum of the particles from $1/T$ to $1/T^2$ [1]. With slowdown taken into account, the energy spectra of both particles become proportional to $1/\sqrt{T}$. Finally, ionization slowdown prevents the particles from being perfectly isotropic. Indeed, according to (14), (25), and (26), the mean cosines of multiple scattering angles for the low-energy ions and atoms are

$$\langle \cos\Theta\rangle^{(\text{ion})}_{T\to 0} = \frac{2(\lambda + e^{-\lambda} - 1)}{\lambda^2}, \qquad \langle \cos\Theta\rangle^{(\text{at})}_{T\to 0} = \frac{2(\lambda + 3)}{\lambda^2 + 6\lambda + 6}. \quad (27)$$

The value of $\langle \cos\Theta\rangle^{(\text{ion})}_{T\to 0}$ is larger than $\langle \cos\Theta\rangle^{(\text{at})}_{T\to 0}$ at any $\lambda$. This means that the angular distribution of the low-energy cascade atoms is always more isotropic that of the low-energy primary ions. As follows from (27), the angular distributions of both low-energy particles are considerably anisotropic at $\lambda \approx 1$. In this case, the slowdown makes cascade isotropization difficult and a larger number of terms must be left in expansions (10) for $N_{\text{ion}}(\mu, T)$ and $N_{\text{at}}(\mu, T)$. As $\lambda$ increases, the angular distributions of the low-energy ions and recoil atoms become more and more isotropic. At large $\lambda$, the mean cosines $\langle \cos\Theta\rangle^{(\text{ion})}_{T\to 0}$ and $\langle \cos\Theta\rangle^{(\text{at})}_{T\to 0}$ tend to zero but remain finite for $\lambda$ as large as desired. In other words, even if slowdown is weak, the angular distributions of the ions and recoil atoms remain anisotropic as the particle energy decreases.

## CONCLUSION

Based on the solution of the Boltzmann transport equation in the infinite medium approximation (with an ion source uniformly distributed over the medium), we showed that the inclusion of ionization slowdown in the equation radically alters the energy and angular distributions of both primary ions and recoil atoms. Using the energy-independent cross section of hard ball scattering and assuming that the masses of the ions and the atoms equal each other, we obtained the following results.

(1) With slowdown taken into consideration, the divergent energy spectra of the primary ions and recoil atoms (varying as $1/T$ and $1/T^2$, respectively) become integrable (both spectra vary as $1/\sqrt{T}$ at $T \ll T_0$). Thus, the low-energy distributions of the ions and atoms are governed by the energy dependence of the particle scattering cross section and also by that of the electronic stopping power $\bar{\varepsilon}(T)$ of the medium.

(2) With slowdown taken into consideration, the low-energy ($T \ll T_0$) parts of the spectra of both particles vary as $1/\sqrt{T}$. This is an indirect support of the fact that, in the presence of slowdown, the number of atoms per cascade initiated by one primary ion is finite [13, 14].

(3) slowdown prevents the low-energy angular distributions of both particles from being perfectly isotropic. In the absence of slowdown, the angular distributions tend to become isotropic at $T/T_0 \longrightarrow 0$. Moreover, it is slowdown that is responsible for the anisotropy of the angular spectra of the ions and recoil atoms.

Since atomic cascading is a basic mechanism of sputtering [2, 3], the above theoretical considerations clearly demonstrate the need for taking into account ionization slowdown in analysis of the angular and energy spectra of sputtered atoms.

## ACKNOWLEDGMENTS

We are indebted to E.S. Mashkova for the support and critical comments.

## REFERENCES

1. M. M. R. Williams, Prog. Nucl. Energy **3**, 1 (1979).
2. *Sputtering by Particle Bombardment*, Ed. by R. Behrisch (Springer-Verlag, New York, 1981; Mir, Moscow, 1984), Vol. I.
3. *Sputtering of Solids: Principles and Applications: Collection of Articles*, Ed. by E. S. Mashkova (Mir, Moscow, 1989).
4. E. S. Mashkova and V. A. Molchanov, Poverkhnost, No. 3, 5 (1995).
5. P. Sigmund, Phys. Rev. **184**, 383 (1969).
6. P. Sigmund, Rev. Roum. Phys. **17**, 823 (1972); **17**, 969 (1972); **17**, 1079 (1972).

7. J. B. Sanders and H. E. Roosendaal, Radiat. Eff. **24**, 161 (1975).
8. H. E. Roosendaal and J. B. Sanders, Radiat. Eff. **52**, 137 (1980).
9. K. T. Waldeer and H. M. Urbassek, Nucl. Instrum. Methods Phys. Res. B **18**, 518 (1987).
10. K. T. Waldeer and H. M. Urbassek, Appl. Phys. A **45**, 207 (1988).
11. M. M. R. Williams, Philos. Mag. A **43**, 1221 (1981).
12. A. I. Tolmachev, Poverkhnost, No. 8, 102 (1994).
13. M. M. R. Williams, J. Phys. D **11**, 801 (1978).
14. M. M. R. Williams, Radiat. Eff. **30**, 47 (1976).
15. M. W. Thompson, Philos. Mag. **18**, 377 (1968).
16. N. P. Kalashnikov, V. S. Remizovich, and M. I. Ryazanov, *Collisions of Fast Charged Particles in Solids* (Atomizdat, Moscow, 1980).
17. L. D. Landau and E. M. Lifshitz, *Course of Theoretical Physics*, Vol. 1: *Mechanics* (Nauka, Moscow, 1988; Pergamon, New York, 1988).
18. J. Lindhard, V. Nielsen, and M. Scharff, K. Dan. Vidensk. Selsk. Mat.-Fys. Medd. **36** (10), 1 (1968).
19. J. Lindhard and M. Scharff, Phys. Rev. **124**, 128 (1961).
20. B. Davison, *Neutron Transport Theory*, with the collaboration of J. B. Sykes (Clarendon, Oxford, 1957; Atomizdat, Moscow, 1960).
21. E. Kamke, *Differentialgleichungen*, Bd. I: *Gewöhnliche Differentialgleichungen* (Geest and Portig, Leipzig, 1964; Nauka, Moscow, 1976).
22. *Handbook of Mathematical Functions*, Ed. by M. Abramowitz and I. A. Stegun (National Bureau of Standards, Washington, 1964; Nauka, Moscow, 1979).

*Translated by V. Isaakyan*

*Technical Physics, Vol. 46, No. 10, 2001, pp. 1242–1246. Translated from Zhurnal Tekhnicheskoĭ Fiziki, Vol. 71, No. 10, 2001, pp. 36–40.*




# On Calculation of the Heat Flux from a Spherical Particle in a Molecular Gas

**S. A. Savkov, A. A. Yushkanov, and Yu. I. Yalamov**

*Orel State University, Orel, 302015 Russia*

Received January 9, 2001

**Abstract**—The problem of calculation of the heat flux from a spherical particle in a molecular gas is considered. The results of numerical calculations for the collision integral similar to that in the BGK model are presented under the condition of purely diffuse reflection of gas molecules from the surface of a particle. © *2001 MAIK "Nauka/Interperiodica".*

Study of the heat-transfer process in the intermediate range of the Knudsen number is still one of the topical problems of the kinetic theory of gases. However, in theoretical studies of this phenomenon, the translational degrees of freedom are only taken into account, whereas most experiments are performed for molecular gases which requires allowance for internal degrees of freedom [1]. The contribution of particular kinds of motion is defined by the pattern of the energy spectrum. As is well-known (see, e.g., [2]), the energy level spacing for rotational degrees of freedom is defined by the relation $\hbar^2/2J$ ($J$ is the moment of inertia of a molecule) and is comparable to the thermal motion energy $kT$ for the lightest gases only. For example, $\hbar^2/2Jk = 85.4$ K for hydrogen molecules. For heavier molecules, this constant is substantially smaller. This makes it possible to neglect the discrete character of the rotational energy and consider the rotational degrees of freedom classically. Vibrational degrees of freedom are excited at temperatures of $\sim 10^3$ K, and, hence, they can be considered totally frozen.

Consider a spherical particle of radius $R$ uniformly heated to a temperature $T_w$. We assume that the particle is placed in a gas with a constant temperature $T_0$. The temperature difference $\Delta T = T_w - T_0$ is assumed to be sufficiently small in order to linearize the problem. We introduce a spherical coordinate system with the origin at the center of the particle. The state of the gas surrounding the particle is described by the equation [3]

$$C_r\frac{\partial\varphi}{\partial r} + \frac{C^2 - C_r^2}{r}\frac{\partial\varphi}{\partial C_r} = I[\varphi]. \qquad (1)$$

Here, $\mathbf{C} = \mathbf{V}\sqrt{m/2kT_0}$ is the dimensionless proper velocity of the translational motion of gas molecules; $I$ is the integral collision operator; $\varphi$ is the correction to the equilibrium (Maxwellian) distribution function

$$f_0 = n_0\beta\left(\frac{m}{2\pi kT_0}\right)^{3/2}\exp\left(-\frac{\varepsilon}{kT_0}\right),$$

where

$$\beta = 1, \quad \frac{J}{kT_0}, \quad \text{and} \quad \frac{(J_1J_2J_3)^{1/2}}{(2\pi kT_0)^{3/2}}$$

for mono-, di-, and polyatomic gas, respectively; $J_i$ are the principal moments of inertia for a molecule; and $\varepsilon$ is the total kinetic energy of its translational and rotational motions.

In view of the lack of reliable models for the potential of intermolecular interaction, we restrict ourselves to the analogue of the BGK model [4]:

$$I[\varphi] = \nu(F - \varphi), \quad F = \sum_{i=1}^{3} P_iM_i,$$

$$\nu = (s+2)\frac{n_0}{\kappa}\sqrt{\frac{k^3T_0}{8m}} = \frac{1}{\chi}\sqrt{\frac{kT_0}{2m}}, \qquad (2)$$

$$M_i = \pi^{-s/2}\int P_i\varphi\exp(-\xi^2)d^s\xi,$$

$$P_1 = 1, \quad P_2 = \sqrt{\frac{2}{s}}\left(\xi^2 - \frac{s}{2}\right), \quad P_3 = \sqrt{2}C_r,$$

where $s$ is the number of degrees of freedom for gas molecules; $\kappa$ and $\chi$ are the coefficients of thermal conductivity and thermal diffusivity; and $\xi$ is the $s$-dimensional vector of the dimensionless velocity. The first three components of this vector $\{\xi_1, \xi_2, \xi_3\} = \mathbf{C}$ describe the translational motion and the other $(s-3)$, the rotational one with $\xi_i = \sqrt{\varepsilon_i/kT_0}$ in both cases.

1063-7842/01/4610-1242$21.00 

We take the purely diffuse reflection of gas molecules from the particle surface

$$\varphi|_{C_r>0,\ r=R} = \Phi_w = \frac{\Delta n}{n_0} + \left(\xi^2 - \frac{s}{2}\right)\frac{\Delta T}{T_0} \qquad (3)$$

as the boundary condition on the particle surface.

The density difference of gas molecules $\Delta n$ is defined by the condition of the lack of mass gas motion, which is equivalent to

$$\int C_r \varphi(R) \exp(-\xi^2) d^2\xi = 0. \qquad (4)$$

This yields

$$\frac{\Delta n}{n_0} = -\frac{1}{2}\frac{\Delta T}{T_0} - 2\pi^{(1-s)/2} \int\limits_{C_r<0} C_r \varphi(R) \exp(-\xi^2) d^s\xi. \qquad (5)$$

The desired heat flux is given by the expression

$$q = n_0 \sqrt{\frac{2k^3 T_0^3}{\pi^s m}} \int C_r \xi^2 \varphi \exp(-\xi^2) d^s\xi$$

and, on account of the energy conservation law, can be represented in the form

$$q = n_0 \sqrt{\frac{2k^3 T_0^3}{m}} \frac{R^2}{r^2} Q.$$

The dimensionless variable $Q$ can be evaluated at any point, e.g., on the surface of a particle. In view of (3) and (5), this yields

$$Q = \frac{s+1}{4\sqrt{\pi}}\frac{\Delta T}{T_0} + \pi^{-s/2} \int\limits_{C_r<0} C_r \left(\xi^2 - \frac{s+1}{2}\right) \times \varphi(R) \exp(-\xi^2) d^s\xi. \qquad (6)$$

It is clear that the influence of a small particle on the distribution function for molecules in a gas is negligible, and the correction $\varphi$ in the range of integration in (6) can be considered equal to zero. Thus, the augend describes the heat flux in the free-molecule mode. This result depends neither on the form of the collision integral nor on the method for solving the problem.

In the gas-dynamic limit, i.e., at $R\nu \gg 1$, the distribution function for molecules incident on the particle is described by the Chapman–Enskog distribution

$$\Phi = \frac{R}{r^2\nu}\frac{\Delta T}{T_0}\left(\xi^2 - \frac{s}{2} - 1\right)(C_r + \nu r),$$

which yields

$$Q_\infty = \frac{s+2}{4}\frac{\Delta T}{T_0}\frac{1}{R\nu} \qquad (7)$$

and, in view of the definition of $\nu$, corresponds to

$$q = \frac{\kappa R \Delta T}{r^2}.$$

In this sense, the solutions of the problem considered for mono-, di-, and polyatomic gases coincide with each other.

In order to calculate the heat flux for the intermediate values of the Knudsen number, one has to solve Eq. (1). Turning to the variable

$$\mu = \frac{(\mathbf{C}\cdot\mathbf{r})}{Cr},$$

we represent it in the form

$$\mu\frac{\partial\varphi}{\partial r} + \frac{1-\mu^2}{r}\frac{\partial\varphi}{\partial\mu} = \frac{\nu}{C}(F-\varphi). \qquad (8)$$

Considering $F$ as a given function, we write the set of the characteristic equations:

$$\frac{dr}{\mu} = \frac{r d\mu}{1-\mu^2} = \frac{C}{\nu}\frac{d\varphi}{F-\varphi}.$$

The first equality

$$\frac{dr}{\mu} = \frac{r d\mu}{1-\mu^2}$$

is solved straightforwardly and gives the characteristic

$$K_1 = r\sqrt{1-\mu^2}. \qquad (9)$$

We choose

$$\frac{dr}{\mu} = \frac{C}{\nu}\frac{d\varphi}{F-\varphi}$$

as the second equation.

Substituting

$$\mu = \pm\sqrt{1 - K_1^2/r^2}$$

found from formula (9) into this equation, we arrive at

$$\mathrm{sgn}(\mu)\sqrt{1 - \frac{K_1^2}{r^2}}\frac{C}{\nu}\frac{d\varphi}{dr} = F - \varphi.$$

This results in

$$\varphi = K_2 \exp\left(-\mathrm{sgn}(\mu)\frac{\nu}{C}\sqrt{r^2 - K_1^2}\right) + \mathrm{sgn}(\mu)\frac{\nu}{C}\int\limits_R^r \exp\left(\mathrm{sgn}(\mu)\frac{\nu}{C}\left(\sqrt{r_1^2 - K_1^2} - \sqrt{r^2 - K_1^2}\right)\right) \times F\left(r_1, \mathrm{sgn}(\mu)\sqrt{1 - K_1^2/r_1^2}\right)\frac{r_1 dr_1}{\sqrt{r_1^2 - K_1^2}}. \qquad (10)$$

The arguments of the function $F$ mean that one has to take $r_1$ and $\mathrm{sgn}(\mu)\sqrt{1-K_1^2/r_1^2}$ as $r$ and $\mu$, respectively. Taking into account the structure of expression (10) and the discontinuity of the distribution function along the characteristic $r\sqrt{1-\mu^2} = R$, we divide the variability domain for the variables $(r, \mu)$ into three ranges: I for $\mu \in [-1, 0]$; II, $\mu \in [0, \sqrt{1-R^2/r^2}]$; and III, $\mu \in [\sqrt{1-R^2/r^2}, 1]$.

In order to distinguish the distribution functions in the aforementioned ranges, we denote them by the corresponding indices.

It is clear that the condition (3) describes the distribution function in range III and corresponds to

$$\varphi_3(R, \mu) = \Phi_w. \tag{11}$$

Besides that, the desired solution has to be bounded. For $\mu > 0$, this condition is satisfied *a priori* and makes it possible to determine the distribution function in range I:

$$\varphi_1 \longrightarrow 0 \quad \text{at} \quad r \longrightarrow \infty. \tag{12}$$

The values of the function in range II are determined by the continuity condition for this function at the boundary between ranges I and II, i.e., at $\mu = 0$:

$$\varphi_2(r, 0) = \varphi_1(r, 0). \tag{13}$$

The solution to Eq. (8) satisfying these conditions can be represented in the form

$$\varphi = \varphi_1 H_1 + \varphi_2 H_2 + \varphi_3 H_3, \tag{14}$$

where

$$H_1 = H(-\mu), \quad H_3 = H(\mu - \sqrt{1-R^2/r^2}),$$

$$H_2 = 1 - H_1 - H_3,$$

$H(x) = \dfrac{|x| + x}{2x}$ is the Heaviside step function,

$$\begin{aligned}\varphi_1 &= \frac{\nu}{C}\int_r^\infty \exp\left(-\frac{\nu}{C}(r\mu + \sqrt{r_1^2 - r^2(1-\mu^2)})\right)\\ &\times F\left(r_1, -\sqrt{1-\frac{r^2}{r_1^2}(1-\mu^2)}\right)\frac{r_1 dr_1}{\sqrt{r_1^2 - r^2(1-\mu^2)}},\end{aligned} \tag{15}$$

$$\begin{aligned}\varphi_2 &= \frac{\nu}{C}\int_{r\sqrt{1-\mu^2}}^\infty \exp\left(-\frac{\nu}{C}(r\mu + \sqrt{r_1^2 - r^2(1-\mu^2)})\right)\\ &\times F\left(r_1, -\sqrt{1-\frac{r^2}{r_1^2}(1-\mu^2)}\right)\frac{r_1 dr_1}{\sqrt{r_1^2 - r^2(1-\mu^2)}}\\ &+ \frac{\nu}{C}\int_{r\sqrt{1-\mu^2}}^r \exp\left(\frac{\nu}{C}(\sqrt{r_1^2 - r^2(1-\mu^2)} - r\mu)\right)\\ &\times F\left(r_1, \sqrt{1-\frac{r^2}{r_1^2}(1-\mu^2)}\right)\frac{r_1 dr_1}{\sqrt{r_1^2 - r^2(1-\mu^2)}},\end{aligned} \tag{16}$$

$$\begin{aligned}\varphi_3 &= \Phi_w \exp\left(\frac{\nu}{C}(\sqrt{R - r^2(1-\mu^2)} - r\mu)\right)\\ &+ \frac{\nu}{C}\int_R^r \exp\left(\frac{\nu}{C}(\sqrt{r_1^2 - r^2(1-\mu^2)} - r\mu)\right)\\ &\times F\left(r_1, \sqrt{1-\frac{r^2}{r_1^2}(1-\mu^2)}\right)\frac{r_1 dr_1}{\sqrt{r_1^2 - r^2(1-\mu^2)}}.\end{aligned} \tag{17}$$

The substitution of (14)–(17) into the definition (2) results in a set of integral equations in $M_i$. The integration with respect to the components of the generalized velocity, corresponding to the rotational degrees of freedom, is performed analytically. In order to do this, the distribution function should be regarded as a vector

$$\begin{aligned}\varphi &= \varphi^1 e_1 + \varphi^2 e_2, \quad e_1 = 1,\\ e_2 &= \sqrt{\frac{2}{s-3}}\left(\xi^3 - C^2 - \frac{s-3}{2}\right).\end{aligned} \tag{18}$$

Then, the integration may be represented in the form of the scalar product

$$\begin{aligned}&\pi^{(3-s)/2}\int P\varphi \prod_{l=s-3}^{s} \exp(-\xi_l^2)\, d\xi_l\\ &= (P\varphi) = P^1\varphi^1 + P^2\varphi^2.\end{aligned}$$

Besides that, in view of (4), $M_3 = 0$. Finally, the problem reduces to the set of two integral equations

$$\begin{aligned}M_i(r) &= \frac{2}{\sqrt{\pi}}\int_0^\infty \left(\int_{-1}^0 (P_i\varphi_1)\, d\mu + \int_0^{\sqrt{1-R^2/r^2}} (P_i\varphi_2)\, d\mu\right.\\ &\left. + \int_{\sqrt{1-R^2/r^2}}^1 (P_i\varphi_3)\, d\mu\right) C^2 \exp(-C^2)\, dC \quad (i = 1, 2),\end{aligned}$$

$$\varphi_1 = \frac{\nu}{C}\sum_{j=1}^{2} P_j \int_r^\infty \exp\left(-\frac{\nu}{C}(r\mu + \sqrt{r_1^2 - r^2(1-\mu^2)})\right) \times \frac{M_j(r_1) r_1 dr_1}{\sqrt{r_1^2 - r^2(1-\mu^2)}},$$

$$\varphi_2 = \frac{\nu}{C}\sum_{j=1}^{2} P_j \int_{r\sqrt{1-\mu^2}}^{r} \exp\left(\frac{\nu}{C}(\sqrt{r_1^2 - r^2(1-\mu^2)} - r\mu)\right) \times \frac{M_j(r_1) r_1 dr_1}{\sqrt{r_1^2 - r^2(1-\mu^2)}} + \frac{\nu}{C}\sum_{j=1}^{2} P_j \times \int_{r\sqrt{1-\mu^2}}^{\infty} \exp\left(-\frac{\nu}{C}(r\mu + \sqrt{r_1^2 - r^2(1-\mu^2)})\right) \frac{M_j(r_1) r_1 dr_1}{\sqrt{r_1^2 - r^2(1-\mu^2)}}, \quad (19)$$

$$\varphi_3 = \frac{\nu}{C}\sum_{j=1}^{2} P_j \int_R^r \exp\left(\frac{\nu}{C}(\sqrt{r_1^2 - r^2(1-\mu^2)} - r\mu)\right) \times \frac{M_j(r_1) r_1 dr_1}{\sqrt{r_1^2 - r^2(1-\mu^2)}} + \Phi_w \exp\left(\frac{\nu}{C}(\sqrt{R^2 - r^2(1-\mu^2)} - r\mu)\right)$$

where

$$P_1^1 = 1, \quad P_1^2 = 0, \quad P_2^1 = \sqrt{\frac{2}{s}}\left(C^2 - \frac{3}{2}\right),$$

$$P_2^2 = \sqrt{1 - \frac{3}{s}},$$

$$\Phi_w^1 = (C^2 - 2)\frac{\Delta T}{T_0} - 4\int_0^\infty C^3 \exp(-C^2) dC \int_{-1}^{0} \mu \varphi_1^1 d\mu,$$

$$\Phi_w^2 = \sqrt{\frac{s-3}{2}}\frac{\Delta T}{T_0}.$$

In this case, the relation (6) takes the form

$$Q = \frac{s+1}{4\sqrt{\pi}}\frac{\Delta T}{T_0} + \frac{2\nu}{\sqrt{\pi}}\sum_j \int_0^\infty P_j^1 C^2 (C^2 - 2) dC \int_{-1}^{0} \mu d\mu \times \int_R^\infty M_j(r_1) \exp\left(-\frac{\nu}{C}(R\mu + \sqrt{r_1^2 - R^2(1-\mu^2)}) - C^2\right) \times \frac{r_1 dr_1}{\sqrt{r_1^2 - R^2(1-\mu^2)}}.$$

We search for the solution of this set of equations in the form of a series in terms of the Chebyshev polynomials. Having limited ourselves to its first $K$ terms, we write

$$M_i(r) = \sum_{j=0}^{K} A_j^i T_j(\rho(r)),$$

$$\rho = 1 - 2\exp(-\gamma\sqrt{r^2 - R^2}).$$

The expansion coefficients are defined by the condition

$$\sum_{k=0}^{K}\sum_{l=0}^{K} T_j(\rho_l) T_k(\rho_l) = \frac{K+1}{2}(\delta_{0j} + 1)\delta_{jk},$$

$$\rho_l = \cos\frac{(2l+1)\pi}{2K+2}.$$

The constant $\gamma$ is chosen in accordance with the requirement that most of interpolation points are in the basic domain of variability for the distribution function.

The results obtained are shown in Fig. 1. The curves *1*, *2*, and *3* correspond to mono-, di-, and polyatomic gas, respectively. The open circles denote the results of direct numerical integration of the model kinetic equation under consideration for the atomic gas [5].

It is worth noting that most authors present the results in the form of the ratio between $Q$ and the gasdynamic solution $Q_\infty$. Figure 2 shows that such a representation of the results does not reflect the actual dependence of the heat flux on the particle size and results in an incorrect conclusion [6] about the same behavior of the experimental data for mono- and polyatomic gases. The general character of the curves is in agreement with the data presented in [6] and the results of further experiments [7].

Note also that the idea of transforming the Boltzmann equation into a set of integral equations in the dis-

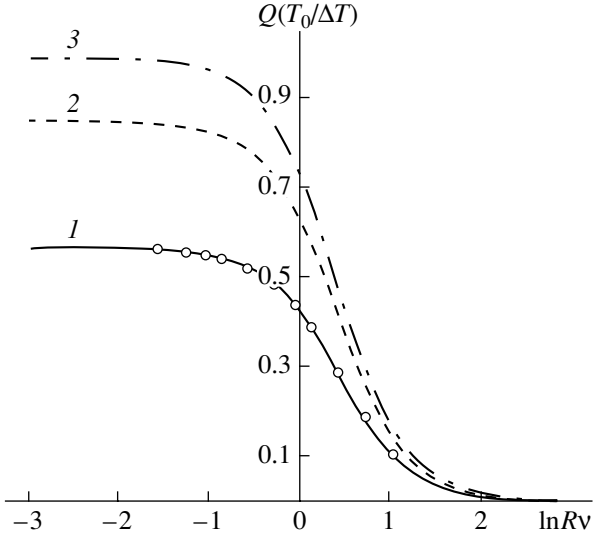


**Fig. 1.** The dependence of the heat flux on the particle size. Open circles show the values of $Q$ for the collision integral in the case of an atomic gas [5].

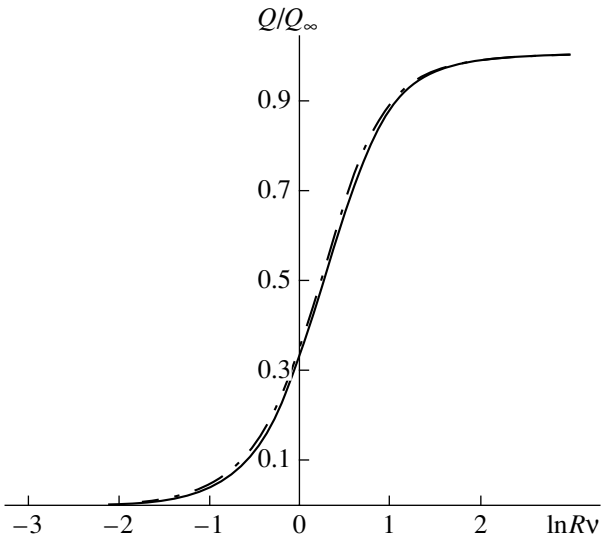


**Fig. 2.** The curves for the ratio of $Q$ to the gas-dynamic solution (7).

tribution-function moments was used when considering similar problems in [8–10]. The variational method was used in [8, 9] to solve the obtained system. The trial function was chosen according to the condition of exact asymptotic behavior of the macroscopic parameters in the gas-dynamic domain. Finally, the heat flux was described by the relation $q = C_1/r^2$, which is actually satisfied due to the energy conservation law. The temperature and density fields were defined in the form $T = C_2/r$ and $n = C_3/r$, respectively. These formulas are only valid relatively far from the particle. The constants $C_i$ were calculated with the condition that the corresponding functional takes the minimum value. In [10], the Galerkin method was used, but the trial function was chosen in a similar way.

The use of the Chebyshev polynomials allows one to avoid the additional integration required in the Galerkin method. This decreases the calculation time and makes it possible to take into account a larger number of polynomials.

## REFERENCES

1. V. M. Zhdanov and M. Ya. Alievskiĭ, *Transfer and Relaxation Processes in Molecular Gases* (Nauka, Moscow, 1989).
2. L. D. Landau and E. M. Lifshitz, *Course of Theoretical Physics*, Vol. 5: *Statistical Physics* (Nauka, Moscow, 1976; Pergamon, Oxford, 1980), Part 1.
3. M. N. Kogan, *Dynamics of Rarefied Gas* (Nauka, Moscow, 1967).
4. A. V. Latyshev and A. A. Yushkanov, in *Mathematical Models of Non-Linear Excitations, Transfer, Dynamics, and Control in Condensed Systems and Other Media*, Ed. by L. A. Uvarova, A. E. Arinstein, and A. V. Latyshev (Plenum, New York, 1999), pp. 3–16.
5. S. Takata, Y. Sone, D. Lhuillier, and M. Wakabayashi, Comput. Math. Appl. **35** (1/2), 193 (1998).
6. L. Lees and Liu Chung-Yen, Phys. Fluids **5** (10), 1137 (1962).
7. Yu. G. Semyonov, S. F. Borisov, and P. E. Suetin, Int. J. Heat Mass Transf. **27** (10), 1789 (1984).
8. C. Cercignani and C. D. Pagani, Rarefied Gas Dynamics **2**, 555 (1967).
9. A. E. Margilevskiĭ, P. E. Chernyak, and P. E. Suetin, Inzh.-Fiz. Zh. **39**, 428 (1980).
10. V. G. Chernyak and A. Ye. Margilevskiy, Int. J. Heat Mass Transf. **32**, 2127 (1986).

*Translated by M. Fofanov*

*Technical Physics, Vol. 46, No. 10, 2001, pp. 1247–1255. Translated from Zhurnal Tekhnicheskoĭ Fiziki, Vol. 71, No. 10, 2001, pp. 41–49.*


**GAS DISCHARGES, PLASMA**

# Arc Discharge with a Vaporizable Anode: Why Is the Fullerene Formation Process Affected by the Kind of Buffer Gas?

**N. I. Alekseyev and G. A. Dyuzhev**

*Ioffe Physicotechnical Institute, Russian Academy of Sciences, St. Petersburg, 194021 Russia*
*e-mail: dgan@hm.csa.ru*

Received January 26, 2001

**Abstract**—A model for calculating an arc discharge with the vaporizable graphite anode used in production of fullerenes has been proposed. Calculations with the use of this model give a clue to the dependence of fullerene formation efficiency on the kind of buffer gas used. © *2001 MAIK "Nauka/Interperiodica".*

## INTRODUCTION

In the physics of gas discharge there is practically no theoretical or experimental studies on arcs with vaporizable anodes. Such arcs are of interest for a new direction in plasma technologies dealing with the deposition of coats and, especially, as a basic method for the production of fullerenes. It is known that for the fullerenes to form in an arc discharge, a buffer gas should be present. In a vacuum discharge or at a low buffer gas pressure no fullerenes are formed. It is thought that the buffer gas is necessary for taking away the excess of vibrational energy from the growing carbon cluster. However, this explanation encounters some problems when trying to take into account the kind of gas used.

In [1] the fullerene formation process in three inert gases (helium, neon, and argon) was studied. The experiments have shown that with the increasing molecular weight of the gas, from helium to argon, the content of fullerenes in the soot diminished, whereas the arc current necessary for achieving a certain rate of anode erosion increased. The proposed explanation of the observed effects as due to collisions of pairs of buffer gas atoms with carbon clusters appears inconclusive. With heavier gases, quenching of the vibrational energy should be more efficient, but experimental data attest to the contrary.

However, the effect of the buffer gas on the fullerene formation efficiency could be of a different nature. Perhaps, the buffer gas is not acting through elementary reactions, but rather is affecting the parameters of the gas stream with an admixture of carbon ejected from the interelectrode gap. Indeed, in lighter helium the carbon ions have higher mobility and easily escape from the discharge. It can be surmised that for the plasma to be highly ionized they should be confined to the interelectrode gap. This can be achieved using the drop in potential of the positive anode [2]. In this case the anode is heated more intensively and the erosion rate is higher. In heavy buffer gases the mobility of carbon ions is lower, their escape to the electrodes less intensive, and the same rate of anode erosion is reached at a much higher current. However, with the rising current the speed of the gas-plasma jet increases [3], decreasing the efficiency of the fullerene formation [4].

This speculative argumentation can only be proved or disproved by calculations and such calculations will be the subject of the present work.

### *A Physical Model of the Arc Discharge*

The fullerene arc, in an optimum regime for the production of fullerenes [5], burns between graphite electrodes of a diameter $2r_0 = 0.6$ cm in an interelectrode gap of $L \sim 0.6$ cm, in an atmosphere of inert buffer gas held at a pressure of ~100 torr containing carbon vaporized from the anode. The arc current is variable in a range of 50–150 A; the voltage across the gap is about 20 V. Such an arc is a typical low-temperature thermal emission discharge, because in the experiment no spots have been detected on the electrodes.

The most closely related process that has been given theoretical treatment is a high-current arc at atmospheric pressure in inert gases [6]. It was shown that in argon the drop in potential of the anode is negative, whereas in helium it could be positive. Calculations were carried out for high current densities ($j \sim 300$–$500$ A/cm$^2$), at which the arc column could be considered stabilized by radiation. The anode temperature was assumed to be low enough for erosion of the anode material and emission of electrons from the anode to be negligible.

It is evident that in a fullerene arc the assumptions used in [6] are not valid. Therefore, it is necessary to adopt an arc model that would account for the specific features of the process and be simple enough, because it should become a component part of a general algorithm for calculation of the fullerene formation process.

The system of equations was written under the following simplifying assumptions.

1063-7842/01/4610-1247$21.00 

The problem is one-dimensional, i.e., the arc parameters are independent of the distance from the discharge axis. The removal of energy and particles in the radial direction is not taken into account despite the fact that the diameter of the electrodes is close to the interelectrode separation. Accurate solution of the two-dimensional problem is extremely difficult.

The buffer gas in the interelectrode gap is immobile and not ionized. Because the ionization potential of carbon is less than that of inert gases, for electron temperatures that are not too high this assumption is quite acceptable. It is also supported by measured spectra of the fullerene arc [5], which contain no lines of the buffer gas ions.

The carbon concentration is much less than the concentration of buffer gas atoms. This assumption does not cover all the regimes of practical interest, especially those using heavy buffer gases, but is quite sufficient for deriving qualitative relationships and significantly simplifies the calculations.

The flow of carbon atoms is directed from the anode to the cathode, which corresponds to the experiment in [5], because the weight of carbon deposited on the cathode (cathode deposit) is comparable to the weight of soot deposited on the walls of the plasma reactor. The accommodation coefficient for the carbon atoms and ions on the cathode is equal to unity. The carbon flows in the gap are described in terms of diffusion and mobility; there is no convection of carbon.

The plasma in the greater part of the gap is in the state of local thermodynamic equilibrium (LTE).

### *System of Equations*

The system of equations describing the fullerene arc should comprise equations for the transfer of energy; the current; the heavy component in the plasma volume; and the boundary conditions at the cathode and anode, which simulate solution of the problem in the layer adjacent to the electrode. As the electrodes represent active elements of the process (electrons are emitted from the cathode and carbon is vaporized from the anode), it is also necessary to take into account the balance equation for the energy and particles at the anode and cathode, and the heat transfer in the bulk of the electrodes.

The electron current in the plasma bulk has field and diffusion components

$$J_e = \mu_e\left(nE - \frac{dP_e}{dx}\right), \tag{1}$$

where $\mu_e$ is the electron mobility determined by Coulomb collisions, $P_e = nT_e$ is the electron pressure, $n$ is the plasma density, $T_e$ is the electron temperature, and the $x$-axis is directed from cathode ($x = 0$) to anode ($x = L$).

The electron transfer through the interelectrode gap is determined by the balance of forces for electrons and ions and atoms of carbon. The buffer gas concentration in the gap is assumed to be constant and its velocity equal to zero.

$$-V_e n\left(\frac{1}{\mu_{ei}} + \frac{1}{\mu_{ea}} + \frac{1}{\mu_{eg}}\right) - \frac{dP_e}{dx} + nE = 0, \tag{2}$$

$$-V_e\frac{n}{\mu_{ei}} - V_i\frac{n}{\mu_{ig}} - (V_i - V_a)\frac{n}{\mu_{ia}} - \frac{dP_i}{dx} - nE = 0, \tag{3}$$

$$-V_e\frac{N_a}{\mu_{ae}} - V_i\frac{N_a}{\mu_{ag}} - (V_a - V_i)\frac{N_a}{\mu_{ia}} - \frac{dP_a}{dx} = 0. \tag{4}$$

Here and in all subsequent formulas, subscripts in small letters have the following meanings: *e*—electrons; *i*—ions; *a*—carbon atoms; and *g*—atoms of the buffer gas. The first subscript by the mobility symbols denotes the particle scattered, and the second denotes the scatterer; $N_a$ is the concentration of carbon atoms; and $V$ is the velocity of the components.

In calculations of the mobility of carbon atoms in the buffer gas an empirical Fuller–Schletter formula [7] is used. The mobility of ions in their own gas $\mu_{ia}$ is determined by resonant recharging. For carbon no data are available; however, a comparison with ions, whose other properties are close, $O^+$ and $N^+$, gives an estimate of the cross section at $\sigma_{ia} \sim 3 \times 10^{-15}$ cm$^2$. The ion mobility in the buffer gas is determined by polarization effects and is calculated following [8].

The estimates have shown that, as a rule, the scattering lengths responsible for the resonant recharging are large and the corresponding terms can be left out. Then, excluding electric field $E$ from (2) and (3), we get the following expression for the total flow $J$ of the atoms and ions of carbon in the gap:

$$J = -\mu_{ig}\frac{d(P_e - P_i)}{dx} - \mu_{ag}\frac{dP_a}{dx} + j_e\left(\frac{\mu_{ag}}{\mu_{ea}} - \frac{\mu_{ig}}{\mu_{ea}} - \frac{\mu_{ig}}{\mu_{eg}}\right). \tag{5}$$

Preliminary calculations have shown that the last term in Eq. (5) is also insignificant.

The equation for the energy transfer by electrons has the form

$$j_e E = S_{ei} + S_{\text{rad}} + \frac{d}{dx}\left(3.2T_e j_e - \kappa_e\frac{dT_e}{dx}\right). \tag{6}$$

The energy transfer to ions when the heavy component temperature $T$ is different from the electron temperature $T_e$ is given by

$$S_{ei} = \frac{3m}{M_a}(T_e - T)V_{T_e}n^2Q_{ei}, \tag{7}$$

where $Q_{ei}$ is the Coulomb cross section; $V_{T_e}$ is the thermal velocity of electrons; and $M_a$ is the mass of the car-

bon atom. Compared to this quantity, the energy transfer in a highly ionized plasma to atoms of both species is negligibly small.

According to [9], the total radiation intensity in a bremsstrahlung and recombination continuum is

$$S_{\text{rad}} = 1.53\times 10^{-32} T_e^{1/2}[\text{eV}] n^2\left(1+\frac{E_g}{T_e}\right)\left[\frac{\text{W}}{\text{cm}^3}\right], \quad (8)$$

where $E_g$ is the ionization energy of the lower excited state.

The product $j_eE$ is determined from the transfer equation for the electron current (1)

$$j_eE = \frac{j_e^2 T_e}{nD_e} + \frac{j_e}{n}\frac{dP_e}{dx}, \quad (1')$$

in the highly ionized plasma the product $D_en \sim T_e^{3/2}$ and almost independent of $n$.

The energy transfer equation for the heavy component has the form

$$2J\frac{dT}{dx} - \kappa\frac{d^2T}{dx^2} = S_{ei}, \quad (9)$$

where $\kappa$ is the heat conductivity of the heavy component determined mainly by the buffer gas; dependence of the heat conductivity on the gas temperature is neglected.

The system of equations describing the plasma volume is complemented with a condition for local thermodynamic equilibrium (LTE)

$$n^2 = \left(\frac{2\pi mT}{h^2}\right)^{3/2} N_a \exp\left(-\frac{E_{\text{ion}}}{T_e}\right), \quad (10)$$

where $E_{\text{ion}}$ is the ionization potential of carbon atoms.

Boundary conditions for the energy transfer equations are formulated from the following considerations. From the experimentally observed anode erosion rates [5], anode temperature and the plasma concentration near its surface can be estimated. These estimates show that the plasma concentration is close to values typical of the LTE plasma. Under these conditions detailed treatment in the first approximation of the region of nonequilibrium ionization, as distinct from the conditions of a nonemitting and erosionless anode considered in [6], appears unjustified. It is assumed that up to the anode the plasma may be considered to be LTE plasma.

Therefore, the boundary condition for Eq. (6) is specified directly at the anode in the form

$$\frac{1}{T_e^{(A)}}\frac{dT_e^{(A)}}{dx} = 0. \quad (11)$$

A boundary condition for Eq. (9) can be formulated as an energy balance at the anode surface. This happens in the following way. The anode is heated by the incident flow of plasma electrons, by heat conduction in the buffer gas, whose temperature is decreasing along the path from plasma to the anode, and by radiation from the heated cathode. Heat is taken away from the anode with the flow of vaporized carbon atoms radiating from its surface and by way of heat conduction in graphite. If the anode potential barrier is negative, a considerable amount of energy will be lost due to thermal electron emission. If the anode potential drop is positive, then this channel of energy loss is not available. It is impossible to account for the sign of the anode barrier in a general calculation, but the assumption of a positive anode drop is fairly reasonable; therefore, the energy loss due to emission current from anode is not considered.

Thus, the energy balance equation at the anode has the form

$$\begin{aligned} j_e(2T_{eA} + \chi_A) - \kappa\frac{dT^{(A)}}{dx} + \sigma T_K^4 \\ = -JH - \kappa_{gr}\frac{dT_A}{dx} + \sigma T_A^4. \end{aligned} \quad (12)$$

Here, $\kappa_{gr}$ is the heat conductivity of graphite; $\chi = 4.6$ eV is the work function; $H \sim 7.2$ eV is the evaporation heat of graphite. $A$ and $K$ denote quantities relating to the anode and the cathode, respectively. The temperature derivatives in the gas

$$\frac{dT^{(A)}}{dx} = \frac{dT}{dx}(L-0)$$

and in graphite

$$\frac{dT_A}{dx} = \frac{dT_{gr}}{dx}(L+0)$$

correspond to the anode surface.

The boundary condition at the cathode end of the LTE plasma region defines a relation between the energy brought to the region of nonequilibrium ionization by electrons emitted from the cathode, which passed through the near-cathode potential drop $\varphi_K$ and the energy flow in the LTE region

$$\begin{aligned} j_{es}(2T_K + \varphi_K) - \frac{1}{4}n_K V_{T_e}\exp\left(-\frac{\varphi_K}{T_e}\right)(2T_{eK} + \varphi_K) \\ = j_iE_{\text{ion}} + j_E^* + 3.2j_eT_e^{(K)} - \kappa_e\frac{dT_e^{(K)}}{dx}, \end{aligned} \quad (13)$$

where $j_{es}$ is the current due to emission from the cathode, which is related to the electron current as

$$j_e = j_{es} - \frac{1}{4}n_K V_{T_e}\exp\left(-\frac{\varphi_K}{T_e}\right), \quad (14)$$

where $j_E^*$ is the energy lost because of excitation of atoms; this quantity is approximately estimated as $j_E^* = j_i E_{\text{ion}}$.

Consider the balance equation for carbon particles. The flow of carbon atoms from the anode arises due to the difference between the carbon concentration near the anode $N_A$ and the equilibrium concentration $N_S(T_A)$ corresponding to the pressure of saturated carbon vapor at the anode temperature $T_A$. Hence,

$$J = \frac{1}{4}(N_A - N_S(T_A))V_{T_A}, \quad (15)$$

where $V_{T_A}$ is the thermal velocity of carbon atoms at the anode temperature.

At the cathode we have

$$J = \frac{1}{4}(N_S(T_K) - N_K)V_{T_k} - j_i. \quad (16)$$

The ion current to the cathode $j_i$ is assumed to be the Bohm's current, with the plasma concentration corresponding to the cathode end of the LTE region

$$j_i = \gamma_i n(T_{eK}/M_a)^{1/2}, \quad (17)$$

where $\gamma_i = 0.7$ is a numerical factor given by the theory of near-electrode layer [10].

This derivation of the ion current to cathode does not take into account variations of the plasma concentration in the region of nonequilibrium ionization [10]. However, these variations are insignificant and, besides, cannot be accounted for accurately having no reliable information on the rates of direct and step ionization of carbon.

The system of equations is complemented with the energy balance at the cathode

$$j_i(E_{\text{ion}} + \varphi_K) + \sigma T_A^4 - \kappa\frac{dT^{(K)}}{dx} + j_K^* + \frac{1}{4}n_K V_{T_e} \times \exp(-\varphi_K/T_{eK})(2T_{eK} + \chi) - JH = -\kappa_{gr}\frac{dT_K}{dx} + j_{es}(2T_{eK} + \chi) + \sigma T_K^4. \quad (18)$$

Equation (18) accounts for the cathode heating due to the current of carbon ions from the plasma, the reverse current of electrons from the plasma, the heat conduction in the buffer gas and the thermal emission from the anode. It also accounts for the cathode cooling due to electron emission producing the arc current, heat conduction in the graphite, and the radiation of heat from the cathode surface. Besides, the cathode absorbs the energy $JH$ transferred from the anode.

It is assumed in the calculations that the current density $j_{es}$, due to electron emission from the cathode, is determined by the cathode temperature $T_K$ and follows the Richardson formula. Generally speaking, the emission current is enhanced due to the Schottky effect and the effect of the hollow cathode [11]. The effect of the hollow cathode on a developed porous surface of cathode deposit in a fullerene arc was noted in [5]. In the calculation, these factors are taken into account by increasing the emission current tenfold over the value given by the Richardson formula. The calculation results proved to be insignificantly affected by this increase.

### *The Solution Technique*

The operating parameters that have to be specified are the emission current, which is nearly equal to the total current, and the buffer gas pressure. All other quantities are calculated. The solution process consists of two alternating iterative procedures. The first procedure is the solving of the system of algebraic equations (5), (10), and (14)–(18) (balance equations at the cathode and the cathode-end boundary of LTE plasma and the equation for heavy component transfer integrated from 0 to $L$) under fixed $T_A$, $T_{eA}$, $dT^{(K)}/dx$, and $dT_e^{(K)}/dx$. This system of equations can yield parameters of the gas and plasma near the electrodes, i.e., the quantities $n_K$, $N_K$, $\varphi_K$, $n_A$, and $N_A$. Iterations are necessary because the system includes a transcendental equation, the Sakha condition, from which the electron temperature near the cathode $T_{eK}$ is determined.

The second procedure consists in solving boundary-value problems (6) and (9) together with the heavy component transfer equation (5) and the Sakha condition. The boundary conditions for Eq. (6) are specified in the form $T_e(x = 0) = T_{eK}$ at the cathode and as Eq. (11) at the anode. The value of $T_{eK}$ is assigned a result of the first iteration. The boundary conditions for Eq. (9) are specified in the form $T(x = 0) = T_K$ at the cathode and as Eq. (12) at the anode.

In every iteration step Eq. (9) is solved directly by the sweep method as a linear boundary problem of the second order. The result is a gas temperature curve corresponding to a given iteration step. Then Eq. (6) is solved, written in terms of concentration $n$ (rather, of dimensionless quantity $\eta = (n^*/n)^2$, where $n^*$ is a characteristic unit for $n$). This is explained by the fact that $n$ is exponential in $T_e$, and since variation of $n$ along the gap is known only with an accuracy of the previous iteration step, the divergence is unavoidable. Use of the quantity $\eta$ makes the equation more involved, but, on the other hand, the temperature at every point of the gap is now calculated as a logarithm of $n$ and successive runs rapidly converge.

Because the parameters $T_A$, $T_{eA}$, and $dT^{(A)}/dx$ appear in the boundary conditions not explicitly but in combinations, solutions of the boundary problems give their new values, which are substituted when the first iteration procedure is run again. Alternation of the first and

second procedures is repeated until the discharge parameters are reproduced with required accuracy.

In order to solve the balance equations at the cathode and anode, it is necessary to know the value of the electrode temperature derivative at the surface. It is determined by solving the heat conduction problem in graphite. A one-dimensional problem is considered, i.e., the temperature is assumed to be independent of the distance to the discharge axis. Then, the heat condition equation, taking into account the evolved energy and cooling due to radiation from the lateral surface, has the form

$$\pi r_0^2 j_e^2 \rho = 2\pi r_0 \sigma T^4 - \pi r_0^2 \kappa_{gr} \frac{d^2T}{dx^2}. \qquad (19)$$

Temperature dependences of the heat conductivity $\kappa_{gr}$ and the specific resistance of graphite $\rho$ are obtained from data on reactor graphite [12].

Equation (19) is integrated in quadratures of the form $x = x(T, dT_{K,A}/dx)$. The derivative $dT_{K,A}/dx$ on the electrode surface is calculated for a condition that the temperature of the cooler $T_{cool} = 300$ K is achieved at a point $x_{cool}$ corresponding to the distance from the cooler to the electrode surface, and is calculated by dividing in two.

Variations of the temperature $T(x)$ and the quantity $dT_{K,A}/dx(T_{K,A})$ for $x_{cool} = 2$ cm are shown in Figs. 1 and 2. Actually, the arbitrariness in the choice of $x_{cool}$ is not important. The role of the heat condition in the energy balance at the cathode at $T_K \sim 2600$–$2800$ K is a minor one. Regarding the anode, at $T_A \geq 3700$ K and $x_{cool} \geq 2$ cm the derivative $dT_A/dx$ is almost independent of $x_{cool}$.

### *Calculation Results and Comparison with an Experiment*

The calculations have shown that for each gas there exists a minimum value of the arc current density, below which the solution does not exist. At currents slightly higher than the minimum value, the solution is formally obtainable but physically appears unrealistic, because the electric field strength near the cathode boundary of the LTE region changes sign, becoming negative. Therefore, the critical current density is considered to be the value at which $E_K = 0$. Values of the critical current density for various gases are given in the table.

Shown in Fig. 3 are distributions along the gap of the electron temperature $T_e$, temperature of the heavy plasma components $T$, concentrations of carbon atoms $N$ and ions $n$, and the plasma potential $V$ for an arc in helium at a pressure of 100 torr and current 80 A ($j$ = 284 A/cm$^2$). The point $x = 0$ is at the cathode surface; the interelectrode gap is 6 mm; the cathode potential is $V = 0$; and $U$ is the total voltage between the electrodes.

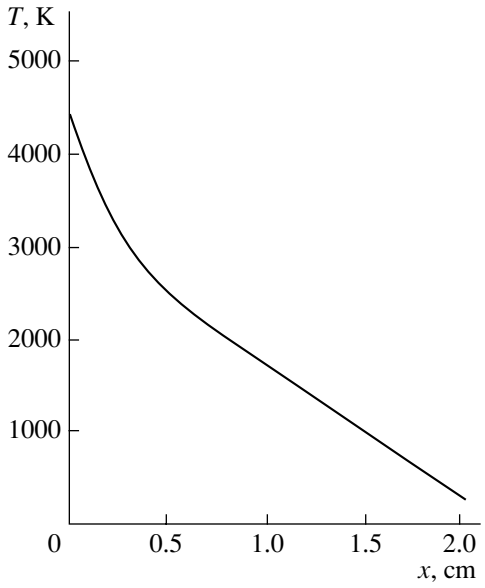


**Fig. 1.** Temperature distribution along the graphite electrode. $I = 80$ A ($j = 284$ A/cm$^2$); $2r_0 = 6$ mm.

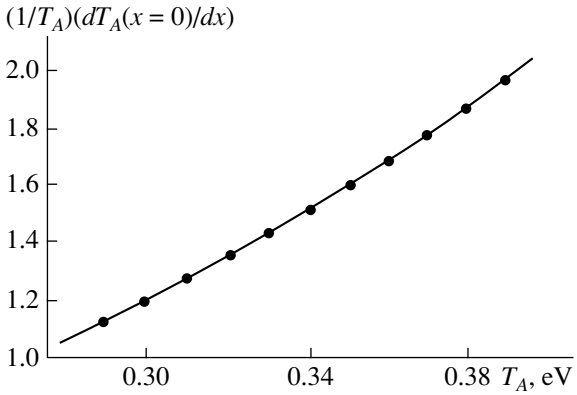


**Fig. 2.** Dependence of the logarithmic derivative of the temperature inside graphite on the surface temperature.

It is seen that the difference between the electron temperature and the temperature of the heavy component is significant only near the electrodes. Throughout greater part of the gap, the plasma is close to complete thermodynamic equilibrium. A gas temperature of $T \sim$ 5000–5600 K measured in [13] in a fullerene arc under similar operating parameters is somewhat lower than the calculated values. This discrepancy, in our opinion, can be explained as follows. In [13] the temperature was determined from relative intensities of the lines in emission hands of $C_2$ molecules. In the center of the arc column the concentration of $C_2$ is small and the temperature determined in [13] without the Abelian correction corresponds to the discharge periphery, where it is obviously lower because of the boundary effects.

The concentration of carbon atoms fairly monotonously decreases from anode to cathode by more than an order of magnitude. At the same time, gradients of

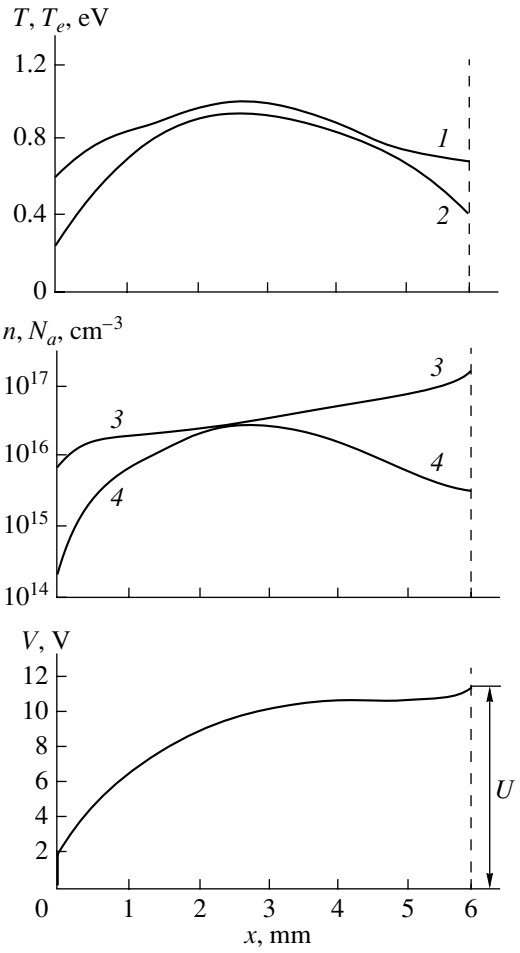


**Fig. 3.** Distribution along the interelectrode gap of the electron temperature (*1*), temperature of the plasma heavy component (*2*), concentrations of carbon atoms $N_a$ (*3*) and ions $n$ (4), and the plasma potential $V$. Helium. $P_{He}$ = 100 torr, $I$ = 80 A, $L$ = 6 mm.

the concentration of charged particles are large, especially near the electrodes. Large values of the diffusion component of electron current caused by concentration gradients affect the potential distribution. In the near-cathode region of the plasma, where the diffusion current is flowing towards the cathode, the electric field is considerably stronger than near the anode, where the directions of the field and diffusion components coincide. The cathode potential drop is small ($\varphi_K \sim 3$ V) and the anode potential drop ($\varphi_A \sim T_e$) is positive.

The above qualitative characteristics of the distribution of plasma parameters in the interelectrode gap have been observed for neon and argon as well. In Fig. 4 data for argon at a pressure of 100 torr and a current of 102 A ($j$ = 361 A/cm$^2$) are shown.

A similar local probing of the fullerene arc has not yet been implemented; therefore, comparison of calculations with experimental results is possible only for integrated characteristics: arc voltage and the anode erosion rate $q = JM_a\pi r_0^2$.

Figure 5 shows dependences of the anode erosion rate in helium on current, pressure, and interelectrode separation. The solid curves are calculation results, and the broken lines are experimental curves from [4]. It is seen that the theoretical and experimental curves of $q$ versus $I$ are in good agreement (Fig. 5a). The calculated curve of $q$ as a function of helium pressure (Fig. 5b) is seen not to have a minimum. The origin of the maximum in the erosion rate at pressures of 400–500 torr observed experimentally in [4] is not quite clear. Possibly, it is related to the different shape of the arc attachment to anode at high pressures. Calculations for small interelectrode separations ($L$ < 3 mm), where a drastic increase of erosion is observed in the experiment, are not possible, because the adopted assumptions are not valid in this case.

Quantitative characteristics of some calculated regimes for different gases are given in the table. All calculations were carried out for the buffer gas pressure of 100 torr, electrode diameter $2r_0$ = 0.6 cm, and the interelectrode separation of $L$ = 0.6 cm. In the table the current values used in the calculation are given, as are the value of the near-cathode potential drop $\varphi_K$, the total arc voltage $U$, the maximum values of the electron temperature $T_e^{max}$, the gas temperature $T^{max}$, the surface temperatures $T_A$, and the anode erosion rate. Also given here are the available experimental data: content of fullerenes in the soot $\alpha$ determined from absorption spectra of solution in toluene [5] and the ratio of the rates of the cathode deposit growth and the anode erosion, $m_c/q$.

It can be seen that the calculated data on the anode erosion rate for helium are in satisfactory agreement with the experiment and give a qualitatively true account of the experimental observation that with heavier buffer gases the same rate of anode erosion is reached at higher currents. The reason is evident: in a heavier gas the carbon mobility is lower and the transport from anode to cathode is impeded. This is evident in the experiment as well: in helium $m_c/q$ = 0.4, whereas in heavy gases $m_c/q \sim 0.1$. The most considerable difference between the theory and experiment is observed in the arc voltage in helium and the rate of erosion for heavy gases.

### *Calculation of the Near-Anode Layer and Discussion of Results*

The difference in the arc voltages calls for a more detailed consideration of the nonequilibrium ionization layer near the anode. It is known [6, 10] that the layer width is about $\xi \sim 2L_{ion}$, where

$$L_{ion} = \frac{\mu_{ia}(T_{eA} + T_A)}{\beta_{ion} N_a} \qquad (20)$$

is the ionization length and $\beta_{ion}$ is the ionization constant.

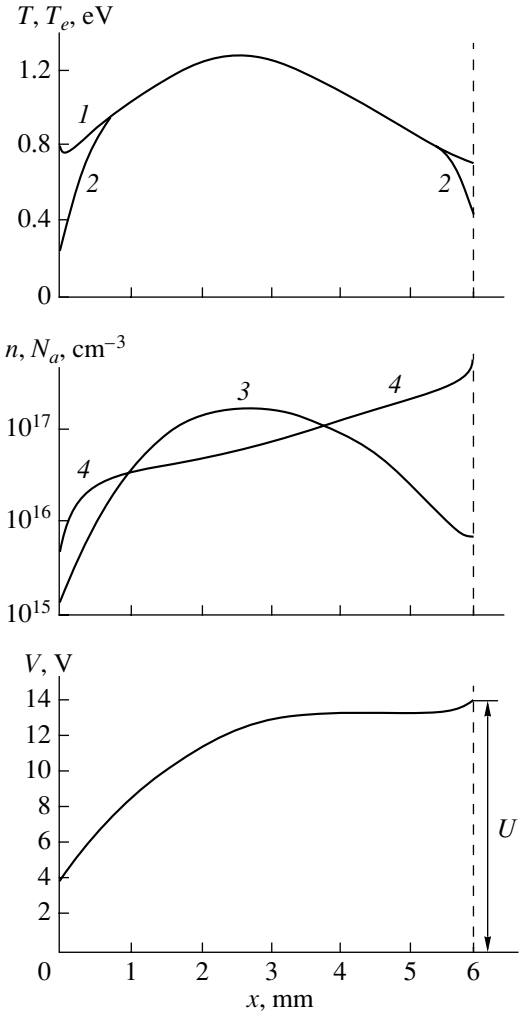


**Fig. 4.** Same as in Fig. 3 for argon. $P_{Ar}$ = 100 torr, $I$ = 102 A, $L$ = 6 mm.

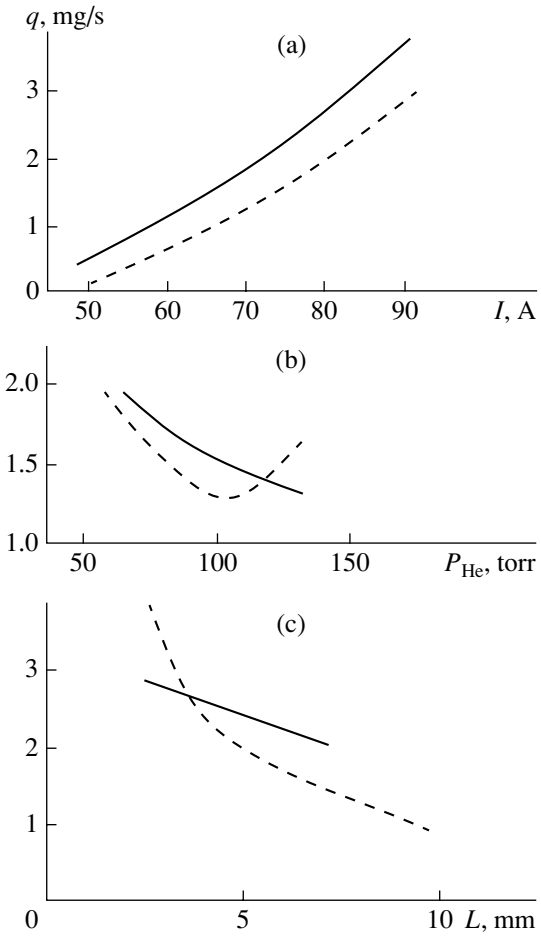


**Fig. 5.** Dependence of the anode erosion rate for arc in helium. (a) Dependence on the arc current, $P_{He}$ = 100 torr, $L$ = 6 mm; (b) dependence on helium pressure, $I$ = 80 A, $L$ = 6 mm; (c) dependence on the interelectrode separation, $P_{He}$ = 100 torr, $I$ = 80 A.

If $\beta_{ion}$ is calculated by the Gurevich-Pitaevskii formula [10], an estimate of the ionization length for helium will be $L_{ion} \sim 0.03$–$0.05$ cm and for argon $L_{ion}$ is less than 0.01 cm. The electric field strength $E$ in the anode layer can be estimated by formula (1') assuming that the electron concentration varies monotonously from $n_A$ at the anode end of the LTE plasma to the electron vapor concentration $n_A^*$ corresponding to a given anode temperature. Such an estimate for helium gives a field strength of $E \sim 100$–$200$ V/cm and an anode drop of $\varphi_a \sim \xi E \sim 5$–$10$ V. For argon $E \sim 10$ V/cm and $\varphi_A$ is on the order of a few tenths of a volt. Therefore, the calculated arc voltage in helium should be increased by 5–10 V to bring $U$ in agreement with the experiment.

Naturally, this arbitrary addition of the layer to the LTE plasma region is not quite conclusive because the gas temperature in the layer can vary significantly [6] and in the case of intensive emission from the anode the electron concentration profile can be nonmonotonous. Therefore, for helium, a calculation for the entire arc was made explicitly taking into account the layer of nonequilibrium ionization.

The system of energy balance equations for the plasma components was complemented with a similar system for the layer and a balance equation for ionization–recombination. The calculation procedure was modified in the following way.

The gas temperature and its derivative in the heat condition equation (9) for the LTE plasma were joined with an analytical solution of the same equation for the layer. The analytical solution was obtained using the following premises. In the absence of electron emission from the anode the plasma concentration could have been found from Eq. (10)

$$\frac{d^2n}{dx^2} = -\frac{\beta_{ion} N_a T}{D_{ia}(T_e + T)} \frac{n}{n_A^2}(n_A^2 - n^2) \qquad (21)$$

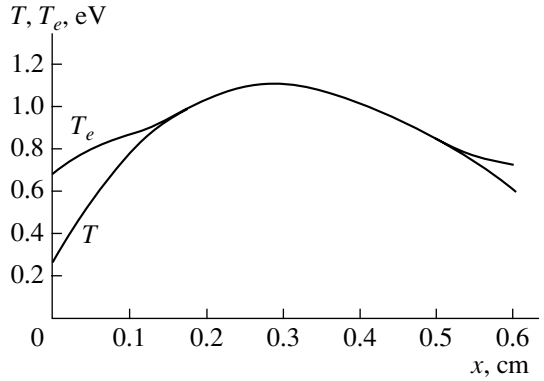


**Fig. 6.** Distributions of the electron and gas temperatures in the LTE region. $P_{He}$ = 100 torr, $I$ = 80 A, $L$ = 6 mm. Calculated taking into account the nonequilibrium ionization region near the anode.

with boundary conditions $n(x \longrightarrow -\infty) = n_A$ and $n(\xi) = n_A^{(0)} = 4j_e/V_{T_e}$. Here, the origin of coordinates at the boundary of LTE plasma near the anode and the anode surface has a coordinate $\xi$.

Assuming weak temperature variation, $T_e \approx T_{eA}$, the solution of Eq. (21) has the form

$$\frac{n}{n_A} = \frac{1 - \varepsilon \exp(-2(\xi - x)/L_{ion})}{1 + \varepsilon \exp(-2(\xi - x)/L_{ion})}, \qquad (22)$$

where

$$\varepsilon = \frac{n_A - n_A^{(0)}}{n_A + n_A^{(0)}}. \qquad (23)$$

The layer boundary was considered to be at a position $x_1$, where the ratio $n(x_1)/n_A$ is close to unity, say 0.9. This criterion was used for determining the layer width, which is numerically equal to $\xi \sim 2L_{ion}$.

Equation (9) lends itself to analytical integration with the concentration given by Eq. (22). The integration results are too cumbersome to be given here.

Equation (22) was considered applicable up to point $x'$, where concentration $n$ becomes equal to that of the electron gas retained by the anode potential. The calculation procedure for the potential profile to the right of $x'$ was similar to the above estimation, except that the potential and the position of point $x'$ were determined in a self-consistent manner. Parameters of the solution thus corrected are marked by an asterisk. It is seen that the arc parameters changed insignificantly. Distributions of the plasma potential and the concentration of plasma components along the interelectrode gap also changed very little. The only significant difference is seen in the profile of the gas temperature (Fig. 6), which varies markedly in the near-anode layer. In the regime of Fig. 6 the anode barrier $\varphi_A$ is 4.8 V, in agreement with the rough estimates above.

With neon and argon the anode barrier is low and the calculated arc voltages are in good agreement with the experiment. The systematic discrepancy between calculated and measured anode erosion rates in heavy gases can be partially explained by underestimation of the anode evaporation heat $H$. Increasing $H$ from 7.2 to 7.5 V reduces the erosion rate in argon from 0.73 to 0.45 mg/s. Another possible reason for this discrepancy could be the overestimated mobility of the carbon atoms, because the Fuller–Schletter formula (as well as other relevant formulas) gives a fair description of experimental data at temperatures not higher than 1000°C.

So, the model proposed for calculating the fullerene arc is in satisfactory agreement with the experimental data, adequately describes the major physical relationships, and can be incorporated in a general algorithm for calculating the fullerene formation in arc discharge.

**Table**

| Characteristics | Helium | | | | Neon | | Argon | |
|---|---|---|---|---|---|---|---|---|
| | calculation | | | experiment | calculation | experiment | calculation | experiment |
| $I_{min}$, A | 48 | | | | 75 | | 85 | |
| $I$, A | 50 | 80 | 80* | 80 | 85 | 85 | 102 | 105 |
| $\varphi_K$, eV | 3.0 | 1.8 | 1.6* | – | 3.1 | – | 3.6 | – |
| $U$, V | 8.8 | 11.1 | 12.1* | 21.5 | 13.4 | 14 | 13.7 | 14 |
| $T^{max}$, eV | 0.77 | 0.99 | 1.08* | – | 1.20 | – | 1.26 | – |
| $T_e^{max}$, eV | 0.84 | 0.93 | 1.08* | – | 1.20 | – | 1.26 | – |
| $T_A$, K | 3865 | 4160 | 4144* | – | 4216 | – | 4385 | – |
| $g$, mg/s | 0.55 | 2.32 | 2.46* | 1.20 | 0.96 | 0.14 | 0.70 | 0.11 |
| $\alpha$, % | – | – | – | 9.7 | – | 4.3 | | 1.8 |
| $m_c/q$ | – | – | – | 0.41 | – | 0.10 | – | 0.12 |

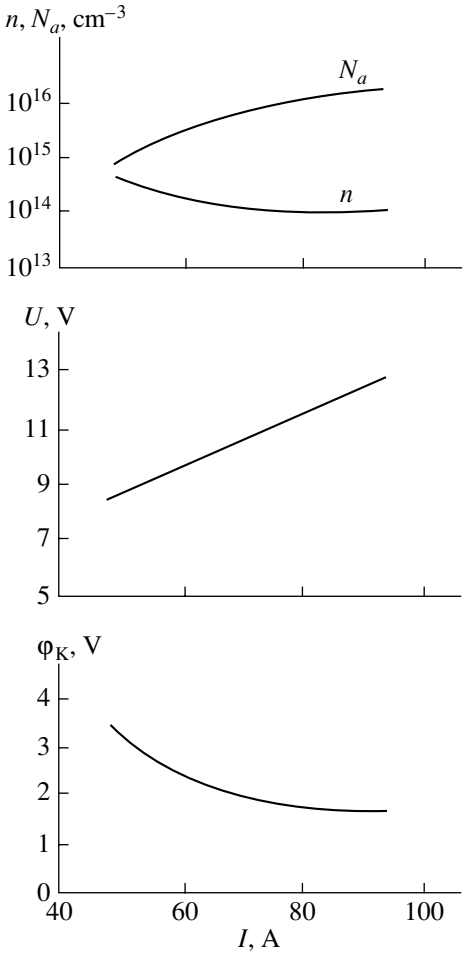


**Fig. 7.** Dependences of the current on the carbon concentration, plasma concentration, total voltage drop and the near-cathode potential drop. Helium. $P_{He}$ = 100 torr, $L$ = 6 mm.

## CONCLUSION

It necessary to emphasize that the fullerene arc is a very specific kind of gas discharge. It is radically different from both the low-voltage arc with a thermal-emission cathode [10] and the high-current arc at atmospheric pressure [14]. This is illustrated in Fig. 7 showing the dependence on current of some calculation parameters of the arc for an electrode diameter of 0.6 cm. It is seen that the carbon concentration in the gap rises with current while the plasma concentration is decreasing. The arc voltage rises with current, and it is not due to the growth of near-anode potential, which, on the contrary, decreases with current, but is the result of increasing voltage across the arc volume.

Calculation of the arc burning in a vapor of the anode material is of interest not only for fullerene production but also for a comparatively new branch of plasma technologies: the deposition of coatings of anode material in vacuum arc.

## ACKNOWLEDGMENTS

The authors are grateful to D. V. Afanas'ev for making available to them his latest experimental results.

This study was carried out in the framework of the Russian program "Fullerenes and Atomic Clusters" and supported in part by the Russian Foundation for Basic Research (project no. 00-02-16928).

## REFERENCES

1. D. V. Afanas'ev, A. A. Bogdanov, G. A. Dyuzhev, *et al.*, Zh. Tekh. Fiz. **67** (2), 125 (1997) [Tech. Phys. **42**, 234 (1997)].
2. G. A. Dyuzhev, V. A. Nemchinskiĭ, S. M. Shkol'nik, and V. G. Yur'ev, in *Chemistry of Plasma* (Énergoatomizdat, Moscow, 1983), Vol. 10, pp. 169–209.
3. S. Ramakrishnan, A. D. Stokes, and J. J. Lowke, J. Phys. D **11**, 2267 (1978).
4. D. V. Afanas'ev, G. A. Dyuzhev, and A. A. Kruglikov, Zh. Tekh. Fiz. **71** (7), 137 (2001) [Tech. Phys. **46**, 923 (2001)].
5. D. V. Afanas'ev, I. O. Blinov, A. A. Bogdanov, *et al.*, Zh. Tekh. Fiz. **64** (10), 76 (1994) [Tech. Phys. **39**, 1017 (1994)].
6. V. A. Nemchinskiĭ and L. N. Peretts, Zh. Tekh. Fiz. **47**, 1868 (1977) [Sov. Phys. Tech. Phys. **22**, 1083 (1977)].
7. R. C. Reid, J. M. Prausnitz, and T. K. Sherwood, *Properties of Gases and Liquids* (McGraw-Hill, New York, 1977; Khimiya, Leningrad, 1982).
8. B. M. Smirnov, *Atomic Collisions and Elementary Processes in Plasma* (Atomizdat, Moscow, 1968).
9. Yu. P. Raizer, *Gas Discharge Physics* (Nauka, Moscow, 1987; Springer-Verlag, Berlin, 1991).
10. *Thermionic Converters and Low-Temperature Plasma* (Nauka, Moscow, 1973).
11. G. A. Dyuzhev and N. K. Mitrofanov, Zh. Tekh. Fiz. **48**, 2500 (1978) [Sov. Phys. Tech. Phys. **23**, 1429 (1978)].
12. *Tables of Physical Quantities. Handbook*, Ed. by I. K. Kikoin (Atomizdat, Moscow, 1976).
13. A. Huczko, H. Lange, *et al.*, J. Phys. Chem. A **101**, 1267 (1997).
14. M. F. Zhukov, N. P. Kozlov, A. V. Pustogarov, *et al.*, *Near-Electrode Processes in Arc Discharges* (Nauka, Novosibirsk, 1983).

*Translated by B. Kalinin*

*Technical Physics, Vol. 46, No. 10, 2001, pp. 1256–1259. Translated from Zhurnal Tekhnicheskoĭ Fiziki, Vol. 71, No. 10, 2001, pp. 50–53.*


**GAS DISCHARGES, PLASMA**

# A Study of Cold Cathodes for the Plasma Sources of Hydrogen Ion Beams

**L. P. Veresov, O. L. Veresov, M. I. Dzkuya, Yu. N. Zhukov, G. V. Kuznetsov, and I. A. Tsekvava**

*Sukhumi Physicotechnical Institute, Sukhumi, 384914 Abkhazia, Georgia*

Received January 31, 2001

**Abstract**—Two types of cold cathodes (the hollow and magnetron) of a duoplasmatron used for the production of proton beams are comparatively studied. © *2001 MAIK "Nauka/Interperiodica".*

## INTRODUCTION

A facility for producing short-lived "medical" radionuclides based on a proton linear accelerator is presently under construction at the Sukhumi Physicotechnical Institute [1]. The accelerator injector will be based on a duoplasmatron with a cold cathode, which has a substantially longer service life than a hot cathode. This study is aimed at choosing the proper type of cold cathode. The main parameters under investigation are the cathode service life, the energy and plasma-forming gas consumption, and the source emissivity.

There are three types of cold cathodes used in plasma ion sources: the hollow cathode, the magnetron cathode, and the Penning cell. Since the latter is difficult to incorporate into the duoplasmatron, we studied only the hollow and magnetron cathodes.

## CATHODE DESIGN

There is a variety of hollow cathode designs. When choosing the proper cathode design, we took into account the parameters and operational data of the cathode. The use of a hollow cathode in a duoplasmatron is described in [2]. It consisted of a barrel-like cavity placed into a longitudinal magnetic field to ensure a longer path length for the emitted electrons. The operation of a duoplasmatron with a hollow cathode in the injector of a linear accelerator was described in [3]. The cathode consisted of three in-series tubes with different cross sections. The plasma-forming gas was supplied into the first tube. The plasma jet flowing out of the last tube underwent magnetic contraction. In our opinion, the disadvantages of a source with this type of a cathode are the high discharge ignition voltage (up to 2 kV) and the low gas efficiency. Better characteristics were achieved using a hollow cathode with an increased (by setting additional ribs) emission surface [4].

Based on this idea, we designed a hollow cellular (HC) cathode. It is a 10-mm-long metal cylinder 17 mm in diameter with 37 holes 2 mm in diameter. The cylinder is placed in the cathode housing.

The cathode housing is a stainless-steel cylindrical cup. At one of its ends, there is a 10-mm-diameter aperture. The plasma-forming gas ($H_2$) is supplied through the other end. The components of the magnetron cathode are also set in this housing. One of the versions of a magnetron cathode was previously successively used in the source of negative hydrogen ions [5]. It was an inverted coaxial magnetron with an increased (as compared to the noninverted magnetron) emission surface area.

We improved the design of this magnetron cathode by decreasing its size, modifying the magnet system, and using a multichamber scheme. Using diaphragms to divide the hollow cathode into several separate chambers enabled us (i) to decrease the cathode size keeping the emission surface unchanged, (ii) to increase the gas efficiency, and (iii) to ensure the stable operation of the plasma generator. For a single-chamber magnetron cathode, jumplike transitions of the discharge to the anomalous glow or arc discharge mode resulted in the disruption of the operation of the entire plasma generator. In a multichamber magnetron cathode, such transitions are suppressed almost completely. The discharge disruption in one of the chambers of the magnetron cathode does not affect the operation of the other chambers because, as soon as at the next pulse, the normal discharge mode is restored. The reason for this is that (i) deionization in a small volume proceeds more rapidly than in a large volume and (ii) breakdown is easier to develop in a large chamber than in several small chambers connected in parallel (Fig. 1). As a result, the operation of the entire plasma generator is stable, without transitions to the anomalous glow or arc discharge modes.

The HC cathode and the inverted coaxial multichamber magnetron (ICMM) cathode were comparatively studied while operating in a duoplasmatron. The parameters under investigation were the plasma-forming gas consumption, the discharge voltage and current, and the source emissivity.

1063-7842/01/4610-1256$21.00 © 2001 MAIK "Nauka/Interperiodica"

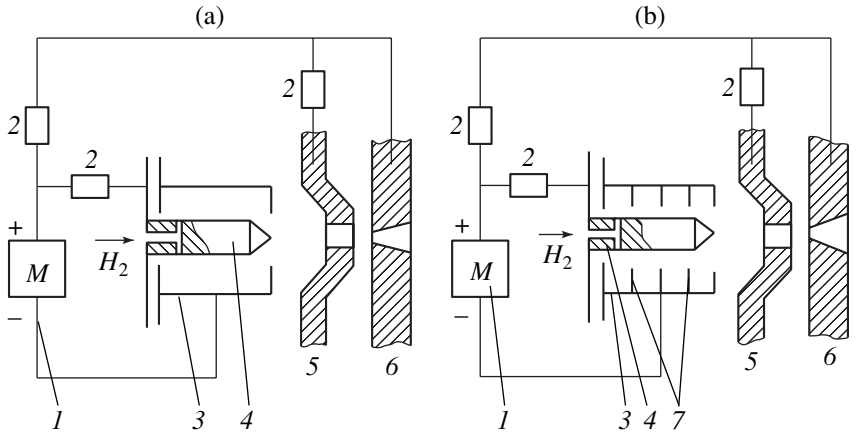


**Fig. 1.** Schematic of a plasma source with (a) a single-chamber and (b) multichamber magnetron: (*1*) modulator, (*2*) ballast resistors, (*3*) magnetron cathode, (*4*) magnetron anode, (5) intermediate electrode, (*6*) emitting electrode (anode), and (*7*) cathode diaphragms.

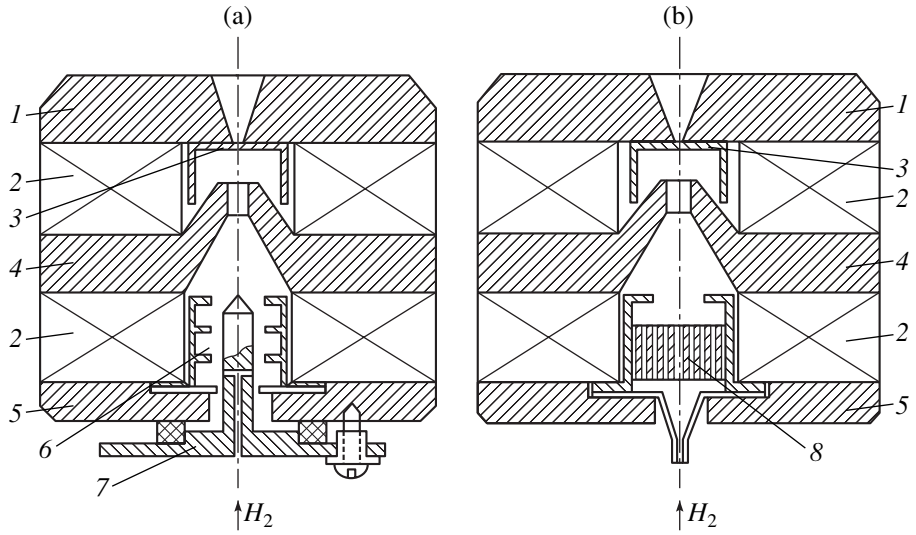


**Fig. 2.** Schematic of a plasma source with (a) an ICMM and (b) HC cathodes: (*1*) anode magnet pole, (*2*) ring permanent magnet, (*3*) emitting electrode diaphragm, (*4*) intermediate electrode, (*5*) cathode magnet pole, (*6*) ICMM cathode, (*7*) magnetron anode, and (*8*) HC cathode.

## SOURCE DESIGN

To investigate cold cathodes, the duoplasmatron design was substantially modified. The source consists of two chambers (gas discharge cells) connected in a series (Fig. 2). The plasma generator with a cold cathode is placed in the first cell. The second (duoplasmatron) cell provides the compression (contraction) of the plasma with the help of both its intrinsic pressure and a nonuniform magnetic field; then, the plasma is expelled into the expander. The second cell is of the same shape as the former duoplasmatron. In this cell, the electromagnet was replaced with an FeBa ring magnet (with an induction on the axis of ~1100 G). The cathode housing, in which either the HC or ICMM cathode components are installed, is placed in the first chamber. The housing is placed into an FeBa ring magnet identical to the first, which creates a nonuniform magnetic field in the duoplasmatron cell. Thus, in both cells, the magnetic field on the axis is almost the same. While operating with an HC cathode, the ring magnet was replaced with a duralumin ring of the same size.

The volume of the gas discharge chamber in the source with a cold cathode was decreased by a factor of 7 (from 56 to 8 $cm^3$) as compared to the initial version with a hot cathode.

The pulse duration and the repetition rate ranged within 0.1–1 ms and 1–10 Hz, respectively. The electromagnetic valve enabled pulsed puffing of the plasma-forming gas ($H_2$) into the source [6].

In our comparative studies, the simplest two-electrode ion-optical system was used to extract, form, and

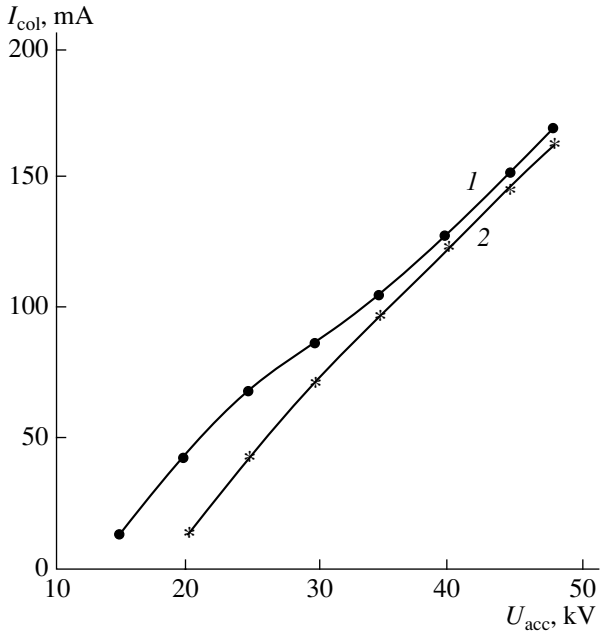


**Fig. 3.** Beam current vs. the accelerating voltage for (*1*) $I_p$ = 60 A and $U_p$ = 350 V and (*2*) $I_p$ = 22 A and $U_p$ = 500 V; $pV$ value is minimum.

accelerate hydrogen ion beams. In this case, the source operates in a mode with higher (more) stress (with a return electron current and a weak beam compensation and focusing) than with other ion-optical systems.

## EXPERIMENTAL RESULTS

The plasma-forming gas consumption was estimated by the change in the pressure in a 1-l reference vessel for a certain number of operating cycles. The reference vessel was filled with hydrogen and connected to the source. The pressure in the reference vessel was constantly measured with a gauge. The plasma-forming gas was puffed through an electromagnetic valve into the duoplasmatron, which operated in the optimum mode. The pressure in the vessel was kept within 1–1.2 atm (standard operating pressure range of the source). The number of pulses was recorded with an electronic counter. After the complete operating pressure range had been passed several times, the average pressure change was determined.

The plasma-forming gas consumption per pulse was determined by the formula $\Delta pV/n$, where $\Delta p$ is the pressure change, $V$ is the volume, and $n$ is a number of pulses. The estimated consumption amounts to 30–50 torr cm$^3$ per pulse (depending on the operation mode) for a duoplasmatron with an HC cathode and no more than 10–12 torr cm$^3$ per pulse for a duoplasmatron with an ICMM cathode. The discharge characteristics depend on the cathode type. For the HC cathode, the discharge current reaches 175 A at a voltage of 120–130 V, whereas for the ICMM cathode, the discharge current reaches 230 A at a voltage of 400 V.

We note that, in the source with an HC cathode, the discharge voltage strongly depends on the plasma-forming gas consumption. It increases up to 400 V or drops to 50 V for gas shortage or excess, respectively. In either case, the source generates an ion beam. Hence, with an HC cathode, it is possible to operate in both the glow and arc discharge modes.

When the HC cathode was placed in the longitudinal magnetic field, the parameters of the source did not changed as compared to the case without a magnetic field. This means that the electrical screening of the wall of this type of a hollow cathode is quite sufficient.

In the source with an ICMM cathode, the discharge voltage changes within the 300–500 V range, depending on the plasma-forming gas consumption. The source generates an ion beam only when operating in the glow discharge mode; a transition to the arc mode terminates the ion beam generation.

The ignition voltage for the HC and ICMM cathodes is approximately the same (500–800 V).

In both cases, low-frequency oscillations (at a frequency of several MHz) in the discharge current were observed. However, for the HC cathode, in addition to the current oscillations, numerous sharp jumps and kinks occurred in the discharge current waveforms, which badly hampered the start-up of the source and worsened its stability.

Usually, the ion beam was extracted, formed, and accelerated at a constant extraction voltage of ~40 kV. Depending on the discharge current in the source, the ion beam current ($H^+$, $H_2^+$, and $H_3^+$) attained 100–180 mA. The ion beam current was measured by a Faraday cup with a 60-mm-diameter aperture [7], which, due to the beam divergence and lack of additional focusing, intercepted only about one-third of the total beam current.

In the source with an ICMM cathode, the beam current attained 100–150 mA at a discharge current of 50–60 A. For the HC cathode, the same beam currents were attained at a discharge current of 20–40 A.

Figure 3 shows the beam current versus the accelerating voltage for the ICMM cathode. For the HC cathode, the dependence is the same. The linear dependence indicates that the source emissivity is not saturated. The diameter of the source emitting opening is 1.2 mm, so the density of the emission current is higher than 35 A/cm$^2$.

The measurements of the beam composition showed that the proton fraction is equal to 50–70 and 60–80% for the HC and ICMM cathodes, respectively. This difference is explained by the higher discharge current in the source with an ICMM cathode. The mass analyzer resolution did not allow us to evaluate the fraction of heavy ions possibly produced due to the sputtering of the source electrodes.

At particle energies of 40 keV, the estimated normalized beam emittance is equal to ~$9.4 \times 10^{-5}$ rad cm.

It should be noted that the HC cathode is eroded more rapidly than the ICMM one. Even when the duralumin cylinder of the HC cathode was replaced with a tantalum one, it was still (although more slowly) sputtered due to the bombardment by the discharge ions. Indeed, for the HC cathode, the bombardment influences only the cathode head, whereas, for the ICMM cathode, the ions bombard the entire cathode inner surface, whose area is several times larger than that of the HC cathode head.

## CONCLUSION

Our study has shown that both HC and ICMM cathodes can be used in plasma sources. The duoplasmatron emissivity is nearly the same in both cases; however, the other source parameters, such as the gas efficiency, voltage, and discharge current (energy consumption), differ greatly. Thus, the gas efficiency of the duoplasmatron with an ICMM cathode is three times higher than with an HC cathode. In generating hydrogen ion beams with the same currents, the energy consumption of the HC cathode is substantially less than that of the ICMM cathode. In the latter case, however, the proton content in the beam is larger due to the higher discharge current.

In the duoplasmatron with an ICMM cathode, the stray oscillations are not so intense as for the HC cathode. Consequently, the stability of duoplasmatron operation and the beam quality are higher for the ICMM cathode.

The service life of the duoplasmatron with any of these cathodes is much longer compared to that with a hot cathode and amounts to several thousand hours. The HC cathode erodes more rapidly than the ICMM cathode. However, the design of the HC cathode is simpler than that of the ICMM cathode.

We have chosen the ICMM cathode because the ion source in the injector of a linear proton accelerator should combine the high gas efficiency, high emissivity, high beam stability, and high proton content in the beam.

## REFERENCES

1. L. V. Arinin, G. V. Kuznetsov, A. I. Markoliya, *et al.*, in *Proceedings of the 9th All-Russia Conference on Applications of Charged-Particle Accelerators in Industry and Medicine, St. Petersburg, 1998*, p. 122.
2. V. T. Barchenko, S. N. Zagranichnyĭ, and A. Yu. Sokolovskiĭ, Izv. Leningr. Élektrotekh. Inst. **303**, 42 (1982).
3. V. V. Nizhegorodtsev, in *Proceedings of the 5th All-Union Conference on Charged-Particle Accelerators, Protvino, 1978*, Vol. 1, p. 368.
4. V. T. Barchenko, V. P. Golubev, A. A. Potsar, and G. V. Tarvid, USSR Inventor's Certificate No. 866610; Priority from November 16, 1979.
5. P. A. Litvinov, Vopr. At. Nauki Tekh., Ser. Yad.-Fiz. Issled. **11** (4–5), 48 (1997).
6. L. P. Veresov, P. A. Litvinov, Yu. P. Neustroev, and É. S. Nikolaev, USSR Inventor's Certificate No. 4364894; Priority from May 8, 1989.
7. L. P. Veresov, O. L. Veresov, and L. P. Skripal', Zh. Tekh. Fiz. **67** (9), 135 (1997) [Tech. Phys. **42**, 1104 (1997)].

*Translated by N. Ustinovskiĭ*

*Technical Physics, Vol. 46, No. 10, 2001, pp. 1260–1264. Translated from Zhurnal Tekhnicheskoĭ Fiziki, Vol. 71, No. 10, 2001, pp. 54–58.*


**SOLID-STATE ELECTRONICS**

# Variation of the Electrophysical Properties of $La_{0.67}Ca_{0.33}MnO_3$ Epilayers during Secondary Recrystallization

**Yu. A. Boĭkov*, T. Klaeson**, and A. Yu. Boĭkov*****

** Ioffe Physicotechnical Institute, Russian Academy of Sciences, Politekhnicheskaya ul. 26, St. Petersburg, 194021 Russia*

*** Chalmes Technical University, S-41296 Göteborg, Sweden*

**** St. Petersburg State University, Universitetskaya nab. 7/9, St. Petersburg, 198904 Russia*

Received October 16, 2000

**Abstract**—$La_{0.67}Ca_{0.33}MnO_3$ epitaxial films are grown by laser evaporation on $(LaAlO_3)_{0.3} + (Sr_2AlTaO_6)_{0.7}$ substrates. The films have single-crystalline mosaic blocks (grains), which are distinctly oriented in both the azimuth direction and the substrate plane. During the heat treatment of the manganite films in the oxygen atmosphere, their microstructure is improved both in the bulk and in the intergranular regions. The maximal value of the temperature coefficient of resistance for the heat-treated $La_{0.67}Ca_{0.33}MnO_3$ films increases by nearly two times, while the magnetoresistance increases by no more than 10%. © *2001 MAIK "Nauka/Interperiodica".*

## INTRODUCTION

Perovskite-like manganites $(La, Nd)_{1-x}R_xMnO_3$, where $R$ = Ca, Sr, Ba, Pb, or Sn, have received much attention, because they are candidate materials for heads reading information from magnetic disks and for bolometers [1, 2]. Anomalously high values of magnetoresistance (*MR*) and temperature coefficient of resistances (β) are observed at temperatures close to the temperature $T_C$ of ferromagnetic phase transition. In $(La, Nd)_{1-x}R_xMnO_3$, the value of $T_C$ depends on $x$ [3]. Also, it sharply drops at a deficiency of oxygen [4] and increases in a magnetic field and under conditions of hydrostatic compression [5, 6]. Among perovskite-like manganites, those for which $T_C$ is close to 300 K are of special interest. The maximal values of *MR* and β for $La_{0.67}Ca_{0.33}MnO_3$ (LCMO) solid solution films of stoichiometric composition are observed in the temperature interval 255–275 K [1, 5]. In silver-doped LCMO films, the peak in the $MR(T)$ curve shifts toward higher temperatures by 20–30 K [7]. It has been found [2, 5] that heat treatment in oxygen considerably affects the parameters of $La_{1-x}R_xMnO_3$ films and bulk ceramic crystals. To date, however, a correlation between the microstructure of $La_{1-x}R_xMnO_3$ films and the temperature and magnetic-field dependences of their resistivity has not been adequately studied. For example, the effect of grain boundaries on the parameters of thin ceramic and epitaxial films has not been clearly established. In [5], it was noted that crystallites may be shunted by the surrounding regions, while in [1] it was reported that intergranular regions serve as an additional resistance series-connected to the grain resistance.

In this work, we analyze mechanisms responsible for variations of LCMO epitaxial film properties during heat treatment in oxygen.

## EXPERIMENT

The method of laser evaporation (Compex 100 KrF, λ = 248 nm, τ = 30 ns) was used to grow LCMO films on polished $(LaAlO_3)_{0.3} + (Sr_2AlTaO_6)_{0.7}$ (LSATO) substrates with (100) orientation. An initial ceramic LCMO target was evaporated at an oxygen pressure $P_0$ = 0.5 mbar. The laser emission density on the target surface was 2.0 J/cm$^2$. LCMO films with a thickness $d$ = 150 nm were grown on the LSATO(100) at a temperature $T_s$ = 780°C. After the structure and the electrical parameters of the films have been studied, they were heat-treated in the oxygen atmosphere ($T$ = 850°C, $P_0$ = 1 atm, $t$ = 60 min).

The structure and the phase composition of the LCMO films were investigated with X-ray techniques (Philips X'pert MRD, Cu$K_\alpha$ radiation, ω/2θ and φ scans, rocking curves). To determine the lattice parameters of the manganite films in the substrate plane, $a_\parallel$, and along the normal to the substrate, $a_\perp$, the substrate during recording of the diffraction pattern was fixed so that the plane made by the incident and reflected beams was perpendicular to either the (001) or (100) plane of LCMO. The surface morphology was examined with the NanoScope-IIIa atomic force microscope.

The resistance of the LCMO films was measured by the Van der Pauw method with the hp 4263A LCR meter at a frequency of 100 Hz both in and without a magnetic field ($H$ = 0.4 T). The magnetic field was directed normally to the LCMO film plane. The resis-

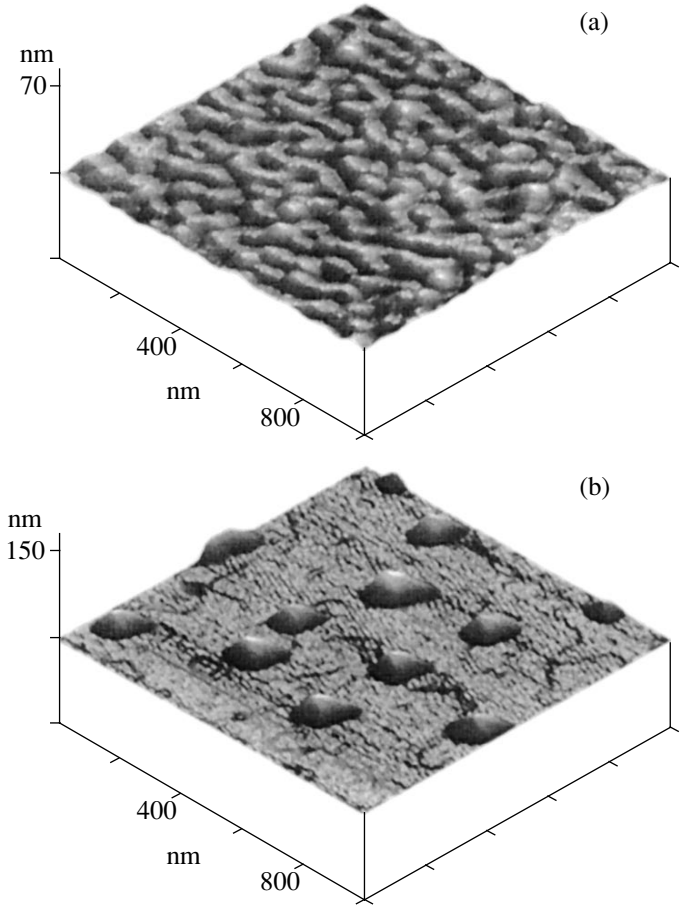


**Fig. 1.** (a) Morphology of the LCMO/LSATO(100) film surface (150 nm); the grain boundaries in the manganite film are decorated by characteristic pits. (b) The surface morphology of the same film after oxygen heat treatment; the free surface of the LCMO film exhibits steps with a height multiple of the unit cell parameter (AFM images).

tivity of the manganite films was calculated from the relationship $\rho = (\pi d/\ln 2)R$ [8]. Four silver contacts were evaporated onto the films from a tungsten boat.

## RESULTS AND DISCUSSION

The heteroepitaxial films of perovskite-like oxides grown by laser evaporation usually consist of single-crystalline grains separated by low-angle boundaries [9, 10]. A basic reason for the azimuth misorientation of the grains is a lattice mismatch between the film and the substrate. The choice of LSATO(100) as a substrate was dictated by the extremely small difference between the lattice parameters of LSATO and LCMO. The parameter of the LCMO pseudocubic unit cell is 3.870 Å [4], and that of the LSATO cell is 3.869 Å [11]. Also, these materials have close thermal expansion coefficients.

As follows from the data shown in Fig. 1a, the as-prepared LCMO films consist of 50- to 100-nm grains. Since the regions adjacent to the grains have an excess free energy, the grain boundaries are clearly decorated by characteristic pits.

The X-ray diffraction patters recorded when the plane made by the incident and reflected beams was normal to LCMO(100) contain only ($n$00) reflections from LCMO and LSATO (Fig. 2a). When the plane made by the beams was orthogonal to the (101) plane of the substrate, the patterns had only ($n$0$n$) reflections from LCMO and LSATO (Fig. 2b). The half-height width of the X-ray peaks from the manganite film was two or three times as large as that for the single-crystal substrate (inset in Fig. 2a). The patterns in Figs. 2a and 2b imply that the films grown were free of precipitates that have the cell parameters differing from those of LCMO. The $\phi$ scans of the (111) reflection from LCMO show four equidistant peaks (in every 90°) with the half-widths (0.21° ± 0.02°) nearly coincident with those for the single-crystal substrate. This fact indicates that the azimuth misorientation of the crystallites in the LCMO film does not exceed several hundredths of a degree. From the X-ray data ($\omega/2\theta$ and $\phi$ scans), we found that the orientation relation between the as-prepared manganite film and the substrate is (100)[010]LCMO || (100)[010]LSATO and also determined the unit cell parameters for the as-prepared

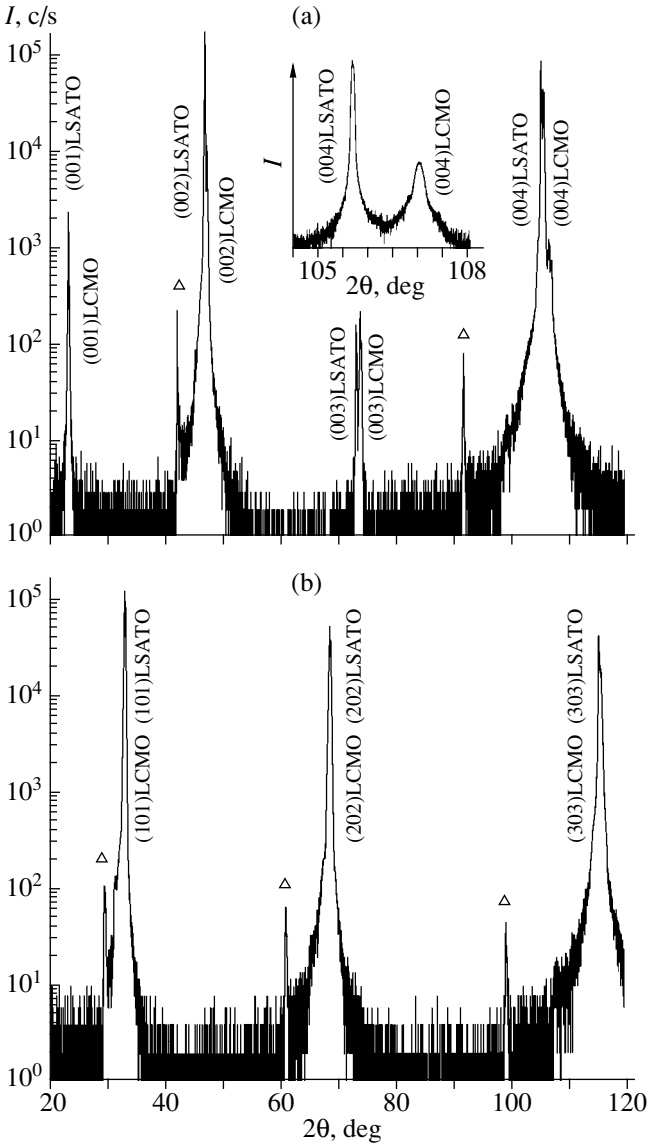


**Fig. 2.** (a) X-ray diffraction pattern (Cu$K_\alpha$, ω/2θ) taken from the LCMO/LSATO(100) film when the plane made by the incident and reflected beams is orthogonal to the substrate plane (Δ refers to Cu$K_\beta$ peaks from the substrate). The inset shows a part of the diffraction pattern from the same film obtained with the four-crystal Ge(220) monochromator. (b) X-ray diffraction pattern (Cu$K_\alpha$, ω/2θ) taken from the LCMO/LSATO(100) film when the plane made by the incident and reflected beams is orthogonal to the (101) plane of LSATO (Δ refers to Cu$K_\beta$ peaks from the substrate).

LCMO film: $a_\perp = 3.833 \pm 0.004$ Å and $a_\parallel = 3.866 \pm 0.004$ Å. The difference between $a_\perp$ and $a_\parallel$ indicates that the LCMO films are subjected to tensile mechanical strains in the substrate plane. The effective lattice parameter is $a_{\text{eff}} = (a_\perp \times a_\parallel^2)^{1/3} = 3.855$ Å. Comparing the value of $a_{\text{eff}}$ with the dependence of the lattice parameter of bulk ceramic LCMO samples on the charge state of manganese ions [12], we can conclude that the relative concentration of $Mn^{4+}$ ions in the films is about 40%. After oxygen heat treatment, the unit cell parameters of the LCMO film, as well as its orientation relative to the preferential directions in the substrate, remain unchanged.

However, the heat treatment in oxygen substantially changed the surface morphology of the manganite film (Fig. 1b). After the treatment, the surface pits decorating the boundaries of the single-crystal mosaic blocks disappeared; instead, ~30-nm-high hills with a density of $10^9$ cm$^{-2}$ emerged.

The X-ray data in combination with the results of manganite film surface study before and after the heat treatment suggest that the grain boundary structure in the LCMO film appreciably depends on the nonstoichiometry of the phase adsorbed on the growing film surface. The nonstoichiometric composition of the adsorbed phase may be a reason why the film of a multicomponent perovskite-like oxide has the mosaic structure in the case of its homoepitaxial growth as well. Nonstoichiometric inclusions are accumulated at the boundaries of growing nuclei. In this situation, the intergranular regions may have a composition other than that inside the single-crystalline grains. During high-temperature annealing, the secondary recrystallization of the LCMO film may take place, which changes the microstructure both inside and between the grains. If the azimuth misorientation of the grains is small, the recrystallization displaces the nonstoichiometric phase to the free surface, causing dislocations to appear at the grain boundaries. The driving force of this process is the minimization of the free energy of the grain boundaries. The improvement of the grain boundary microstructure during heat treatment explains why the characteristic pits, decorating the grain boundaries, disappear and hills arise (Fig. 1b). Special studies using a four-crystal Ge(220) monochromator did not reveal macroprecipitates in the annealed LCMO films. The absence of reflections from side crystalline phases (inset in Fig. 2a) may indicate the amorphous structure of the hills.

Direct evidence that the grain microstructure in the LCMO films is improved during heat treatment is a decrease in the half-width of the rocking curve for the (200) reflection from LCMO (inset II in Fig. 3b).

To explain the temperature dependence of the resistivity of oxide manganites at $T < T_C$, we used a model that includes double charge exchange in the $Mn^{+3}$–$O^{-2}$–$Mn^{+4}$ chain [13], as well as the polaronic mechanism of conduction [14, 15]. At a $Mn^{+4}$ concentration of ≈40%, the (La, Ca)$MnO_3$ solid solution has the highest value of $T_C$ [12], while the resistivity is minimal when the concentration of $Mn^{+4}$ manganese ions is about 33% [16].

The ρ($T$) curve for the LCMO films has a distinct peak. For the as-grown films, it is observed at $T_R \approx$ 256 K (Fig. 3a). The value of ρ drastically drops at $T < T_C$ because of an increase in the effective mobility.

According to the Zener theory, spin ordering on manganese ions at the temperature of ferromagnetic phase transition stimulates charge exchange between $Mn^{+3}$ and $Mn^{+4}$ ions, which is accompanied by a sharp increase in their effective mobility. This is the reason for the sharp drop of ρ. In the interval $T_R + 70\ \mathrm{K} > T > T_R$, the $\rho(T)$ curve is well approximated by the dependence

$$\rho \sim \rho_0 \exp(E_A/kT), \qquad (1)$$

where $\rho_0$ is a temperature-independent parameter; $k$ is the Boltzmann constant; and $E_A$ = 0.083 or 0.055 eV, respectively, before and after heat treatment in oxygen.

After heat treatment, the resistivity of the LCMO film (at $T = T_R$) decreased roughly by one third and the peak in the $\rho(T)$ curve shifted toward higher temperature by 8–10 K. This high-temperature shift was also observed when the resistivity was measured in a magnetic field (the inset in Fig. 3a). The rise in the film conductivity during heat treatment can be related both to the improvement of the microstructure in the bulk of the grains and to the decrease in the resistivity of the intergranular layers. The appreciable dependence of the electrophysical properties of the LCMO films on the microstructure of the grain boundaries follows from the fact that the parameter $a_{\mathrm{eff}}$ for the heat-treated films does not change in parallel with the changes in the $\rho(T)$ curve. In other words, the curve changes but the $Mn^{+4}$ ion concentration inside the grains remains the same.

A sharp minimum in the temperature dependence of the magnetoresistance for the LCMO films, $MR = [R(H = 0.4\ \mathrm{T}) - R(H = 0\ \mathrm{T})]/R(H = 0.4\ \mathrm{T})$, was observed at a temperature approximately 10 K lower than $T_R$ (Fig. 3). This minimum almost coincides with the position of the peak in the $\beta(T)$ curve (Figs. 3a, 3b). For the heat-treated films, the temperature interval where the values of $|MR|$ and β are the highest is much narrower than for the unannealed films. One reason why the temperature interval of the highest $|MR|$ for the as-grown LCMO films is wider than for the annealed ones is stoichiometry breaking at the grain boundaries. The secondary recrystallization of the LCMO/LSATO films improves their stoichiometry in the bulk and primarily at the grain boundaries. The annealed manganite films become more uniform in composition. Unlike $|MR|$, the maximal values of the temperature coefficient of resistance for the annealed LCMO films ($\beta = 14 \times 10^{-2}\ \mathrm{K}^{-1}$) were almost twice as large as those for the unannealed films ($\beta = 8 \times 10^{-2}\ \mathrm{K}^{-1}$).

Thus, heteroepitaxial LCMO films obtained by laser evaporation have a mosaic structure. The microstructure of single-crystal grains and intergranular layers depends on the substrate material and growth conditions. Oxygen heat treatment improves the microstructure of both grains and intergranular regions. The structure improvement is accompanied by a sharp increase in the maximal value of the temperature coefficient of resistance. The secondary recrystallization of the LCMO films makes their composition more uniform, thereby narrowing the temperature interval where $MR$ and β are the highest.

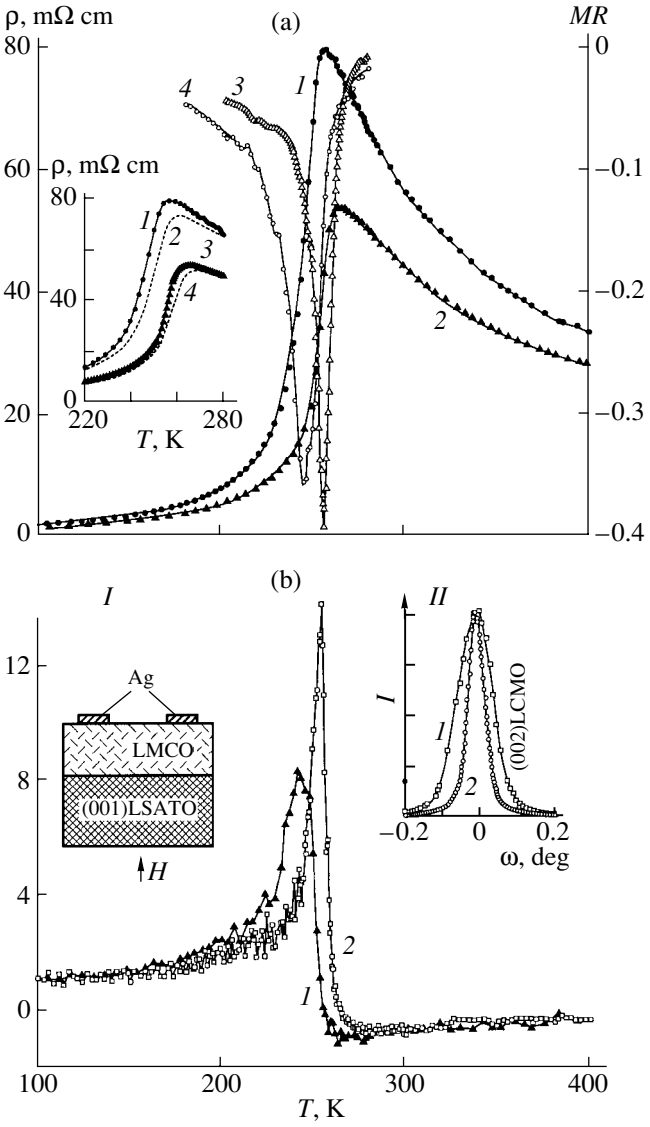


**Fig. 3.** (a) Temperature dependences of the (*1*, *2*) resistivity ρ and (*3*, *4*) magnetoresistance *MR* for the LCMO film that were obtained (*1*, *4*) before and (*2*, *3*) after heat treatment in oxygen. The inset shows the $\rho(T)$ curves for the LCMO film that were taken at temperatures near $T_C$ (*2*, *4*) in and (*1*, *3*) without a magnetic field. (b) Temperature dependences of the temperature coefficient of resistance β for the LCMO film (*1*) before and (*2*) after heat treatment in oxygen. Inset I schematically shows the LCMO/LSATO heterostructure with contacts. Inset II depicts the rocking curves (ω – 2θ) about the (002) reflection from the manganite film that were taken (*1*) before and (*2*) after heat treatment in oxygen.

## ACKNOWLEDGMENTS

This work is a result of the scientific cooperation between the Russian and Swedish Academies of Sci-

ences and was financially supported in part by the Russian Foundation for Basic Research (grant no. 98-02-18222) and by TRF projects (no. 240-97-382).

## REFERENCES

1. A. Goyal, M. Rajeswari, R. Shreekala, *et al.*, Appl. Phys. Lett. **71**, 2535 (1997).
2. M. Rajeswari, A. Goyal, A. K. Raychaudhuri, *et al.*, Appl. Phys. Lett. **69**, 851 (1996).
3. H. Asano, J. Hayakawa, and M. Matsui, Phys. Rev. B **57**, 1052 (1998).
4. H. L. J. Gopalakrishnan, J. L. Peng, Q. Li, *et al.*, Phys. Rev. B **51**, 6143 (1995).
5. S. Jin, T. H. Tiefel, M. McCormack, *et al.*, Science **264**, 413 (1994).
6. H. Y. Hwang, T. T. M. Palstra, S.-W. Cheong, and B. Batlogg, Phys. Rev. B **52**, 15046 (1995).
7. R. Shreekala, M. Rajeswari, S. P. Pai, *et al.*, Appl. Phys. Lett. **74** (19), 2857 (1999).
8. T. I. Kamins, J. Appl. Phys. **42**, 4357 (1971).
9. Yu. A. Boĭkov, D. Erts, and T. Claeson, Fiz. Tverd. Tela (St. Petersburg) **42** (11), 2042 (2000) [Phys. Solid State **42**, 2103 (2000)].
10. M. E. Tidjani, R. Gronsky, J. J. Kingston, *et al.*, Appl. Phys. Lett. **58** (7), 765 (1991).
11. Crystec Specification on LSATO Substrates.
12. E. O. Wollan and W. C. Koehler, Phys. Rev. **100**, 545 (1955).
13. C. Zener, Phys. Rev. **82**, 403 (1951).
14. A. J. Millis, P. B. Littlewood, and B. I. Shraiman, Phys. Rev. Lett. **74**, 5144 (1995).
15. M. F. Hundley, M. Hawley, R. H. Heffner, *et al.*, Appl. Phys. Lett. **67** (6), 860 (1995).
16. J. H. van Santen and G. H. Jonker, Physica **16**, 599 (1950).

*Translated by V. Isaakyan*

*Technical Physics, Vol. 46, No. 10, 2001, pp. 1265–1269. Translated from Zhurnal Tekhnicheskoĭ Fiziki, Vol. 71, No. 10, 2001, pp. 59–64.*


**SOLID-STATE ELECTRONICS**

# GaAsN-on-GaAs MBE Using a DC Plasma Source

**A. E. Zhukov*, E. S. Semenova*, V. M. Ustinov*, and E. R. Weber****

** Ioffe Physicotechnical Institute, Russian Academy of Sciences, Politekhnicheskaya ul. 26, St. Petersburg, 194021 Russia*

*** Department of Materials Science and Mineral Engineering, University of California, Berkeley, California 94720-1760, USA*

Received October 30, 2000

**Abstract**—A new dc plasma source for MBE growth of GaAsN layers is suggested. The efficiency of nitrogen incorporation, crystal perfection, surface morphology, and luminescent properties of the epilayers vs. operation conditions of the source are studied. © *2001 MAIK "Nauka/Interperiodica".*

(In)GaAsN semiconductors MBE-grown on a GaAs substrate are candidates for active layers in long-wave injection lasers [1, 2]. Recently, 1.3-μm InGaAsN quantum-well face-pumped [3] and surface-emitting [4] lasers have been designed. Moreover, 1.52-μm luminescence from InGaAsN/GaAs quantum dots has been observed [5].

Nitrogen is difficult to incorporate into the growing epitaxial structure because of the high binding energy of $N_2$ molecules. Therefore, molecular nitrogen cannot be activated at temperatures typical of arsenic-containing compound deposition. In MBE, rf plasma sources are usually used today for generating active, i.e., capable of being incorporated into the growing film, nitrogen radicals. However, problems, such as a low degree of nitrogen activation and surface damage due to plasma ions still remain to be solved. Therefore, it would be desirable to have alternative sources for growing good InGaAsN/GaAs heterostructures by MBE. One of these sources is a dc plasma source.

Basically, a dc plasma source can reproducibly provide a high efficiency of nitrogen activation. The low power consumption and cost of the dc sources render them very attractive for using in noncommercial epitaxial equipment. Yet, little is known about the properties of (In)GaAsN/GaAs structures grown with a dc plasma source [6].

This work represents the systematic investigation of GaAsN layers MBE-grown on a GaAs substrate with a new, so-called dc constricted plasma source (CPS) [7]. The nitrogen incorporation efficiency, crystal perfection, surface morphology, and optical properties of the layers depending on plasma source operating conditions are reported.

The structures were grown in the Intevac Gen II MBE equipment provided with solid sources of Ga, In, and As evaporation; ion and cryogenic sorption pumps; and a standard RHEED system. First, an AKhT GaAs(100) substrate was covered by a 0.1-μm-thick buffer GaAs layer at 580°C. Then, the process was interrupted for 5 min. Within this time, the substrate temperature dropped to 450°C and a nitrogen plasma was initiated and stabilized. Next, a 0.35-μm-thick (In)GaAsN layer was deposited under certain operating conditions of the CPS. The final step was the deposition of a 20-nm-thick GaAs cap. The deposition rate was 1 monolayer/s, and the arsenic pressure measured by an ion transducer, $2.5 \times 10^{-5}$ torr. The Siemens D5000 X-ray diffractometer was used to evaluate the amount of nitrogen incorporated and to study the structure of the layers grown. Photoluminescence was excited by a 20-mW 514.5-nm $Ar^+$ laser and detected by a cooled Ge photodiode.

In a CPS, a plasma is initiated in a gas flowing into the MBE growth chamber. The degree of ionization is low; that is, the ion concentration is much smaller than the concentration of neutral radicals. Yet, a considerable amount of atoms and molecules may be in the excited state and incorporated into the growing film. The nitrogen flow rate $F$ in the source and the direct current $I$ passing through the discharge chamber of the source are parameters that control the flow of active radicals and, hence, the nitrogen amount in the growing film. The nitrogen flow rate was precisely controlled by the Tylan (Millipore) FC-2950M mass controller. The plasma was initiated and controlled with the Glassman ER-series dc voltage source (100 mA, 3 kV).

First of all, we determined the range of input parameters (gas-flow rate and direct current of the source). While the maximal values of $I$ and $F$ are equipment-limited (100 mA and 5 sccm, respectively), their minimal values depend on physical processes taking place in the discharge chamber. To each given nitrogen flow rate, there corresponds a minimal current value $I_{min}$ at which the plasma still exists. In other words, we can select the minimal nitrogen flow rate for a given current. In Fig. 1, the experimental $I_{min}$ vs. $F$ curve (continuous line) shows the sharp rise in $I_{min}$ at low values of $F$ (0.2–0.8 sccm), while at large flow rates (1–5 sccm), $I_{min}$ remains nearly unchanged.

1063-7842/01/4610-1265$21.00 

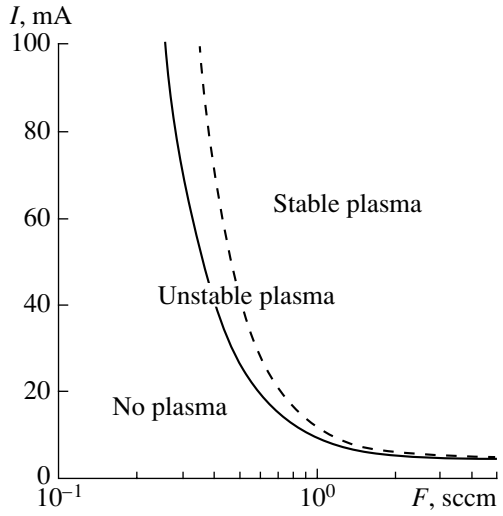


**Fig. 1.** Minimal value of the current, $I_{min}$, at which the plasma gradually disappears and the current $I_s$ at which the plasma may exist for a long time vs. nitrogen low rate $F$.

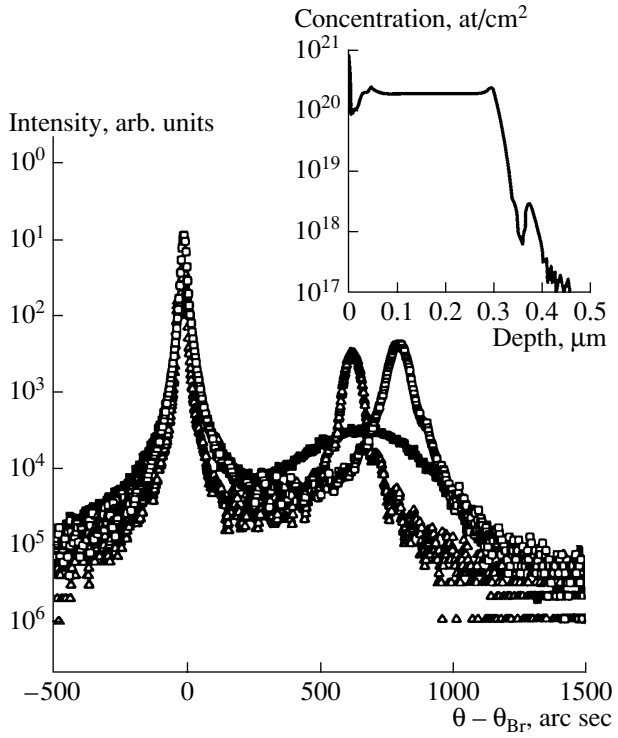


**Fig. 2.** Rocking curves about the (004) reflection that were taken from the 0.35-μm-thick GaAsN films. (□) 1.5 sccm, 10 mA; (■) 1.0 sccm, 10 mA; and (△) 1.5 sccm, 7 mA. The inset shows the SIMS profile of the nitrogen concentration (1.5 sccm, 7 mA).

It was also found that there exists a critical current value that characterizes the temporal stability of the plasma source. If the operating current is smaller than some value $I_s$ related to the nitrogen flow rate, the plasma may be quenched several minutes after its initiation. The $I_s$ vs. $F$ dependence is shown in Fig. 1 by the dashed curve. It is qualitatively similar to the $I_{min}(F)$ dependence, but the difference between the curves, which specifies the range of temporal instability, increases with decreasing flow rate. We believe that this phenomenon can be explained by the fact the operating flow rate randomly fluctuates. Although a sharp drop in the flow rate is hardly probable, this deviation can quench the plasma if the instantaneous flow rate becomes smaller than the minimal value for a given current. Obviously, the range $I_{min}$–$I_s$ is inappropriate for the growth of thick layers. However, such conditions may be used for growing quantum-well structures.

A series of films with different nitrogen flow rates and source currents was grown to estimate the nitrogen incorporation efficiency vs. CPS operating conditions. The nitrogen concentration and structure perfection were determined by high-resolution X-ray diffraction. The rocking curves about the (004) and (224) reflections were taken. Figure 2 shows typical (004) rocking curves for the samples grown with different values of $I$ and $F$. As either parameter increases, the diffraction peaks shift toward larger angles, as follows from the results for the samples grown with the same $F$ (1.5 sccm) and different $I$ (7 and 10 mA) and with the same $I$ = 10 mA but different $F$ (1.0 and 1.5 sccm).

From the difference between the angular positions of the (004) peaks, one can determine the composition of the compound if the degree of stress relaxation is known. Specifically, for two limiting cases (pseudomorphic growth and complete stress relaxation), the same position of a diffraction peak corresponds to the nitrogen concentrations differing roughly by a factor of 2. Assuming the pseudomorphic growth of the films in Fig. 2, we estimated the nitrogen concentration at 1.5–2.0%. Calculations within the Matthews–Blakeslee model of mechanical equilibrium [8] show that the critical thickness of films with such a nitrogen concentration varies between 98 and 130 nm, which is much smaller than the thickness of our GaAsN layers (0.35 μm). Hence, one can assume complete or partial stress relaxation.

To determine the extent of relaxation, we performed measurements near the (224) asymmetric reflection. The difference between the angular positions of the substrate and the epilayer in the $(224)^+$ and $(224)^-$ reflections allowed us to calculate the lattice mismatch in the growth direction $(\Delta a/a)_\perp$ and in the growth plane $(\Delta a/a)_\parallel$. Closed circles in Fig. 3 depict experimental data for the lattice mismatch $(\Delta a/a)_\parallel$ as a function of $(\Delta a/a)_\perp$. Throughout the experimental range, the value of $(\Delta a/a)_\parallel$ remains surprisingly small. Even if $(\Delta a/a)_\perp$ is as large as 1.1% (the nitrogen concentration is about 2.7%), the lattice constants of the film and the GaAs substrate diverge by no more than 0.1%. These findings suggest pseudomorphic growth conditions in spite of the considerable nitrogen concentration in our films. This statement is also corroborated by the excellent agreement between the values of $(\Delta a/a)_\perp$ derived from

the (224) and (004) reflections (open circles in Fig. 3). Similar results have recently been obtained in studying thick MOCVD-grown GaAsN layers [9]. The reason why misfit dislocations do not develop and thus the thick GaAsN/GaAs layers grow pseudomorphically still remains unclear. These layers call for further investigation by transmission electron microscopy.

In general, during epitaxial growth of GaAs, nitrogen atoms may incorporate both into the Group-V atom sublattice, forming the GaAsN solid solution, and into interstices of the lattice because of the small atomic radius of nitrogen. In the former case, the lattice constant decreases in comparison with that of pure GaAs. In the latter case, the lattice constant remains the same or slightly increases. Because of this, the incorporated nitrogen concentration determined by X-ray diffraction (i.e., from data for the lattice constant) must be refined by secondary ion mass spectroscopy (SIMS). The inset in Fig. 2 shows the SIMS profile of the nitrogen in the sample grown with $F$ = 1.5 sccm and $I$ = 7 mA. The mean nitrogen concentration is $2.08 \times 10^{20}$ at./cm$^3$, or $Y$ = 1.15%. The value of $Y$ obtained from the X-ray diffraction data is 1.19%, in excellent agreement with the SIMS data. Thus, there is no reason to assume that the nitrogen is incorporated into the interstices of the layers grown with the use of the CPS.

In Fig. 4, balls are data points for the nitrogen concentration as a function of flow rate and constant current. The concentration depends sublinearly on both $I$ and $F$, that is, tends to saturation when one of the control parameters rises.

It should also be noted that the films grown at the minimal plasma-stabilizing current ($I_s$) exhibit a nonzero nitrogen concentration. Since a high nitrogen concentration in the layers is sometimes undesirable, the least possible value of the nitrogen concentration in the GaAsN layers MBE-grown with the CPS was studied in greater detail. Clearly, the nitrogen concentration in the layer grown at $I = I_s$ is minimal for a given flow rate. Moving along the $I_s(F)$ curve toward higher flow rates, we see that the nitrogen content drops although the flow rate rises. This is explained by the decrease in the current. The minimal nitrogen content, 0.84%, was observed in the sample grown under the maximal flow rate (3.5 sccm) and a relatively low current of 7 mA, which is close to $I_s$ for the given $F$. Layers with still lower nitrogen concentrations could not be grown under our experimental conditions because of the temporal instability discussed above. Also, we can conclude that current is a more efficient composition-controlling parameter than nitrogen flow rate when this nitrogen plasma source is applied.

At the same time, the CPS provides the nitrogen incorporation efficiency as high as 3.7% ($I$ = 45 mA, $F$ = 0.7 sccm). A flow rate of 1 sccm corresponds to an atomic flux of $9.27 \times 10^{17}$ nitrogen atoms per second. When distributed within a solid angle of $2\pi$, this flux gives an atomic flux density $f_N = 3.69 \times 10^{14}$ at./(cm$^2$ s) at a distance of 20 cm between the CPS aperture and the substrate. At the same time, a growth rate of 1 monolayer/s is equivalent to $f_{Ca} = 6.26 \times 10^{14}$ at./(cm$^2$ s). The nitrogen incorporation efficiency $\eta_{in}$ depends on the efficiency of nitrogen activation in the plasma source and on the growth-condition-related

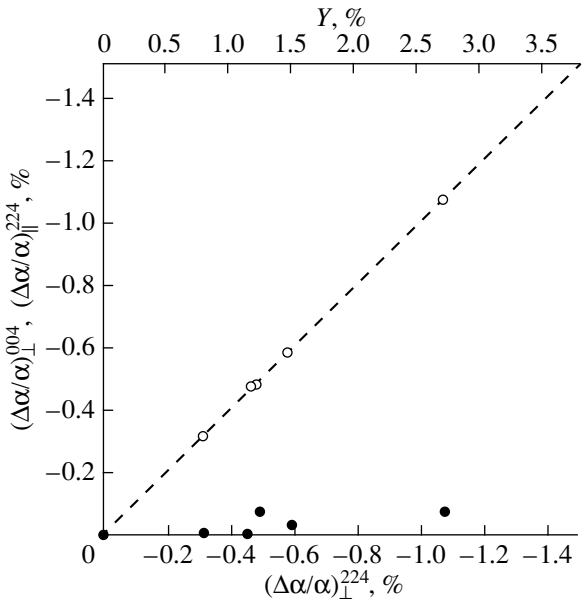


**Fig. 3.** Relationships between the GaAsN/GaAs lattice mismatches in the growth direction, $(\Delta a/a)_{\perp}$, and in the plane of the heterojunction, $(\Delta a/a)_{\parallel}$, as follows from the rocking curves about (•) (224) asymmetric and (○) (004) symmetric reflections.

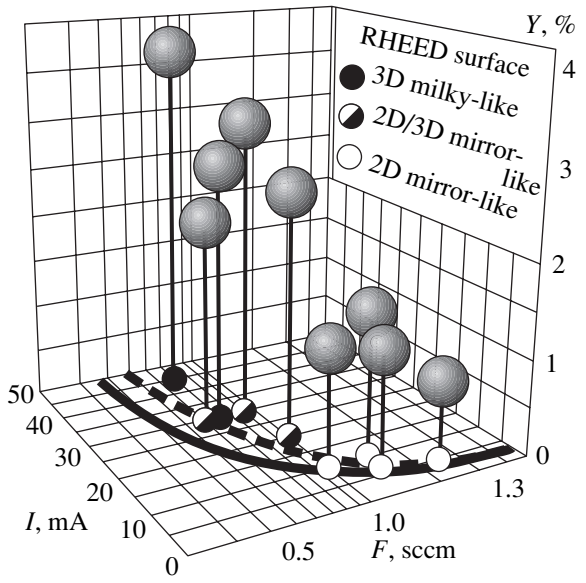


**Fig. 4.** Nitrogen concentration in the GaAsN layers grown at different values of direct current and nitrogen flow rate. Closed circles, spotty (3D) diffraction pattern and milky surface; half-closed circles, mixed diffraction pattern and mirror-smooth surface; and open circles, pattern with fringes (2D) and mirror-smooth surface.

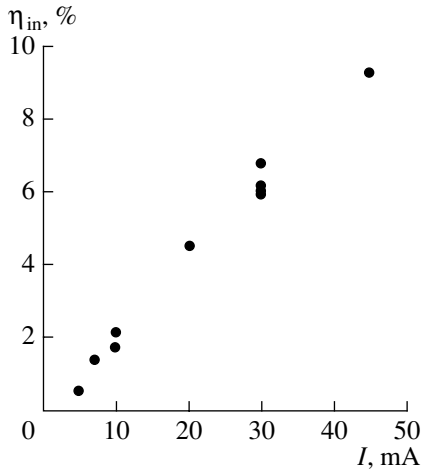


**Fig. 5.** Nitrogen incorporation efficiency vs. source current.

sticking coefficient of active nitrogen particles $\eta_{st}$. The nitrogen concentration in a thick layer is given by

$$Y = \eta_{ac}\eta_{st}\frac{f_N}{f_{Ga}}. \quad (1)$$

For 100% activation and a 100% sticking coefficient, a flow rate of 1 sccm would provide a nitrogen concentration as high as 57%:

$$Y_{max} = \frac{f_N}{f_{Ga}}. \quad (2)$$

However, the experimentally found nitrogen concentrations for $F = 1$ sccm are only 1.22 and 2.56% at currents of 10 and 20 mA, respectively (Fig. 4). Combining expressions (1) and (2) with the experimental data, we calculated the incorporation efficiency as a function of applied current (Fig. 5). The efficiency is seen to vary in proportion with the current. Note that a change in the flow rate affects $\eta_{in}$ insignificantly.

Since all the samples were grown under identical conditions (substrate temperature, growth rate, and arsenic pressure), we can assume the constancy of the sticking coefficient for all the samples. Thus, the current dependence of the sticking coefficient reflects the current dependence of the efficiency of activation although we do not assume a sticking coefficient of 100%. The strong current dependence of the efficiency of activation seems to be quite natural. The current is directly proportional to the flow density of charged particles (electrons and ions), which are accelerated by the electric field in the plasma-initiating chamber and activate neutral gas particles by collision.

The data in Fig. 4 demonstrate that various values of the source parameters (*F* and *I*) may result in the same nitrogen concentration. For example, the combinations 7 mA, 1.5 sccm and 10 mA, 1 sccm give *Y* about 1.2%, as shown in Fig. 2. However, the crystal perfection of these two GaAsN layers is different. The rocking curves about the (004) reflection show that the peak for the sample grown at 10 mA, 1 sccm is much wider (400 arc sec) than when the sample was grown at 7 mA, 1.5 sccm (60 arc sec). We found that the crystal was more perfect (the diffraction peak was narrower) when the flow rate was higher. For example, even the sample with the higher $Y = 1.5\%$ that was grown at 10 mA, 1.5 sccm has the peak narrower (about 100 arc sec) than the sample grown at 10 mA, 1 sccm. It is believed that a basic reason for the peak broadening is nitrogen flow rate fluctuations, which modulate the film composition during the growth. The *Y* vs. *F* dependence is strongly nonlinear. Thus, even small changes in the flow rate may cause great composition inhomogeneities when flow rates are low. Conversely, flow rate fluctuations may be ignored in the saturation region of the *Y*(*F*) curve (high flow rates).

We also studied the surface morphology of the films, combining RHEED and Nomarski optical microscopy. In Fig. 4, the surface morphology map according to the operation conditions of the plasma source is shown. A strong correlation between the current applied during the growth and the surface condition. In the layers grown at low current values (10 mA or lower, $Y = 0.8$–$1.5\%$), the surface was always smooth and regular. The RHEED pattern remains two-dimensional (diffraction fringes) throughout the growth process. The surface of the layers grown at moderate current values (20–30 mA, $Y = 2.1$–$3.1\%$) is still smooth (except the sample grown at 30 mA, 0.7 sccm), but the RHEED pattern contains spots and fringes. Finally, the sample grown at the highest current (45 mA, $Y = 3.7$ sccm) has the milky surface, and the RHEED pattern was three-dimensional (spots).

It should be emphasized that, during the high-current growth, the RHEED pattern did not change gradually as the film thickened. The spots appeared from the very beginning of the GaAsN growth. This means that the surface morphology does not depend on the strain, as in high-strained InGaAs layers [10]. According to the RHEED patterns, the morphology depends largely on the current applied, not on the lattice mismatch (nitrogen concentration). We suppose that such behavior is associated with an increase in the current of ions bombarding the surface during the high-current growth.

To check this supposition, we grew two thick $In_XGa_{1-X}As_{1-Y}N_Y$ layers lattice-mismatched with GaAs, using the conditions 7 mA, 1.5 sccm ($Y = 1.2\%$ or 0.0012) and 20 mA, 1 sccm ($Y = 2.6\%$ or 0.0026). The addition of In allows the mismatch strain to relax; therefore, its effect on the surface morphology can be excluded from consideration. The In source temperature was taken such that the In content in the layers was roughly 4 and 8%. While the X-ray diffraction curves confirmed lattice match in the two samples, the RHEED patterns during the growth and the surface morphologies greatly differed. The RHEED pattern from the first sample had fringes, and its surface was mirror-smooth. The RHEED pattern taken from the sec-

ond layer had spots from the very beginning, and the surface was also mirror-smooth. These data are consistent with the results on the surface morphology of the above-mentioned GaAsN films grown without adding In.

The bandgap of the GaAsN films was estimated from data for room-temperature photoluminescence (PL). Neither high-temperature treatment in the growth chamber nor post-growth rapid thermal annealing were performed. Closed circles in Fig. 6 show the PL peak vs. nitrogen concentration. The continuous curve is the approximation of the data points by a second-order polynomial. At low nitrogen concentrations (<1.5%), the shift of the peak toward larger wavelengths is estimated as 200 meV/%. In the sample with the highest nitrogen content ($Y$ = 3.7%), the PL peak is at 0.93 eV (1.33 μm). Note that our experimental data for PL in the low-nitrogen ($Y$ < 1.5%) samples are in good agreement with the bandgap value measured by the absorption method in strained GaAsN films grown by MOCVD [9] (open circles in Fig. 6). However, in the high-nitrogen ($Y$ > 2%) films, the PL peak is noticeably shifted (up to 70 meV) from the absorption maximum toward larger wavelengths. We believe that this shift is due to composition fluctuations, since strongly localized states associated with greater-than-average nitrogen concentrations are largely responsible for the PL signal at low and moderate excitation densities.

We also found that the PL intensity in the GaAsN layers depends on the CPS current stronger than on the net nitrogen content, as shown in Fig. 6 (inset). This well correlates with the effect of the current on the surface morphology discussed above. Presumably, the surface damage induced by fast ions causes a large number of defects that act as nonradiative recombination centers. As a result, the PL intensity heavily drops in comparison with pure GaAs, especially at high current values. The optical quality of thin (In)GaAsN films (quantum wells) grown with a CPS calls for further investigation.

Thus, we studied a series of GaAsN films grown by MBE with a CPS (constricted plasma source), which is a new type of sources generating active nitrogen. It was found that the resulting nitrogen concentration is controlled by both the nitrogen flow rate and the applied current, the latter being a more powerful controlling parameter. The CPS provides a practically reasonable nitrogen concentration, up to 3.7%. Even if the nitrogen concentration is high, the GaAsN layers 0.35 μm thick are elastically strained. The nitrogen concentration in thick GaAsN films is minimal at the lowest value of the current from the temporal stability range. Room-temperature PL is observed throughout the composition interval. However, both the PL intensity and the surface morphology of the films degrade when the source current increases. This is explained by the fast-ion irradiation of the surface. At low nitrogen concentrations, the position of the PL peak well correlates with the bandgap value (absorption maximum). For high concentrations of nitrogen, the PL peak is noticeably shifted toward larger wavelengths because of composition fluctuations.

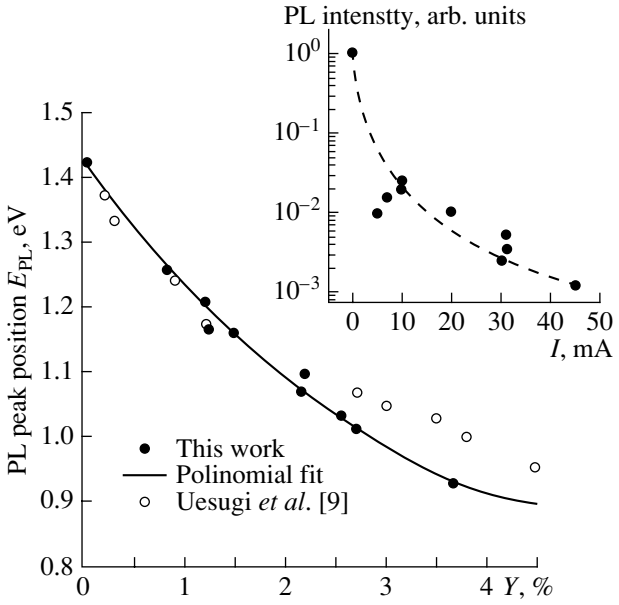


**Fig. 6.** Positions of the (●) PL peak and (○) absorption maximum [9] vs. nitrogen content in the GaAsN layer.

## ACKNOWLEDGMENTS

This work was supported by the NATO Science for Peace Program (grant SfP-972484), CRDF grant (RE1-2221), and the Program "Physics of Solid-State Nanostructures" (project no. 99-2034).

## REFERENCES

1. M. Kondow, K. Uomi, A. Niwa, *et al.*, Jpn. J. Appl. Phys. **35**, 1273 (1996).
2. V. M. Ustinov and A. E. Zhukov, Semicond. Sci. Technol. **15**, R41 (2000).
3. D. A. Livshits, A. Yu. Egorov, and H. Reichert, Electron. Lett. **36** (16), 1381 (2000).
4. K. D. Choquette, J. F. Klem, A. J. Fischer, *et al.*, Electron. Lett. **36** (16), 1388 (2000).
5. M. Sopanen, H. P. Xin, and C. W. Tu, Appl. Phys. Lett. **76** (8), 994 (2000).
6. Z. Pan, L. H. Li, Y. W. Lin, *et al.*, J. Cryst. Growth **209**, 648 (2000).
7. A. Anders and M. Kühn, Rev. Sci. Instrum. **69**, 1340 (1998).
8. J. W. Matthews and A. E. Blakeslee, J. Cryst. Growth **27**, 118 (1974).
9. K. Uesugi, N. Morooka, and I. Suemune, Appl. Phys. Lett. **74** (9), 1254 (1999).
10. A. E. Zhukov, V. M. Ustinov, and Zh. I. Alferov, Int. J. High Speed Electron. Syst. **9** (4), 1109 (1998).

*Translated by V. Isaakyan*

*Technical Physics, Vol. 46, No. 10, 2001, pp. 1270–1273. Translated from Zhurnal Tekhnicheskoĭ Fiziki, Vol. 71, No. 10, 2001, pp. 65–69.*


**OPTICS, QUANTUM ELECTRONICS**

# Generation of the Third Harmonic in Fullerene-Containing Polyimide Films by Picosecond Radiation of the Nd : YAG Laser

**R. A. Ganeev*, A. I. Ryasnyanskiĭ**, I. A. Kulagin*, and T. Usmanov***

** NPO Akadempribor, Tashkent, 700143 Uzbekistan*

*** Navoi State University, Samarkand, 703004 Uzbekistan*

*e-mail: ganeev@acpr.silk.org*

Received September 27, 2000

**Abstract**—The results of the studies on the transformation of the frequency of laser radiation in polyimide films doped by $C_{70}$ are presented. The nonlinear susceptibility ($\chi^{(3)}$) of polyimide 6B films with various concentrations of $C_{70}$ is studied by third-harmonic generation. At a wavelength of 1064 nm, the value of $\chi^{(3)}(-3\omega; \omega, \omega, \omega)$ is $9 \times 10^{-13}$ esu. The effect of the nonlinear variation in the refractive index of the fullerene-containing films on the phase matching between the pumping and third-harmonic waves is analyzed. The third harmonic of the Nd : YAG laser radiation was generated with the efficiencies $6 \times 10^{-6}$ and $10^{-6}$ in the films with the $C_{70}$ concentration of 0.5 and 0.2%, respectively. © *2001 MAIK "Nauka/Interperiodica".*

## INTRODUCTION

Interest in the fullerene-containing structures is related to their various practical and scientific applications (optical confinement, high-temperature superconductivity, optoelectronics, etc.). Fullerene-containing materials are used in optoelectronics owing to their fast, large, and intrinsically electronic nonlinear optical response. Such a response is determined by the large polarizability of delocalized $\pi$ electrons. Nonlinear optical characteristics of fullerene solutions and films were studied in numerous works (see, for example, [1–6]). Note the studies on the transformation of the laser-radiation frequency in such media [7–11]. The studies of nonlinear susceptibilities responsible for the stimulated four-photon light scattering [1, 3, 4] were supplemented by the investigation of the spectral dependences of $\chi^{(3)}$ determining the transformation of the laser-radiation frequency in these media [2, 10, 11]. The value of the nonlinear susceptibility $\chi^{(3)}(-3\omega; \omega, \omega, \omega)$ is rather large in the vicinity of the Nd : YAG laser line. In particular, thin $C_{60}$ films exhibit a strong peak in the dispersion curve of the cubic susceptibility in the vicinity of the Nd : YAG laser line, which was interpreted as related to a three-photon resonance with the excitonic state $T_{1u}$. The value of $\chi^{(3)}$ at this wavelength was $8.7 \times 10^{-11}$ esu [11]. Hoshi *et al.* [7] reported on an even larger value: $\chi^{(3)} = 2 \times 10^{-10}$ esu. At the same time, there are no data regarding the effect of the nonlinear contribution to the refractive index of the medium on the phase matching of the pumping and third-harmonic waves in the course of the third-harmonic generation (THG). Note also that there are insufficient data on the phase mismatching of the interacting waves in the media considered under various focusing conditions.

Below we present the results of the studies of THG ($\lambda$ = 354.7 nm) by the radiation of a picosecond Nd : YAG laser in polyimide films containing 0.2 and 0.5% of $C_{70}$. We determined the efficiency of transformation and $\chi^{(3)}$, and analyzed the effect of the nonlinear contribution to the refractive index on the transformation of the laser-radiation frequency.

## EXPERIMENTAL

The output parameters of the Nd : YAG laser were as follows: pulse duration, 35 ps; pulse energy, 2 mJ; and wavelength, $\lambda$ = 1064 nm. The radiation was focused by a lens with a 25-cm focal length onto the fullerene films. The spatial distribution of the focused beam was close to Gaussian. The pumping radiation was detected by an FD24K photodiode connected to a V4-17 digital voltmeter. The radiation of the third harmonic ($\lambda$ = 354.7 nm) was separated from the pumping beam by an UFS-2 color-glass filter and directed into a DFS-452 spectrograph equipped with a photomultiplier (PMT) FÉU-106. The signal was digitized by a V4-17 digital voltmeter.

We paid special attention to avoiding saturation of the photomultiplier. The absolute values of the transformation efficiency were measured by two methods. First, we calculated the number of TH photons arriving at PMT based on the value of the PMT signal, its amplification, and the efficiency of the photocathode. Knowing the parameters of the calibrated filters and the losses in the spectrograph, we could calculate the number of TH photons generated in the fullerene-containing film. The transformation efficiency was determined as the ratio of the TH energy to the energy of the pumping radiation. The latter was detected by a photodiode cali-

brated by a calorimeter. The second method employed generation of the second and third harmonics in KDP crystals. TH radiation passed through the film and its energy was measured by a calorimeter. After that, the energy of TH radiation was attenuated by calibrated filters. Knowing the losses in the spectrograph, we calculated the calibration factor between the TH energy and the signal measured by PMT. These two methods yield slightly differing absolute values of the efficiency of transformation into the third harmonic.

Experiments used polyimide 6B films with a thickness of 1 μm doped with $C_{70}$. Fullerene-containing polyimide films were deposited onto quartz substrates. The concentrations of $C_{70}$ in the films were 0.2 and 0.5 wt %.

## RESULTS AND DISCUSSION

Figure 1 shows a plot of the TH intensity versus the intensity of the pumping beam ($I_\omega$) for the film with the fullerene concentration of 0.5%. The slope of this curve obeys a cubic law up to $I_\omega = 5 \times 10^{10}$ W/cm$^2$. Further increase in the intensity leads to a deviation from the cubic law. In the case of the film with a fullerene concentration of 0.2%, the slope of the curve $I_{3\omega}(I_\omega)$ was 2.8 for almost the entire range of the intensity variation. The maximum transformation efficiencies were $10^{-6}$ and $6 \times 10^{-6}$ for the films with fullerene concentrations of 0.2 and 0.5%, respectively. For the films with two concentrations of fullerene (0.2 and 0.5%), the ratio of the TH intensities measured at various intensities of the pumping radiation ($I_\omega < 5 \times 10^{10}$ W/cm$^2$) obeys a quadratic law with respect to the concentration. The experiments were carried out at an intensities of the pumping beam below the threshold of the optical breakdown of the fullerene-containing film ($I_\omega = 4 \times 10^{11}$ W/cm$^2$).

We observed no THG in the fullerene-free polyimide 6B film in the entire range of variation of the pumping intensity. We also tried to detect the radiation of the second harmonic (λ = 532 nm). None of the samples exhibited second harmonic generation (SHG). In this connection, note that Hoshi *et al.* [12] studied SHG in $C_{70}$ films within the framework of the mechanisms (electroquadrupole and magnetodipole) allowing generation of an even harmonic in centrosymmetrical media, which is forbidden under electrodipole approximation. Apparently, the reason for the absence of SHG in our experiments is the small concentration of fullerene in the polyimide films in comparison with that in the aforementioned study and in the works [7, 9] (experiments with pure $C_{60}$ and $C_{70}$ films).

Based on the results obtained, we propose the following interpretation of the nonlinear optical transformation in the polyimide films doped with fullerenes. The optical properties of aromatic polyimides [13] determined by excitation of π electrons can substantially be modified by introducing fullerenes into their

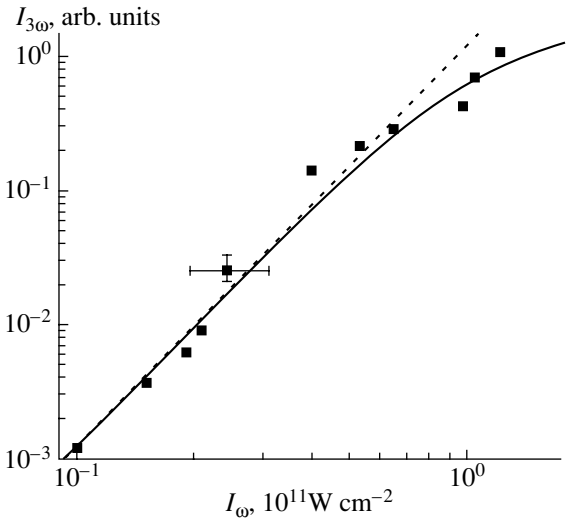


**Fig. 1.** The TH intensity versus the intensity of the pumping radiation for a film with 0.5% of $C_{70}$.

matrix. Interest in such systems is related to studies of the effect of inverse saturation [14] and the similarity of the mechanisms of the nonlinear response in fullerenes and aromatic hydrocarbons. $C_{70}$ represents a medium with double conjugated bonds and delocalized electrons and exhibits a large value for the induced dipole moment. The presence of conjugated π electrons accounts for high hyperpolarizability of these media.

One can use such a medium as a nonlinear one for effective transformation of the laser-radiation frequency. However, this is possible only in the case of phase matching between the pumping and generated waves. In our experiments, we focused the pumping radiation by a lens with the focal length $f = 25$ cm and the value of the confocal parameter was $b = 23$ mm at the length of the nonlinear medium $l = 1$ μm. Therefore, the experiments met the condition of weak focusing into the center of the nonlinear medium ($l \ll b$). In this case, the intensity of the third harmonic ($I_{3\omega} = n_3 c|E_{3\omega}|^2/8\pi$) generated by the lower mode of the Gaussian pumping beam is given by a relatively simple formula [15]

$$I_{3\omega} = \gamma^2 l^2 I_{10}^3 \exp(-6k_1 r^2/b)\frac{\sin^2\Delta(l, r)}{\Delta^2(l, r)}. \qquad (1)$$

Here, $\gamma = 24\pi^3\chi^{(3)}(-3\omega; \omega, \omega, \omega)/(n_1^{3/2} n_3^{1/2} c\lambda_1)$; $\Delta(l, r) = 2b/l - \alpha - \beta$; $\alpha = 2l\Delta k$ is the normalized value of the phase mismatch; $\beta = 72\pi^3 l\Delta\chi_k I_{10}\exp(-2k_1 r^2/b)(n_1^2 c\lambda_1)$; $\Delta k = 3k_1 - k_3$; $\Delta\chi_k = \chi^{(3)}(-\omega; \omega, \omega, -\omega)/2 - n_1\chi^{(3)}(-3\omega; 3\omega, \omega, -\omega)/n_3$ is the difference of the Kerr nonlinearities responsible for the variation in the refractive indices at the fundamental frequency and the frequency of the harmonic in the field of the fundamental radiation; $\lambda_i$, $k_i$, and $n_i$ are the wavelength, the wave number, and the refractive index at the frequency of the $i$th radiation;

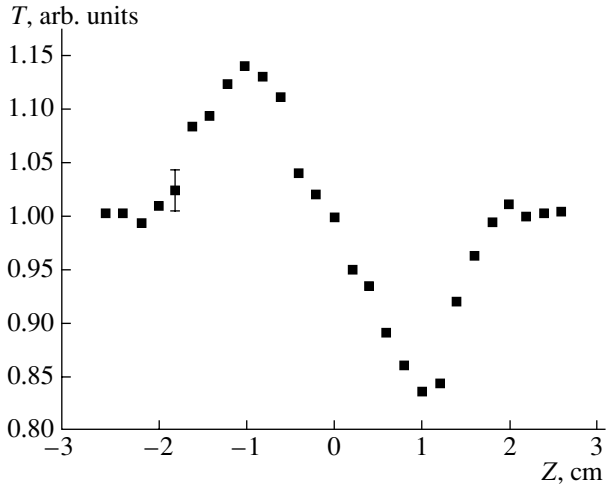


**Fig. 2.** The normalized transmittance versus the position of the plate with polyimide film doped by $C_{70}$ (0.5%) for the scheme with a limiting diaphragm.

and $I_{10}$ is the maximum intensity in the focal plane of the beam.

Expression (1) is valid in the case of relatively weak self-action ($|\beta| \ll b/l$) leading to a nonlinear variation in the value of the phase mismatch. To describe THG with stronger self-action and the position of the beam waist outside the nonlinear medium, we employed more complicated expressions taking into account the variation in the wave fronts of the interacting beams (self-focusing and self-defocusing) [15]. The calculations of the efficiency of the energy conversion used the integration of formula (1) over the transverse coordinates and time.

It is known that the phase synchronism ($\Delta k = 0$) can be achieved only if the frequency of the generated radiation falls into the region of the anomalous dispersion of the medium [16]. Both $C_{70}$ and polyimide 6B exhibit normal dispersion at $\lambda$ = 354.7 nm. However, our experiments were carried out at such a concentration of $C_{70}$ that the estimated value of the parameter $\alpha$ did not exceed 0.05. This means that the phase mismatch and linear absorption of $C_{70}$ must not substantially affect the process of frequency transformation. The dependence of the intensity of the generated harmonic on the concentration of $C_{70}$ must be almost quadratic which was nearly the case in experiments. At low intensities of the fundamental radiation, the dependence of the TH intensity on the fundamental-harmonic intensity is cubic (dashed line in Fig. 1). Based on this curve, we calculated the third-order nonlinearity responsible for THG in the films with 0.5% of $C_{70}$ to be $9 \times 10^{-13}$ esu.

Earlier, Meth *et al.* [10] and Kajzar *et al.* [11] reported on THG in $C_{60}$ films. Rigorously speaking, the difference in the positions of the excitonic transitions in $C_{60}$ and $C_{70}$ in the vicinity of the TH wavelength does not enable one to compare the nonlinear susceptibilities of these media. Note that the experiments on harmonic generation by the radiation of a Nd : YAG laser in solutions and films made of $C_{70}$ [11, 17] yielded the third-order nonlinear susceptibilities of $10^{-13}$ and $2.6 \times 10^{-11}$ esu, respectively.

It follows from formula (1) that an increase in the intensity of the fundamental radiation leads to a decreasing slope of the intensity dependence of the TH intensity due to the effect of Kerr nonlinearities responsible for variation in the refractive index of the nonlinear medium at the fundamental and TH frequencies in the field of the fundamental radiation (solid line in Fig. 1). The difference in the Kerr nonlinearities $|\Delta\chi_k|$ was estimated to be $8 \times 10^{-11}$ esu. This means that the nonlinearities responsible for the self-action are larger than the nonlinearity responsible for THG by almost two orders of magnitude. For weak focusing into the center of the nonlinear medium without using the methods for compensating the effect of Kerr nonlinearities, the known expressions [16] predict that the transformation efficiency will not exceed $1.3 \times 10^{-5}$. Thus, the transformation efficiency obtained in our experiments ($6 \times 10^{-6}$) is close to the upper limit that can be achieved without using the methods for compensating for the effect of Kerr nonlinearities. The transformation efficiency can be substantially increased by various compensation techniques (e.g., introduction of additional phase mismatch and the changes in the focusing of the pumping radiation).

Note that the decrease in the slope of the $I_{3\omega}(I_{1\omega})$ curve with increasing intensity of the fundamental radiation can also be related to the effect of the nonlinear absorption. However, we did not observe significant nonlinear absorption in polyimide films doped by fullerenes in the intensity range studied.

To determine the value of the Kerr nonlinearity responsible for the variation in the refractive index at the fundamental frequency, we carried out independent measurements of the nonlinear contribution to the refractive index. We measured the nonlinear refractive index $n_2$ by using the *Z*-scheme [18] to determine its value and sign. Figure 2 shows a typical $T(Z)$ curve enabling one to determine the sign and the absolute value of the nonlinear refractive index of the film with 0.5% of $C_{70}$. The measurements of $n_2$ of a fullerene-free polyimide film under the same conditions yielded no nonlinear contribution to the refractive index.

For the film with 0.5% of $C_{70}$ and the wavelength $\lambda$ = 1064 nm, the nonlinear refractive index was determined to be $n_2 = -1.4 \times 10^{-9}$ esu. The value of the Kerr nonlinearity corresponding to this nonlinear contribution to the refractive index is $\chi^{(3)}(\omega; \omega, \omega, -\omega) = 1.5 \times 10^{-10}$ esu which is in reasonable agreement with the results of the analysis of the $I_{3\omega}(I_{1\omega})$ curves. Thus, an increase in the intensity of radiation must lead to an increasing difference between the refractive indices of the medium at the pumping and TH wavelengths and, hence, to an increasing phase mismatch. This, in turn,

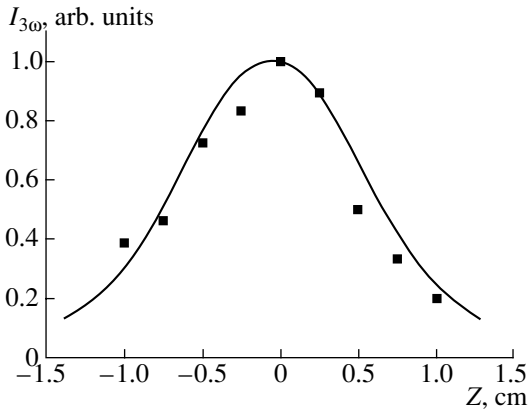


**Fig. 3.** The TH intensity versus the position of the film with 0.5% of $C_{70}$ relative to the focal point ($Z = 0$).

results in a slower increase in $I_{3\omega}$ as a function of $I_{1\omega}$ than predicted by the cubic law. The same effect was observed in experiments. Such a phenomenon was observed earlier in the case of strong focusing in gas media when the high-frequency Kerr effect leads to a phase mismatch and slows down the increase in TH intensity with the intensity of the pumping beam [19, 20]. Note the opposite effect consisting in an additional increase in the harmonic intensity with an increase in the intensity of the pumping beam owing to compensation of the phase mismatch in the media with positive $n_2$. This can be used for optimizing the phase matching in THG [20].

Figure 3 shows a plot of TH intensity versus the position of the film with 0.5% of $C_{70}$ relative to the focal point ($Z = 0$). A slight asymmetry of $I_{3\omega}(Z)$ can be related to a nonlinear contribution to the refractive index. In front of the focal point, self-defocusing of the fundamental radiation must lead to a decreasing divergence of the radiation and, hence, to a higher efficiency of THG in comparison with the zone lying behind the focal point. However, the calculations at the given ratio of the confocal parameter to the length of the nonlinear medium yield a nearly symmetric curve (solid line in Fig. 3). The growth of the intensity of the pumping beam must lead to a broadening of this curve. At higher intensities, a dip in the central part of the curve makes the position of the beam waist outside the nonlinear medium more preferable.

## CONCLUSIONS

We have studied the generation of the third harmonic of picosecond radiation of a Nd : YAG laser in polyimide films. For the first time, the nonlinear susceptibility $\chi^{(3)}$ of polyimide films with various concentrations of $C_{70}$ was studied by the THG technique. The nonlinear susceptibility of the polyimide film with 0.5% of $C_{70}$ was $9 \times 10^{-13}$ esu. The effect of the Kerr nonlinearity on phase matching of the pumping and TH waves accounts for the deviation of the $I_{3\omega}(I_\omega)$ curves from the cubic law. The maximum efficiency of transformation into the third harmonic was $10^{-6}$ and $6 \times 10^{-6}$ for the films with 0.2 and 0.5% concentrations of fullerene molecules, respectively.

## ACKNOWLEDGMENTS

We are grateful to N. V. Kamanina for providing us with fullerene-containing polyimide films.

## REFERENCES

1. W. J. Blau, H. J. Byrne, D. J. Kardin, *et al.*, Phys. Rev. Lett. **67**, 1423 (1991).
2. E. Westin and A. Rosen, Mater. Res. Soc. Symp. Proc. **270**, 221 (1992).
3. R. J. Knize and J. P. Partanen, Phys. Rev. Lett. **68**, 2704 (1992).
4. Z. H. Katafi, J. R. Lindle, R. H. C. Pong, *et al.*, Chem. Phys. Lett. **188**, 492 (1992).
5. J. Kallaghan, D. N. Weldon, F. Z. Henari, *et al.*, in *Electronic Properties of Fullerenes*, Ed. by H. Kuzmany, J. Fink, H. Mehring, and S. Roth (Springer-Verlag, New York, 1993), pp. 307–309.
6. M. P. Joshi, S. R. Mishra, H. C. Rawat, *et al.*, Appl. Phys. Lett. **62**, 1763 (1993).
7. H. Hoshi, N. Nakamura, Y. Maruyama, *et al.*, Jpn. J. Appl. Phys. **30**, L1397 (1991).
8. Y. Wang and L.-T. Cheng, J. Phys. Chem. **96**, 1530 (1992).
9. X. K. Wang, T. G. Zhang, W. P. Lin, *et al.*, Appl. Phys. Lett. **60**, 810 (1992).
10. J. S. Meth, H. Vanherzeele, and Y. Wang, Chem. Phys. Lett. **197**, 26 (1992).
11. F. Kajzar, C. Taliani, M. Muccini, *et al.*, Proc. SPIE **2284**, 59 (1994).
12. H. Hoshi, T. Manaka, K. Ishikawa, and H. Takezoe, Jpn. J. Appl. Phys. **36**, 6403 (1997).
13. M. Ree, T. L. Nunes, and K.-J. R. Chen, J. Polym. Sci., Part B: Polym. Phys. **33**, 453 (1995).
14. N. V. Kamanina, L. N. Kaporskii, and B. V. Kotov, Opt. Commun. **152**, 280 (1998).
15. I. A. Kulagin and T. Usmanov, Quantum Electron. **28**, 1092 (1998).
16. J. F. Reintjes, *Nonlinear Optical Parametric Processes in Liquids and Gases* (Academic, New York, 1984).
17. D. Neher, G. I. Stegeman, F. A. Tinker, and N. Peygambarian, Opt. Lett. **17**, 1491 (1992).
18. M. Sheik-Bahae, A. A. Said, T. H. Wei, *et al.*, IEEE J. Quantum Electron. **26**, 760 (1990).
19. L. J. Zych and J. F. Young, IEEE J. Quantum Electron. **14**, 147 (1978).
20. R. A. Ganeev, I. A. Kulagin, I. A. Begishev, *et al.*, Nonlinear Opt. **16**, 109 (1996).

*Translated by A. Chikishev*

*Technical Physics, Vol. 46, No. 10, 2001, pp. 1274–1280. Translated from Zhurnal Tekhnicheskoĭ Fiziki, Vol. 71, No. 10, 2001, pp. 70–76.*


**ACOUSTIC, ACOUSTOELECTRONICS**

# Interaction of Light with Acoustic Microwave Waves Excited by Nonperiodic Multielement Transducers. Part I

**M. A. Grigor'ev, A. V. Tolstikov, and Yu. N. Navrotskaya**

*Chernyshevskiĭ State University, Universitetskaya ul. 42, Saratov, 410071 Russia*

*e-mail: magrig@sgu.ssu.ru nnet.ru*

Received July 3, 2000; in final form, February 10, 2001

**Abstract**—The feasibility of effective wide-band acoustooptic interaction in the short-wave part of the microwave range by means of nonperiodic multielement piezoelectric transducers is analyzed. The variation of the pitch or the period of the transducer sections is discussed. The impedance of a piezoelectric element with an arbitrary number of transformable layers and the acoustic power radiated from each of the piezoelements of the transducer are calculated. A 13-section transducer designed for a center frequency of 9 GHz is considered as an example. © *2001 MAIK "Nauka/Interperiodica".*

## INTRODUCTION

In this work, we analyze the use of variable-pitch multielement electroacoustic piezoelectric transducers (MEATs) in deflectors operating in the short-wave part of the microwave range. Impetus to writing this article has been given by the erroneous statement that "the use of the MEATs makes it possible to substantially extend the bandwidth of acoustooptic interaction and improve the diffraction efficiency" [1]. Another reason is work [2], where acoustooptic (AO) interaction in lithium niobate crystals was experimentally studied in the frequency range of 7.5–10.5 GHz. The data obtained in [2], as well as the prospects for using this phenomenon in applications, have stimulated us to check whether nonperiodic MEATs can really improve the AO interaction efficiency at the above frequencies.

It is known [3–5] that the variation of the MEAT frequency generates scanning acoustic waves, allowing self-tuning to "the Bragg angle" in AO devices. Such transducers, which are nonperiodic structures, have been carefully analyzed in [6–13]. However, self-tuning with the conventional transducers does not completely satisfy the Bragg law. This generates a need for limiting the MEAT length in order to compensate (correct) for the discrepancy by the acoustic beam divergence. Thus, the actual MEAT length turns out to be insufficiently long for a high AO efficiency to be reached in a wide frequency band. Efforts to design periodic MEATs, which could provide perfect self-tuning at microwaves, have failed, as far as we know. Moreover, piezoelements based on conventional piezoelectric films (CdS, ZnO, or AlN) cannot be equally effective in a frequency band as wide as desired. This, naturally, narrows the passband of the acoustooptic device as a whole.

The idea of a variable-pitch multielement transducer has been put forward in [1]. The chain of argument was as follows. For a periodic multielement transducer, the Bragg condition is given by [7]

$$\alpha_m - \Theta_{0i} = (-1)^i \Theta_B(f). \quad (1)$$

Here, $\Theta_B(f)$ is the Bragg angle between the wave vector of light and the acoustic wave front, $f$ is frequency, $\Theta_{0i}$ is the angle between wave vector of the incident light and the end face of an acoustic line, $m$ is the number of a spatial harmonic of an exciting electric field, $i$ is the number of a possible direction of the incident light ($i = 1$ or 2), and $\alpha_m$ is the angle between the front of the $m$th partial elastic wave and the end face of the MEAT acoustic line. The angle $\alpha$ is given by [7]

$$\alpha_m = \arcsin[v_{ac}\varphi_m(f)/2\pi fl], \quad (2)$$

where $\varphi(f) = \varphi_0(f) + 2\pi m$ is the phase shift per MEAT period for the $m$th spatial harmonic, $\varphi_0(f)$ is the phase shift between neighboring piezoelements, and $l$ is the MEAT period.

Based on these formulas, the authors of [1] concluded that "precise self-tuning in a given bandwidth (i.e., the variation of $\alpha_m$ in strict accordance with the variation of $\Theta_B$) is possible only if the phase shift per period $\varphi_m(f)$ or the period $l$ changes with frequency. In the latter case, the system becomes nonperiodic."

As for the former possibility, it is beyond question and has been studied in detail in the works cited above. The latter statement, however, provokes objections: a change in the period $l(f)$ does not necessarily mean that the transducer becomes nonperiodic. What actually happens is that its length changes with the number of the elements retained. The transducer must remain periodic, having another period. Otherwise, the expansion of the electric field in an MEAT becomes impossible and formulas (1) and (2), invalid. Obviously, such a transducer cannot be designed for a complex-spectrum

1063-7842/01/4610-1274$21.00 

signal, since the transducer must have different periods, remaining periodic at the same time.

Certainly, a nonperiodic MEAT where the pitch along its length varies according to some law, including a law meeting Bragg condition (1), can be suggested. In [1], such a possibility is considered only qualitatively, so that the question of pitch variation law remains open.

The variability of $l(f)$ following from (1) and (2) should be perceived as the feasibility of a sectioned transducer consisting of MEAT sections with different periods. Each of the sections acts as an independent MEAT having its own center frequency and passband. It can be assumed that the combination of the sections will provide the MEAT operation in a given frequency band with a desired efficiency. Physically, it is clear that the AO efficiency can be improved by lengthening the sections; in this case, however, it is necessary to have a larger number of the sections, since the frequency band of self-tuning for each of them (subband) shrinks in this case. The periods of the sections are defined by formulas (1) and (2) and also by the center frequencies of the subbands, and the section lengths depend on the subband width. To provide a high AO efficiency, the piezoelements in each particular section must operate in a sufficiently narrow operating subband to which this section is tuned; otherwise, "sound" will uselessly be generated also by sections whose period is inappropriate for a given frequency. Thus, the minimal bandwidth where real piezoelements can operate specifies the subband width and, hence, the number of sections and the maximal AO efficiency.

Hereafter, we assume that the photoelastic medium is an *X*-cut lithium niobate crystal and that the center frequency of the operating band is 9 GHz. The wavelength of light in a vacuum is set to be equal 0.63 μm. Without loss of generality, the damping of the elastic waves is assumed to be zero. The transducers will be considered as quasi-steady-state chains of lumped-parameter piezoelements with a constant phase shift between neighboring elements and a negligibly small impedance of wires. The fact that the wavelength of an electromagnetic wave far exceeds the linear size of the chain validates our quasi-steady-state representation. For example, the length of a 13-section ≈10-GHz MEAT consisting of 1345 elements is ≈4.9 mm.

In what follows, we will find the frequency dependences of the AO efficiency when "sound" is generated by both sectioned MEATs and various nonperiodic MEATs with a smoothly varying pitch. Also, we will consider nonperiodic MEATs that are modifications of a periodic opposite-phase transducer.

## PITCH VARIATION LAW

First, we will select the periods for different sections of a sectioned transducer. From (1) and (2), it follows that, if the angle $\Theta_0$ of incidence of light is constant, the MEAT period must depend on frequency as

$$l = \frac{v_{ac}|\varphi_m(f)|}{2\pi f \sin[\Theta_{0i} + (-1)^i \Theta_B(f)]}. \quad (3)$$

Given the center frequencies of the subbands and the angle of incidence $\Theta$, one can easily calculate the periods of all the sections. For self-tuning at least in one of the sections to take place in a frequency band as wide as possible, the period of this section must obey the condition [7]

$$(d\alpha_m/df)_{f=f_0} = (-1)^i (d\Theta_B/df)_{f=f_0}, \quad (4)$$

where $f_0$ is the center frequency.

We will restrict our analysis by a sectioned transducer whose prototype is a periodic opposite-phase device [7]. For this and also for inphase transducers, it was shown [8] that

$$l = k_m n_0 v_{ac}^2 / f_0^2 \lambda_0 \quad (5)$$

(where $k_m = |\varphi_0/\pi + 2m|$), as follows from (4).

Such a period will be referred to as optimal. Note that formula (5) cannot yield the periods for different sections, since one should find from (1) a new angle of incidence $\Theta_0$ for each new frequency. If a period $l$ is found by formula (5) and then the angle $\Theta_0$ for one of the sections is found by (1), the value of $l$ for the other sections must be determined from (3) assuming $\Theta_0$ = const.

Consider an *X*-cut $LiNbO_3$ crystal ($n_0 = 2.2$, $v_{ac} = 6.57 \times 10^3$ m/s) as a photoelastic medium. For $\lambda_0 = 0.63$ μm in the case of an opposite-phase (OP) MEAT ($k_m = 1$), we obtain, from (5), $l = 1.9$ and 3.076 μm for frequencies $f_0 = 8.9$ and 7 GHz, respectively. From (1), we obtain, respectively, $\Theta_0 = 0.39$ and 0.302 rad. For these constant angles, frequency dependences (3) will take the form shown in Fig. 1. Both curves are seen to have a minimum: at $f_0 = 8.9$ GHz ($l_{min} \approx 1.9$ μm) and ≈7 GHz ($l \approx 3.1$ μm). Clearly, self-tuning in the greatest possible frequency band will take place in the section near the minimum of the $l(f)$ curve, since here the period required depends on the frequency only slightly. The sections operating at other frequencies must have a larger period according to the curve in Fig. 1. The widths of the self-tuning subbands for the other sections will increasingly shrink with distance from the minimum because of the growing slope of the $l(f)$ curve. The recovery of the frequency subband width of these sections by their shortening is impossible, because the AO efficiency will degrade in this case. Therefore, for the MEAT passband to remain unchanged, it is necessary to increase the number of sections, since those operating far away from $f_0$ will decrease the subband width at a fixed length of the device.

Figure 1 shows that the upper curve requires much larger periods in the sections. For example, at 9 GHz,

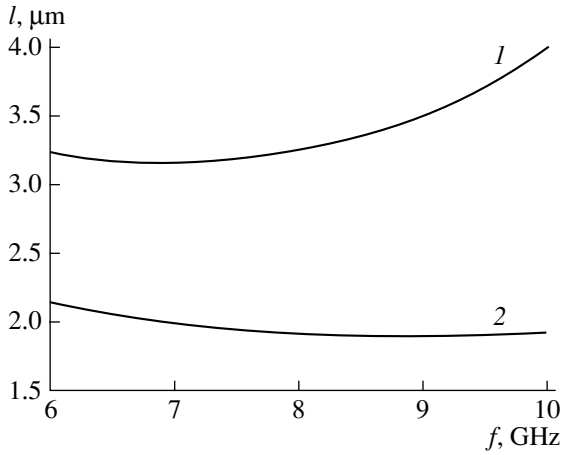


**Fig. 1.** MEAT period vs. frequency. $\Theta_0$ = (*1*) 0.3 and (*2*) 0.39 rad.

the lower curve implies that the period must be 1.9 μm, while from the upper curve, it follows that the period must be 3.5 μm. The latter size is preferable from technology considerations. Therefore, we will address to the upper curve in subsequent analysis.

The periods in particular MEAT sections can be found only if the widths and center frequencies of the subbands are known. The frequency properties of the piezoelements play a crucial role here. In a given section, the elements must operate mostly in an appropriate frequency band. The implementation of such piezoelements is of special importance in creating sectioned MEATs.

Now consider an MEAT with the smooth variation of the pitch $l(x)$ along the transducer. A high AO efficiency can be attained in this case if the device has a sufficiently large number of elements. Then, to each of the spectral components of the signal, a group of the elements with an appropriate pitch will correspond, hence, a desired AO efficiency. It is obvious that the pitch must not considerably change within a group just because the total number of the elements is large. It follows that the distribution of the resulting acoustic field (induced by all the groups) resembles the case of a sectioned transducer. The only difference is that the problem of pitch selection disappears, because the distance between the sections smoothly varies. Clearly, the pitch at the center of a group must be found from formula (3), as for sectioned MEATs.

In [1], it was suggested to relate the functions $l(x)$ and $l(f)$. However, the form of the former function is still unclear. For the nonperiodic MEATs with a smoothly varying pitch, we will use a linear relationship between the frequency and the longitudinal coordinate. The algorithm for deriving this relationship is as follows. The operating frequency range of an MEAT consisting of $M$ elements is subdivided into $M-1$ intervals, each corresponding to a particular pair of neighboring elements. Let the number of a specific frequency interval coincide with the "continuous" number of the first element of the corresponding pair. From formula (3), a desired value of $l$ for the lower bound of each of the intervals is found and taken as the center distance of the corresponding pair of the elements. We omit other ways of specifying the $l(x)$ function. Note only that the above procedure does not yield the optimal form of $l(x)$, since the curve $l(f)$ is of variable slope: $k = dl/df$. As a result, the efficiency of MEAT operation in various frequency ranges will be different. It seems that the higher the slope $k(f)$, the lower the AO efficiency. Appropriate corrections to the $l(x)$ function are needed to improve the frequency response of the AO device.

## IMPEDANCE OF PIEZOELEMENT

To predict the MEAT performance, it is required to find the frequency dependence of the impedance $Z_\Sigma$ of an individual piezoelectric element. From this dependence, one can estimate the acoustic power radiated from each of the elements and, hence, the efficiency of AO interaction for a particular MEAT version.

To construct a desired frequency response of the transducer, we will consider a model of multilayer piezoelement shown in Fig. 2. Piezoelectric layer *1* is sandwiched in infinitely long media: photoelastic crystal *2* and passive load *3*. Between these media and the piezolayer, there are sets of intermediate transformable layers. The bottom layers are assigned numbers $2m$, where $m = 1, 2, \ldots$; $M$ is the number of a layer reckoned from the acoustic line. The top layers are assigned numbers $3n$, where $n = 1, 2, \ldots$; $N$ is reckoned from the passive load. The figures 2 and 3 in the numbering mean that the associated layers are arranged on the side of the 2nd and 3rd media. The layers with the numbers $2M$ and $3N$ are assumed to be metallic electrodes that are in direct contact with the piezoelectric and will be referred to as "underlayer" and "overlayer."

Let us assume that the longitudinal normal of the crystalline piezoelectric layer is directed along the $x$ axis perpendicularly to the end face of the photoelastic acoustic line. Such a situation occurs, for example, when a ZnO film thus oriented due to the hexagonal axis generates a longitudinal wave. The underlayer, overlayer, all intermediate layers, and acoustic line are assumed to be isotropic (their longitudinal normal is aligned with the $x$ axis). This condition is met when a longitudinal elastic wave propagates in a $LiNbO_3$ acoustic line along the $X$ axis of the crystallographic coordinate system. Under such conditions, the equations describing electromechanical processes in the piezoelectric become scalar.

Proceeding as in [14, 15], one can obtain the equation for dimensionless impedance of a piezoelement:

$$Z_\Sigma(\omega)\omega C_0 = \delta_\Sigma + j\tau_\Sigma = -j + j\frac{k^2}{(\beta_1 h_1)} \times [(e^{-j\beta_1 h_1} - 1)u'_{1+} + (e^{j\beta_1 h_1} - 1)u'_{1-}], \quad (6)$$

where $C_0$ is the static capacitance of the piezolayer; $\delta_\Sigma$ and $\varepsilon_\Sigma$ are the active and reactive components of the impedance, respectively; $k$ is the electromechanical coupling coefficient; $(\beta_1 h_1)$ is the universal independent variable (the product of the wave number in the piezoelectric, $\beta_1$, by its thickness $h_1$); and $u'_{1+}$ and $u'_{1-}$ are the dimensionless complex amplitudes of the direct and backward waves of mechanical displacement, respectively, in the piezoelectric:

$$u'_1 = u_1 Z_{10} \varepsilon \omega / e D_0,$$

where $u_1$ is the dimensional complex amplitude of mechanical displacement.

From the conditions at the piezoelectric boundary, we have

$$\left[\frac{Z_{2M}}{Z_{10}} - 1\right] e^{-j\beta_1 h_1} u'_{1+} + \left[\frac{Z_{2M}}{Z_{10}} + 1\right] e^{j\beta_1 h_1} u'_{1-} = -j, \quad (7)$$

$$\left[\frac{Z_{3N}}{Z_{10}} + 1\right] u'_{1+} + \left[\frac{Z_{3N}}{Z_{10}} - 1\right] u'_{1-} = j. \quad (8)$$

Here, $Z_{2M}$ is the acoustic resistance resulting when the wave impedance $Z_{20}$ of the acoustic line is affected by the sequence of $M$ layers below the piezoelectric (Fig. 2), and $Z_{3N}$ is the acoustic resistance resulting when the wave impedance $Z_{30}$ of the acoustic line is affected by the sequence of $N$ layers above the piezoelectric. If damping is absent, each of the underlying layers affects the resistance by the law

$$Z_{2m} = Z_{2,m0} \frac{Z_{2,m-1}\cos(a_{2m}\beta_1 h_1) + jZ_{2,m0}\sin(a_{2m}\beta_1 h_1)}{Z_{2,m0}\cos(a_{2m}\beta_1 h_1) + jZ_{2,m-1}\sin(a_{2m}\beta_1 h_1)}, \quad (9)$$

where $Z_{2,m0}$ is the acoustic wave impedance of layer no. $2m$; $Z_{2m}$ is the acoustic resistance of the layer with the same number at its boundary facing the piezoelectric; $Z_{2,m-1}$ is the impedance of the preceding layer at the same boundary, $a_{2m}$ is the normalized thickness of the layer,

$$a_{2m} = \frac{v_1}{v_{2m}} \frac{h_{2m}}{h_1},$$

and $v_1$ and $v_{2m}$ are the sound velocities in the associated layers.

For the top layers, the law of resistance modification has the form of (9) with the subscript $2m$ replaced by $3n$. In the absence of the passive acoustic load, one can put $Z_{30} = 0$.

Thus, the algorithm for calculating the normalized impedance $\delta_\Sigma + j\tau_\Sigma$ of the piezoelement is as follows. First, the values of $Z_{2M}$ and $Z_{3N}$ are found from (9) by iteration. Then, the system of algebraic equations (7) and (8) is solved and the dimensionless amplitudes $u'_{1+}$ and $u'_{1-}$ found are substituted into (6). Eventually, we obtain the active and reactive components

$$\delta_\Sigma = R_\Sigma \omega C_0, \quad \tau_\Sigma = x_\Sigma \omega C_0. \quad (10), (11)$$

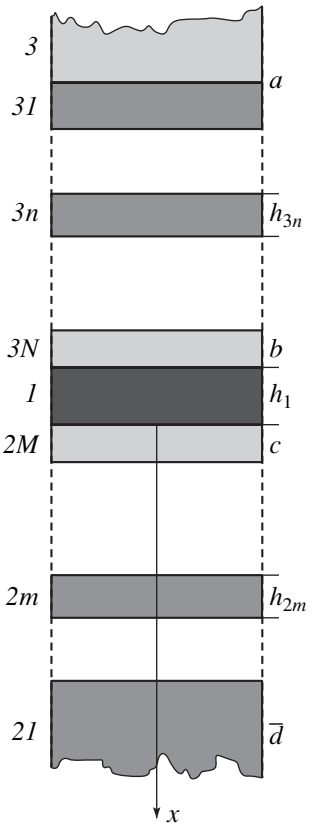


**Fig. 2.** Piezoelement model. (*a*) Passive load, (*b*) overlayer, (*c*) underlayer, and (*d*) photoelastic medium.

The active resistance $\delta_\Sigma = \delta_{ac} + \delta_{load}$ load, where $\delta_{ac}$ and $\delta_{load}$ are the resistances that excite an acoustic wave in the acoustic line and in the passive layer, respectively. If acoustic loss in the layers is absent, these parameters can be found in the following way.

The piezoelement is connected from above and from below to the complex acoustic resistances $Z_{3N}$ and $Z_{2M}$ (Fig. 2). The former arises when the intermediate layers affect the acoustic wave impedance of the passive load, and the latter is the result of transformation of the wave impedance of the acoustic line. The respective powers absorbed by these resistances are

$$P_{load} = (\mathrm{Re} Z_{3N})\omega^2 |u_1(x = 0)|^2/2,$$

$$P_{ac} = (\mathrm{Re} Z_{2M})\omega^2 |u_1(x = h_1)|^2/2.$$

Then, passing to the dimensionless displacement, we easily come to

$$\frac{\delta_{ac}}{\delta_\Sigma} = \frac{P_{ac}}{P_{ac} + P_{load}} = \frac{(\mathrm{Re} Z_{2M})|u'_1(x = h_1)|^2}{[(\mathrm{Re} Z_{2M})|u'_1(x = h_1)|^2 + (\mathrm{Re} Z_{3N})|u'_1(x = 0)|^2]}. \quad (12)$$

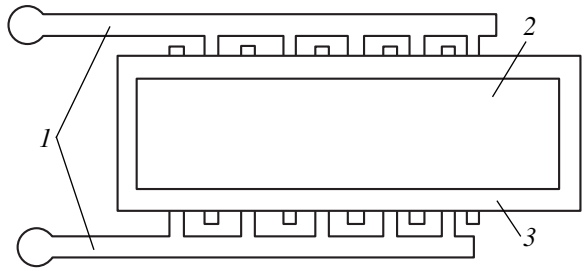


**Fig. 3.** Design of a multielement transducer: (*1*) interdigitation; (*2*) metal; and (*3*) piezoelectric.

Here, $u_1'(x = h_1) = u_{1+}'e^{-j\beta_1 h_1} + u_{1-}'e^{j\beta_1 h_1}$ and $u_1'(x = 0) = u_{1+}' + u_{1-}'$. If the passive load is absent (that is, $Z_{30} = 0$), we have $\mathrm{Re}Z_{3N} = 0$ and accordingly $\delta_{ac} = \delta_\Sigma$. Similarly, we can write

$$\frac{\delta_{load}}{\delta_\Sigma} = \frac{(\mathrm{Re}Z_{3N})|u_1'(x = 0)|^2}{[(\mathrm{Re}Z_{2M})|u_1'(x = h_1)|^2 + (\mathrm{Re}Z_{3N})|u_1'(x = 0)|^2]}.$$

## ACOUSTIC POWER RADIATED BY A PIEZOELEMENT

Consider a multielement transducer with $M$ elements that electrically represents a series connection of two groups of elements connected in parallel within either group (Fig. 3). The acoustic line is covered by a thin-film metallic interdigital structure. On this structure, in turn, piezoelectric and metal strips are deposited. An ac voltage is applied to the interdigitation. The tangential electric fields between the wires in the piezoelectric are shunted by the metal strip. The normal fields between the metal strip and the wires cause a sequence of opposite-phase piezoelements to appear. Odd elements enter one group, and even elements fall into the other. Let the $\chi$th element have the impedance $Z_\chi$. Then, the impedance of the odd elements is given by

$$Z_{od} = \left[\sum_{\chi=1}^{M} \frac{(1-(-1)^\chi)}{2Z_\chi}\right]^{-1} \quad (13)$$

and that of the even elements,

$$Z_{ev} = \left[\sum_{\chi=1}^{M} \frac{(1+(-1)^\chi)}{2Z_\chi}\right]^{-1}. \quad (14)$$

The total impedance is

$$Z_\Sigma = Z_{od} + Z_{ev} = R_\Sigma + jX_\Sigma. \quad (15)$$

Consider the simplest case where an MEAT represents a termination of a transmission line with a wave impedance $Z_0$. We assume that the generator is matched with the line; i.e., its internal resistance is also $Z_0$. Then, it can be shown the acoustic power radiated from the $\chi$th piezoelement is expressed by the formula

$$P_\chi = \frac{4Z_0P_{al}\{[(1+(-1)^\chi)/2]|Z_{ev}|^2 + [(1-(-1)^\chi)/2]|Z_{od}|^2\}}{|Z_0 + Z_\Sigma + Z_k|^2|Z_\chi|^2}\mathrm{Re}(Z_\chi), \quad (16)$$

where $P_{al}$ is the power released in the matched termination and $Z_c$ is the impedance of contact wires connecting the MEAT and the transmission line.

From this formula, it follows that the $P_\chi$ vs. $Z_0$ dependence has a peak at a so-called optimal value of the wave impedance:

$$Z_{0,\,opt} = |Z_\Sigma + Z_c|. \quad (17)$$

Thus, the optimal wave impedance of the transmission line must equal the absolute value of the MEAT impedance in view of loss. A line with such an impedance will also be called optimal. This line can be matched with a standard 50-Ω line in a wide frequency band, for example, using a Chebyshev step junction. With such a way of electromagnetic power delivery to the MEAT, there is no need for reactive matching elements and the transducer can operate in a wide frequency band.

Analysis based on these formulas has shown that narrow-band piezoelements suitable for the use in MEAT sections are easy to implement. It turns out that the thickness of the piezoelectric, the metal type, and the thickness of the underlayer can be the same for all sections. In this case, desired center frequencies of the subbands can be provided by varying only the thickness of the overlayer. A piezoelement using an *X*-cut $LiNbO_3$ acoustic line, a 0.32-μm-thick ZnO film, a 0.16-μm-thick aluminum underlayer, and a gold overlayer (with a thickness of 0.48–0.61 μm) can operate in a frequency band of ≈3% and tuned in the range of 8–10 GHz by varying the overlayer thickness. The table lists the basic parameters of the 13-section MEAT with a total number of such piezoelements $M$ = 1345. The center frequencies of the subbands, the number of the elements in a section, the thicknesses of the overlayer, and the periods $l$ calculated from formula (3) for $\Theta$ = 0.3019 rad are presented. The width of the piezoelements was taken equal to 50 μm. The total length of the sections was ≈4.9 mm. The last column lists the width of the frequency dependence of the 3-dBm AO efficiency ($\eta_{AO}$) for each of the sections.

**Table**

| Section no. | Center frequency $f_0$ of subband, GHz | Number $M$ of elements in a section | Period $l$, μm | Overlayer thickness $P$, 0.1 μm | Subband width, MHz |
|---|---|---|---|---|---|
| 1 | 8.16 | 112 | 3.278 | 6.153 | 275 |
| 2 | 8.41 | 110 | 3.329 | 5.932 | 230 |
| 3 | 8.612 | 108 | 3.379 | 5.766 | 200 |
| 4 | 8.804 | 107 | 3.435 | 5.616 | 180 |
| 5 | 8.97 | 106 | 3.489 | 5.484 | 165 |
| 6 | 9.13 | 105 | 3.546 | 5.379 | 155 |
| 7 | 9.272 | 103 | 3.605 | 5.275 | 140 |
| 8 | 9.404 | 102 | 3.663 | 5.187 | 135 |
| 9 | 9.53 | 101 | 3.724 | 5.101 | 125 |
| 10 | 9.65 | 100 | 3.786 | 5.024 | 120 |
| 11 | 9.77 | 98 | 3.854 | 4.949 | 120 |
| 12 | 9.88 | 97 | 3.921 | 4.881 | 100 |
| 13 | 9.98 | 96 | 3.986 | 4.821 | 100 |

Figure 4 depicts the frequency dependence of the absolute value of the impedance for this MEAT. It was calculated with formula (17) in view of (13)–(15). The run of the curve depends primarily on the reactance $1/\omega C_\Sigma$ of the MEAT total capacitance. The active component makes the curve slightly oscillate. It follows from this figure that the optimal wave impedance in this case is $Z_{0,\,\mathrm{opt}} = 1.6$–$1.7\ \Omega$.

The frequency dependences of the acoustic power radiated by individual piezoelements in the sections are shown in Fig. 5. The calculations were performed with formula (16) and relationships (12)–(14). The power released in the matched termination was taken to be equal to $P_{al} = 1$ W and the ohmic loss resistance, $R_{\mathrm{loss}} = 0.1\ \Omega$. The figure at each of the curves is the number of an element for which the calculations were made. The acoustic power at the peaks is seen to roughly equal to 500 μW. Thus, a section with ≈100 elements radiates an acoustic power of ≈50 mW at the center frequency of the subband.

It should be noted that the curves have approximately equal half-power bandwidths for all sections. The fact that the curves approach each other with increasing frequency is explained by the narrowing of the self-tuning bandwidth because of an increase in the period, as follows from the curve in Fig. 1, and also by an increase in the slope of this curve. The calculated distribution of the radiated power over the elements is illustrated in Fig. 6 for three center frequencies (8.37, 9.36, and 9.84 GHz) of the subbands. It is seen that the acoustic signal at any of these frequencies comes largely from elements of one section. Sections immediately adjacent to the radiating section emit much weaker power. As the frequency grows, the MEAT

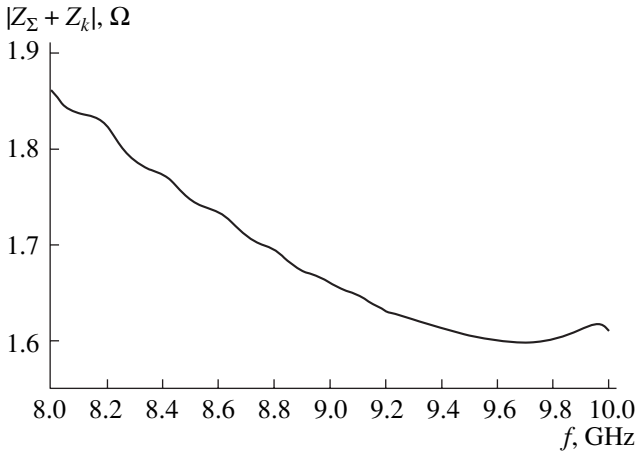


**Fig. 4.** MEAT impedance absolute value vs. frequency.

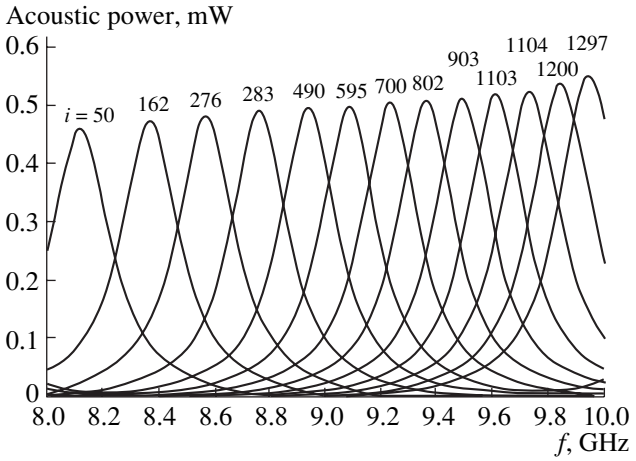


**Fig. 5.** Acoustic power radiated from individual piezoelements vs. frequency.

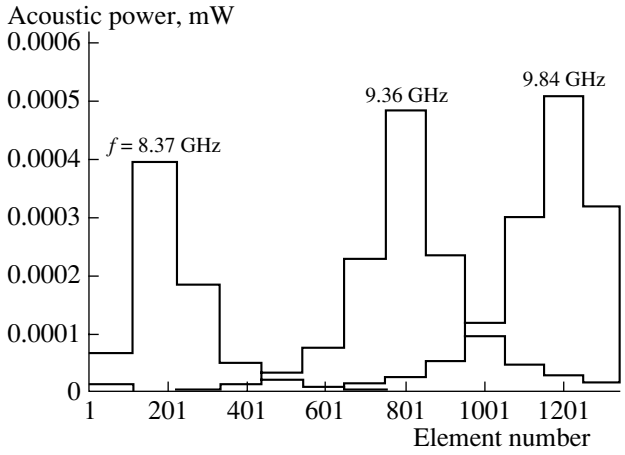


**Fig. 6.** Acoustic power per element vs. element number.

region exciting elastic waves moves toward greater element numbers.

## CONCLUSION

We discussed the principles of creating nonperiodic MEATs that provide self-tuning to the Bragg angle in acoustic devices. Relationships necessary for the analysis of the AO interaction efficiency as a function of frequency were derived for various nonperiodic MEATs with opposite-phase adjacent elements. Formulas for calculating the impedance of piezoelements with an arbitrary number of passive layers, including rear, acoustic, and absorbing loads, were obtained. These relationships, which are easily programmable on a computer, are of independent value, since they can be used in designing microwave piezoelectric transducers with desired properties. Among them are plate-like transducers, where several coupling layers are placed between the piezoelectric and the acoustic line. Formulas for calculating the acoustic power radiated from an MEAT element were deduced for the case when the elements or groups of the elements differ in frequency properties. The geometry of a 13-section wide-band MEAT with narrow-band elements that is designed for the operation in the short-wave part of the microwave range was demonstrated. The dependence of the radiated acoustic power on the frequency and on the element number was shown.

## REFERENCES

1. V. V. Petrov, Zh. Tekh. Fiz. **67** (11), 53 (1997) [Tech. Phys. **42**, 1289 (1997)].
2. V. V. Petrov, M. A. Grigor'ev, and A. V. Tolstikov, Opt. Spektrosk. **89**, 505 (2000) [Opt. Spectrosc. **89**, 463 (2000)].
3. A. Korpel, R. Adler, P. Desmares, and T. M. Smith, IEEE J. Quantum Electron. **QE-1** (1), 60 (1965).
4. E. I. Gordon, Proc. IEEE **54**, 1391 (1966).
5. G. A. Alphonse, RCA Rev. **33**, 543 (1972).
6. V. N. V'yukhin, Avtometriya, No. 1, 100 (1977).
7. M. A. Grigor'ev, Yu. A. Zyuryukin, V. V. Petrov, and A. V. Tolstikov, Izv. Vyssh. Uchebn. Zaved., Radiofiz. **25**, 948 (1982).
8. M. A. Grigor'ev, V. V. Petrov, and A. V. Tolstikov, Izv. Vyssh. Uchebn. Zaved., Radiofiz. **28**, 908 (1985).
9. M. A. Grigor'ev, V. V. Petrov, and A. V. Tolstikov, Izv. Vyssh. Uchebn. Zaved., Radiofiz. **28**, 1053 (1985).
10. I. A. Deryugin, A. P. Pogibel'skiĭ, M. A. Talalaev, and G. É. Teterin, Radiotekh. Élektron. (Moscow) **27**, 182 (1982).
11. Y. A. Zyuryukin, in *Proceedings of Ultrasonics World Congress, Duisburg, Germany, 1995*, Part 1, p. 297.
12. B. Guriev, Y. Zyuryukin, V. Colosov, and L. Shechtman, in *Proceedings of the International Conference on Optical Information Processing, Bellingham, Washington, 1996*; Proc. SPIE **2969**, 467 (1996).
13. Y. A. Zyuryukin, V. V. Colosov, S. V. Zavarin, and L. A. Shechtman, in *Proceedings of the IV International Symposium on Surface Waves in Solid and Layered Structures and International Conference for Young Researchers on Acoustoelectronic and Acoustooptic Information, State University of Aerospace Instrumentation, St. Petersburg, 1998*, p. 357.
14. M. A. Grigor'ev, V. V. Petrov, and A. V. Tolstikov, Radiotekh. Élektron. (Moscow) **35**, 1977 (1990).
15. M. A. Grigor'ev, S. S. Kuryshov, and A. V. Tolstikov, Akust. Zh. **36**, 255 (1990) [Sov. Phys. Acoust. **36**, 139 (1990)].

*Translated by V. Isaakyan*

*Technical Physics, Vol. 46, No. 10, 2001, pp. 1281–1290. Translated from Zhurnal Tekhnicheskoĭ Fiziki, Vol. 71, No. 10, 2001, pp. 77–86.*


**RADIOPHYSICS**

# The Effect of Bound States in Microwave Waveguides on Electromagnetic Wave Propagation

**E. N. Bulgakov* and A. F. Sadreev*, ****

** Institute of Physics, Siberian Division, Russian Academy of Sciences, Krasnoyarsk, 660036 Russia*

*** Department of Physics and Measurement Technology, Linköping University, S-581 83 Linköping, Sweden*

*e-mail: almas@tnp.krasn.ru, almsa@ifm.liu.se*

Received July 17, 2000

**Abstract**—The transmission of a *TE* microwave field with a frequency ω through Γ, *T*, and *X* waveguide junctions filled with a ferromagnetic is considered. These junctions are known to have bound states with below-cutoff frequencies. A probing microwave radiation with a frequency Ω applied to the scattering region generates magnetic oscillations with frequencies $\omega + n\Omega$ (where $n = 0, \pm1, \pm2, \ldots$), which resonantly combine with the bound waveguide states. This effect provides for a new method of studying bound waveguide states and efficiently controlling the transmission of microwave radiation. © *2001 MAIK "Nauka/Interperiodica".*

## INTRODUCTION

It is well-known [1] that *TE* electromagnetic waves propagating through a planar waveguide of constant width may be represented in terms of scalar potential $\Psi(x, y)$,

$$\mathbf{E}(x, y) = ik\hat{z}\Psi(x, y), \quad \mathbf{B}(x, y) = -\hat{z}\nabla\Psi, \qquad (1)$$

which satisfies the Helmholtz equation

$$[\nabla^2 + \omega^2]\Psi = 0 \qquad (2)$$

(where $\nabla$ is the Hamiltonian operator) with $\psi|_s = 0$ on the waveguide walls. The velocity of light is assumed to equal unity. Equation (2) coincides with the Schrödinger equation that describes ballistic electron transport in electron waveguides [2].

If the waveguide is curved (as shown in Fig. 1a), the Helmholtz equation has an additional bound solution (state) with a *TE* frequency below the cutoff frequency of the propagating *TE* waves: $\omega^2 < (\pi/d)^2$ [3], where *d* is the waveguide width. This bound state is localized near the waveguide bend. Such bound states, as particular solutions of Eq. (2), have been originally found for Γ waveguide junctions [4, 5] and *T* and *X* waveguide junctions [6, 7] (Figs. 1b–1d). These states are illustrated in Fig. 2. In [8, 9], the bound states were theoretically and experimentally studied as applied to *TE* modes in microwave Γ waveguides. When a probing radiation field was applied to the center of the waveguide bend, the reflected power of the microwave field propagating in the waveguide showed a resonant minimum from which the frequency of coupled electromagnetic oscillations was found [8]. The spatial field structure of localized bound states was also found. Different bound states have also been observed in dielectric waveguides artificially created in two-dimensional photon crystals [10].

However, these bound states by no means affect the propagation of *TE* waves in waveguides. Earlier [11, 12], we proposed a technique for combining bound states with ballistic transport of electrons in waveguides, using a radiation field with a frequency that is tuned to the resonance between the Fermi energy of electrons being transported and the energy of a

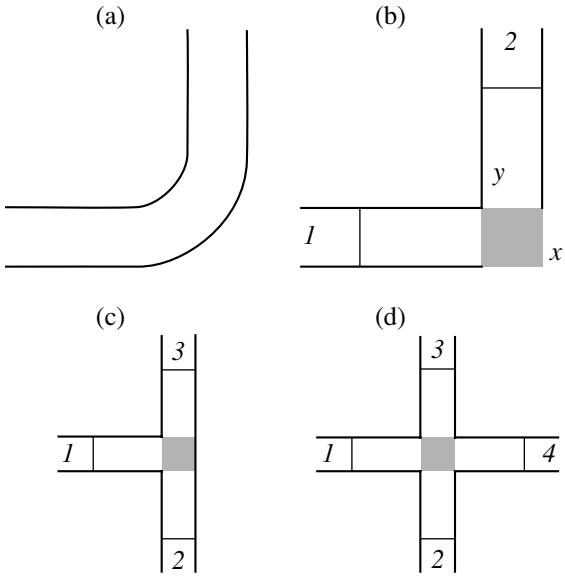


**Fig. 1.** Waveguide structures that support the bound states illustrated in Fig. 2. (a) Curved waveguide; (b) Γ, (c) *T*, and (d) *X* waveguide junctions. (*1–4*) Waveguide arms (shaded regions are those to which the probing field is applied).

1063-7842/01/4610-1281$21.00 

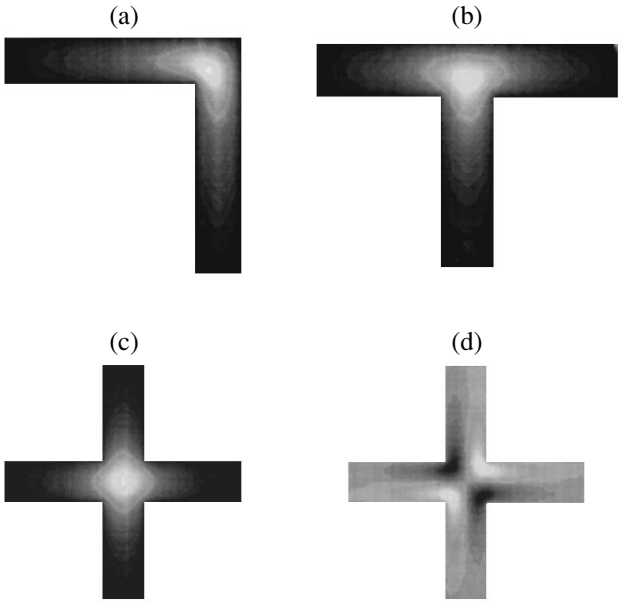


**Fig. 2.** Spatial structures of the electric field of the bound states in the waveguide junctions shown in Fig. 1.

bound state. As a result, a small-amplitude radiation field is capable of producing deep resonance dips in the waveguide transmittance. A similar approach is considered in this paper for *TE* waves propagating in Γ, *T*, and *X* waveguide junctions. However, in a linear medium, electromagnetic fields do not interact. Therefore, a medium is necessary that would cause such an interaction. In this paper, we consider a waveguide filled with a magnetically ordered material of magnetization *M*. Then, the interaction of the magnetic component of the probing field with the magnetic moment of the ferromagnetic will produce magnetic oscillations with frequencies $\omega + n\Omega$, where $n = 0, \pm1, \pm2, \ldots$ and $\Omega$ is the frequency of the probing field. If the frequency of one of these harmonics coincides with that of the coupled oscillations, one can expect resonance interaction between the *TE* wave traveling through the junction and the bound state of the waveguide. Thus, by tuning $\Omega$ to the resonance between the propagating microwave radiation and the coupled electromagnetic oscillations, one may observe resonance anomalies in the transmission of microwave radiation through curved waveguides. This resonance technique for controlling the transmission of microwave radiation and studying the bound states may also be of applied value.

## DYNAMICS OF THE MAGNETIZATION

The equation of motion for magnetic moment **M** in impressed electromagnetic fields [13] is written as

$$\frac{\partial \mathbf{M}}{\partial t} = g(\mathbf{M} \times (\mathbf{H}^{(m)} + \mathbf{H}^{(e)})), \qquad (3)$$

where $\mathbf{H}^{(e)}$ is the applied magnetic field consisting of the constant field $H_0$ and variable magnetic field of the probing radiation aligned with the *z* axis, and $\mathbf{H}^{(m)}$ is the magnetic component of the microwave field propagating in the waveguide ($\mathbf{H}^{(m)}$ lies in the *xy* plane).

It is convenient to introduce the complex amplitudes

$$M_\pm = M_x \pm iM_y, \quad H_\pm^{(m)} = H_x^{(m)} \pm iH_y^{(m)}, \qquad (4)$$

in terms of which Eq. (3) takes the form

$$\begin{aligned} \frac{\partial M_+}{\partial t} &= -igH^{(e)}M_+ + igM_zH_+^{(m)}, \\ \frac{\partial M_z}{\partial t} &= -\frac{1}{2}ig[H_+^{(m)}M_- - H_-^{(m)}M_+]. \end{aligned} \qquad (5)$$

For harmonic oscillations, $\xi_+ = M_+/M$ is small. Then,

$$M_z \approx M\left(1 - \frac{M_+M_-}{2M^2}\right) = M\left(1 - \frac{1}{2}|\xi_+|^2\right).$$

Accordingly, Eq. (5) can be written in the linear approximation as

$$\begin{aligned} i\frac{\partial \xi_+}{\partial t} &= gH^{(e)}\xi_+ - gH_+, \\ -\frac{1}{2}\frac{\partial |\xi_+|^2}{\partial t} &= g\,\mathrm{Im}(H_+^{(m)}\xi_-). \end{aligned} \qquad (6)$$

Let the probing microwave field have the simplest form, $H^{(e)}(\mathbf{r}, t) = H_0 + \lambda\cos\Omega t$, and be directed along the *z* axis. We assume that the alternating component of this field acts only in the waveguide region occupied by the bound state. Consider the amplitude $H_+^{(m)}(t) = H_+^{(0)}e^{i\omega t}$ that describes the field rotating counterclockwise with a circular frequency $\omega$ in the *xy* plane.

If the probing field is absent ($\lambda = 0$), the coupling between magnetization oscillations $\xi_+(t) = \xi_+^{(0)}e^{i\omega t}$ and the microwave field propagating in the waveguide is expressed in terms of the susceptibility [13] as $\xi_+^{(0)} = \chi(\omega)H_+^{(0)}$, where

$$\chi(\omega) = \frac{g}{\omega + gH_0}. \qquad (7)$$

In general, when $\lambda \neq 0$, we substitute $\xi_+(t) = \xi_+^{(1)}e^{i\omega t}$ into Eqs. (6) to obtain

$$i\frac{\partial \xi_+^{(1)}(t)}{\partial t} = (\omega + gH_0 + g\lambda\cos\Omega t)\xi_+^{(1)}(t) - gH_+^{(0)}. \qquad (8)$$

A solution to Eq. (8) can be sought in the form

$$\xi_+^{(1)}(t) = F(t)\exp\left[-i(\omega + gH_0)t - i\frac{g\lambda}{\Omega}\sin\Omega t\right].$$

Substituting it into Eq. (8) yields

$$F(t) = F_0 + igH_+^{(0)} \times \int \exp\left[i(\omega + gH_0)\tau + i\frac{g\lambda}{\Omega}\sin\Omega\tau\right]d\tau. \quad (9)$$

Since we consider forced oscillations, $F_0 = 0$. Therefore, the solution to Eq. (8) can again be represented in terms of susceptibility $\chi(t)$, which is now a periodic function of time:

$$\xi_+^{(1)}(t) = \chi_+(t)H_+^{(0)},$$

$$\chi_+(t) = ig\exp\left[-i(\omega + gH_0)t - i\frac{g\lambda}{\Omega}\sin\Omega t\right] \times \int \exp\left[i(\omega + gH_0)\tau + i\frac{g\lambda}{\Omega}\sin\Omega\tau\right]d\tau \quad (10)$$

$$= g\exp\left(-i\frac{g\lambda}{\Omega}\sin\Omega t\right)\sum_m \frac{J_m\left(\frac{g\lambda}{\Omega}\right)}{\omega + gH_0 + m\Omega}\exp(im\Omega t).$$

As follows from (10), the susceptibility $\chi_+(t)$ is a periodic function of time, with its period being equal to that of the applied probing field. Therefore, the solutions for the probing field and the magnetization have the form of a superposition of *TE* modes of different circular polarizations with frequencies $\omega + n\Omega$, where $n = 0, \pm1, \pm2, \ldots$:

$$H_+(t) = \sum_n \{h_n e^{i(\omega + n\Omega)t} + \tilde{h}_n e^{-i(\omega + n\Omega)t}\},$$
$$\xi_+(t) = \sum_n \{\xi_n(t)e^{i(\omega + n\Omega)t} + \tilde{\xi}_n(t)e^{-i(\omega + n\Omega)t}\}. \quad (11)$$

Then

$$\xi_n(t) = \xi_{(+)n}(t)h_n, \quad \tilde{\xi}_n(t) = \chi_{(-)n}(t)\tilde{h}_n,$$

where $\chi_{(\pm)n}(t)$ is the response of magnetic system (10) to the magnetic field rotating with a frequency $\omega + n\Omega$ counter- or clockwise (the plus and minus subscripts, respectively).

As follows from (10), the susceptibility $\chi_{(\pm)n}(t)$ has the period $2\pi/\Omega$. Therefore, we represent it as a Fourier series over this period:

$$\chi_{(+)n}(t)e^{in\Omega t} = \sum_m \chi_{(+)nm}e^{im\Omega t},$$
$$\chi_{(-)n}(t)e^{-in\Omega t} = \sum_m \chi_{(-)nm}e^{-im\Omega t}, \quad (12)$$

where

$$\chi_{(+)nm} = \frac{\Omega}{2\pi}\int_0^{2\pi/\Omega} \chi_{(+)n}(t)e^{i(n-m)\Omega t},$$
$$\chi_{(-)nm} = \frac{\Omega}{2\pi}\int_0^{2\pi/\Omega} \chi_{(-)n}(t)e^{-i(n-m)\Omega t}. \quad (13)$$

The best way to calculate $\chi_{(\pm)nm}$ is to make advantage of the fact that, as follows from Eqs. (8) and (10), $\chi_{+n}(t)$ satisfy the equations

$$i\frac{d\chi_{(+)n}}{dt} = (\omega + n\Omega + gH_0 + g\lambda\cos\Omega t)\chi_{(+)n} - g,$$
$$i\frac{d\chi_{(-)n}}{dt} = (gH_0 - \omega - n\Omega + g\lambda\cos\Omega t)\chi_{(-)n} - g. \quad (14)$$

Substituting expansions (12) into Eqs. (14), we arrive at the system of algebraic equations for $\chi_{(+)nm}$:

$$\frac{\lambda}{2}\chi_{(+)n,\,m-1} + (H_0 + \omega/g + m\Omega/g)\chi_{(+)nm} + \frac{\lambda}{2}\chi_{(+)n,\,m-1} = \delta_{nm},$$
$$\frac{\lambda}{2}\chi_{(-)n,\,m-1} + (H_0 - \omega/g - m\Omega/g)\chi_{(-)nm} + \frac{\lambda}{2}\chi_{(-)n,\,m+1} = \delta_{nm}. \quad (15)$$

## EQUATIONS FOR ELECTROMAGNETIC FIELDS

Let us write the Maxwell equations in a magnetic medium:

$$\mathbf{B}^{(m)} = \mathbf{H}^{(m)} + 4\pi\mathbf{M}, \quad \nabla\times\mathbf{E} = -\frac{\partial\mathbf{B}^{(m)}}{\partial t},$$
$$\nabla\times\mathbf{H}^{(m)} = 4\pi\mathbf{j} + \frac{\partial\mathbf{E}}{\partial t}, \quad \nabla\mathbf{B}^{(m)} = 0, \quad \nabla\mathbf{E} = 0. \quad (16)$$

Solutions to (16) in view of (11) will be sought such that the electric field is directed along the $z$ axis, the magnetic field $\mathbf{H}^{(m)}$ lies in the $xy$ plane, and both fields are functions of $x$ and $y$. We represent $E_z$ in terms of complex fields $\Psi_n$ as

$$E_z(x, y, t) = \mathrm{Im}\left[\sum_n \Psi_n(x, y)e^{i(\omega + n\Omega)t}\right]. \quad (17)$$

It is convenient to introduce the Cauchy derivative

$$\frac{\partial}{\partial u} = \frac{1}{2}\left(\frac{\partial}{\partial x} - i\frac{\partial}{\partial y}\right),$$

with which the following useful relationships can be written:

$$(\nabla\times\mathbf{M})_z = 2M\mathrm{Im}\left(\frac{\partial\xi_+}{\partial u}\right) = 2M\mathrm{Re}\left(-i\frac{\partial\xi_+}{\partial u}\right),$$

$$\nabla\mathbf{M} = 2\mathrm{Re}\left(\frac{\partial\xi_+}{\partial u}\right),$$

$$(\nabla\times\mathbf{H}^{(m)})_z = 2\mathrm{Im}\left(\frac{\partial H_+^{(m)}}{\partial u}\right) = 2\mathrm{Re}\left(-i\frac{\partial H_+^{(m)}}{\partial u}\right), \quad (18)$$

$$\nabla\mathbf{H}^{(m)} = \mathrm{Re}\left(\frac{\partial H_+^{(m)}}{\partial u}\right).$$

It is also useful to reduce Maxwell equations (16) to the second-order differential equations

$$\nabla\times\nabla\times\mathbf{E} = -\frac{\partial\nabla\times\mathbf{B}^{(m)}}{\partial t},$$

$$\nabla\times(\mathbf{B}^{(m)} - 4\pi\mathbf{M}) = 4\pi\mathbf{j} + \frac{\partial\mathbf{E}}{\partial t},$$

from which one more equation follows:

$$\nabla\times\nabla\times\mathbf{E} = -4\pi\frac{\partial\mathbf{j}}{\partial t} - 4\pi\nabla\times\frac{\partial\mathbf{M}}{\partial t} - \frac{\partial^2\mathbf{E}}{\partial t^2}.$$

Since the impressed current is zero ($\mathbf{j} = 0$), we have

$$\nabla^2\mathbf{E} - \frac{\partial^2\mathbf{E}}{\partial t^2} - 4\pi\nabla\times\frac{\partial\mathbf{M}}{\partial t} = 0. \quad (19)$$

Next, we combine the equation $\nabla(\mathbf{H}^{(m)} + 4\pi\mathbf{M}) = 0$ and (18) to obtain

$$\mathrm{Re}\left(\frac{\partial H_+^{(m)}}{\partial u} + 4\pi M\frac{\partial\xi_+}{\partial u}\right) = 0.$$

Substituting representation (11) for $H_+$ and $\xi_+$ into this formula, we come to

$$\mathrm{Re}\sum_n\left\{\mu_{(+)n}(t)\frac{\partial h_n}{\partial u}e^{i(\omega+n\Omega)t} + \mu_{(-)n}(t)\frac{\partial\tilde{h}_n}{\partial u}e^{-i(\omega+n\Omega)t}\right\} = 0, \quad (20)$$

where

$$\mu_{(\pm)n}(t) = 1 + 4\pi M\chi_{(\pm)n}(t),$$
$$\mu_{(\pm)nm} = \delta_{nm} + 4\pi M\chi_{(\pm)nm} \quad (21)$$

is the permeability.

From expansions (12),

$$\mathrm{Re}\left\{\sum_{nm}\left[\frac{\partial h_n}{\partial u}e^{i(\omega+n\Omega)t}\mu_{(+)nm} + \frac{\partial\tilde{h}_n}{\partial u}e^{-i(\omega+m\Omega)t}\mu_{(-)nm}\right]\right\} = 0,$$

hence,

$$\sum_n\frac{\partial h_n}{\partial u}\mu_{(+)nm} = -\sum_n\left(\frac{\partial\tilde{h}_n}{\partial u}\right)^*\mu^*_{(-)nm}. \quad (22)$$

Now consider the second Maxwell equation

$$\frac{\partial E_z}{\partial t} = 2\mathrm{Im}\left(\frac{\partial H_+}{\partial u}\right).$$

With Eqs. (11) and (17), we obtain

$$\sum_n\mathrm{Im}\left\{e^{i(\omega+n\Omega)t}\left[i(\omega+n\Omega)\Psi_n - 2\left(\frac{\partial h_n}{\partial u}\right)\right] - 2\left(\frac{\partial\tilde{h}_n}{\partial u}\right)e^{-i(\omega+n\Omega)t}\right\} = 0$$

or

$$i(\omega+n\Omega)\Psi_n - 2\left(\frac{\partial h_n}{\partial u}\right) = -2\left(\frac{\partial\tilde{h}_n}{\partial u}\right)^*. \quad (23)$$

Substituting this equation into (22), we have

$$\frac{1}{2}\sum_n\left(\frac{\partial h_n}{\partial u}\right)[\mu_{(+)nm} + \mu^*_{(-)nm}] = \frac{i}{4}\sum_n\mu^*_{(-)nm}(\omega+n\Omega)\Psi_n. \quad (24)$$

Formula (24) is a system of linear algebraic equations that relates $\partial h_n/\partial u$ and $\Psi_n$:

$$\frac{\partial\mathbf{h}}{\partial u} = \hat{A}\boldsymbol{\Psi}, \quad (25)$$

where $\mathbf{h} = (\ldots h_1, h_0, h_{-1}, \ldots)$ and $\boldsymbol{\Psi} = (\ldots\Psi_1, \Psi_0, \Psi_{-1}, \ldots)$.

Relationship (24) allows us to write a closed equation for $\Psi_n$. In fact, in view of Eqs. (18), Eq. (19) takes the form

$$\nabla^2E_z - \frac{\partial^2E_z}{\partial t^2} - 8\pi M\frac{\partial}{\partial t}\mathrm{Im}\frac{\partial\xi_+}{\partial u} = 0. \quad (26)$$

As follows from (11),

$$\frac{\partial \xi_+}{\partial u} = \sum_{nm}\left\{e^{i(\omega + n\Omega)t}\chi_{(+)nm}\left(\frac{\partial h_n}{\partial u}\right) + e^{-i(\omega + n\Omega)t}\chi_{(-)nm}\left(\frac{\partial \tilde{h}_n}{\partial u}\right)\right\}.$$

Substituting this relationship into (26), we obtain, in view of (17),

$$\mathrm{Im}\sum_{nm}\left\{e^{i(\omega + n\Omega)t}\left[\delta_{nm}(\nabla^2\Psi_m + (\omega + n\Omega)^2\Psi_m) - 8\pi M i(\omega + m\Omega)\chi_{(+)nm}\left(\frac{\partial h_n}{\partial u}\right)\right] + 8\pi M i e^{-i(\omega + n\Omega)t}(\omega + m\Omega)\chi_{(-)nm}\left(\frac{\partial \tilde{h}_n}{\partial u}\right)\right\} = 0$$

or

$$\nabla^2\Psi_m + (\omega + m\Omega)^2\Psi_m + 8\pi M i\sum_n(\omega + m\Omega) \times\left[\chi^*_{(-)nm}\left(\frac{\partial \tilde{h}_n}{\partial u}\right)^* - \chi_{(+)nm}\left(\frac{\partial h_n}{\partial u}\right)\right] = 0.$$

With the expression for $(\partial\tilde{h}_n/\partial u)^*$ from (23), we eventually derive the closed equation for $\Psi_n$:

$$\nabla^2\Psi_m + (\omega + m\Omega)^2\Psi_m + 4\pi M\sum_n(\omega + m\Omega) \times(\omega + n\Omega)\chi^*_{(-)nm}\Psi_n - 8\pi M i\sum_n(\omega + m\Omega) \times\left(\frac{\partial h_n}{\partial u}\right)(\chi_{(+)nm} - \chi^*_{(-)nm}) = 0, \quad (27)$$

where the derivatives $(\partial h_n/\partial u)$ are defined through $\Psi_n$ by Eq. (25).

Let us check that, in the limit $\lambda \longrightarrow 0$, Eq. (27) describes the well-known problem of microwave propagation through a magnetic medium [14]. As follows from (10) and (13), the susceptibility matrix is diagonal:

$$\chi_{(+)nn} = \frac{g}{gH_0 + \omega + n\Omega}, \quad \chi_{(-)nm} = \frac{g}{gH_0 - \omega - n\Omega}.$$

Accordingly, Eqs. (24) and (27) take the form

$$\frac{1}{2}\left(\frac{\partial h_m}{\partial u}\right)[\mu_{(+)m} + \mu^*_{(-)m}] = \frac{i}{4}\mu^*_{(-)m}(\omega + m\Omega)\Psi_m,$$

$$\nabla^2\Psi_m + (\omega + m\Omega)^2\mu_{(-)m}\Psi_m - 2i(\omega + m\Omega)(\mu_{(+)m} - \mu_{(-)m})\left(\frac{\partial h_m}{\partial u}\right) = 0,$$

where

$$\mu_{(\pm)m} = 1 + 4\pi M\chi_{(\pm)mm}.$$

Combining the last two equations, we obtain the equation given in [14]:

$$\nabla^2\Psi_m + (\omega + m\Omega)^2\frac{\mu^2 - \mu_a^2}{\mu}\Psi_m = 0, \quad (28)$$

where $\mu_{(\pm)m} = \mu \pm \mu_a$.

Let us turn back to the case when a waveguide is filled with a magnetic and is subjected to a local radiation field with a frequency $\Omega$. Consider the simplest spatial inhomogeneity in the probing field when it is uniform in the region of the bound state and vanishes outside. In order to derive the boundary conditions at the interface, we invoke one more Maxwell equation

$$-\frac{\partial B_x}{\partial t} = \frac{\partial E_z}{\partial y}, \quad \frac{\partial B_y}{\partial t} = \frac{\partial E_z}{\partial x}, \quad (29)$$

where the magnetic induction can also be represented as a series in $h_m$ and $\tilde{h}_m$ by virtue of (11).

Substituting these series for the magnetic induction $B_+$ and expansion (17) of the electric field $E_z$ in $\Psi_n(x, y)$ into Eqs. (29) yields the equations

$$\frac{\partial \Psi_n}{\partial y} = (\omega + n\Omega)\sum_m(\mu_{(+)mn}h_m + \mu^*_{(-)mn}\tilde{h}^*_m), \quad (30)$$

$$\frac{\partial \Psi_n}{\partial x} = i(\omega + n\Omega)\sum_m(\mu_{(+)mn}h_m + \mu^*_{(-)mn}\tilde{h}^*_m), \quad (31)$$

where the matrix $\mu$ is defined by Eqs. (21).

From these two equations, one readily deduces the expressions for Cauchy's derivatives:

$$\frac{\partial \Psi_n}{\partial u} = -i(\omega + n\Omega)\sum_m\mu^*_{(-)mn}\tilde{h}^*_m,$$
$$\frac{\partial \Psi_n}{\partial u^*} = i(\omega + n\Omega)\sum_m\mu_{(+)mn}h_m. \quad (32)$$

Equation (22), which follows from the equation $\nabla\mathbf{B} = 0$ (where $B$ is the scalar product), can be extended to the nonuniform case as follows:

$$\sum_n\left\{\frac{\partial h_n}{\partial u}\mu_{(+)nm} + \frac{\partial \mu_{(+)nm}}{\partial u}h_n\right\} = -\sum_n\left\{\left(\frac{\partial \tilde{h}_n}{\partial u}\right)^*\mu^*_{(-)nm} + \frac{\partial \mu^*_{(-)nm}}{\partial u^*}\tilde{h}^*_n\right\}. \quad (33)$$

If the medium is inhomogeneous along the $x$ axis, Eq. (33) can be used to show that the jumps at the inter-

face satisfy the equation

$$\Delta\left\{\sum_n h_n \mu_{(+)nm}\right\} = -\Delta\left\{\sum_n \tilde{h}_n^* \mu^*_{(-)nm}\right\}$$

or, by virtue of Eqs. (32),

$$\Delta\left\{\frac{\partial \Psi_n}{\partial u}\right\} = \Delta\left\{\frac{\partial \Psi_n}{\partial u^*}\right\}. \quad (34)$$

Equation (23), which follows from the third Maxwell equation in (16), is satisfied everywhere:

$$\left(\frac{\partial \tilde{h}_n}{\partial u}\right)^* = \frac{\partial h_n}{\partial u} - \frac{i}{2}(\omega + n\Omega)\Psi_n. \quad (35)$$

The electric field must be continuous at the interface. Otherwise, as follows from (32), the fields $h_m$ would be singular. Hence, Eq. (35) gives one more boundary condition:

$$\Delta \tilde{h}_m^* = \Delta h_m. \quad (36)$$

If the interface is perpendicular to the $y$ axis, Eqs. (32), (33), and (35) yield the similar boundary conditions

$$\Delta\left\{\frac{\partial \Psi_n}{\partial u}\right\} = -\Delta\left\{\frac{\partial \Psi_n}{\partial u^*}\right\}, \quad \Delta \tilde{h}_n^* = -\Delta h_m. \quad (37)$$

It is convenient to represent the equation for the generalized vector $\mathbf{\Psi}$ in the matrix form:

$$\frac{\partial \mathbf{\Psi}}{\partial u} = \hat{L}_- \tilde{\mathbf{h}}^*, \quad \frac{\partial \mathbf{\Psi}}{\partial u^*} = \hat{L}_+ \mathbf{h}, \quad (38)$$

where

$$\hat{L}_{(-)nm} = -(\omega + n\Omega)\mu^*_{(-)mn}, \quad \hat{L}_{(+)nm} = i(\omega + n\Omega)\mu_{(+)mn}. \quad (39)$$

Then, Eqs. (24) and (27) take the more compact form

$$(\hat{\mathbf{L}}_+ - \hat{\mathbf{L}}_-)\frac{d\mathbf{h}}{\partial u} = -\frac{1}{2}\hat{\mathbf{L}}_-\hat{\mathbf{P}}\mathbf{\Psi}, \quad (40)$$

$$\nabla^2\mathbf{\Psi} + \hat{\mathbf{L}}_-\hat{\mathbf{P}}\mathbf{\Psi} - 2(\hat{\mathbf{L}}_+ + \hat{\mathbf{L}}_-)\frac{d\mathbf{h}}{\partial u} = 0, \quad (41)$$

respectively, where

$$\hat{\mathbf{P}} = i\,\mathrm{diag}(\omega + n\Omega).$$

Combining Eqs. (40) and (41) gives the closed equation for $\Psi$:

$$\nabla^2\mathbf{\Psi} + \hat{\mathbf{L}}_-\hat{\mathbf{P}}\mathbf{\Psi} + (\hat{\mathbf{L}}_+ + \hat{\mathbf{L}}_-)(\hat{\mathbf{L}}_+ - \hat{\mathbf{L}}_-)^{-1}\hat{\mathbf{L}}_-\hat{\mathbf{P}}\mathbf{\Psi} = 0. \quad (42)$$

Using the matrix

$$\hat{\mathbf{D}} = (\hat{\mathbf{L}}_-^{-1} - \hat{\mathbf{L}}_+^{-1})\{(\hat{\mathbf{L}}_-\hat{\mathbf{P}} + (\hat{\mathbf{L}}_+ + \hat{\mathbf{L}}_-)(\hat{\mathbf{L}}_+ - \hat{\mathbf{L}}_-)^{-1}\hat{\mathbf{L}}_-)\hat{\mathbf{P}}\}$$

and the equality

$$(\hat{\mathbf{L}}_-^{-1} - \hat{\mathbf{L}}_+^{-1})\hat{\Delta} = 4\frac{\partial}{\partial u^*}\hat{\mathbf{L}}_-^{-1}\frac{\partial \mathbf{\Psi}}{\partial u} - 4\frac{\partial}{\partial u}\hat{\mathbf{L}}_+^{-1}\frac{\partial \mathbf{\Psi}}{\partial u^*},$$

we rewrite Eq. (42) as

$$4\frac{\partial}{\partial u^*}\hat{\mathbf{L}}_-^{-1}\frac{\partial \mathbf{\Psi}}{\partial u} - 4\frac{\partial}{\partial u}\hat{\mathbf{L}}_+^{-1}\frac{\partial \mathbf{\Psi}}{\partial u^*} + \hat{\mathbf{D}}\mathbf{\Psi} = 0. \quad (43)$$

In this case, boundary conditions (34) and (36) take the form

$$\Delta\left\{\hat{\mathbf{L}}_-^{-1}\frac{\partial \mathbf{\Psi}}{\partial u} - \hat{\mathbf{L}}_+^{-1}\frac{\partial \mathbf{\Psi}}{\partial u^*}\right\} = 0, \quad \Delta\frac{\partial \mathbf{\Psi}}{\partial u} = \Delta\frac{\partial \mathbf{\Psi}}{\partial u^*}. \quad (44)$$

For the interface orthogonal to the $x$ axis, the latter boundary condition means that $\partial\Psi/\partial y$ is continuous at the interface; hence, it is satisfied automatically. The former boundary condition in (44) is easily taken into account in Eq. (43), which also includes the interface where $\hat{\mathbf{L}}_\pm$ exhibits a jump. It can easily be checked that Eq. (43) is also consistent with boundary conditions (37) for the interface orthogonal to the $y$ axis. This conclusion is important, because it allows us to solve Eq. (43) everywhere, including the interfaces at which $\hat{\mathbf{L}}_\pm$ is discontinuous.

## Γ, *T*, AND *X* WAVEGUIDE JUNCTIONS

Consider Γ, *T*, and *X* waveguide junctions with the interfaces shown in Fig. 1. The shaded regions are those to which the probing field $\lambda\cos\Omega t$ is applied. We assume that the probing radiation is weak and its magnetic field crosses the two-dimensional waveguide orthogonally, i.e., along the $z$ axis. In our calculations, we will use the following values typical of ferromagnetic materials: $M = 1700$ G and $g = 2 \times 10^7$ CGS. Let us introduce the dimensionless quantities

$$\tilde{\mathbf{r}} = \mathbf{r}/d, \quad \tilde{\omega} = d\omega/c, \quad \tilde{\Omega} = d\Omega/c, \quad \tilde{H}_0 = gH_0 d/c, \quad \tilde{\lambda} = g\lambda d/c, \quad m = gMd/c, \quad (45)$$

where $c$ is the velocity of light.

When the probing field is absent, the equation for the microwave field in terms of the dimensionless quantities takes the form

$$\nabla^2\Psi + k^2\Psi = 0, \quad k^2 = \tilde{\omega}^2\frac{2\mu_+\mu_-}{\mu_+ + \mu_-}, \quad (46)$$

$$\mu_{\pm} = 1 + 4\pi\frac{m}{\tilde{H}_0 \pm \tilde{\omega}}.$$

For a typical centimeter-wave waveguide with the width $d = 1$ cm subjected to a constant magnetic field $H_0 = 1000$, formulas (45) yield $m \approx 1$, $\tilde{H}_0 \sim 1$, $\omega = 3 \times 10^{10}$ s$^{-1}$, and $\tilde{\omega} \sim 1$.

## NUMERICAL SOLUTIONS

Our numerical analysis of the scattering of an incident microwave radiation in a magnetic-filled waveguide relies on system (43) of second-order linear differential equations for amplitudes $\{\Psi_n\}$. The boundary conditions specify the asymptotic behavior of the electromagnetic waves far away from the scattering region (waveguide diffraction conditions). A typical scattering scenario considers an incident wave only in one arm of the waveguide junction that will referred to as the first one. The scattered field penetrates into all the waveguide arms.

System (43) was numerically solved on a square mesh, which is natural for the waveguide junctions under study (Fig. 1). Since the probing radiation field is applied only to the region of scattering (the shaded region in Fig. 1), the operator $\hat{L}_{\pm}$ is no longer diagonal in this region, and the propagating microwave field mixes with coupled electromagnetic oscillations in the waveguide structure. In the waveguide arms (i.e., far from the scattering region), Eq. (43) is the Helmholtz equation and describes *TE* waves with frequencies $\omega + n\Omega$ in a perfect ferromagnetic [see Eq. (28)]. The waveguide diffraction problem is solved by joining a solution to Eq. (43) in the scattering region and all *TE* waves outside it. The problem is almost the same as that of ballistic electron transport in electron waveguides. The basis for the numerical solution of this problem in the steady-state case was set by Ando [15]. A generalization to the dynamic problem of electron scattering was given in our previous paper [12].

Let us define the transmission coefficient $T_{ij}$ as the ratio of the output power in the $i$th waveguide arm to the input power in the $j$th waveguide arm, where $i$ and $j$ are the respective numbers of the input and output arms. Clearly, if there is no probing field,

$$1 + G = \sum_j T_{ij} = 1,$$

as follows from the energy conservation law.

However, when the probing field is applied, the electromagnetic power may be derived (or transmitted) as the microwave field passes through the junction. Thus, $G$ defines the absorbed power of the probing field.

The power can be calculated in terms of the Poynting vector

$$\mathbf{\Pi} = \frac{c}{4\pi}\mathbf{E} \times \mathbf{H}.$$

With representations (11) and (17), this equation yields after time averaging

$$\bar{\Pi}_x = \frac{c}{8\pi}\mathrm{Re}\sum_m \{\Psi_m \tilde{h}_m - \Psi_m^* h_m\},$$
$$\bar{\Pi}_y = \frac{c}{8\pi}\mathrm{Im}\sum_m \{\Psi_m \tilde{h}_m - \Psi_m^* h_m\}. \quad (47)$$

Figure 3 shows the resonant distribution of the powers $\bar{\Pi}$ for all the waveguide junctions considered above. It is clearly seen that the resonant mixing of the localized bound states causes the vortex structure of the power fluxes. The lower right panel in Fig. 3 demonstrates how the nodal lines of the second bound state of the *X* junction affect the power-flux pattern. These effects were also considered for ballistic electron transport through electron waveguides [12].

In order to find the power flux of the microwave field in the waveguide arms (outside the scattering region), we represent $h_m$ in terms of $\Psi_m$ using Eq. (38). Consider waveguide arm *1* (Fig. 1) to be the input and integrating over its cross section of unit width, we obtain the time-averaged power from (47) as

$$W_1 = -\frac{icL}{16\pi}\sum_m \left\{([\hat{L}_+]_m^{-1} - [\hat{L}_-]_m^{-1})\mathrm{Im}\left(\Psi_m^*\frac{\partial \Psi_m}{\partial x}\right)\right\}. \quad (48)$$

The power flux in the other waveguide arms are calculated likewise. As a result, we find the transmission coefficients

$$T_{ij} = W_j/W_i.$$

Figures 4a and 4c plot the frequency dependences of the transmission coefficient for the *TE* wave passing through the $\Gamma$ waveguide junction when the frequency of the probing field is $\tilde{\Omega} = 0.4$. The thin lines refer to the zero probing field. These figures clearly show the resonant transmission of the *TE* wave at $\tilde{\omega} = 1.204$. Accordingly, the frequency of the bound electromagnetic oscillations in the $\Gamma$ junction is $\tilde{\omega}_b = \tilde{\omega} - \tilde{\Omega} = 0.804$. At $\tilde{H}_0 = 1$, $m = 1$, and the frequency of the bound oscillations $\tilde{\omega}_b = 0.804$, formulas (45) yield $k_b^2 = 0.92$, which is close to the theoretical value $0.9291\pi^2$ for a $\Gamma$ junction [4]. The bandwidth of the resonance dip in the transmission coefficient $T_{12}$ is proportional to the probing field amplitude squared, as naturally follows from the dynamic perturbation theory.

Figure 4b plots the absorbed power of the microwave field versus frequency. It is seen that absorbed power (48) exhibits the resonant behavior due to the dynamic addition of the bound state. Note that, at certain frequencies of the probing field, the absorbed power exceeds unity. This means that, when passing through the scattering region, the microwave field takes

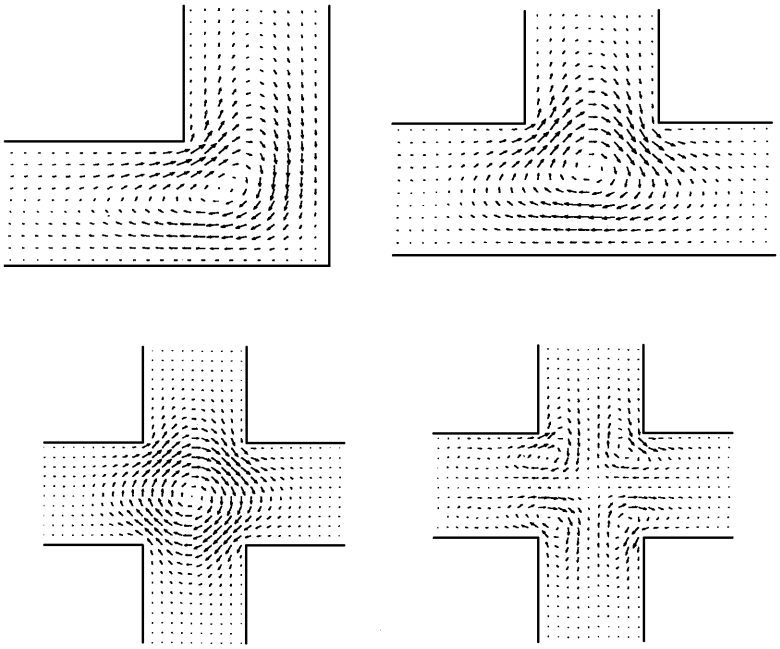

**Fig. 3.** Fluxes of the electromagnetic field power in the case of the resonance addition of the localized states. The lower right panel illustrates the addition of the second bound state to the *X* junction, which is antisymmetric with respect to the $x \longrightarrow -x$ and $y \longrightarrow -y$ reversals.

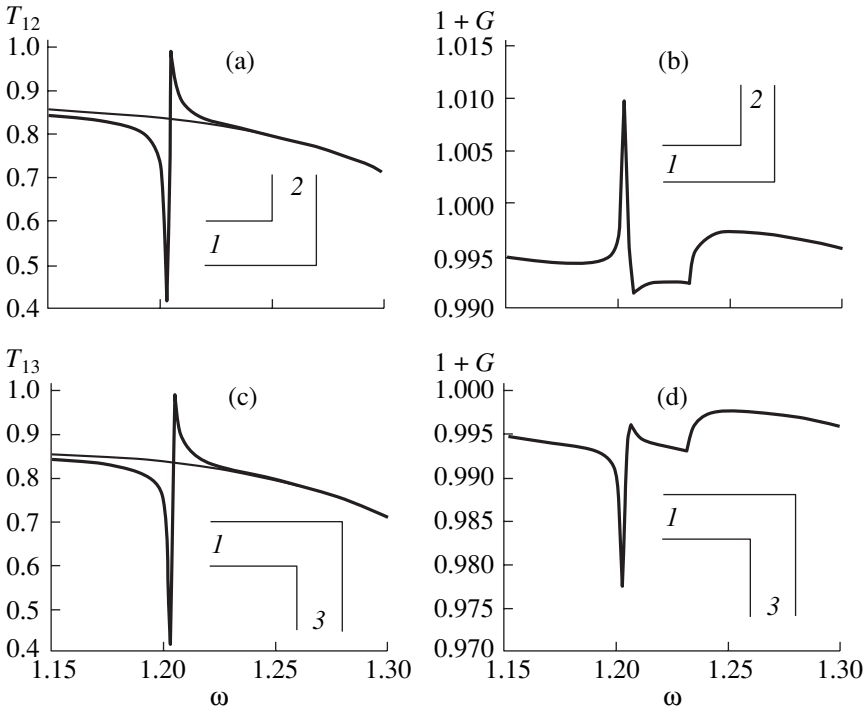


**Fig. 4.** Coefficient of the *TE* mode ($n = 1$) transmission through the Γ junction and the absorbed power *G* versus frequency at $\tilde{H}_0 = 1$ and $m = 1$. Thick line, resonance probing field with $\lambda = 0.1$; thin line, no probing field.

a small portion of the power of the probing radiation. Figures 4c and 4d refer to a Γ junction that guides the microwave field in the direction opposite to that considered in Figs. 4a and 4b. The Poynting vector is not invariant under the $y \longrightarrow -y$ reversal. Therefore, as follows from Figs. 4b and 4d, the frequency behavior of the absorbed power depends on the direction the output arm of the Γ junction. Accordingly, the transmission

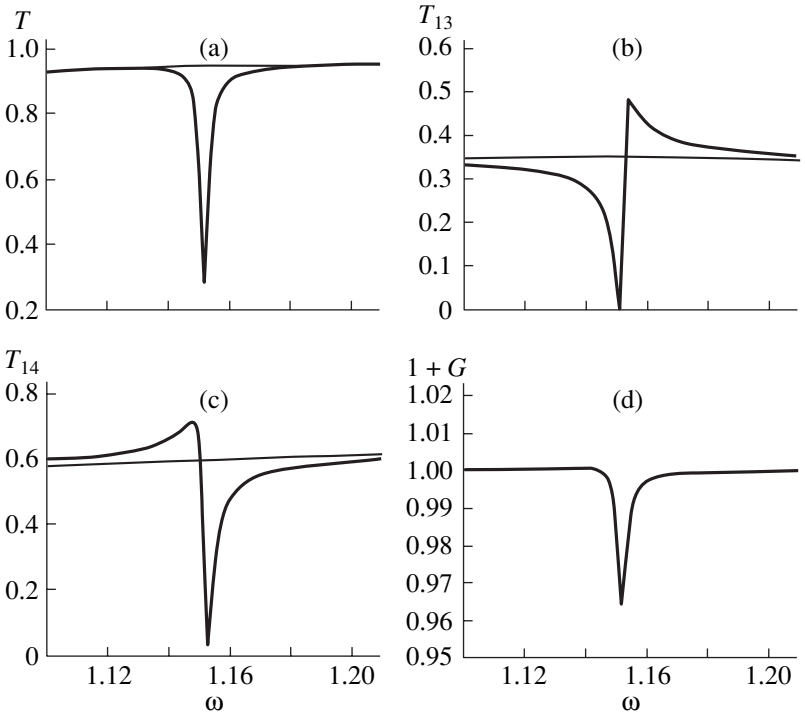


**Fig. 5.** Same as in Fig. 4 for the *T* junction at $\tilde{H}_0 = 1$, $m = 1$, $\tilde{\Omega} = 0.4$, and $\lambda$ = (thin line) 0 and (thick line) 0.2. (a) Total transmission coefficient; (b, c) coefficients of transmission to waveguide arms *3* and *4*, respectively; and (d) coefficient of probing radiation absorption.

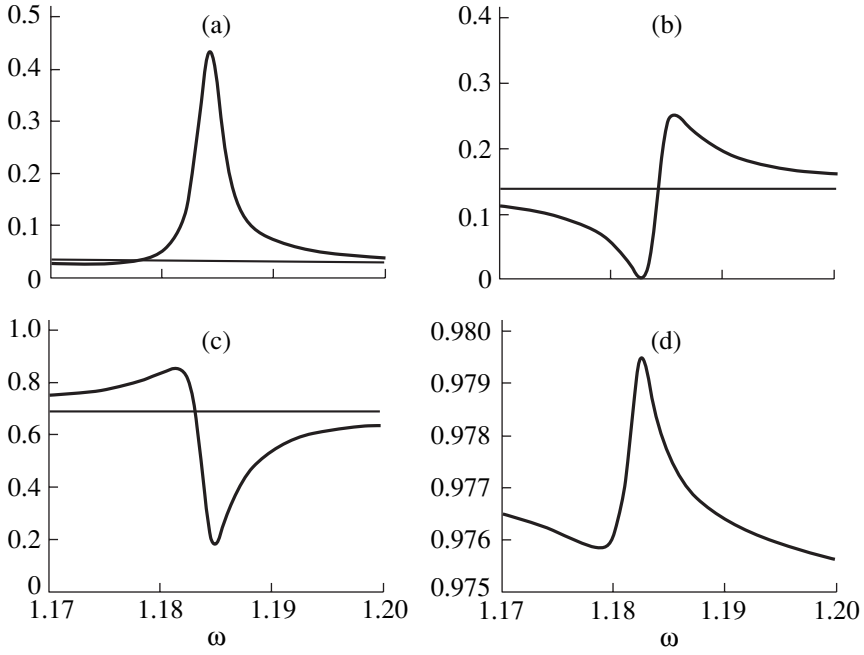


**Fig. 6.** Same as in Fig. 4 for the *X* junction at $\tilde{H}_0 = 1$, $m = 1$, $\tilde{\Omega} = 0.5$, and $\lambda$ = (thin line) 0 and (thick line) 0.2. (a) Reflection coefficient; (b, c) coefficients of transmission to waveguide arms *2*(*3*) and *4*, respectively; and (d) coefficient of probing radiation absorption. The probing field is tuned to excite the fundamental bound state of the electromagnetic field in the structure.

coefficients, which are defined as the output-to-input microwave power ratio, are also not invariant. The difference in the absorbed power is, however, small, about 1%.

Figures 5–7 show similar effects for the *T* and *X* junctions. Figure 7 illustrates the possibility of resonantly controlling the transmission of the microwave field through the *X* junction via the resonance addition

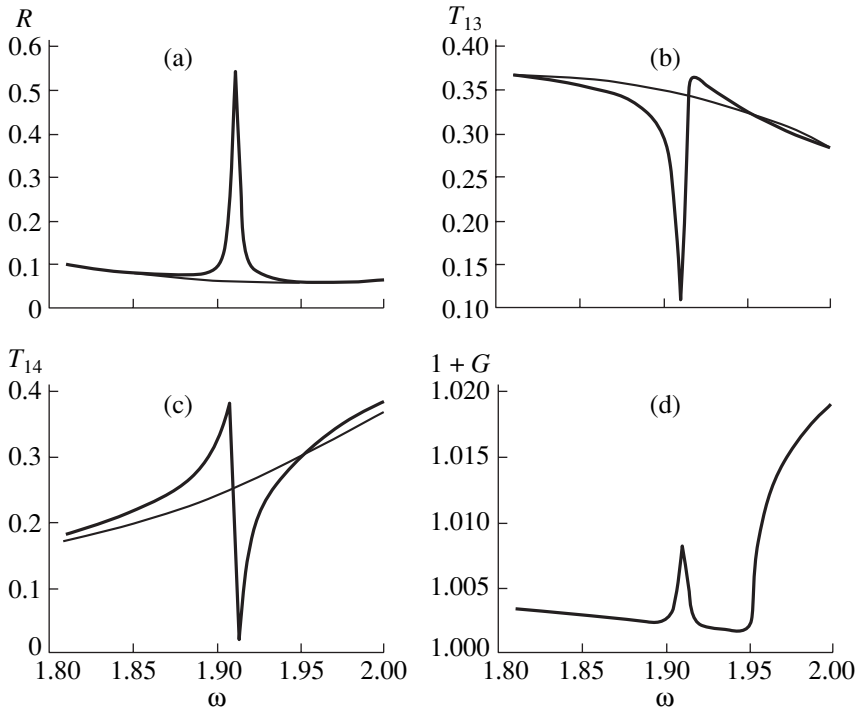


**Fig. 7.** Same as in Fig. 6 at $\tilde{H}_0 = 1$, $m = 1$, $\tilde{\Omega} = 0.4$, and $\lambda$ = (thin line) 0 and (thick line) 0.15. The probing field tuned to excite the first bound state with the frequency above the cutoff frequency of the waveguide arms.

of the second bound state with the eigenfrequency $\omega_b = 1.91$. For a hollow waveguide *X* junction, the frequency of the second bound state is $\omega_b = 606.91$. The range of $w \geq 1.95$ includes the second passband for the electromagnetic waves, hence, the specific behavior of the absorbed microwave power at these frequencies. Recall that, because of the high permeability of ferromagnetics, all the frequency responses (the frequencies of the bound states and frequency transmission thresholds) of the waveguide junctions are significantly shifted towards the low-frequency region.

## ACKNOWLEDGMENTS

A.F. Sadreev is grateful to P. Exner for the valuable explanation for the physics of bound states.

This work was supported in part by the Russian Foundation for Basic Research (grant no. 01-02-16077).

## REFERENCES

1. L. de Broglie, *Problémes de propagations guidées des ondes électromagnétiques* (Gauthier-Villars, Paris, 1941; Inostrannaya Literatura, Moscow, 1948).
2. S. Datta, *Electronic Transport in Mesoscopic Systems* (Cambridge Univ. Press, Cambridge, 1995).
3. J. Goldstone and R. L. Jaffe, Phys. Rev. B **45**, 14100 (1992).
4. P. Exner and P. Šeba, J. Math. Phys. **30**, 2574 (1989).
5. P. Exner, P. Seba, and P. Štoviček, Czech. J. Phys., Sect. B **39**, 1181 (1989).
6. R. L. Schult, D. G. Ravenhall, and H. W. Wyld, Phys. Rev. B **39**, 5476 (1989).
7. F. M. Peeters, Superlattices Microstruct. **6**, 217 (1989).
8. J. P. Carini, J. T. Londergan, K. Mullen, and D. P. Murdock, Phys. Rev. B **46**, 15538 (1992).
9. J. P. Carini, J. T. Londergan, K. Mullen, and D. P. Murdock, Phys. Rev. B **48**, 4503 (1993).
10. A. Mekis, S. Fan, and J. D. Joannopolous, Phys. Rev. B **58**, 4809 (1998).
11. E. N. Bulgakov and A. F. Sadreev, Pis'ma Zh. Éksp. Teor. Fiz. **66**, 403 (1997) [JETP Lett. **66**, 431 (1997)].
12. E. N. Bulgakov and A. F. Sadreev, Zh. Éksp. Teor. Fiz. **114**, 1954 (1998) [JETP **87**, 1058 (1998)].
13. A. I. Akhiezer, V. G. Bar'yakhtar, and S. V. Peletminskiĭ, *Spin Waves* (Nauka, Moscow, 1967; North-Holland, Amsterdam, 1968).
14. A. G. Gurevich, *Magnetic Resonance in Ferrites and Antiferromagnets* (Nauka, Moscow, 1973).
15. T. Ando, Phys. Rev. B **44**, 8017 (1991).

*Translated by A. Khzmalyan*

*Technical Physics, Vol. 46, No. 10, 2001, pp. 1291–1293. Translated from Zhurnal Tekhnicheskoĭ Fiziki, Vol. 71, No. 10, 2001, pp. 87–89.*


**ELECTRON AND ION BEAMS, ACCELERATORS**

# Transaxial Mirror with Combined Static Electric and Magnetic Fields

**L. G. Glickman and Yu. V. Goloskokov**

*Institute of Nuclear Physics, National Nuclear Center of Kazakhstan, Almaty, 480082 Kazakhstan*

*e-mail: lev_glikman@hotmail.com*

Received November 13, 2000; in final form, February 14, 2001

**Abstract**—Combined transaxial mirrors are studied. In the areas of motion of charged particles, the fields of these mirrors are symmetric relative to the axis and mid-plane representing the plane of symmetry for the electric field and the plane of asymmetry for the magnetic one. An image equation is inferred and simple relationships between the linear and angular dispersions with respect to mass and energy are obtained. Aberration properties of the mirrors in the directions parallel to the mid-plane are considered. Expressions for the coefficients of the third-order geometric aberration corresponding to the beam divergence angle in the mid-plane are obtained. These expressions are especially simple when both object and image are located in the principal planes of the mirror. The aforementioned coefficients are expressed via parameters characterizing the mirror under the first-order approximation. © *2001 MAIK "Nauka/Interperiodica".*

Theoretical studies of the focusing and dispersive properties of the electrostatic transaxial systems in the case of a curvilinear axial trajectory of a beam of charged particles were reported earlier (see, for example, [1–3]). This study is devoted to the transaxial mirrors with combined static electric and magnetic fields. In the cylindrical coordinates $R$, $\Psi$, and $Y$, these fields are described by the scalar potential $\varphi(R, Y)$ and the vector potential $\mathbf{A}$ with only one nonzero component $A_\Psi(R, Y)$. The $Y$ axis and the $Y = 0$ plane coincide with the axis of symmetry of the field and the mid-plane, respectively. The mid-plane represents the plane of symmetry for the electric field and the plane of asymmetry for the magnetic one. The axial trajectory of a beam of charged particles moving in the vicinity of the mid-plane belongs to this plane.

Figure 1 shows an example of the transaxial mirror with combined electric and magnetic fields. This mirror represents a concave two-electrode transaxial mirror with two-plate electrodes. The plates of the first *1* and second *2* electrodes simultaneously serve as the screen and poles of the magnet, respectively. Curve *3* is the axial trajectory; $\varphi_1$ and $\varphi_2$ are the electrostatic potentials of the first and the second electrode, respectively. The field-generating surfaces facing the mid-plane are parallel to this plane. The plates of the neighbor electrodes (screen and poles) are separated by curvilinear slits the projections of which onto the mid-plane represent fragments of concentric circles centered at the axis of symmetry of the field. For convenience, we use scalar magnetostatic potential for calculating the distributions of the magnetic field strength. This potential equals zero at the screen of the magnet and at the mid-plane. The upper and lower plates of the second electrode (poles of the magnet) have the magnetostatic potentials $C$ and $-C$, respectively. The electric and magnetic field strengths rapidly decrease when moving from the boundary between electrodes (screen and poles) toward the axis of symmetry. In the area $R_1 - R > 3d$, the trajectories of particles are virtually rectilinear. Here, $R_1$ is the radius of the center of the slit separating the plates of electrodes (screen and poles), $\delta$ is the slit width, and $d/2$ is the distance of the field-generating surfaces from the mid-plane. The absence of grids or holes in electrodes at the beam path is one of the main advantages of the mirror proposed. Owing to this, the number of secondary and scattered particles distorting the spectrum is insignificant.

Let us consider the electron–optical properties of the transaxial mirror with combined electric and mag-

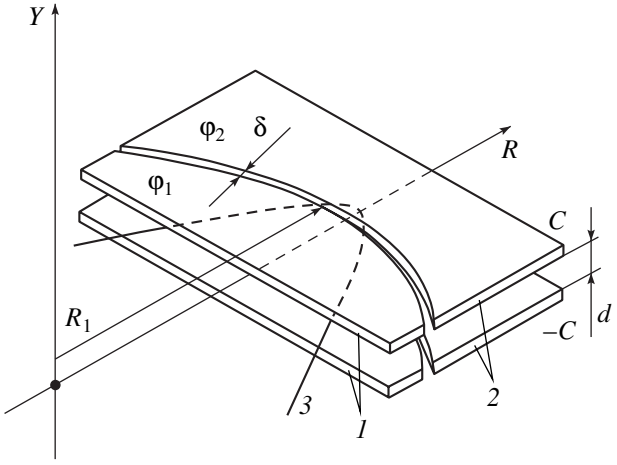


**Fig. 1.** Transaxial mirror with combined electric and magnetic fields.

1063-7842/01/4610-1291$21.00 

netic fields using the constancy of the total energy of a charged particle and the generalized momentum $P_\Psi$ corresponding to the cylindrical coordinate $\Psi$:

$$P_\Psi = mR^2\dot{\Psi} + \frac{e}{c}RA_\Psi = \text{const}. \quad (1)$$

Here, $m$ and $e$ are the mass and the charge of a particle, respectively, and $c$ is the speed of light in vacuum. Let us introduce the curvilinear orthogonal coordinates $x$, $y$, and $s$ so that $s$ and $y$ axes coincide with the axial trajectory of the beam of charged particles and $Y$ axis, respectively, and $x$ axis belongs to the mid-plane and is orthogonal to the tangent to the axial trajectory of the beam.

Let us expand variables $x$ and $y$ in series with respect to their values and their first derivatives over $s$ in the object plane, relative energy spread in the beam ($\varepsilon_0$), and relative mass spread ($\gamma$) [3]. Subscript 0 corresponds to the values of the variables in the object plane. Primes denote differentiation with respect to $s$. Let the expansions be accurate to the terms of the second order of smallness. In the expansion of $x$, we also take into account the spherical aberration of the third order relative to the beam divergence angle $\alpha$ in the mid-plane.

The quantities $RA_\Psi$ are equal in the object and image areas outside the region of the field of the mirror. These quantities are related to the magnetic flux $N$ through a circle of the radius $R$ located in the mid-plane and centered in the origin of the cylindrical coordinates (see, for example, [4]):

$$RA_\Psi = \frac{N}{2\pi}. \quad (2)$$

Under the first-order approximation, it can be deduced from expressions (1) and (2) that, in the image plane,

$$x' = \frac{x_1 + b_0x_0' - x_0}{b_1}. \quad (3)$$

Subscript 1 corresponds to the values of the variables in the plane of the Gaussian image where $K_\alpha = 0$. We introduced the notation $b = r\cos\sigma$, where $r = r(s)$ is the $R$ coordinate of the particle moving along the axial trajectory and $\sigma$ is the angle between the radius vector $\mathbf{r}$ and the tangent to the axial trajectory counted counter-clockwise from the radius vector. Under the first-order approximation,

$$x_1 = x_0K_x + K_\varepsilon\varepsilon_0 + K_\gamma\gamma. \quad (4)$$

Then it follows from formula (3) that

$$x' = \frac{b_0x_0' + (K_x - 1)x_0 + K_\varepsilon\varepsilon_0 + K_\gamma\gamma}{b_1}. \quad (5)$$

Here, $K_x$ is the linear magnification in the $x$ direction of focusing and $K_\varepsilon$ and $K_\gamma$ are the linear dispersions with respect to energy and mass, respectively. Expression (5) can also be rewritten as

$$x' = x_0'\Gamma_x - \frac{x_0}{f_x} + K_\varepsilon'\varepsilon_0 + K_\gamma'\gamma, \quad (6)$$

where $\Gamma_x$ is the angular magnification, $f_x = -1/K_x'$ is the focal length of the mirror, $K_\varepsilon'$ and $K_\gamma'$ are the angular dispersions with respect to energy and mass, respectively.

Based on the equality of the coefficients at $x_0$, $x_0'$, $\varepsilon_0$, and $\gamma$ in the right-hand sides of expressions (5) and (6), we obtain

$$\Gamma_x = \frac{b_0}{b_1}, \quad K_\varepsilon = K_\varepsilon'b_1, \quad K_\gamma = K_\gamma'b_1 \quad (7)$$

and write the image equation as

$$\frac{1}{b_1} - \frac{1}{b_0} = \frac{1}{f_x}. \quad (8)$$

It follows from formulas (7) and (8) that the image equation and the simple relationship between the linear and angular dispersions with respect to energy obtained for the electrostatic transaxial mirror (see, for example, [2]) remain valid for the transaxial mirror with combined electric and magnetic fields. However, a simple relationship between the linear and angular dispersions with respect to mass obtained in this work for a transaxial mirror with combined electric and magnetic fields is a new result.

It follows from the relationship between the linear and angular dispersions (7), that the equality to zero of one of the angular dispersions implies equality to zero of the corresponding linear dispersion in any plane of the image area.

Of larger interest is the case when the object is located in the principal plane of the transaxial mirror $H_{x_0}$ corresponding to the $x$ direction of focusing and the conditions of stigmatic focusing are met ($K_\alpha = M_\beta = 0$). Then, the stigmatic image is located in the other principal plane $H_{x_1}$. In this case, $\sigma_0 = \sigma_1 = 90°$ and $b_0 = b_1 = 0$ (Fig. 2). The schematic drawing, representing a projection onto the mid-plane, shows the effective reflecting surface, axial trajectory, angle of deflection of the beam in the field of the mirror $\theta$, and the principal planes $H_{x_0}$ and $H_{x_1}$ of the concave transaxial mirror. The principal planes of any transaxial mirror pass through the axis of symmetry of the field 0 and are orthogonal to the incident and reflected beams. The case of the concave mirror is of special interest, since the object and the image can be real and located outside the field of the mirror. In the case considered, the linear magnification in the mid-plane $K_x$ equals +1 and the linear magnification in the direction orthogonal to the mid-plane $M_y$ equals +1

or –1. The linear dispersions with respect to mass and energy equal zero at any values of the angular dispersions (see formulas (7)). Simple expressions for the coefficients of the second-order geometric and chromatic aberrations in $H_{x_1}$ plane of the transaxial mirror with combined electric and magnetic fields are represented in the same way as those for the electrostatic transaxial mirror [1–3]. There is no second-order spherical aberration in $H_{x_1}$ plane for both directions of focusing ($K_{\alpha\alpha} = K_{\beta\beta} = M_{\beta\alpha} = 0$). For the $x$ direction of focusing, other coefficients of the second order are represented as

$$K_{\alpha x} = -r_0 K'_x, \quad K_{xx} = -\frac{1}{2} r_0 K'^2_x, \quad K_{\beta y} = -M_y r_0 M'_y,$$

$$K_{yy} = -\frac{1}{2} r_0 M'^2_y, \quad K_{\alpha\varepsilon} = -r_0 K'_\varepsilon, \quad K_{x\varepsilon} = -r_0 K'_x K'_\varepsilon, \quad (9)$$

$$K_{\varepsilon\varepsilon} = -\frac{1}{2} r_0 K'^2_\varepsilon.$$

Let us find a simple expression for the coefficient of the third-order spherical aberration $K_{\alpha\alpha\alpha}$. This aberration corresponds to the beam divergence angle $\alpha$ in the mid-plane. Let us use the formula [1]

$$K_{\alpha\alpha\alpha} = -r_0 K'_{\alpha\alpha} \quad (10)$$

and the equality [3]

$$K'_{\alpha\alpha} = -\frac{r_0}{2 f_x}. \quad (11)$$

Here, $K'_{\alpha\alpha}$ is the angular spherical aberration of the second order. It follows from formulas (10) and (11) that

$$K_{\alpha\alpha\alpha} = \frac{r_0^2}{2 f_x}. \quad (12)$$

If the angular dispersion with respect to energy equals zero, the system considered ($b_0 = b_1 = 0$) also exhibits zero coefficients of the second-order chromatic aberration in the $x$ direction of focusing (see (9)). If the system is telescopic in both directions of focusing ($K'_x = M'_y = 0$), then neither geometric aberrations of the second order nor spherical aberrations of the third order related to the angle $\alpha$ are observed for the $x$ direction of focusing.

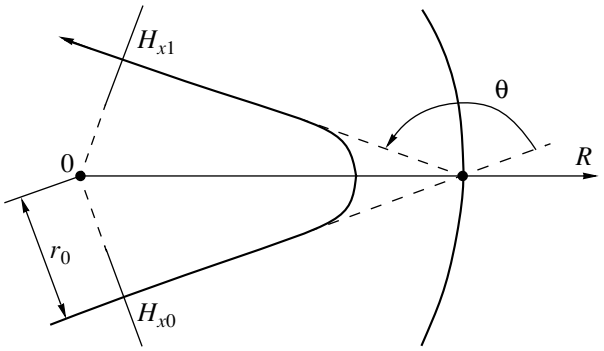


**Fig. 2.** Transaxial mirror with unity magnification in the mid-plane.

A more detailed study of the properties of the transaxial mirror with combined electric and magnetic fields implies consideration of the specific electron–optical and ion–optical systems with high-quality focusing. In particular, a compact combined mirror with $K'_\varepsilon = 0$ is of substantial interest for mass spectrometry. Such a mirror exhibits focusing of the first order with respect to energy in any plane of the image area. By varying electric, magnetic, and geometrical characteristics, one can obtain the conditions of focusing formulated in this paper in the case of large dispersion with respect to mass. A magnetic transaxial mirror allows nondispersive deflection of the beam and high-quality focusing which is substantial for the systems of beam transport.

## REFERENCES

1. S. P. Karetskaya and L. V. Fedulina, Zh. Tekh. Fiz. **52**, 735 (1982) [Sov. Phys. Tech. Phys. **27**, 466 (1982)].
2. S. P. Karetskaya, L. G. Glickman, L. G. Beizina, and Yu. V. Goloskokov, Adv. Electron. Electron Physics **89**, 391 (1994).
3. L. G. Glikman, Yu. V. Goloskokov, and S. P. Karetskaya, Zh. Tekh. Fiz. **66** (7), 213 (1996) [Tech. Phys. **41**, 737 (1996)].
4. V. M. Kel'man and S. Ya. Yavor, *Electron Optics* (Nauka, Leningrad, 1968).

*Translated by A. Chikishev*

*Technical Physics, Vol. 46, No. 10, 2001, pp. 1294–1298. Translated from Zhurnal Tekhnicheskoĭ Fiziki, Vol. 71, No. 10, 2001, pp. 90–94.*


**SURFACES, ELECTRON AND ION EMISSION**

# Precursor Radical Recombination and Its Attendant Effects on the Surface of Solids in a Dissociated Carbon Dioxide Medium

**V. F. Kharlamov, L. Yu. Frolenkova, and T. S. Rogozhina**

*Orel State Technical University, Orel, 302020 Russia*

*e-mail: Kharl@ostu.ru*

Received October 4, 2000

**Abstract**—The atomic-hydrogen-initiated ejections of materials from the surface of solids (ZnS, Ni) preliminary treated with dissociated carbon dioxide are revealed. The glow of a crystalline phosphor and the dynamic effect of the reaction are observed in the dissociated carbon dioxide medium. It is found that the observed variations in the dynamic effect of the reaction are unrelated to changes in the reaction rate. These effects are used to elucidate the mechanism of heterogeneous radical recombination on the surface of solids ($Al_2O_3$, ZnS, Ni) in dissociated carbon dioxide. It is revealed that, under the experimental conditions, the reaction rate is independent of the chemisorbed radical concentration, because the reaction involves radicals entrapped into the precursor state with a short lifetime at the surface. © *2001 MAIK "Nauka/Interperiodica".*

## INTRODUCTION

It is known that, upon collision with a solid surface, a molecule incoming from the gaseous medium can occur in a weakly bound precursor state in which this molecule diffuses over the surface until it forms a stronger bond or is desorbed [1, 2]. This weakly bound state with a short lifetime at the surface can represent either a physical adsorption state or an intermediate "excited" chemisorption state in which the rearrangement of all chemical bonds and the relaxation over all the possible degrees of freedom have not had time to occur. The precursor states provide an increase in the chemisorption cross section as compared to direct capture of gas molecules by adsorption centers. When migrating over the surface, the precursor molecules can be involved in chemical reactions with other molecules. The capture of molecules incoming from the gaseous medium into the precursor state results in the formation of two channels of heterogeneous chemical reactions. In the first case, the precursor molecules react with chemisorbed molecules. In the second case, the precursor molecules undergo an interaction with other precursor molecules. These channels of reactions can compete with reaction channels in which chemisorbed molecules either react with each other (the Langmuir–Hinshelwood mechanism) or react with molecules incoming from the gaseous medium (the impact Eley–Rideal mechanism).

The occurrence of additional channels and stages of the heterogeneous reactions involving precursor molecules, as compared to the reactions governed by the Langmuir–Hinshelwood and Eley–Rideal mechanisms, leads to an increase in the rate of the chemical reaction and, most likely, can be one of the chief causes for catalytic acceleration of the chemical reactions in the gas phase by solids.

In order to investigate experimentally the chemical processes involving precursor gas molecules, it is necessary within the framework of the relaxation measurement method to modulate the flow of materials directed to the catalyst surface with the time resolution $\Delta t \ll \tau$, where $\tau$ is the lifetime of reacting molecules in the precursor state ($\tau < 10^{-5}$ s). Unfortunately, these methods remain to be devised. For this reason, the reactions involving precursor molecules have not been adequately studied (a review of the papers discussing the participation of precursor molecules in heterogeneous reactions is given in the monograph by Krylov and Shub [3]).

The majority of the works concerned with the elucidation of the possible mechanisms of heterogeneous chemical reactions occurring at the solid–gas interface have been performed at relatively low pressures (see, for example, [4]). At a low pressure of the gas involved in the chemical reaction on the solid surface, the concentrations of the precursor and chemisorbed molecules are rather low. In this case, judging only from the experimentally observed kinetic parameters, it is impossible to distinguish the reaction channel through which the precursor molecules react with chemisorbed molecules from the reaction channel in which the molecules incoming from the gaseous medium react with chemisorbed molecules. The currently available facilities make it possible to distinguish experimentally the channels of heterogeneous reactions involving precursor molecules from other reaction channels only in the case of sufficiently high pressures of the gases involved in these reactions on the solid surface. To accomplish

1063-7842/01/4610-1294$21.00 

this, the reaction channel in which precursor molecules react with chemisorbed molecules should make a substantial or dominant contribution to the reaction rate. The fulfillment of this condition can be checked against the measured dependence of the reaction rate on the concentration of chemisorbed molecules. However, as far as we know, this dependence has been analyzed in only few works.

The aim of the present work was to investigate the dependence of the rate of the heterogeneous chemical reaction proceeding at the solid–gas interface on the concentration of chemisorbed particles involved in this reaction (by the example of adsorption and heterogeneous recombination of radicals incoming from dissociated carbon dioxide).

## EXPERIMENTAL

In the experiments, we used the modulated flows of reactants and the simultaneous recording of the kinetic curves $N(t)$ of their adsorption and the dynamic effects of reaction (DER) $F(t) = P_r(t) - P = GJ(t)$, where $t$ is the time, $P_r$ is the gas pressure on the surface of the catalyst, $P$ is the gas pressure on the walls of the vessel, $G$ is the coefficient, and $J$ is the rate of the heterogeneous reaction [5, 6].

The measurement scheme and the facilities used were described earlier in [7]. The gas at pressure $P$ = 30 Pa was continuously pumped through a vacuum chamber. The adsorption measurements were carried out using a piezoelectric quartz balance. A layer ($d \approx$ 0.1 mm) of the material to be studied was coated onto both surfaces of the piezoelectric element. The dynamic effects of the reaction were measured using an automated balance with a magnetic suspension [7, 8]. In this case, a layer ($d \approx 0.1$ mm) of the studied material was coated onto the upper surface of the balance pan which was positioned near the piezoelectric element.

The experiments were performed with hydrogen and carbon dioxide of spectroscopic purity. Carbon dioxide was produced by thermal decomposition of $CaCO_3$ and was passed through a column filled with silica gel. The dissociation of gas molecules into radicals was achieved with a high-frequency electric discharge in the gas. The radical concentration in the reactor was equal to $n \approx 10^{14}$ cm$^{-3}$. The samples were prepared in the form of ultradisperse powders of aluminum oxide and nickel with spherical particles 100 nm in diameter and in the form of a finely disperse ZnS–Cu phosphor with a specific surface of $\approx$1 m$^2$ g$^{-1}$. With the aim of cleaning the sample surface from adsorbed contaminants, the samples were held in an atomic–molecular hydrogen mixture at a temperature of 400 K for 1.5 h. The surface finish quality of the ZnS–Cu phosphor was checked against the intensity $I$ and the spectrum of radical recombination luminescence (RRL) excited in the course of the surface chemical reaction [9]. In order to modify the surface state of solids, carbon dioxide was replaced by hydrogen and the sample was treated with atomic hydrogen. After the replacement of one gas by the other, the reactor was washed with a molecular flow for 5 min, and then, the discharge was switched on.

## RESULTS AND DISCUSSION

The results obtained are as follows (in "blank" experiments when the studied material was not coated onto the piezoelectric elements, the effects described below were not observed).

After switching on the discharge in carbon dioxide, the piezobalance frequency $f$ decreases as a result of the adsorption of CO and O radicals on the surface of solids. The discharge switching off is accompanied by an increase in the frequency $f$ due to recombination desorption of "weakly" adsorbed radicals. In the case of zinc sulfide and nickel, the frequency $f$ does not regain its initial value, which indicates the second "stable" form of the radical adsorption. No stable radical adsorption occurs at the surface of aluminum oxide. After the replacement of carbon dioxide by hydrogen and switching on the source of atomic hydrogen in the case of zinc sulfide and nickel, the piezobalance frequency $f$ increases jumpwise due to the ejection of the chemisorbed material from the solid surface. After ejection of the material and switching off the discharge, hydrogen molecules are readily captured into dangling chemical bonds on the surface. For $Al_2O_3$, this effect is not observed for the lack of strongly bound CO and O

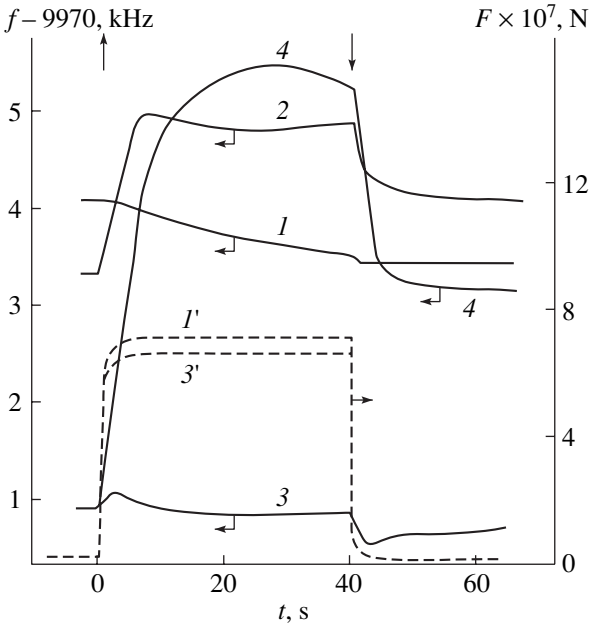


**Fig. 1.** Time dependences of (*1–4*) the piezobalance frequency and (*1'*, *3'*) the dynamic effect of the reaction in dissociated carbon dioxide for nickel after switching on (↑) and switching off (↓) a radical source in (*1*, *3*, *1'*, *3'*) carbon dioxide and (*2*, *4*) hydrogen (*1*, *2*, *1'*) prior to and (*3*, *4*, *3'*) after treatment of the sample in dissociated carbon dioxide for 20 min. $T$ = 295 K.

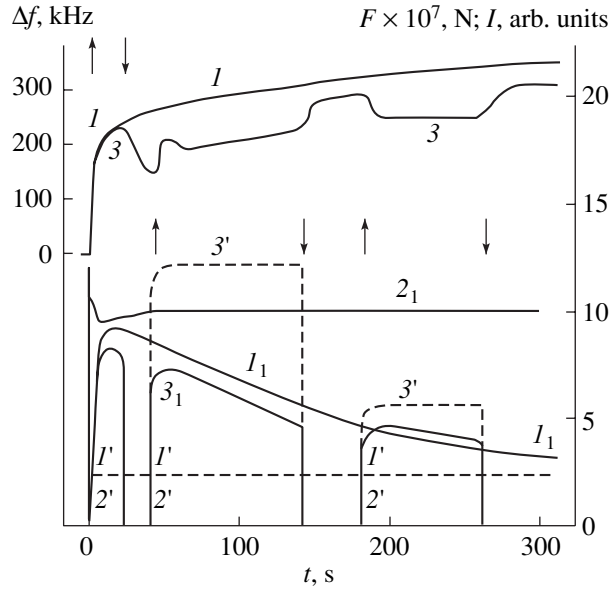


**Fig. 2.** Time dependences of (*1*, *3*) the change in the piezobalance frequency, (*1*'–*3*') the dynamic effect of the reaction, and ($1_1$–$3_1$) the RRL intensity for the ZnS–Cu phosphor after the first switching on the discharge in carbon dioxide and subsequent dark pauses. $T$ = (*1*, *1*', $1_1$, *3*, *3*', $3_1$) 295 and (*2*', $2_1$) 400 K.

radicals on the surface. Figure 1 shows the adsorption curves for nickel (curves *1*, *3*) and the curves corresponding to the cleaning of its surface from adsorbed particles by hydrogen atoms (curves *2*, *4*) before (curves *1*, *2*) and after (curves *3*, *4*) prolonged treatment of the sample in dissociated carbon dioxide.

The mass ejections from the surface of solids in an atomic hydrogen medium are brought about by the formation of volatile hydrides in the course of heterogeneous chemical reaction. It is quite possible that, in the adsorbed layer, there occur chain reactions initiated by hydrogen atoms and the sputtering of adsorbed molecules at the expense of the energy released in acts of chemical conversions on the surface (analogs of these presumed effects are described in [10–12]).

In this work, we observed for the first time the radical recombination luminescence, the dynamic effect of reaction, and the surface sputtering when placing solids in the dissociated carbon dioxide medium (earlier [6, 7, 9, 13], these effects were experimentally investigated by the example of heterogeneous reactions of recombination of hydrogen, oxygen, and nitrogen atoms).

Upon prolonged treatment (for several tens of minutes) or heating of the samples to the temperature $T$ = 400 K in dissociated carbon dioxide, no considerable changes in the dynamic effect of the reaction are observed (Fig. 2, curves *1*', *3*'). The dynamic effect of the reaction in dissociated carbon dioxide is several times less than that in atomic hydrogen, all other factors being the same. Note that the kinetic curves $F(t)$, which were measured after switching on and switching off the radical source in dissociated carbon dioxide, have a nearly rectangular shape in all the cases, whereas similar curves $F(t)$ measured in atomic hydrogen contain portions of smooth variations stemming from the changes in the sample temperature in the course of the surface exothermic reaction [7]. This result is explained by the fact that, in the carbon dioxide medium, the rate of establishment of the thermal equilibrium between the catalyst surface and the gas is considerably higher than that in hydrogen. This conclusion is confirmed by the fact that, upon heating of the sample in the carbon dioxide medium with the use of the light of an incandescent lamp, the curves $F(t)$ also have a nearly rectangular shape.

After short-term treatment (of the order of a minute) of solids in atomic hydrogen (in the case of ZnS and Ni, the strongly adsorbed CO and O radicals are removed), the dynamic effect of the reaction remains unchanged. The cycles of alternate two-minute treatment of the samples with dissociated $H_2$ and $CO_2$ gases were performed up to 10 times. For nickel, the $f(t)$ and $F(t)$ curves measured many times in both media coincided with each other, respectively. For ZnS, the $f(t)$ curves only slightly change in shape from experiment to experiment. The reproducibility of the results obtained attests the cleanliness of the experiments, the purity of the initial surface of the sample, and the chemical stability of nickel in these corrosive media. For aluminum oxide in the atomic hydrogen medium, the piezobalance frequency $f$ is characterized by a continuous irreversible decrease. This is associated with the absorption of hydrogen atoms by crystals and, most likely, the high imperfection of the crystal lattice of the studied samples.

For the ZnS–Cu phosphor samples untreated with atomic hydrogen, the RRL intensity decreases to zero with time after first switching on the discharge in carbon dioxide. As the phosphor temperature increases to $T \approx 400$ K, the phosphor exhibits a weak steady-state glow. After switching off the discharge, no phosphor persistence is revealed ($T$ = 293–400 K). A similar behavior of the radical recombination luminescence of the ZnS–Cu phosphor is observed upon its excitation by atomic oxygen. For comparison, we should note that, in the case when the ZnS–Cu phosphor is excited by atomic hydrogen, there occurs a steady-state bright glow ($T$ = 293–400 K), whereas after switching off the discharge, the phosphor exhibits a long recombination afterglow due to the occurrence of trapping centers in the bulk of the crystalline phosphor. These results can be explained by the fact that the oxygen atoms chemisorbed from the gaseous medium bring about the RRL quenching, because they serve as centers of radiationless recombination of electrons and holes created in acts of radical recombination on the phosphor surface. Moreover, the band bending in the course of oxygen atom chemisorption hinders the migration of holes from the surface into the bulk (as evidenced by the lack of afterglow), which stimulates radiationless recom-

bination of electrons and holes on the defect-rich surface of the phosphor.

The first contact between dissociated carbon dioxide and solids pretreated in atomic hydrogen for 1.5 h is accompanied by changes in the surface state of these solids, which affects the dynamic effect of the reaction. Below, this effect will be considered by the example of zinc sulfide.

In the case of ZnS subjected to preliminary prolonged treatment in the atomic hydrogen medium, the dynamic effect of reaction and the intensity of radical recombination luminescence in the dissociated carbon dioxide medium increase by more than one order of magnitude. For the ZnS–Cu phosphor samples preliminarily treated in atomic hydrogen, the bright RRL with characteristic recombination luminescence is observed in dissociated carbon dioxide (the glow spectrum consists of a band with a maximum at $\lambda_{max} = 530$ nm). At a temperature $T \approx 300$ K, the RRL intensity monotonically decreases to zero with time. As can be seen from Fig. 2, the $F(t)$ curves have a rectangular shape and the $f(t)$ dependence corresponds to the surface sputtering due to the radical recombination reaction (Fig. 2, curves $1_1$, $1'$, and $1$, respectively). Under the same conditions but at a temperature $T \approx 400$ K, the crystalline phosphor exhibits a relatively stable glow (which decays in the course of the RRL excitation within a few ten minutes); in this case, the temperature variation does not affect the dynamic effect of reaction and the shape of the $F(t)$ curve (curves $2_1$, $2'$). No phosphor persistence occurs upon switching off the discharge. After "dark" pauses of the "discharge switching on–switching off," the dynamic effect of reaction first increases by a factor of five or eight and then decreases irreversibly; however, the $F(t)$ curve remains rectangular in shape (curves $3'$).

A drastic increase in the dynamic effect of reaction and the RRL intensity in the dissociated carbon dioxide medium after the prolonged treatment of the phosphor in atomic hydrogen is associated with the change of the state of its surface (owing to the occurrence of anionic vacancies, superstoichiometric metal, etc. as the result of reduction of zinc sulfide by hydrogen atoms [6]). Judging from the $f(t)$ dependence (curve $1$) the cleaning of the surface from adsorbed particles in the course of the reaction dominates over their chemisorption; that is, an increase in the reaction rate is unrelated to the increase in the concentration of chemisorbed radicals.

After the first dark pause, during which the adsorption of $CO_2$ molecules prevails, the RRL intensity decreases (curve $3_1$). Reasoning from this circumstance, it can be assumed that the adsorption of $CO_2$ molecules results in RRL quenching (probably, due to the band bending and the formation of radiationless electron–hole recombination centers). At the sample temperature $T \approx 400$ K, the cleaning of the surface from CO, O, and $CO_2$ adsorbed particles in the course of the reaction dominates over their chemisorption, which provides a relatively stable glow of the phosphor (curve $2_1$). A comparison of the RRL curves ($1_1$, $3_1$) shows that, after the dark pause, the rate $J$ of heterogeneous radical recombination remains unchanged. Therefore, the increase observed in the dynamic effect of reaction after the first dark pause (curve $3'$) is explained by the change in the coefficient $G$ in the expression $F = GJ$, which, in turn, results from the increase in the kinetic energy of the translational motion of molecules (products of the reaction) [5, 6] due to the change in the surface state of ZnS in the course of the dark pause, as judged from the capture of $CO_2$ molecules into dangling chemical bonds on the surface. The change in the surface state leads to the fact that the recombination desorption of radicals weakly bound to the surface prevails in the course of the second dark pause (curve $3$). After this pause, the RRL intensity does not decrease, but the dynamic effect of reaction decreases and the concentration of chemisorbed radicals increases.

According to the results obtained, the rate of radical recombination on the surface of solids (Ni, $Al_2O_3$, ZnS) in the dissociated carbon dioxide medium does not increase as the concentrations of the strongly and weakly chemisorbed radicals increase. This can be explained by the fact that the reaction involves radicals entrapped into the precursor state whose concentrations are small compared to the concentrations of chemisorbed radicals.

Let us now assume that the reaction of radical recombination proceeds through an impact mechanism. According to the experimental data, the reaction rate is independent of the chemisorbed radical concentration $N$. Therefore, we can assume that a reaction channel dominates provided it involves chemisorbed radicals of one sort (for example, CO) whose concentration $N_1$ is rather small: $N_1 \ll N$ (for example, $O + CO + Z \longrightarrow O + COZ \longrightarrow CO_2 + Z$. The cross section of this reaction can be estimated at $\sigma = J(jN_1)^{-1} = 10^{16}$ $(10^{18} \times 10^{12})^{-1}$ cm$^2$ $= 10^{-14}$ cm$^2$, where $j$ is the flux of radicals impinging on the surface. Such an anomalously high value of $\sigma$ cannot be used in the description of the reactions involving both particles incoming from the gaseous medium and chemisorbed particles (the impact Eley–Rideal mechanism). Therefore, the above assumption is not true.

## CONCLUSION

Thus, the catalytic acceleration of the radical recombination reaction in dissociated carbon dioxide by solids is explained by the trapping of radicals (incoming from the gaseous medium) into the mobile precursor state, which provides an increase in the effective cross section of the reaction. Unfortunately, judging only from the results obtained in this work, it is impossible to decide between two possible variants: (1) the reaction predominantly proceeds through the channel in

which precursor radicals recombine with precursor radicals, and (2) the reaction involves precursor radicals (for example, O atoms) and chemisorbed radicals (CO), whose concentration is small compared to the concentration of chemisorbed radicals of the first sort (O atoms).

We revealed a nontrivial effect of the drastic increase in the rate of heterogeneous recombination of CO and O radicals at the surface of zinc sulfide under the conditions when the cleaning of the surface from chemisorbed radicals in the course of the reaction dominates over their chemisorption. This result is in close agreement with the data obtained in [7, 14], according to which the chemisorbed H and O atoms at $n \approx 10^{14}$ cm$^{-3}$ inhibit the surface, thus preventing the reactions of their recombination.

As follows from the results obtained in this study and the data available in the literature [1–3, 7, 14], the investigation into the mechanism of participation of the precursor molecules in surface chemical transformations cannot be reduced to the determination of one of the kinetic parameters of the heterogeneous reactions and requires solving the basic problem on the mechanism of catalytic activity of solids.

## ACKNOWLEDGMENTS

We are grateful to I.P. Denisov, A.P. Il'in, and A.G. Karengin (Tomsk Polytechnical University, Tomsk, Russia) kindly providing the powders for our investigations.

This work was supported by the Russian Foundation for Basic research (project no. 99-03-32097) and the Ministry of Higher Education of the Russian Federation (project no. 97-12-11-26).

## REFERENCES

1. M. Roberts and C. McKee, *Chemistry of the Metal–Gas Interface* (Oxford Univ. Press, Oxford, 1978; Mir, Moscow, 1981).
2. Yu. G. Ptushinskiĭ and V. A. Chuĭkov, Poverkhnost, No. 9, 5 (1992).
3. R. V. Krylov and B. R. Shub, *Nonequilibrium Processes in Catalysis* (Khimiya, Moscow, 1990).
4. S. A. Kiperman and N. A. Gaĭdaĭ, Kinet. Katal. **40**, 705 (1999).
5. V. F. Kharlamov, Poverkhnost, No. 11, 122 (1993).
6. V. F. Kharlamov, *Atom Recombination on Solid Surfaces and Its Concomitant Effects* (Tomsk. Gos. Univ., Tomsk, 1994).
7. V. F. Kharlamov and K. M. Anufriev, Pis'ma Zh. Tekh. Fiz. **25** (15), 27 (1999) [Tech. Phys. Lett. **25**, 603 (1999)].
8. K. M. Anufriev and V. F. Kharlamov, Prib. Tekh. Éksp., No. 1, 152 (2000).
9. F. F. Vol'kenshteĭn, A. N. Gorban', and V. A. Sokolov, *Radical Recombination Luminescence of Semiconductors* (Nauka, Moscow, 1976).
10. N. N. Semenov, *Chain Reactions* (Nauka, Moscow, 1986).
11. B. E. Stepanov and V. M. Tapilin, React. Kinet. Catal. Lett. **4** (1), 1 (1976).
12. V. A. Grankin, N. D. Tolmacheva, and Yu. I. Tyurin, Zh. Fiz. Khim. **73**, 1185 (1999).
13. V. N. Lisetskiĭ, *Dynamic Effect by Heterogeneous Atom Recombination* (Tomsk. Gos. Univ., Tomsk, 1996).
14. V. F. Kharlamov, V. N. Lisetskiĭ, and O. A. Ivashchuk, Zh. Fiz. Khim. **72**, 297 (1998).

*Translated by M. Lebedev*

*Technical Physics, Vol. 46, No. 10, 2001, pp. 1299–1302. Translated from Zhurnal Tekhnicheskoĭ Fiziki, Vol. 71, No. 10, 2001, pp. 95–98.*


**EXPERIMENTAL INSTRUMENTS AND TECHNIQUES**

# A New Concept for a Current Switch Based on a High-Temperature Superconductor

**S. G. Ovchinnikov*, V. I. Kirko**, A. G. Mamalis***, M. I. Petrov*, V. V. Ivanov**, D. A. Balaev*, D. M. Gokhfel'd*, S. A. Kharlamova*, S. V. Militsyn**, and K. A. Shaĭkhutdinov***

** L. V. Kirenskiĭ Institute of Physics, Siberian Division, Russian Academy of Sciences, Krasnoyarsk, 660036 Russia*

*** Research Physicotechnical Institute of Krasnoyarsk State University, Krasnoyarsk, 660036 Russia*

**** National Technical University of Athens, 10682 Athens, Greece*

Received July 6, 2000

**Abstract**—A new concept for a device for protecting an alternating-current network is offered. It is based on a combination of a superconducting limiter of a short-circuit current and a circuit breaker. A high-temperature superconductor in the form of a pile of plane rings is used as the active element of the limiter. The test results of a model of such a limiter are obtained in the steady-state short-circuit regime. The characteristics of composite silverless materials used for design of the breaker are given. © *2001 MAIK "Nauka/Interperiodica"*.

## INTRODUCTION

The possibility of using superconductors as active elements for short-circuit (sc) current limiters has long attracted researchers' attention [1, 2]. However, high costs of both the devices and the coolant (liquid helium) for low-temperature superconductors have hampered their wide use. The discovery of high-temperature superconductivity has regenerated interest in investigations in this field, because the high temperatures of the transition to the superconducting state (90–120 K) allow one to use liquid nitrogen as a coolant [3–8].

The simplest current limiter is based on the transition of a superconductor from the superconducting state, in which the resistance equals zero, to the normal state with a finite conductivity value, when the current exceeds the critical value. In the emergency case accompanied by an increase in the circuit current, the presence of an additional ballast resistance (equal to zero in the normal regime) softens the sc regime. The advantage of using a superconducting active element is that the element (unlike a mechanical disconnector) has a very short response time [2] and higher reliability. It should be noted that the behavior of a superconducting active element in the overload regime was mainly investigated in the publications on current limiters [4–8]. In this work, we offer a new concept for the protection apparatus, in which most attention is paid to the combination of a circuit breaker (the contacts are made of composite materials without silver [9–13]) with a current limiter based on a high-temperature superconductor (HTSC).

## COMBINATION OF A BREAKER AND A SUPERCONDUCTING CURRENT LIMITER

Let us consider the load of a superconducting current limiter connected in series with a breaker (switch). In the absence of a current limiter, the switch's ability to protect the load is determined by the critical value of the power $W_{\mathrm{SW}}^{CO}$, which, when reached, trips the switch. In the presence of a current limiter, the total power in the sc regime $W_{\mathrm{ex}}$ is redistributed between the limiter and switch

$$W_{\mathrm{ex}} = W_{\mathrm{CSL}}^{C} + W_{\mathrm{SW}}^{CO}.$$

The critical power $W_{\mathrm{CSL}}^{C}$, at which the current limiter is overwhelmed, is determined by the resistivity of a superconductor in the normal state, its mechanical strength, and specific features of the limiter design. In the combined system of a switch and current limiter, the power released in the switch is lower than that without a superconducting limiter. Hence, the critical power value for the switch $W_{\mathrm{SW}}^{C}$ may be decreased:

$$W_{\mathrm{SW}}^{C} = W_{\mathrm{SW}}^{CO} - W_{\mathrm{SCL}}^{C}. \quad (1)$$

Expression (1) is valid for $W_{\mathrm{SW}}^{CO} > W_{\mathrm{SCL}}^{C}$. If $W_{\mathrm{SW}}^{CO} < W_{\mathrm{SCL}}^{C}$, all the power in the sc regime is released in the superconducting current limiter. The practical importance of expression (1) is that it is possible to reduce the requirements on the circuit breaker in the combined system of the current limiter and switch. Therefore, for such switches cheaper contact materials can be used, for example, silverless composites consisting of copper

1063-7842/01/4610-1299$21.00 

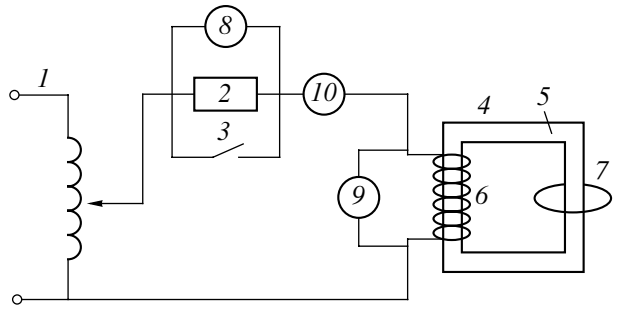


**Fig. 1.** Circuit diagram for HTSC ring tests in the sc regime: (*1*) external network transformer (50 Hz); (*2*) load; (*3*) sc regime simulation switch; (*4*) current limiter, which consists of core *5* made from transformer steel ($\mu = 100$), primary winding *6* (23 turns), and superconducting ring *7*; (*8*, *9*) voltmeters measuring the voltage drop across the load and limiter, respectively; and (*10*) ammeter measuring the circuit current.

with small additions of superdispersed diamonds [9–13]. Another advantage of such a combined system is the higher operation reliability, because the HTSC element protects both the switch and the load.

## A CURRENT LIMITER BASED ON HTSC

Presently, several concepts of current limiters exist [3]. The so-called resistive and inductive limiters are the most widespread [4]. In resistive current limiters, a superconductor is directly included in the circuit with the protected load [4, 7, 8]. Limiters of such a type require the development of a technological process for manufacturing contacts between the HTSC and the current lead. In inductive current limiters, an active superconducting element, usually made in the form of a ring or a cylinder, is inductively coupled to the load [4–7]. To produce such limiters the following factors should be taken into account: the large dimensions of devices, in which the superconductor screens the magnetic field; and the possibility of destruction of superconducting elements under ponderomotive forces at a high current density. In devices of both types, the heat released in the short-circuit regime should be effectively removed from a superconductor.

**Table 1.** Results of bench tests of materials at direct and alternative currents

| Material | Switching wear, g/cycle × $10^6$ | | $R_J$, mΩ | |
|---|---|---|---|---|
| | anode (+) | cathode (–) | current | |
| Cu–Cd–Cdia | –1.2 | –4.4 | 11.9 | 24.0 |
| Cu–Cd–Nb–Cdia | –0.5 | –1.6 | 8.8 | 15.7 |
| Cu–Cd–C | –2.5 | –3.6 | 23.3 | 2.3 |
| Ag–15CdO | –0.6 | –0.7 | 1.2 | 1.2 |

High-temperature superconductors in the form of a hollow cylinder screening the primary winding field are often used in inductive current limiters [4]. An iron core is set inside the superconductor. In devices of this type the space factor is about 0.6. For effective heat removal, the thickness of the cylinder walls should not exceed ~2 mm [4, 5]. The cylinder is exposed to considerable loads under the ponderomotive forces, according to the data in [4], with axial compression up to ~1500 N, and pressure on the outer surface at 0.2 bar, which is close to the ultimate stress of ceramic HTSC. For this reason, most designs need a band to unload the active element.

In this work, we modified the design of an inductive current limiter. High-temperature superconductors were made in the form of a pile of thin rings with relatively large radial size. The rings were separated by a gap equal to the ring thickness of ~2 mm. This allowed one to increase the HTSC volume and, hence, the operating power of the limiter. Calculations showed that a fivefold increase in the radial size (up to 10 mm) allows one to abandon a band, because the axial load on a superconducting ring is distributed over a larger area than in the case described above [4], and the tension on a unit length of the superconducting pile of rings is also less. The space factor in this design is close to unity, since the magnetic circuit and set of rings are separated only by a wall of a styrofoam cryostat. An additional advantage of this design is that the value of the operating current of the limiter can be varied in a wide range by a change in a number of rings.

The $Bi_{1.8}Pb_{0.3}Sr_{1.9}Ca_2Cu_3O_x$ HTSC [14] was synthesized from $Bi_2O_3$, PbO, $SrCO_3$, $CaCO_3$, CuO according to ceramic technology at temperatures of up to 840°C for up to 250 h with multiple intermediate millings. The small-angle Debye powder patterns showed that the Bi-2223 phase is dominant. The resistivity measurements by the four-probe method have shown that the transition to the superconducting state begins at

$$T_C = 113\ \text{K}, \quad T_C(\rho < 10^{-6}\ \Omega\ \text{cm}) = 105\ \text{K},$$
$$\rho(T_c) \approx 2\ \text{m}\Omega\ \text{cm}.$$

The superconducting rings for the measurements were prepared from this powder in a special mold. The pressed rings were finally annealed in a uniform temperature field. The rings obtained had an outer diameter of 10 cm, an inner diameter of 8 cm, and a thickness of 2–6 mm. The critical current density $J_c$ of the dummy rings determined by the four-probe method was 150 A/cm$^2$ at 77 K (according to the criterion of 1 μV/cm).[1]

The rings were tested at a frequency of 50 Hz using the circuit shown in Fig. 1. The measurements showed the following results. At a circuit current of 1 A, the voltage drop across the load was $U_r = 19$ V, the voltage

[1] Investigations on optimization of the final annealing of the rings aimed at increasing the critical current density are currently being conducted.

drop across the limiter was $U_{SC} = 0$ (<10 μV). In the sc mode, the current was 9 A, the voltage drop across the limiter was $U_{SC} = 17$ V (the ring current density was 760 A/cm$^2$), and the voltage drop across the load, $U_r \approx 0$ (the voltage drop at the leads was ≈2 V).

The *I–V* characteristic of one of the rings is shown in Fig. 2. It was measured by the inductive method using the circuit in Fig. 1. It is seen that the active element has a rather high overload ability; i.e., it can operate in a steady-state regime without being overwhelmed at currents much higher than the critical ones. The power released in the ring is ~150 W (20 W/cm$^3$) and is effectively removed by liquid nitrogen. The experiments with a set of rings have shown that the threshold current of the limiter is additive with respect to the critical currents of separate rings.

Note that the experimental results were obtained in the steady-state regime. Naturally, in a quasi-pulse mode, in which the protecting device will operate (we mean the actuation time of the breaker), it is possible to achieve higher characteristics of the limiter [6, 7], at least by a power of ~2 kW per one superconducting ring.

Thus, in our view, the offered design of a superconducting current limiter with an active HTSC element in the form of a set of plane rings is promising, as well as the design, in which the active element is made as a thin-walled cylinder [4, 5].

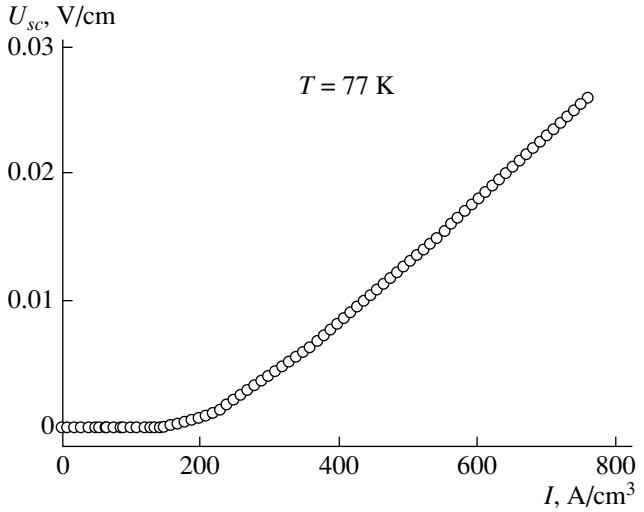


**Fig. 2.** Typical steady-state current–voltage characteristic of the HTSC ring measured at 77 K for the stimulated sc regime.

## INTERRUPTING COPPER-BASED CONTACTS

The current limiter is used as a protection mechanism; its main contacts operate in the long-term switch-on mode and, hence, the main requirement is a low value and long stability of the transitional resistance ($R_J$) in the symmetric contact pair.

The main obstacle in using copper as a basic material for interrupting contacts used in air is its rather high oxygen affinity. Attempts to reduce oxidation of the copper matrix and, thus, the value of $R_J$ are carried out by both doping the material with different additions and introducing a reducing agent (more often graphite).

Contacts of a copper–graphite system have a common drawback: low hardness and strength. Therefore, they cannot usually be used in devices with multicycle shock loading.

It has been suggested to introduce carbon in the form of a relatively cheap diamond powder (obtained by explosive synthesis) with the main fraction <1 μm in size [9, 10]. In this case, the chemical nature of the addition is the same, while the mechanical characteristics of the composite are radically improved. When solid refractory particles of diamond are introduced into the matrix, the durability to welding increases, and the material is additionally strengthened. Diamond increases the erosion durability of the contacts by cooling the arch base (due to the high thermal conductivity of diamond), leading to the quenching of the arc. Refractory metals additionally introduced into the composite reduce the value of $R_J$, and increase its stability, and bolster its mechanical and electrical durability of contacts (Tables 1 and 2).

Up to currents of 1000 A, $\Delta T$ values are within a normalized range. Similar data are obtained for ac contactors ($I$ = 20, 40, 100 A): the absolute $T$ values of contact pairs ranged from 315 to 342 K.

The processing behavior of powder composites [11, 12], their oxidation in air at temperatures close to

**Table 2.** Typical results of the temperature excess of the parts of dc apparatuses

| Rated parameters of apparatus | $\Delta T$, K | | | |
|---|---|---|---|---|
| | upper terminals | lower terminals | mobile contacts | stationary contacts |
| 250 A, 110 V | 32.6–36.5 | 25.6–26.0 | 41.2–43.7 | 40.6–45.1 |
| 870 A, 770 V | 46.2–49.7 | 35.3–40 | 63.7–66.1 | 72.1–74.7 |
| 600 A, 1500 V | 55.7–57.7 | 41.8–42.6 | 66.9–69.6 | 62.6–63.4 |
| 600 A, 1500 V | – | – | 69.7–71.5 | 73.8–74.9 |

the working temperature of contacts (330–390 K) [13], and tests in industrial apparatuses have shown that the contact elements of copper-based powder composites considered have the necessary service properties and are capable of providing the reliable operation of communication apparatuses.

The critical power of the electrical contact $W_{SW}^{CO}$ can hardly be tested experimentally or estimated theoretically. As a rule, it is possible to indicate only an approximate value of $W_{SW}^{CO}$. For the contact pair described in this paper, a power of ~30–50 kW can be considered critical. The current limiter with a set of ten HTSC rings allows one to decrease the critical power of a switch by a value of $W_{\mathrm{SCL}}^{C} \sim 20$ kW which is comparable with the value of $W_{SW}^{CO}$. According to our estimates, the combined device (current limiter + switch) will be able to operate at currents of 100–1000 A to protect unique equipment at industrial enterprises, transport, and during dangerous processing.

Further investigations on the development of a prototype of the sc network protector based on a superconducting current limiter and a breaker with silverless contacts include the following: (i) improvement of the critical parameters of the HTSC rings; (ii) design of an operation element based on silverless contacts; and (iii) study of the behavior of the limiter in the pulse regime.

## ACKNOWLEDGMENTS

The work is carried out in the frame of the joint Russian–Greek project “A New Concept for a Switch Based on a Superconducting Current Limiter and Silverless Contacts” (1998–2000). The work is supported by a target-oriented program of the administration of the Krasnoyarsk region “Investigations and Developments of High-Priority Trends in Science and Technology of the Krasnoyarsk Region” (project no. 18).

## REFERENCES

1. R. McFee, in *Superconductivity and Its Application in Electrical Engineering: Collection of Articles*, Ed. by B. K. Bul’ and B. M. Tareev (Énergiya, Moscow, 1964), pp. 38–59.
2. I. N. Glazkov, *Research of Superconducting Electrical Devices* (ITF Sib. Otd. Akad. Nauk SSSR, Novosibirsk, 1980), pp. 22–29.
3. E. M. W. Leug, Adv. Cryog. Eng. **42**, 961 (1996).
4. W. Paul, M. Lanker, J. Rhyner, *et al.*, Supercond. Sci. Technol. **10**, 914 (1997).
5. M. Chen, Th. Baumann, P. Unternahaher, and W. Paul, Physica C (Amsterdam) **235–240**, 2639 (1997).
6. L. Porcar, D. Bourgault, J. G. Noudem, *et al.*, Physica C (Amsterdam) **235–240**, 2623 (1997).
7. J. C. Noudem, L. Porcar, O. Belmont, *et al.*, Physica C (Amsterdam) **235–240**, 2625 (1997).
8. M. I. Petrov, D. A. Balaev, V. I. Kirko, and S. G. Ovchinnikov, Zh. Tekh. Fiz. **68** (10), 129 (1998) [Tech. Phys. **43**, 1255 (1998)].
9. V. V. Ivanov, V. I. Kirko, and Vl. Vl. Ivanov, RF Patent no. 2073736, S 22 S 9/00 (1997).
10. V. V. Ivanov, V. I. Kirko, Yang Dezhuang, and Shao Vanzhu, in *Abstracts of the V Russian–Chinese International Symposium “Advanced Materials and Process,” 1999*, p. 144.
11. V. V. Ivanov, Perspekt. Mater., No. 3, 64 (1999).
12. V. V. Ivanov and V. M. Denisov, Rasplavy, No. 6, 43 (1998).
13. V. V. Ivanov and Shao Wanzhu, in *Proceedings of the Congress PM-98, 1998*, Vol. 3, p. 545.
14. V. S. Kravchenko, M. A. Zhuravleva, E. M. Uskov, *et al.*, Neorg. Mater. **34**, 1274 (1998).

*Translated by M. Astrov*

*Technical Physics, Vol. 46, No. 10, 2001, pp. 1303–1306. Translated from Zhurnal Tekhnicheskoĭ Fiziki, Vol. 71, No. 10, 2001, pp. 99–103.*


**EXPERIMENTAL INSTRUMENTS AND TECHNIQUES**

# Chemical Purity of Diamond-Like Films Produced by Ion-Beam Deposition

**S. A. Pshenichnyuk* and Yu. M. Yumaguzin****

** Institute of Molecular Crystal Physics, Ufa Scientific Center, Russian Academy of Sciences, pr. Oktyabrya 151, Ufa, 450054 Bashkortostan, Russia*

*** Bashkortostan State University, ul. Frunze 32, Ufa, 450074 Bashkortostan, Russia*

*e-mail: imcp@anrb.ru*

Received December 26, 2000

**Abstract**—Secondary-ion mass spectrometry is applied to determine the elemental composition of thin diamond-like films produced on silicon substrates by high-vacuum deposition from ion beams. Qualitative analysis and comparison of the results with the data gained for graphite and pyrocarbon standard samples indicate a high chemical purity for the diamond-like coatings obtained. *© 2001 MAIK "Nauka/Interperiodica".*

Thin carbon layers produced on various substrates have long since attracted considerable interest because of their unique physical and chemical properties. Due to their chemical inertness, high wear resistance, and transparency in the visible range, diamond-like films are widely used as protective antireflection layers for optical elements and chemical utensils. Another important use of the diamond-like films is as a working layer on disks for magnetic recording [1].

Recently, special attention has been drawn to polycrystalline diamond films on flat substrates [2]. Some of their properties, such as hardness, thermal conductivity, and transparency, are close to those of natural diamond. Varying the production conditions, one can change, within wide limits, the band gap, the impurity concentration, and the conductivity of the diamond layer. This circumstance makes the diamond coatings attractive for the manufacturing of high-power semiconducting devices.

One more area of application for the diamond-like films has been opened in connection with the discovered negative electron affinity of the (111) surface of a natural semiconducting diamond of the IIb type [3]. This feature of the diamond surface basically permits the production of a diamond-based autoemission cathode ensuring stable operation under a technical vacuum in comparatively low electric fields.

Presently, diamond-like coatings are studied most vigorously in the trends concerned with the manufacture of semiconducting devices and with the challenge to increase stability of the field current produced by "cold" electron sources [4]. Carbon coatings intended for these purposes are mainly produced by chemical-vapor deposition either in a glow discharge [5] or with a hot filament [6] in hydrogen or a hydrocarbon gas (the most common choice is methane). To attain the structures of required purity, ultrapure gases (up to 99.999%) should be mixed in perfectly precise ratios (no more than 1% of $CH_4$ content in $H_2$ is acceptable) under precise control of the substrate temperature. Even in the conditions specified, it is difficult to keep control of the elemental composition of the films since the deposition method under discussion implies a comparatively high pressure in the working chamber (about 50 torr), for which a forevacuum pump suffices. This method of pumping inevitably involves residual gas molecules and the vacuum oil components enter the film, making an unacceptable impurity concentration in the film. For comparatively thick carbon coatings (beginning with several microns) prepared on the flat substrates, these impurities are of little consequence [7]. However, in thin films (of several monatomic layers) deposited on apexes with less than 1 μm radius of curvature for investigating the emission properties of carbon coatings, the presence of impurity atoms cannot be tolerated. It should also be noted that it is impossible to gain an atomically clean substrate surface prior to the chemical vapor deposition because of an insufficiently high residual vacuum in the system.

From this point of view, the method of choice for obtaining thin carbon coatings is the deposition from an ion beam [8]. The major advantages offered by this technique are the following: the experiment can be carried out in ultrahigh vacuum conditions, the degree of which is limited only by the high-vacuum pump coping with the gas from the ion source; the parameters responsible for the film structure, in particular, the energy of the deposited particles and the radiation dose, can be easily controlled; ultrapure coatings are obtainable by means of the mass separation of the ion beam; and, finally, ion bombardment provides for a preliminary cleaning of the substrate surface.

Until now, diamond films prepared by the ion-beam deposition on plane substrates have been mainly inves-

1063-7842/01/4610-1303$21.00 

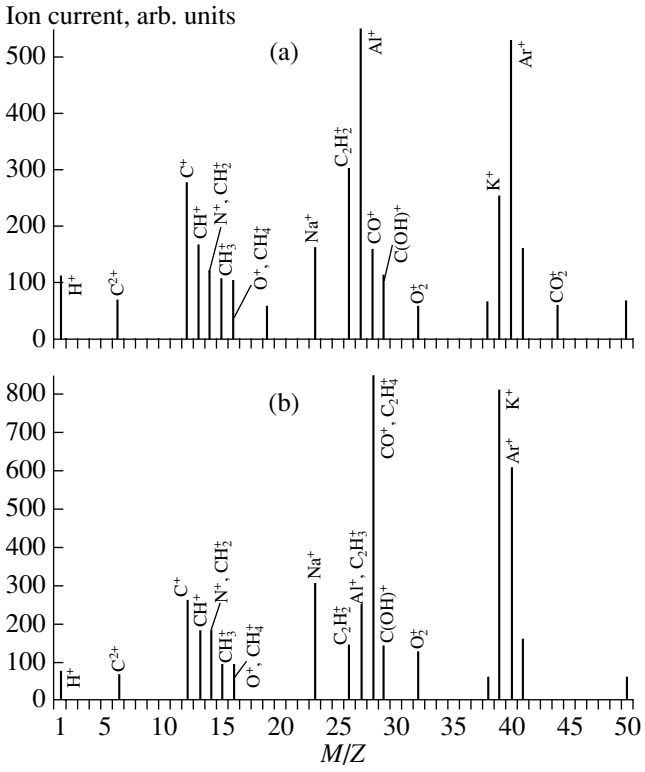


**Fig. 1.** Mass-spectra of (a) graphite and (b) pyrocarbon samples subjected to ion sputtering ($Ar^+$, 8 keV) for 15 min. The primary ion beam current is 5 Å.

tigated by means of the Auger-electron spectrometry (AES). It is known however that the secondary-ion mass spectrometry (SIMS) offers a considerably higher sensitivity [9] and, thus, perfectly complements the AES technique. In this paper, we apply the SIMS method to the study of the mass composition of thin diamond-like films produced on silicon substrates by ion-beam deposition. The chemical purity of the coatings was analyzed in order to give further insight into the charge transport and electron-field emission mechanisms when such layers are deposited on tungsten autoelectronic cathodes [4, 10].

## EXPERIMENTAL SAMPLES

Thin diamond-like films to be studied were obtained by ion deposition on flat substrates of (100)-oriented silicon single crystals. The setup employed is described in detail in [11]. Carbon layers were grown at room temperature under vacuum conditions at a pressure of $10^{-8}$ torr. Deposition conditions for the samples under investigation are listed in the table. According to the data of the scanning electron microscopy (JEOL JXA-6400 microscope), the films are polycrystalline with an average crystallite size of 8 μm. For a detailed analysis of the resultant film structure refer to [12]. The conductivity of the films did not exceed $10^{-7}$ Ω/cm at room temperature. The mass elemental composition of the carbon films was qualitatively studied by the SIMS method on a Polyus-4 (MC7201M) spectrometer. For the sake of lowering the operating pressure, vacuum conditions were produced with an oil-free pumping system based on a NORD-100 magnetic-discharge pump. The residual pressure was not higher than $10^{-7}$ torr. For primary ions we used $Ar^+$ with an energy of 8 keV, and the ion-beam current was maintained at 5 μA with a beam diameter of 2 mm. The sputtering time amounted to 15 min.

Parameters of the diamond-like films deposition

| No. | Deposition time | Ion current, μA | Ion energy, eV |
|---|---|---|---|
| 1 | 2 h 45 min | 22 | 90 |
| 2 | 4 h 10 min | 31 | 200 |

## RESULTS AND DISCUSSION

For accurate interpretation of the data concerning the diamond-like coatings, the samples of pure graphite and pyrocarbon were studied first. The corresponding mass spectra are shown in Fig. 1. The spectra were obtained from the bulk of the samples at a distance from the surface equal to the etching depth. Two peaks related to stable carbon isotopes with masses of 12 and 13 u are evident. Here, the peak attributed to the less abundant $^{13}C$ isotope stems mainly from the ion complex $CH^+$. It is interesting to note that each of the spectra obtained for carbon materials indicates the presence of two-charge ions $^{12}C^{2+}$. There are also peaks associated with hydrocarbon complexes of $C_nH_m^+$ type and carbon compounds with oxygen and with the OH group. The presence of $^{14}N^+$ and $^1H^+$ ions is reasoned by the composition of the residual gas in the SIMS working chamber (air, water vapor). A pronounced peak corresponds to the primary $^{40}Ar^+$ ions and to $^{27}Al^+$ ions contained in the material being sputtered from the cold cathode during the ion source operation. Ions of alkali metals exist in the spectra as a result of contamination of the working chamber with these substances and due to their low ionization potential. The presence of oxygen in the form of $O^+$ and $O_2^+$ ions and in carbon compounds that arise in connection with the materials under study should also be noted. In particular, oxygen and to some extent nitrogen may appear in graphite and pyrocarbon samples as a consequence of their prolonged exposure to atmospheric pressure. This is also related to the ability of graphite to accumulate a considerable amount of substance, which penetrates into the interlayer space between the atomic nets constituting the carbon crystal. On the whole, with the exception of chemical elements and compounds introduced by the setup or experimental conditions, the carbon materials

under study can be considered as highly pure, with small quantities of hydrogen and oxygen present.

The spectra measured for the diamond-like films are shown in Fig. 2. Note the already mentioned presence of two-charge $^{12}C^{2+}$ ions, which is possibly related to the hybridization state of the valence electrons in carbon atoms. The most important difference of the spectra from those of graphite and pyrocarbon is the absence of oxygen (atomic mass of 16) and oxygen-bearing compounds, CO and $CO_2$. This result is true both for the bulk of the film and for its surface thus indicating the small adsorption ability of the diamond-like surface. The spectra also contain a typical group of four peaks attributed to carbon $^{12}C^+$, carbon isotope $^{13}C^+$, and complex $CH^+$, as well as to $CH_2^+$ and $CH_3^+$. Here, the peak corresponding to the ion residual $CH_2^+$ cannot be resolved from the possible peak of the two-charge $^{28}Si^{2+}$ ions. The presence of silicon can be explained by the small thickness of the carbon layer on the Si(100) substrate and by the structure of the diamond-like layer composed, according to the scanning electron microscopy, of separate crystallites. Therefore, $^{28}Si^+$ and $SiO^+$ ions appear in the secondary ion beam as a result of the sputtering of the material from the intervening space between crystallites, since the diameter of the primary ion beam (2 mm) far exceeds the size of each separate crystallite, which is ~8 μm at most. These two sorts of single-charged ions yield intense spectral peaks corresponding to atomic masses of 28 and 29 u. Note that the other two stable silicon isotopes, $^{29}Si$ and $^{30}Si$, have an appreciable natural abundance, comparable with that of the main isotope, $^{28}Si$. The relative values are 4.667% for $^{29}Si$, 3.05% for $^{30}Si$, and 92.28% for $^{28}Si$. The peaks attributable to these isotopes can also be seen in the spectra, but their amplitudes are determined by various $C_nH_m$ compounds with the same mass numbers and thereby do not correlate with their natural occurrence. The relative intensity of the peak associated with silicon oxide in the spectrum measured for sample 2 is significantly below that of the peak observed in the spectrum for sample 1. This is explained by the higher surface density of crystallites in sample 2, being in accordance with the deposition conditions and confirmed by the data of microscopic analysis. The presence of a peak corresponding to an atomic mass of 40 in both spectra cannot be uniquely attributed to SiC since it coincides with another intensive peak due to $^{40}Ar^+$ primary ions.

According to our data, the diamond-like films contain oxygen only in the bound state, specifically, in compound with silicon, which is indicated by the mass spectra displaying no oxygen-related peaks except for those corresponding to SiO. These peaks are due to the sputtering of the material from the intervening space of the diamond crystallites, since the $SiO_2$ layer covering the Si substrate surface is usually very thin (~100 Å).

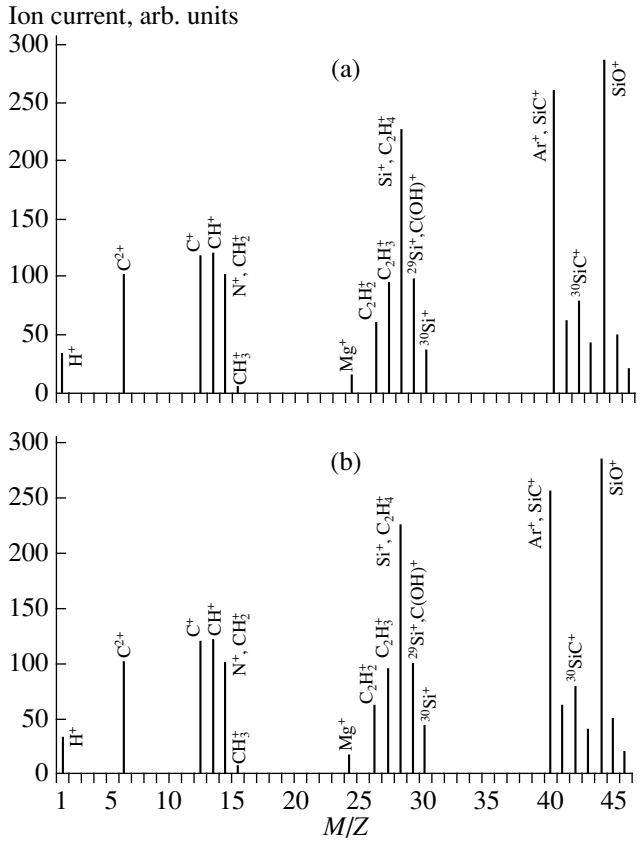


**Fig. 2.** Mass-spectra of the diamond-like films on silicon substrates for (a) sample 1 and (b) sample 2. Deposition conditions are the same as in Fig. 1.

Segregation of Si atoms at the diamond grain boundaries [13] may be a result of the diffusion through the growing film. According to [13], this process is hindered by a silicon carbide layer built up at the substrate/film interface; but in our case, the formation of such a layer is doubtful. This conjecture is in agreement with the results of [14] concerning an AES study of quasi-amorphous diamond films, with crystallite size of 20–50 Å, produced on a Si(100) substrate by cathode sputtering of graphite. The data outlined above suggest that the resulting diamond-like films are pure within the accuracy provided by the SIMS method. The only impurity is represented by hydrogen, which arises in the beam of duoplasmatron operating on propane, since we dispensed with mass separation of the beam. It is likely that, in the resultant coatings, hydrogen plays its customary role saturating the carbon dangling bonds on the crystallite surfaces and especially in the intervening space, which is presumably filled with amorphous carbon. As confirmed by the data obtained in [15], no oxygen is contained in the carbon films produced by the ion beam deposition in ultrahigh vacuum conditions, in contrast to the films obtained by other methods [14].

In summary, the ultrahigh vacuum deposition from an ion beam was used to obtain thin diamond-like car-

bon coatings on single-crystal Si(100) substrates. The elemental composition of the resultant films was studied with the SIMS technique. The main results of this study are as follows: within the accuracy of the SIMS measurements, no impurities are detected in the films, except for hydrogen, which is present in the ion beam during the film deposition; the uniform spread of hydrogen over the layer thickness favors the above hypothesis about its origin; unlike the diamond-like films obtained by other methods, the coatings are oxygen-free; ion-beam deposition of particles with an energy within 200 eV yields a carbon coating without silicon carbide at the interface of the Si substrate and diamond-like film.

## REFERENCES

1. Hsiao-chu Tsai and D. B. Bogy, J. Vac. Sci. Technol. A **5** (6), 3287 (1987).
2. V. S. Vavilov, Usp. Fiz. Nauk **167** (1), 17 (1997) [Phys. Usp. **40**, 15 (1997)].
3. F. J. Himpsel, J. A. Knapp, J. A. van Vechten, and D. E. Eastman, Phys. Rev. B **20**, 624 (1979).
4. S. A. Pshenichnyuk, Yu. M. Yumaguzin, and R. Z. Bakhtizin, Pis'ma Zh. Tekh. Fiz. **25** (15), 46 (1999) [Tech. Phys. Lett. **25**, 612 (1999)].
5. V. R. Raiko, Diamond Relat. Mater., No. 10, 1063 (1996).
6. J. Wei and Y. Tzeng, J. Cryst. Growth **128**, 413 (1993).
7. K. Nishimura, K. Das, and J. T. Glass, J. Appl. Phys. **69**, 3142 (1991).
8. B. S. Danilin, *Application of Low-Temperature Plasma for Thin Film Deposition* (Énergoatomizdat, Moscow, 1989).
9. *Methods of Surface Analysis*, Ed. by A. W. Czanderna (Elsevier, New York, 1975; Mir, Moscow, 1979).
10. S. A. Pshenichnyuk and Yu. M. Yumaguzin, Pis'ma Zh. Tekh. Fiz. **26** (1), 72 (2000) [Tech. Phys. Lett. **26**, 79 (2000)].
11. S. A. Pshenichnyuk, Yu. M. Yumaguzin, and R. Z. Bakhtizin, Prib. Tekh. Éksp., No. 6, 143 (1998).
12. S. A. Pshenichnyuk, Yu. M. Yumaguzin, and R. Z. Bakhtizin, Poverkhnost, No. 10, 9 (2000).
13. C. F. M. Borges, S. Schelz, L. St.-Ongle, and M. Maisan, J. Appl. Phys. **79** (6), 3290 (1996).
14. S. S. Olevskiĭ, V. P. Repko, and G. V. Aleksandrov, Dokl. Akad. Nauk SSSR **245** (6), 1382 (1979) [Sov. Phys. Dokl. **24**, 241 (1979)].
15. É. F. Chaĭkovskiĭ, V. M. Puzikov, and A. V. Semenov, Kristallografiya **26** (1), 245 (1981) [Sov. Phys. Crystallogr. **26**, 122 (1981)].

*Translated by A. Sidorova-Biryukova*

*Technical Physics, Vol. 46, No. 10, 2001, pp. 1307–1313. Translated from Zhurnal Tekhnicheskoĭ Fiziki, Vol. 71, No. 10, 2001, pp. 104–111.*


## EXPERIMENTAL INSTRUMENTS AND TECHNIQUES

*Symmetry holds much promise for developing*
*a unified theory of the fundamental laws of nature*
*Yu. Neéman*

# Properties and Symmetry of the Solid Cluster Phase of Protein

**E. Rapis**

*Neéman Laboratory of Symmetry, Tel Aviv University, Ramat Aviv, Tel Aviv, 69978 Israel*

Received January 22, 2001

**Abstract**—To date, only one solid crystalline form of protein has been discovered and studied. At the same time, we have experimentally found that the solid protein phase may have fundamentally different properties, as well as various types and scales of symmetry, depending on condensation conditions in the water–protein system. The key issue here is the condensation kinetics. For example, in an open system under the equilibrium conditions (low process rate), the equilibrium long-range crystalline protein lattice forms at the microlevel. In a nonequilibrium (high process rate) protein–water system, an autowave process with nonlinear irregular dynamics is established and a polyfilm solid phase with a set of three-dimensional dissipative nanostructures occurs. The type and scale of symmetry change. The crystal order at the microlevel disappears, and the material becomes amorphous. A new allotropic modification of the solid nonequilibrium protein film arises. This modification has the highly ordered (on the nano- to macroscale) superlattice with straight, helical, chiral, mirror, or rotation symmetry. This kind of protein has been identified both *in vitro* and *in vivo* and has been called "protos." © *2001 MAIK "Nauka/Interperiodica"*.

The study of protein structuring and gelling by the methods of colloidal chemistry has shown that the properties of the solid phase of protein depend on the condensation rate [1]. For example, the rapid evaporation of the solvent causes a heterogeneous system with the polydisperse structure to form. This system is thermodynamically unstable and has specific properties.

At the same time, if the solvent is evaporated slowly, the protein crystallizes into the solid phase with a rigid gel-like framework. However, only one of these protein solid phases has attracted the interest of researchers [2, 3]. Today, this equilibrium crystalline form of protein is widely investigated at the microscopic and mesoscopic (atomic and molecular) levels by the methods of X-ray diffraction analysis, NMR spectroscopy, computer simulation, etc. Note once again that the solid crystalline protein phase is formed when the solvent is removed slowly [3]. This form serves as the basis for constructing models of protein self-organization [4, 5].

Comparison studies of the nonequilibrium solid-like (polyfilm) protein phase (its morphology, symmetry, and other properties [6, 7]) and the *in vivo* behavior of the crystalline solid phase of protein have not yet been performed. To bridge this gap, we extended our pioneering (as early as in 1976) investigation [7] into allotropic solid-like protein films by using advanced methods for material modification [8], including polymers [9].

Our goal was to obtain the protein solid phase under different condensation conditions. Two identical substrates (glass or plastic) were covered by equal amounts of the protein–water mixture (with components taken in different proportions). One of the systems was made open, while the other was screened by cover glass. In the open system, unlike the closed one, the condensation and stabilization of protein proceeded in air and under the same thermodynamic conditions: at room temperature and atmospheric pressure. After compaction, the structure and symmetry of the resulting material were examined with optical, polarization, scanning electron (JEOL), and confocal scanning laser microscopes. In addition to this, we analyzed the specimens by X-ray diffraction, determined their magnetic sensitivity, took *I–V* characteristics from the liquid and solid protein phases under nonequilibrium conditions, and studied laser-induced fluorescence and birefringence.

When studying the nonequilibrium protein form, which was stabilized in the open water–protein system in air, we have found the self-assembly of multiple slug-shaped films made of protein clusters. Moreover, previously unknown phenomenological and other properties of the protein films have been discovered [6, 7, 10, 11].

The final solid phase has been found to consist of the polyfilm solid material and three-dimensional dissipative nanostructures with nucleation, fractal geometry,

1063-7842/01/4610-1307$21.00 

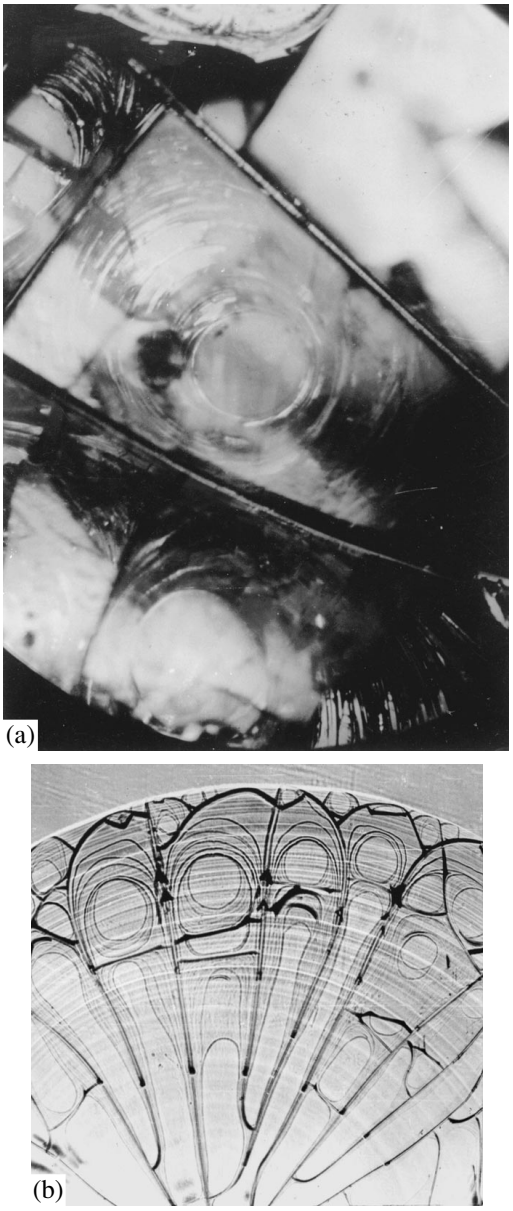


**Fig. 1.** (a, b) Three-dimensional nonequilibrium imperfect multilayer protein films with cells having a vortex core.

as well as autocatalytic and self-complementary properties. Regular cellular geometric structures with the cells having mussel-shaped vortex cores are produced. In each of the cells, free-surface step cascade vortices of opposite vorticity form. Other specific features are treelike forms with dichotomy, helices in helices (superhelices) (Fig. 1), and tubes in tubes. Films on films frequently exhibit the so-called "porcupine" symmetry, like Langmuir–Blodgett films [11, 12], and resemble a nested structure (some successively smaller elements fitted one into another). In these structures, one can distinctly see similarity, size invariance, and alternating density.

As has been found, the above phenomenology of the nonequilibrium protein film in the open system is based on a certain type of constant-scale symmetry (discrete spontaneous symmetry) that is related to defect formation in the film. The order in the structures and the symmetry type were visualized on the nano- (100–200 nm) and macroscales with optical, polarization, and electron microscopes (Figs. 2–4). However, at the microlevel, the material turned out to be disordered, as follows from X-ray diffraction data.

The X-ray data showed [13] that long-range order in the protein form we are interested in is absent. Ordering was observed only at distances of 10.5 and 4.33 Å (Fig. 5).

Discrete rotation symmetry (according to the Weyl classification) specified the general order of the superlattice in space and time, causing nucleation. We found straight (90°) rotation (repeating) parallel symmetry in the radial and transverse directions, which specifies the arrangement of three spatial cells of invariant scales.

Helical and chiral rotation symmetries form the mussel-shaped core in each of the cells. The core is halved by a straight defect passing through its center, so that bilateral (mirror) symmetry occurs. The pattern known as superhelix (with an angle of rotation of 30° to 40°) appears. The pitch of the superhelix depends on the order of quantization of the axis between two vortices and shows up as discrete rotation symmetry with the vectors of rotation parallel to each other (Fig. 6).

The equilibrium material does not have such a complex morphology at either the nano- or the macrolevel. In other words, the self-assembly (self-organization) of the three-dimensional protein structure has not been observed.

Experiments have shown that the drying of the protein condensate in the closed water–protein system results in the formation of two-dimensional birefringent nets made of filaments (Fig. 6).

When observed in the optical microscope, the crystalline protein specimens prepared for X-ray diffraction analysis under the equilibrium conditions appear (at the macrolevel) either as a defect-free block or as a material with a small density of defects in the open-book form.

Further investigations have indicated that the films are magnetically sensitive [12] and birefringent [5, 6] and exhibit laser-induced fluorescence [15]. Also, their *I–V* characteristics are similar to those of high-resistivity semiconductors [14].

Thus, it has been established that one can radically modify the properties of solid protein by varying the material preparation conditions. Not only the thermodynamic but also the kinetic conditions should be varied in this case.

For example, the rates of the chemical reaction and water evaporation, as well as the dynamics of condensation and polymerization, in the open and closed sys-

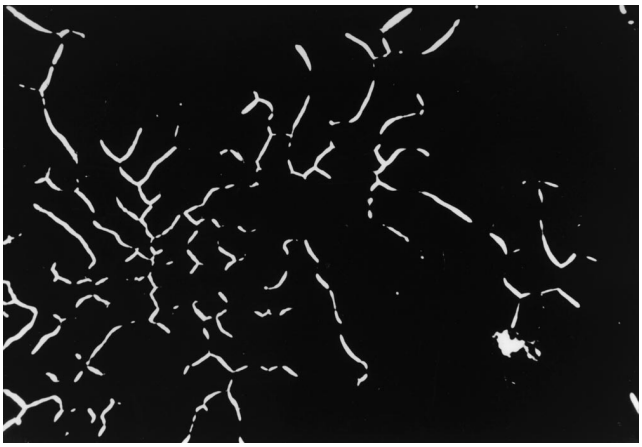

**Fig. 2.** Free-surface step vortices with opposite vorticities observed in the optical microscope (×400). Discrete (spiral and chiral) symmetries are seen.

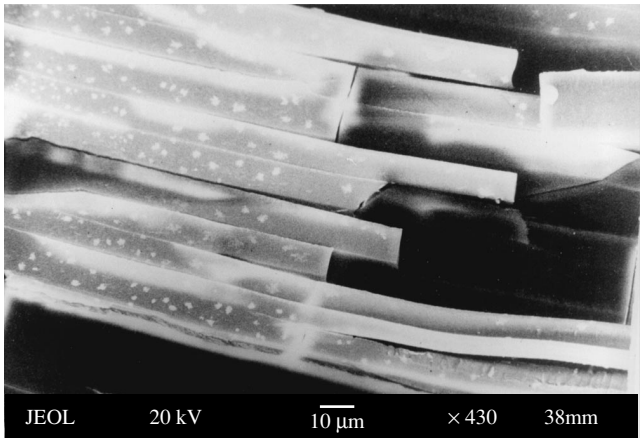


**Fig. 3.** Electron diffraction pattern from the nonequilibrium slug-shaped protein films. JEOL scanning electron microscope, ×10000. Scale division is 10 μm.

tems greatly diverge. It is known that multilayer epitaxial films grow only if the deposition rate is high [16].

However, in the open water–protein system, protein gelling during its condensation (water evaporation) takes place at relatively low rates. Yet, the process results in the formation of multilayer epitaxial films (a pile of films) with helical vortices, nonlinear irregular dynamics, and self-sustained oscillations. Such behavior of gels is typical of film self-assembly during the condensation of inorganic and polymeric sols [17]. The sols were obtained by merely evaporating the solvent at a moderate process rate [17].

These findings have not found adequate explanation for a long time. They ran counter to the conventional theoretical concepts whereby high process rates are necessary for turbulent dynamics with vortex structures and epitaxially growing films to occur. This phenomenon has been accounted for only recently. It has been shown [18] that, when condensing and passing to the gel state, various high-viscosity liquids or colloidal suspensions acquire pronounced elastic properties, which are responsible for specific turbulence called "elastic turbulence" [18]. This type of turbulence appears at moderate process rates.

The results obtained in [18] give an insight into why our experiments, carried out since 1976 [6, 7], have consistently demonstrates self-sustained oscillations and irregular nonlinear dynamics in the case of the nonequilibrium condensation of protein in an open water–protein system. These phenomena have been recently substantiated theoretically in terms of turbulent dynamics in high-viscosity materials, among them protein solutions.

It is essential that such specific behavior of protein is observed only if it condenses in an open system, which is far from equilibrium, and is strongly adherent to the substrate. Only then can one obtain the allotropic nonequilibrium protein modification at the gel–liquid crystal phase transition. This modification changes the fundamental properties of protein, namely, the type and scale of symmetry.

As follows from the X-ray diffraction data, the structure of the allotropic nonequilibrium modification of protein, which results when protein condenses *in vitro* in the open system, changes on the microscale and the local atomic order transforms into the amorphous state. At the same time, ordering takes place on the other scales. As for the closed system, where the kinetics is slower, the long-range order appears irrespective of the scale.

These findings are consistent with the new methods for material modification. Here, the kinetic, rather than thermodynamic, conditions play a key role. "The polycondensation process can be directed toward the forma-

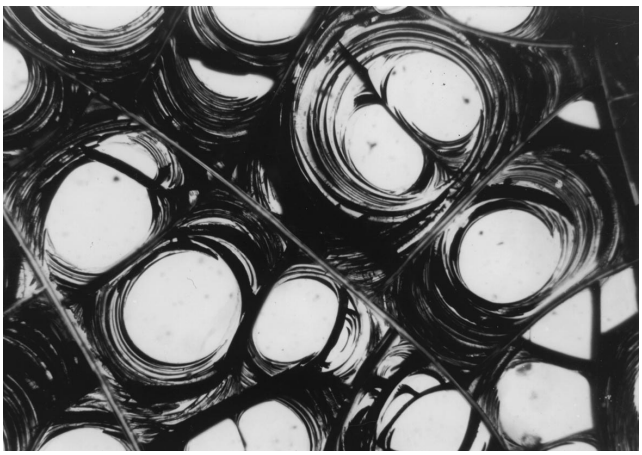

**Fig. 4.** Division of the core by a straight defect running through the core center. The occurrence of mirror (bilateral) symmetry is seen. Quantization of the axis between two vortices with the formation of rotation symmetry with an angle of 30°–40°. Optical microscope, ×800.

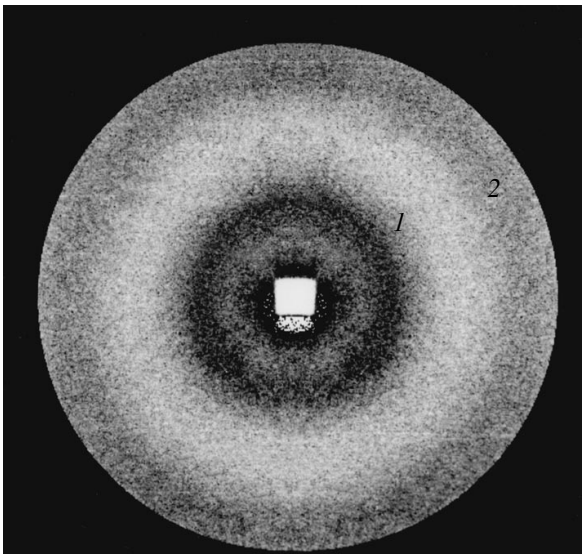


**Fig. 5.** X-ray diffraction pattern from the nonequilibrium film of protein (lysozyme). Long-range order is absent. Ordering at distances of 4.33 and 10.5 Å.

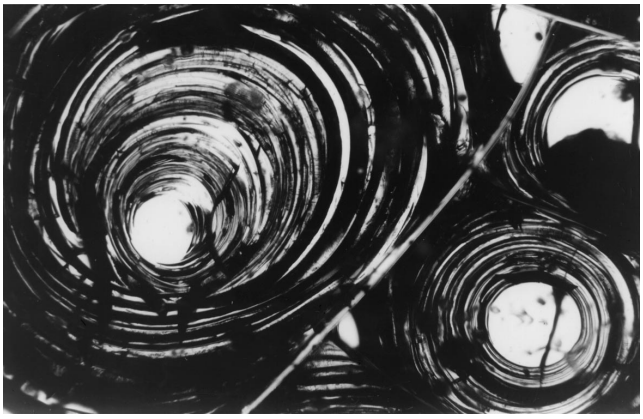

**Fig. 6.** Equilibrium protein phase in the form of two-dimensional nets. Three-dimensional nets and three-dimensional polyfilm structures with helical or mirror symmetry are absent. The material was prepared in the water–protein system closed by cover glass. Optical microscope, ×400.

tion of the amorphous, macrocrystalline, polycrystalline, or epitaxial material by varying the kinetic conditions" [19].

Thus, our experiments with protein confirm the statement that the obtaining of the amorphous materials "is directly related" to conditions for their deposition [20–22]. From the microscopic viewpoint, this fact seems to be rather unexpected although it is consistent with the concept that polymers condense into the glassy, instead of the crystalline, state [23].

At the same time, this protein material can be considered as macrocrystalline, because the lattice scale in it is of crucial importance. In this state, not only the highly structured superlattice but also the high anisotropy of the material are visualized. As follows from the examination in the optical, polarization, and scanning electron microscopes, the superlattice forms when the anisotropic epitaxial films with the characteristic types of discrete anisotropy (helical, chiral, mirror, and porcupine) grow. The establishment of one or other type of symmetry depends on the film size but remains the same at the nano- and macrolevel. It can be said that such an order is to some extent consistent with Schrödinger's prediction that biologic crystals are aperiodic in most cases.

Our observations also agree with a variety of literature data that suggest some relationship between the nano- and macrostructures during the self-assembly of the films [24–28]. For example, it has been shown [29] that a supermolecular size-dependent lattice may form. In this case, the nanostructures serve as an intermediary in going to the macroscopic organization, relating the noncovalent surface chemistry and the amorphism of the material at the microlevel [29]. Polyfilm epitaxial growth, typical of such structures, depends on whether the films are of unlike charge [16]. These factors all contribute to the formation of the large-scale substructures [24–29].

The above data explain the fact that another type of short-range order arises when protein condenses in the closed system. This order is scale-invariant, hence, the absence of the epitaxial films and the meso- and macrolevel symmetries.

Under the nonequilibrium conditions, the phase transition qualitatively changes: the gel passes into the liquid crystal. The latter phase features nonlinearity and irregularity, which set new relations between the elements. A new symmetry at all the scale levels occurs. These changes cover the morphology and the symmetry of the system as a whole (short-range and long-range orders, as well as macroinhomogeneities and defect subsystems).

The reason for the appearance of the new (discrete helical) symmetry—a basic phenomenon for any biologic structure—is the turbulence of the liquid flow. This is related to the spatial behavior of inertial particles [30]. The phenomenon is due to the discrete nonuniform charge distribution in the vortex zone, which causes magnetic fluctuations [28].

In the case of colloidal media, including protein, the fluctuations are explained by aggregate kinetics in colloids, which is made difficult by collective excitations or discrete self-forces [31, 32], as well as by charged particle adsorption/desorption [33]. Hence, the large-scale epitaxial growth of the slug-shaped films [23]. The same properties are inherent in the liquid crystal phase. Therefore, it can be said that the films are interrelated, i.e., form a quantum-size cluster. By a quantum-size cluster, we mean the specific state of a material where the consistency of an aggregate depends on its size [34].

Our experimental data count in favor of such interrelated behavior of the aggregates in the condensed film of protein. They show the presence of geometrically related quantum dots, defects, as well as the formation of fractal structures (Figs. 1a, 2), all conclusively indicating that we are dealing with cluster systems [34]. It is known that the nucleation of three-dimensional clusters (non-Euclidean geometry) in such structures is physically associated with strains and elastic stresses, which may originate from structure defects (dislocations and disclinations) or because of small changes in the bond lengths and angles [35].

Moreover, experiments have demonstrated that the restructuring of protein is accompanied by changes in its mechanical, electrical, magnetic, and optical properties.

These observations also correlate with data obtained with the new method for modifying and studying the structure of noncrystalline materials, including polymers. This method allows one to control the structure-dependent properties of materials [8]. It is known, for example, that structure modification within intermediate-range order, which is typical of semiconducting glasses, affects the mechanical and phase-transition properties of the material.

Modifications on the short-range-order scale, observable in films, radically change nearly all properties [8]. This has been supported by our experiments, which showed that the morphological, electrical, magnetic, and optical properties of protos dramatically differ from those of crystalline protein. An example is specific optical properties depending on morphological variations due to macroinhomogeneities [8]. Furthermore, the similarity between the *I–V* characteristics of amorphous carbon films and amorphous films of protein seems not to be accidental [27].

The adhesion of the film to a solid substrate and the dependence of the self-assembly process on the wettability and temperature of the substrate [36]—the fundamental properties of protos—are also absent in protein crystals. To date, it has been established that the wettability in a solid–film–liquid system is a measure of the energy of interaction in it and is a structure-sensitive parameter that allows the characterization of the surface of a solid substrate and a film applied [36, 37].

All the literature data for the phenomenology of the protos modification, as well as for its symmetry, polarization, optical, electrical, etc. properties, have been corroborated by our *in vitro* and *in vivo* experiments. This seems to be natural, since protein is expected to behave in a similar way under similar kinetic conditions for condensation in the protein–water system. In the *in vitro* experiments, we provided the nonequilibrium conditions (open system), which are typical of the animate nature, and obtained the solid protein form identical to that in biological objects.

Of particular interest is the fact that, according to the literature data, it is microscopically amorphous materials that show the self-organization property under nonequilibrium conditions [37]. Here, the role of short-range order in the atomic structure becomes minor: the geometrical properties of the structure depend on the morphology.

Because of this, we suggested (in 1983) the method for determining the protein topology. With this method, one can easily determine the symmetry and the configuration of aggregates, knowing the size and parameters of the multilayer protein piles self-organized at the nano- and macrolevels. This method makes it possible to distinguish between the normal and pathological behavior of protein during its self-organization.

Using this method (which characterizes the material on the qualitative basis), investigators can detect *in vitro* (at the macro- and mesolevels) adherent multifilm structures, discrete helical symmetry of vortices, and the other types and scales of symmetry in normal protein, comparing the data obtained with the *in vivo* behavior of protein. In this way, they can check that the self-organization of protein proceeds similarly under biotic and abiotic conditions. More reliable and exact identification requires quantitative information. However, even qualitative data are very convincing, demonstrating distinct changes at different pathologies: hemophthalmia, cataract [38], and carcinoma, as will be reported in [39].

## DISCUSSION

Our experiments have shown that the complex phenomena described above are observed only in one allotropic modification of protein, protos, which results *in vitro* when protein condenses in the nonequilibrium open water–protein system. We will briefly summarize the most important results.

It has been found that the supermolecular three-dimensional aggregation of protein at the meso- and macrolevels is accompanied with the symmetrization of the material (discrete helical, chiral, and mirror symmetries). The last type of symmetry is associated with self-similar self-complementary dissipative fractal nanostructures, which can multiply by division. This demonstrates the autocatalytic properties of this active structure, generating self-sustained oscillations with nonlinear irregular dynamics.

The behavior and properties of this system seem to be basic and common for the condensation of various materials under nonequilibrium conditions. Self-assemblies of liquid crystal films, nonequilibrium nanostructures of inorganic and organic semiconductors and superconductors [27, 40], etc. are examples.

During condensation, the system also exhibits discrete helical and mirror symmetries, vorticity, nonuniform distribution of various material phases, film formation, and the appearance of fractal dissipative three-dimensional cluster nanostructures, all showing up from the nano- to macrolevel. In this system, the above-

listed phenomena distinctly correlate with the collective behavior of electrons.

It is well known that the condensation of a material leads to an increase in the electron density and electrical conductivity. In some cases, the insulator–metal transition, typical of superconductors, takes place [23]. The surprising thing is that such a transition was observed in the protein film.

Based on the data obtained, we suppose that the entire set of the complex and poorly studied phenomena reflects the universal behavior of materials upon condensation under nonequilibrium conditions with nonlinear irregular dynamics. These effects are necessarily related to electron collectivization, which gives rise to electron conduction and superconductivity. In a system with strongly bound electrons, molecular orbits due to the self-organization and ordering of various magnetic phases arise. The material ordering extends to larger scales and higher levels up to the macrolevel.

Thus, only one allotropic modification of protein offers the capability for biological self-organization, which assembles macrostructures with the levels of energy and electrical conductivity needed to gain and store information on a living organism.

In-depth comparative analysis of this poorly studied protein modification and the other crystalline from of protein is of crucial importance for biology and medicine.

It is not improbable that the crystalline equilibrium allotropic protein modification results either under pathological (more equilibrium) conditions or when the physicochemical properties of protein are considerably modified. In this case, instead of self-organization, necessary for the living activity, pathological processes develop. One can assume, in particular, that some diseases are associated with the appearance of the crystalline allotropic protein modification *in vivo*. An example is cataract, or the crystallization of the protein in the crystalline lens in one's lifetime [38].

Based on our experiments, we hypothesize that a malignant tumor is a state with the changed protein phase or modification (liquid- or solid-crystal). Certainly, this hypothesis must thoroughly be checked.

## CONCLUSIONS

(1) The method for structure modification of the protein solid phase by altering the kinetic conditions in the water–protein system proved to be efficient. With regard for the basic role of carbon in protein films, the question arises as to whether the phenomena observed are associated with the pronounced tendency of carbon films to such allotropic modifications.

(2) Two solid forms of the protein allotropic modification, crystalline equilibrium and polyfilm nonequilibrium dissipative, are discovered. The latter, called protos, exhibits the nonlinear turbulent dynamics. Both forms possess various short- and long-range atomic orders and, consequently, various types and scales of symmetry, and, hence, much different morphological, electrical, optical, magnetic, etc. properties.

(3) In the dense phase of the nonequilibrium protein film, new previously unknown symmetries in the self-organization of protein under biotic and abiotic conditions appear. The nonequilibrium form of self-assembly (self-organization) loses short-range order, typical of its crystalline form. In the protos phase, local order in the protein crystals disappears at the microlevel. The material becomes amorphous or quasi-amorphous. A new type of symmetry that extends from the nano- to macrolevel arises. This symmetry gives rise to a highly ordered superlattice (or a macrocrystal) and possibly to the glassy phase of the liquid crystal.

(4) Our data on the symmetry and three-dimensional geometry of the allotropic nonequilibrium protein film open wide opportunities for the application of this protein modification in biology, medicine, and device technology. In particular, this form of protein can be used in liquid-crystal and polymer-based devices, which become more and more competitive with metal and semiconductor devices [24]. In medicine and biology, it can be applied in diagnostics tests for qualitatively and quantitatively characterizing the normal and pathological processes of protein self-organization.

## ACKNOWLEDGMENTS

I wish to thank A. Amus'yu, A. Arel†, E. Braudo, V. Buravtsev, V. Volkov, A. Zaikin, M. Klinger, G. Skornyakov, L. Manevich, S. Moiseev, Yu. Neéman, and I. Prigogine for the encouragement, comments, and valuable discussions.

My special thanks to the chairman of the YuZMA organization (Israel) E. Kholmyanskiĭ for the financial support.

## REFERENCES

1. V. I. Izmaĭlova and P. I. Rebinder, *Structure Formation in Protein Systems* (Nauka, Moscow, 1974).
2. Luisi Ben and L. Freedman, Nature **375**, 251 (1995).
3. Takajaki Nishizaka *et al.*, Nature **377**, 251 (1995).
4. P. G. Wolynes and W. A. Eaton, Physics World, September, 39 (1999).
5. D. Baker, Nature **405**, 39 (2000).
6. E. Rapis, Pis'ma Zh. Tekh. Fiz. **21** (9), 13 (1995) [Tech. Phys. Lett. **21**, 321 (1995)].
7. E. Rapis, Zh. Tekh. Fiz. **70** (1), 122 (2000) [Tech. Phys. **45**, 121 (2000)].
8. A. I. Popov, in *Proceedings of the All-Russia Symposium "Amorphous and Microcrystalline Semiconductors," St. Petersburg, 1998*, p. 14.
9. V. A. Ligachev, in *Proceedings of the All-Russia Symposium "Amorphous and Microcrystalline Semiconductors," St. Petersburg, 1998*, p. 17.

10. Yu. F. Biryulin, V. N. Zgonnik, *et al.*, in *Proceedings of the All-Russia Symposium "Amorphous and Microcrystalline Semiconductors," St. Petersburg, 1998*, p. 82.
11. J. J. Langmuir, Chem. Phys., No. 1, 756 (1933).
12. E. Rapis, Pis'ma Zh. Tekh. Fiz. **23** (7), 28 (1997) [Tech. Phys. Lett. **23**, 263 (1997)].
13. E. Rapis and E., Vakhtel', Laboratory of X-ray Structure Analysis, Vaidman Institute, Israel, 1997.
14. E. Rapis and B. Mekhaloshvili, Laboratory of Electron Engineering, Haifa Tekhnion, Israel, 1997.
15. E. Rapis and L. Mitel'man, Confocal Microscopy of Albumen (in press).
16. Surface Science **276**, 356 (1997).
17. O. Giraldo *et al*., Nature **405**, 38 (2000).
18. A. Groibman and D. Steinberg, Nature **405**, 53 (2000).
19. A. P. Rudenko and I. I. Kulakova, in *Proceedings of the All-Russia Symposium "Amorphous and Microcrystalline Semiconductors," St. Petersburg, 1998*, p. 46.
20. Th. Goldacker, V. Abetz, R. Stadler, *et al.*, Nature **398**, 137 (1999).
21. P. Venezuela, Nature **397**, 618 (1999).
22. L. R. Shaginyan, A. A. Onoprienko, and V. V. Artamonov, in *Proceedings of the All-Russia Symposium "Amorphous and Microcrystalline Semiconductors," St. Petersburg, 1998*, p. 66.
23. B. Jerome and J. Commandeur, Nature **386**, 589 (1997).
24. S. Prasad and J. Zabinski, Nature **387**, 761 (1997).
25. J. C. Vassilicos, Nature **374**, 408 (1995).
26. A. Boal, Nature **404**, 746 (2000).
27. S. Mori *et al.*, Nature **392**, 473 (1998).
28. V. Pattiel *et al.*, Nature **403**, 398 (2000).
29. S. J. Stupp *et al.*, Science **276**, 384 (1997).
30. T. Eperlin *et al.*, in *Book of Abstracts of the Bar–Jlan Conference on Physics of Complex Systems on Frontiers in Condensed Matter Physics, 1997*, p. 33.
31. I. S. Osborne, Science **288**, 461 (2000).
32. B. Parsegian, Science **270**, 1157 (1995).
33. Ch. A. Murray, Nature **385**, 203 (1997).
34. J. J. Braurman, Science **271-276**, 889 (1996).
35. A. L. Talis, M. I. Samoĭlovich, and M. I. Mironov, in *Proceedings of the All-Russia Symposium "Amorphous and Microcrystalline Semiconductors," St. Petersburg, 1998*, p. 81.
36. I. F. Masterov and A. V. Prikhod'ko, in *Proceedings of the All-Russia Symposium "Amorphous and Microcrystalline Semiconductors," St. Petersburg, 1998*, p. 81.
37. Sh. Sh. Sereembinov, O. Yu. Prikhod'ko, *et al.*, in *Proceedings of the All-Russia Symposium "Amorphous and Microcrystalline Semiconductors," St. Petersburg, 1998*, p. 48.
38. E. G. Rapis, Oftal'mol. Zh., No. 2, 128 (1976).
39. E. G. Rapis and M. Kutushev, in press.
40. R. Blaauwgkers *et al.*, Nature **404**, 471 (2000).

*Translated by V. Isaakyan*

*Technical Physics, Vol. 46, No. 10, 2001, pp. 1314–1321. Translated from Zhurnal Tekhnicheskoĭ Fiziki, Vol. 71, No. 10, 2001, pp. 112–119.*


## EXPERIMENTAL INSTRUMENTS AND TECHNIQUES

# Multicharged Ion Source Based on the Tornado Closed Magnetic Confinement System

**K. B. Abramova*, A. V. Voronin*, A. N. Smirnov**, and V. G. Zorin****

** Ioffe Physicotechnical Institute, Russian Academy of Sciences, St. Petersburg, Politekhnicheskaya ul. 26, 194021 Russia*

*** Institute of Applied Physics, Russian Academy of Sciences, Nizhni Novgorod, 603600 Russia*

*e-mail: voronin.mhd@pop.ioffe.rssi.ru*

Received January 25, 2001

**Abstract**—It is proposed to use the Tornado closed magnetic confinement system with microwave plasma heating for creating a pulsed source of multicharged ions. The plasma losses in closed confinement systems are determined by the diffusion across the magnetic field, which substantially increases the plasma lifetime as compared to mirror confinement systems. A plasma heating scenario with the successive switching-on of two oscillators is proposed: an oscillator operating at a frequency of 2.45 GHz produces the initial plasma, which is then heated at a frequency of 15 or 53 GHz. It is shown that it is possible to achieve the distribution of ions over charge states with a maximum at $Ar^{16+}$ at a plasma density of $2 \times 10^{13}$ cm$^{-3}$. The extracted ion current in this case can attain 1 A. © *2001 MAIK "Nauka/Interperiodica".*

## INTRODUCTION

Presently, the most commonly used multicharged ion (MCI) sources are those using magnetic mirror confinements system for confining a plasma heated by microwaves at the electron cyclotron resonance (ECR) frequency (ECR sources). Such devices make it possible simultaneously to maintain the high plasma electron temperature required for the multiple ionization of gas atoms; to confine the plasma long enough for the high ionization states of ions to be produced; and to extract the ions from the plasma in the form an ion beam, which can then be transported over distances of tens of meters. Ideally, the plasma losses in this confinement system are determined by the plasma outflow along the magnetic field through the magnetic mirrors, where an extractor is installed. The longitudinal plasma losses limit the lifetime of the plasma ions and, consequently, the highest available ionization state.

The use of closed magnetic confinement systems for confining the plasma in MCI sources seems to be attractive from the standpoint of increasing the plasma lifetime. In an ideal closed magnetic confinement system, magnetic field lines do not leave a certain bounded volume and do not meet any components of the confinement system (the vacuum chamber, etc.). The plasma lifetime in a closed confinement system can be significantly longer as compared to straight confinement systems (by a factor on the order of the ratio between the longitudinal loss rate in a simple confinement system and the diffusion rate across the magnetic field in a closed confinement system). The evident disadvantage of closed confinement systems is that the process of ion extraction is rather complicated. This problem can be resolved with closed confinement systems of the Tornado type [1, 2]. These systems allow one to use an auxiliary coil that partially destroys the closed magnetic confinement structure for a given time without radically affecting the global plasma lifetime and to produce a controlled plasma flow depending on the magnetic field of the auxiliary coil. Thus, it becomes possible to control the plasma flow to the extractor and to regulate the ion lifetime within certain limits.

In this paper, we propose to use the Tornado closed confinement system for creating an ECR source of multicharged ions. A scenario for ECR plasma heating is proposed and the distribution of ions over charge states is calculated for the Tornado-322 device, which is now under testing [3]. It is shown that, by the end of the magnetic field pulse, it is possible to achieve the distribution of ions over charge states with a maximum at $Ar^{+16}$ at a plasma density of $\sim 10^{13}$ cm$^{-3}$. The plan of experiments on ECR plasma heating in the Tornado confinement system is discussed.

## THE TORNADO CONFINEMENT SYSTEM

About forty years ago, the possibility of creating a system in which the magnetic field was closed and increased toward the periphery was demonstrated. A device permitting the creation of such a field can be used as a magnetic confinement system for confining a hot dense plasma. This confinement system was named Tornado.

The magnetic field in the Tornado device is produced by two oppositely directed currents that flow through geometrically similar spherical concentric

helical conductors connected in poles by straight-line conductors (Fig. 1).

If the ratio of the currents flowing through the helical conductors is equal to $m_0 = I_{out}/I_{in} = \sqrt{R_{in}/R_{out}}$, where $R_{in}$ and $R_{out}$ are the radii of the inner and outer spherical surfaces, then there is a spherical separatrix of radius $R_s = \sqrt{R_{in}R_{out}}$ enveloping the inner helical coil. The separatrix divides the magnetic field of the confinement system into two regions. The magnetic field lines inside the separatrix surround the conductors of the inner coil and do not leave the volume bounded by the separatrix. The volume inside the separatrix is used to confine a plasma. This volume includes a region of a lower magnetic field (Fig. 2) which is surrounded by a magnetic barrier. The magnetic barrier is located near the spherical separatrix. The magnetic field of the confinement system has a regular and stable structure [2, 4] (Fig. 3).

The eight-turn coils of the Tornado-322 are installed in a vacuum chamber. The diameters of the outer and inner coils are equal to 350 and 298 mm, respectively. The coils are made of thin-walled stainless-steel tubes 18 mm in diameter and are filled with wires insulated from the tube wall. Such a configuration permits us to avoid breakdowns between turns, because the magnetic field is produced by the current flowing through the conductors situated inside the tube. Since the insulated wires are separated by the tube from the vacuum volume, the residual gas pressure in the chamber can reach $10^{-8}$ torr. The copper wires are cooled by nitrogen vapor, which increases their conductivity by a factor of 4.5 as compared to that at room temperature. Five current-carrying wires inside the tube are insulated from each other and are connected in series. As a result, an electric current of 38 kA is sufficient to produce the magnetic field with a duration of 15 ms and a strength of 2.8 T in the barrier.

## PLASMA LIFETIME IN THE TORNADO CONFINEMENT SYSTEM

In [2, 5, 6], results are presented from an independent series of experiments on studying plasma confinement in the different modifications of the Tornado confinement system. The experimental results allow one to draw the following conclusions: the confinement system is closed; the charged-particle lifetime in it is maximum when the coil current ratio is close to the theoretically predicted value $m_0$; the plasma losses (for a plasma electron temperature of 2–5 eV) are mainly determined by the classical cross-field diffusion and electron–ion recombination; and relatively strong perturbations of the magnetic field in the confinement system increase the plasma losses insignificantly as compared to the classical diffusion losses.

For example, in the Tornado-II device ($R_{in}$ = 10 cm) [5], at a plasma density of $2 \times 10^{12}$ cm$^{-3}$, a barrier magnetic field of 0.1 T, and a pulse duration of 2 ms, the measured plasma lifetime scaled as the square of the magnetic field and the inverse electron density: $\tau_i^D \sim B^2 N_e^{-1}$. In the Tornado-X device [6], at electron densities $N_e \le 10^{14}$ cm$^{-3}$, a magnetic-field pulse duration of 2 ms, and barrier magnetic fields $B \le 0.1$ T, the measured plasma lifetime also scaled as the square of the magnetic field, which corresponded to the classical cross-field diffusion. Hence, the plasma lifetime in the confinement system in this regime can be represented as

$$\tau_i^D \approx \frac{R^2}{D_\perp^{ef}} \approx \frac{\chi R^2 B^2 T_e^{3/2}}{A N_e (T_i + \langle Z \rangle T_e)}. \quad (1)$$

Here, $R$ is the characteristic diffusion length (for a specific confinement system, the minimum between the value of $R_{in}/k$, where $k$ is the number of coil turns, and the magnetic barrier width $R_b \approx R_s - R_{in}$); $D_\perp^{ef}$ is the cross-field diffusion coefficient $T_e$ and $T_i$ (in eV) are the electron and ion temperatures, respectively; $\langle Z \rangle$ is the mean ion charge; $B$ (in T) is the barrier magnetic field; $A \approx 3 \times 10^{-12}$; and $\chi$ is a constant factor allowing for a correction related to the complicated configuration of the magnetic field in the confinement system. By comparing formula (1) with the calculated lifetime [7], the factor $\chi$ was chosen to be 1/6.

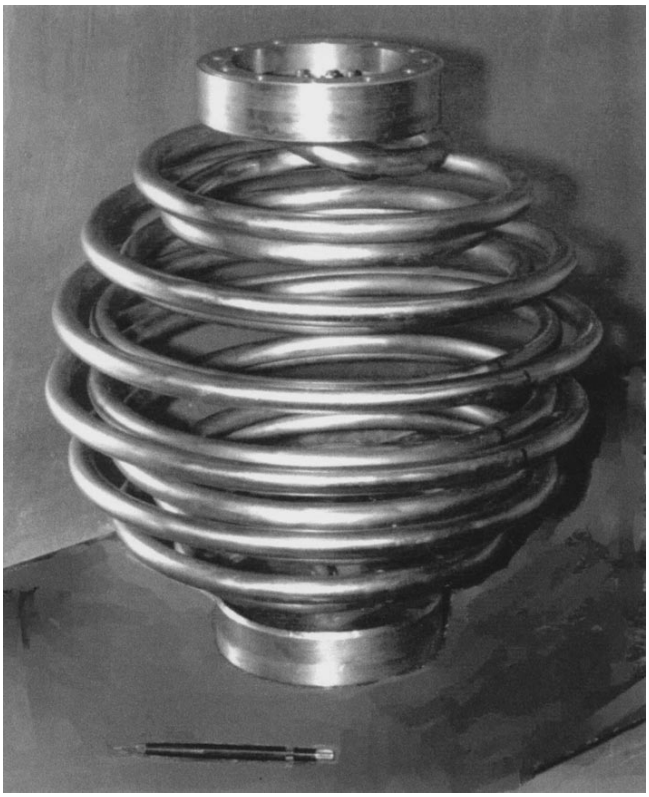

**Fig. 1.** The general view of the Tornado confinement system.

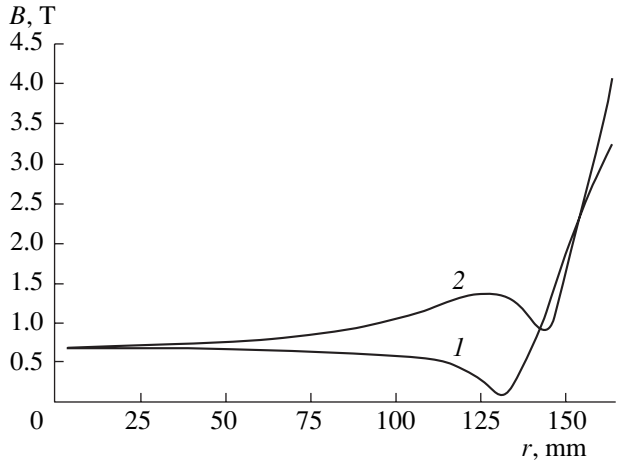


**Fig. 2.** Radial profiles of the magnetic induction $B$ in the Tornado-322 device (*1*) in the equatorial plane [3] and (*2*) in the direction toward the pole ($r$ is the distance from the center of the device; the current is 38 kA).

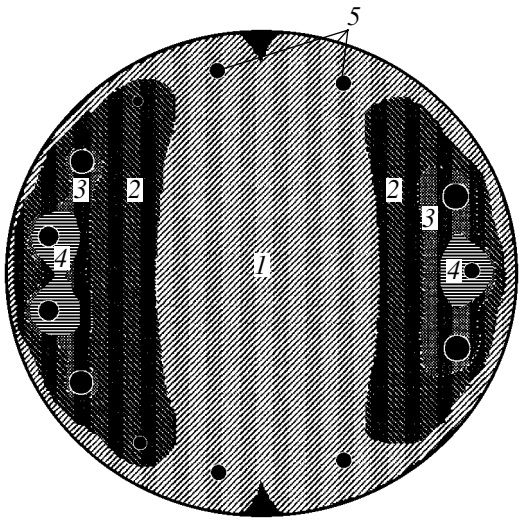


**Fig. 3.** Magnetic field structure in the Tornado-322 device. The characteristic traces of the intersections of magnetic field lines with the meridional plane of the device are shown inside the separatrix: (*1–4*) the regions of "combined" magnetic field lines and (*5*) the regions of "individual" magnetic field lines. The outer circle is the separatrix trace.

When the magnetic field in the Tornado-X device was increased to above 0.1 T, this had little or no effect on the plasma lifetime because of the plasma loss due to bulk electron–ion recombination. In this case, the plasma lifetime is

$$\tau_i^R \approx (k^R N_e)^{-1}, \qquad (2)$$

where $k^R$ is the recombination coefficient.

From the standpoint of plasma confinement, the advantage of closed confinement systems over straight ones can be expressed as the ratio between the plasma lifetimes (for straight confinement systems, we use the expression for classical confinement [8], which is generally used in calculating multicharged ion sources)

$$\frac{\tau_i^D}{\tau_i^C} \approx \frac{R^2 \nu_{ei}}{D_\perp^{ef}} \sim \frac{R^2 B^2}{T_e}. \qquad (3)$$

This advantage is most pronounced with high magnetic fields. For example, in the Tornado-322, at a magnetic field of ~2 T and an electron temperature of 1 keV, ratio (3) is equal to $10^4$.

We emphasize that, in this paper, we assume that the plasma losses are determined by the classical cross-field diffusion and recombination even at substantially higher temperatures than those in [5, 6].

## PLASMA HEATING

The ECR heating of the electron component is the most efficient method for creating a strongly nonequilibrium plasma with parameters that are optimum for producing multicharged ions, namely, a plasma with hot electrons (whose temperature is close to 1 keV) and cold ions (whose temperature is only a few electronvolts). Unfortunately, experimental data from which it might be possible to estimate the efficiency of the ECR heating in the Tornado device are still lacking (such experiments are planned for the immediate future). The magnetic field structure in this confinement system is very complicated; hence, a detailed theoretical analysis of microwave absorption is impossible at this stage of the research. However, some inferences about the possibility of plasma heating can be made based on general considerations.

The longitudinal launching of microwaves (when the wave vector is parallel to the magnetic field) is most efficient with respect to microwave absorption in small experimental devices. However, the specific features of the magnetic field structure in the Tornado device make such launching impossible.

Estimates show that, at nonlongitudinal launching, the single-pass absorption of cyclotron microwaves is low (the optical thickness of the plasma for normal waves is small). A substantial increase in microwave absorption may be achieved due to the multipass wave traveling (because the vacuum chamber containing the confinement system is a microwave cavity) or, probably, to the absorption at the upper hybrid resonance frequency.

The strongly inhomogeneous magnetic field of the confinement system allows us to expect microwave absorption in the plasma over a wide frequency range. In this paper, we assume that the microwave power is totally absorbed by the plasma if there is a resonance region inside the separatrix and that the incident microwave radiation is totally absorbed regardless of the plasma density (provided that the weak reflection condition $N_e < N_{cr}$ is satisfied; i.e., the plasma density is less

than the critical plasma density for a given pumping microwave frequency).

## MCI PRODUCTION IN THE PLASMA OF THE TORNADO CONFINEMENT SYSTEM

The duration of the magnetic field pulse in the Tornado-322 device coincides with the plasma lifetime by an order of magnitude. Hence, in order to calculate the distribution of ions over charge states (DICS), we should solve a set of time-dependent differential ionization-balance equations for ions (in all charge states), electrons, and neutral atoms. The DICS was calculated for an argon plasma within a zero-dimensional model: the densities and temperatures of all particles were assumed to be uniform throughout the entire volume of the device.

The density $N_i$ of ions in the $i$th charge state is determined by the processes of ionization, recombination, charge exchange with neutrals, and the rate of cross-field plasma diffusion

$$\frac{\partial N_i}{\partial t} = (k_{i-1\to i}N_{i-1} - k_{i\to i+1}N_i + k^R_{i+1\to i}N_{i+1} - k^R_{i\to i-1}N_i)N_e + (k^{CX}_{i+1\to i}N_{i+1} - k^{CX}_{i\to i-1}N_i)N_0 - \frac{N_i}{\tau}, \quad (4)$$

where $k_{i,\,i+1}$ are the electron-impact ionization constants calculated by the formula

$$k_{i,\,i+1} = \frac{C_2(1 + C_1\sqrt{\varepsilon_i/T_e})}{C_3 + \varepsilon_i/T_e}\left(\frac{\varepsilon_i}{T_e}\right)^{C_4}\exp\left(-\frac{\varepsilon_i}{T_e}\right)(\mathrm{cm}^3\ \mathrm{s}^{-1}).$$

Here, $\varepsilon_i$ is the ionization energy of the ion in the $i$th charge state (in electron volts) and $T_e$ is the average electron energy. The values of the parameters $C_i$ are tabulated in [9]; $k^R_{i+1\to i} = k^{RR}_{i+1\to i} + k^{DR}_{i+1\to i}$ is the sum of the rate constants of photorecombination and dielectronic recombination:

$$k^{RR}_{i+1\to i} = A_{\mathrm{rad}}(1.16T_e)^{-X_{\mathrm{rad}}}\ (\mathrm{cm}^3\ \mathrm{s}^{-1}),$$

$$k^{DR}_{i+1\to i} = \frac{1}{T_e^{3/2}}\sum_{j=1}^{3} C_j\exp\left(-\frac{E_j}{T_e}\right)(\mathrm{cm}^3\ \mathrm{s}^{-1}),$$

the values of the factors $A_{\mathrm{rad}}$, $X_{\mathrm{rad}}$, $C_j$, and $E_j$ are tabulated in [10, 11]; and $k^{CX}_{i+1,\,i}$ is the rate constant of charge exchange of ions with neutrals [12]:

$$k^{CX}_{i\to i-1} = 1.43\times 10^{-6} i^{1.17}\varepsilon_0^{-2.76}\sqrt{\frac{T_i}{M_i}}\ (\mathrm{cm}^3\ \mathrm{s}^{-1}).$$

Here, $\varepsilon_0$ is the ionization energy of neutral atoms and $T_i$ and $M_i$ are the temperature and mass of ions, respectively. In numerical simulations, the temperatures of ions with different charges were assumed to be equal, because the energy equalization times of different ion components are much shorter than the ion lifetime in the confinement system. The cross-field diffusion time was taken to be the same for ions in all charge states and was calculated by formula (1).

The gas-density equation has the form

$$\frac{\partial N_0}{\partial t} = I + (k^R_{1\to 0}N_1 - k_{0\to 1}N_0)N_e - N_0\sum_{i=2}^{18} N_i k^{CX}_{i\to i-1}, \quad (5)$$

where, $I$ is the power of the neutral gas source in the confinement system.

The electron balance equation has the form

$$\frac{\partial N_e}{\partial t} = N_e\sum_{i=0}^{17}(k_{i\to i+1}N_i - k^R_{i+1\to i}N_{i+1}) - \frac{N_e}{\tau}. \quad (6)$$

The electron temperature is determined by the microwave power $P$ absorbed in the plasma; energy losses due to collisional heating of ions, ionization, and electron–ion recombination; and diffusion electron losses:

$$\frac{\partial(N_eT_e)}{\partial t} = \frac{P}{V} - \frac{2m_e}{M_i}N_e\sum_{i=1}^{18}\nu_{ei}(T_e - T_i) - N_e\sum_{i=0}^{17}(k_{i\to i+1}U_iN_i + T_ek^R_{i+1\to i}N_{i+1}) - \frac{N_eT_e}{\tau}, \quad (7)$$

where $V$ is the confinement system volume and $\nu_{ei}$ is the frequency of electron–ion collisions.

The ion energy balance is described by the equation

$$\frac{\partial\left(T_i\sum_{i=1}^{18}N_i\right)}{\partial t} = P_{\mathrm{col}} + P_{IR} + P_{CX} + P_{\mathrm{loss}}, \quad (8)$$

where the terms on the right-hand side allow for the following processes:

$$P_{\mathrm{col}} = \frac{2m_e}{M_i}N_e(T_e - T_i)\sum_{i=1}^{18}\nu_{ei} - \frac{1}{2}(T_i - T_0)\sum_{i=1}^{18}N_i\nu_{i0}$$

describes the heating of ions due to collisions with electrons and their cooling in collisions with neutral atoms (here, the gas temperature $T_0$ is assumed to be time-independent and $\nu_{i0}$ is the frequency of ion-atom collisions); $P_{IR} = T_0k_{o\to 1}N_eN_0 - T_ik^R_{1\to 0}N_1N_e$ describes the production of ions with temperatures equal to the neutral temperature due to neutral gas ionization and their cooling due to the recombination of singly charged ions;

$$P_{CX} = N_0\left(T_0\sum_{i=0}^{17}k^{CX}_{i+1\to i}N_{i+1} - T_ik^{CX}_{1\to 0}N_1\right)$$

describes the energy exchange between ions and neutrals during charge exchange; and

$$P_{\text{loss}} = -\frac{N_i T_i}{\tau}$$

describes the energy loss associated with ion diffusion.

## RESULTS OF DICS CALCULATIONS

The optimum frequency for plasma heating in the confinement system under study lies in the range $f$ = 30–60 GHz. The radiation at these frequencies will be absorbed near the separatrix, where the magnetic field strength is between 1.07 and 2.14 T. Presently, appropriate high-power gyrotrons are produced at the Institute of Applied Physics (see Tables 1 and 2).

Since the plasma lifetime in the confinement system coincides with the duration of the magnetic field pulse by an order of magnitude, the time of resonance plasma heating is limited by the duration of the magnetic field pulse (Fig. 4). This is a decisive factor determining the possibility of achieving the DICS with a high average charge.

As an example, the production of multicharged ions in the Tornado-322 device was calculated for the case of ECR plasma heating by a gyrotron operating at a frequency of $F$ = 53 GHz and a power of $P$ = 25 kW. The maximum microwave pulse duration of such a gyrotron attains 200 ms (see Tables 1 and 2), which makes it possible to heat the plasma throughout the entire magnetic field pulse. The critical plasma density for the given gyrotron frequency is fairly high: $N_{\text{cr}} = 3.47 \times 10^{13}$ cm$^{-3}$. Therefore, it is possible to maintain a sufficiently high plasma density in the device under the condition of weak microwave reflection $N_e < N_{\text{cr}}$; to achieve the high values of the confinement parameter $N_e\tau$; and, consequently, to obtain the DICS with a high average charge. In calculations, we used the model radiation absorption diagram presented in Fig. 4.

Figure 4 shows the time dependence of the magnetic field strength in the magnetic barrier of the Tornado-322 (for the limiting parameters of the available magnetic-field capacitor banks $C$ = 33 mF, $U$ = 5 kV, and $W$ = 413 kJ). The figure also shows the time dependence of the density of $Ar^{16+}$ ions calculated from Eqs. (4)–(8) for the initial neutral gas pressure in the device $P_0 = 6 \times 10^{-5}$ torr. Figure 5 demonstrates a DICS with the highest average ion charge for the same initial conditions. This DICS is formed at the time when the density of $Ar^{16+}$ ions is maximum (Fig. 4), i.e., after the microwave pulse has finished. Owing to a high absorbed power, the electrons that acquired an energy of $T_e \sim$ 1–3 keV continue to efficiently strip multicharged ions during a certain period of time after switching off the microwave power because the plasma lifetime in the confinement system is fairly long. In the regime presented in Figs. 4 and 5, the maximum electron density in the discharge during ECR plasma heating is $\{N_e(t)\}_{\max} = 2.1 \times 10^{13}$ cm$^{-3} < N_{\text{cr}}$; i.e., the condition of weak microwave reflection is satisfied.

**Table 1.** Best Russian gyrotrons operating in the continuous mode [13] (updated list)

| Frequency, GHz | Output power, kW | Magnetic field, T | Magnet type |
|---|---|---|---|
| 30 | 25 | 0.55 | *Ns*[a] |
| 37.5 | 20 | 1.45 | SCM[b] |
| 83 | 20 | 3.2 | SCM |

Note: *a* and *b* refer to a "warm" solenoid and a superconducting magnet, respectively.

**Table 2.** Russian gyrotrons [13] (updated list)

| Frequency, GHz | Output power, kW | Pulse duration, s |
|---|---|---|
| 28 | 500 | 0.1 |
| 53 | 500 | 0.2 |
| 83 | 500 | 2 |
| 100 | 2100 | $3 \times 10^{-5}$ |
| 110 | 1300 | $10^{-4}$ |
| 110 | 6000 | 2 |
| 140 | 550 | 3 |
| 140 | 500 | 2 |
| 168 | 500 | 0.7 |

## EXTRACTION OF THE ION BEAM

To extract the ion beam from the Tornado device, we propose to use an auxiliary coil disconnecting the magnetic field lines as is shown in Fig. 6.

For the DICS shown in Fig. 5, the maximum current associated with the cross-field diffusion of $Ar^{16+}$ ions is equal to 1.5 mA/cm$^2$. Rough estimates show that, when the auxiliary coil is used, the density of the extracted ion current can substantially exceed this level. Let us estimate by the order of magnitude of the saturation ion current that can be extracted from the confinement system

$$I_s \approx e\langle Z\rangle N_i V_s S_{\max} \approx eN_e\sqrt{\frac{\langle Z\rangle T_e}{M_i}}S_{\max}. \qquad (9)$$

Here, $\langle Z\rangle$ is the average ion charge, $V_s$ is the ion acoustic velocity, and the quantity $S_{\max}$ characterizes the maximum cross section of the magnetic flux tube formed by the field lines that can be "uncoupled" by the auxiliary coil. We estimate $S_{\max}$ by the following formula:

$$S_{\max} \sim S_0\frac{B_{\text{in}}}{B_{\text{b}}}\frac{\Phi_\infty}{\Phi_0},$$

where $S_0$ is the area bounded by the inner helical coil in the equatorial plane of the confinement system; $\Phi_0$ is the characteristic magnetic flux through this area; $\Phi_\infty$ is the "uncoupled" magnetic flux; and $B_{in}$ and $B_b$ are the magnetic field strengths in the inner part of the device and in the barrier, respectively (their ratio is $B_{in}/B_b \sim 0.25$). For estimates, we take $\Phi_0/\Phi_\infty \sim 10^{-4}$. This is justified if the auxiliary extracting coil has no effect on the structure of the magnetic field as a whole. Under this assumption, for the plasma density $N_e = 2 \times 10^{13}$ cm$^{-3}$ and the electron temperature $T_e = 1$ keV, the maximum extracted ion current (9) is approximately equal to 1 A.

## POSSIBLE APPLICATIONS OF AN ECR MCI SOURCE BASED ON THE TORNADO CONFINEMENT SYSTEM

The parameters of the DICS (the average charge and ion current) that can be achieved, according to calculations, with an ECR MCI source based on the Tornado-322 device are presently the record parameters among all types of MCI sources. The possibility of achieving the record average charges and ion currents and a wide range of the DICS parameters that can be obtained with an ECR MCI source based on the Tornado-322 device make this ion source very attractive for various applications, e.g., for accelerators of heavy ions.

One possible application of the proposed source is to use it as an ion source for the medical accelerator of heavy ions in Chibo (Japan) [14]. This medical accelerator requires a pulsed source of argon ions with a relatively high average charge of +8 to +9, an ion current of 10–100 mA, a repetition rate of 2 Hz, and a power consumption that is not too high ($P_B < 100$ kW). To comply with these technical requirements, the ECR MCI source based on the Tornado-322 device should be optimized as follows. To reach an average ion charge of +8 to +9, it is necessary that the confinement parameter be $N_e\tau \sim 6 \times 10^9$ cm$^{-3}$ s (at an electron temperature of $T_e \sim 300$ eV). Here, $\tau$ is, in fact, the duration of the magnetic field pulse for an optimized device, because the plasma lifetime in this device is substantially longer. The value of $\tau$ can be reduced several times as compared to the magnetic field pulse shown in Fig. 4 by reducing the capacitance of the magnetic-field capacitor bank ($\tau \propto \sqrt{C}$). In this case, $\tau$ will be as low as several milliseconds and the required plasma density will be on the order of $10^{12}$ cm$^{-3}$. At the reduced capacitance of the capacitor bank, along with the $\tau$ value, the magnetic field in the confinement system will be reduced by the same factor ($B \propto \sqrt{C}$). This will allow one to use a lower frequency microwave source (e.g., a klystron) for ECR plasma heating instead of an expensive gyrotron. The microwave frequency $f$ should satisfy the condition $N_{cr}(f) \geq 10^{12}$ cm$^{-3}$.

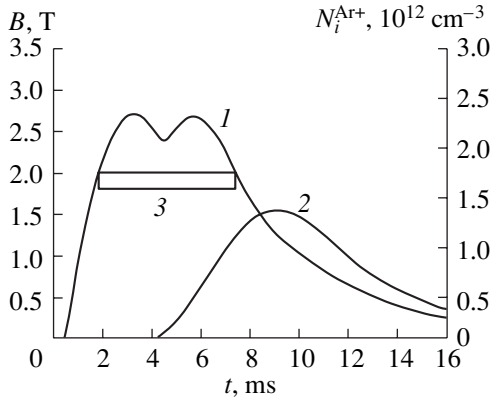


**Fig. 4.** (*1*) Magnetic field pulse in the Tornado-322 device, (*2*) the calculated time dependence of the density of $Ar^{16+}$ ions, and (*3*) the model radiation absorption diagram used in numerical modeling at a frequency of 53 GHz, power of 25 kW, and duration of 6 ms ($t$ is time; the residual gas pressure in the camber is $P_0 = 6 \times 10^{-5}$ torr).

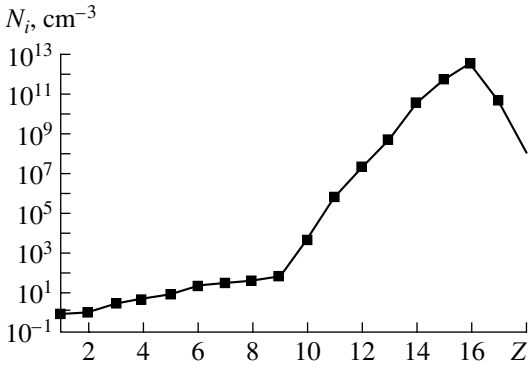


**Fig. 5.** DICS calculated for $F = 53$ GHz, $P = 25$ kW, and the same initial conditions as in Fig. 4 ($N_i$ is the density of argon ions and $Z$ is the ion charge number).

Calculations show that the required DICS can be achieved at a klystron frequency of 15 GHz (the resonance magnetic field is $B_r = 0.54$ T) and a power of 2 kW. The supply voltage of the magnetic-field capacitor bank should be $U = 5$ kV. The capacitance of the capacitor bank should be decreased 16 times as compared to the existing capacitance $C \approx 2$ mF. In this case, the duration of the magnetic field pulse will be approximately 4 ms and the barrier magnetic field will be 0.7 T. At a repetition rate of 2 Hz, the power consumption of the capacitor bank will be 50 kW. Figure 7 shows the DICS calculated for the given parameters of the ECR source. The maximum plasma density during ECR heating is $\{N_e(t)\}_{max} \leq 2.2 \times 10^{13}$ cm$^{-3}$, which is below the critical plasma density for a frequency of 15 GHz ($N_{cr} = 2.79 \times 10^{12}$ cm$^{-3}$). The maximum current associated with the diffusion loss of $Ar^{8+}$ and $Ar^{9+}$ ions is ~0.5 mA/cm$^2$. With an auxiliary coil, the maximum ion current that, according to formula (9), can be extracted from the confinement system is on the order

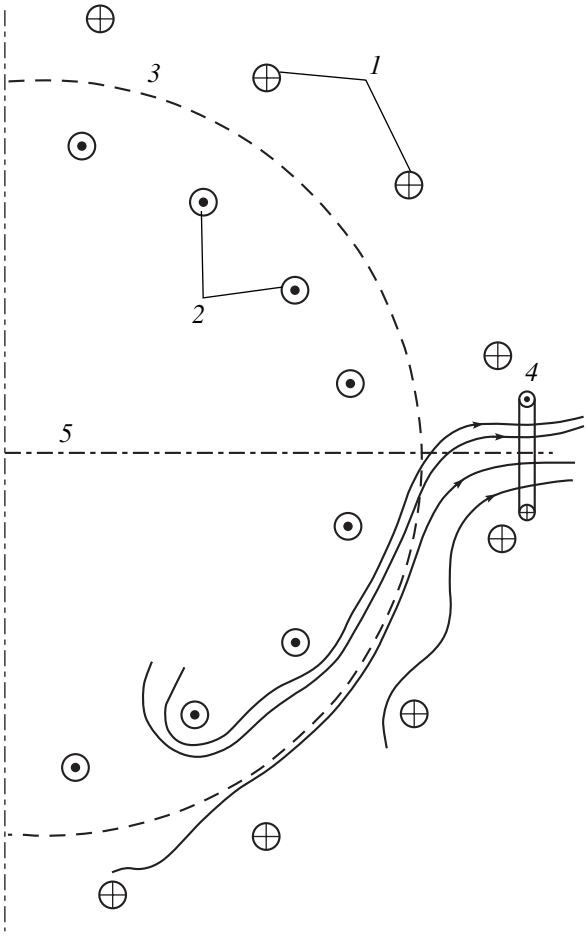


**Fig. 6.** Disconnecting of magnetic field lines in the confinement system with the help of an auxiliary extracting coil: (*1*) outer helical coil, (*2*) inner helical coil, (*3*) separatrix, (*4*) auxiliary coil, and (*5*) equatorial plane.

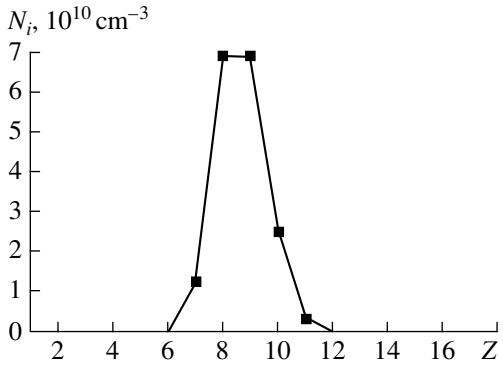


**Fig. 7.** Calculated DICS in a source optimized for the medical heavy-ion accelerator in Chibo (Japan); $F$ = 15 GHz, $P$ = 2 kW, and the initial gas pressure in the device is $P_0 = 1 \times 10^{-5}$ torr ($N_i$ is the density of argon ions and $Z$ is the ion charge number).

of 100 mA. Hence, the DICS that can be obtained in the given modification of the ECR ion source based on the Tornado-322 device is suitable for use in the Chibo medical heavy-ion accelerator.

Presently, we consider a hypothetical possibility of using the ECR ion source based on the Tornado-322 device in the heavy-ion accelerator at CERN. This accelerator requires a pulsed source of multicharged lead ions (from $Pb^{25+}$ to $Pb^{27+}$). The ion current should be ~10 mA at a pulse duration of 100 μs and a repetition rate of 1 Hz. The power consumption can be several hundreds of kilowatts. Unfortunately, exact calculations of the DICS in a lead plasma are still impossible because of the lack of data on the ionization and recombination cross sections for lead ions. However, the record parameters of the calculated DICS for the test gas (argon) allow us to expect that the proposed ion source can also be successfully optimized for use in the heavy-ion accelerator at CERN.

## CONCLUSION

In this paper, we have proposed to use the Tornado closed magnetic confinement system with microwave plasma heating for creating a source of multicharged ions [15]. Plasma losses in closed confinement systems are determined by cross-field diffusion, which substantially increases the plasma lifetime as compared to straight mirror confinement systems. Among the advantages of the Tornado confinement system, we mention the possibility of producing high magnetic fields up to 2 T (which makes it possible to heat and confine a plasma with a high electron density), the possibility of using an auxiliary coil for extracting ions, and a relatively low cost of the confinement system.

It is proposed to use the plasma heating scenario with the successive switching-on of two oscillators: an oscillator operating at a frequency of 2.45 GHz produces the initial plasma, which is the heated at a higher frequency of 15 or 53 GHz. The DICS for the Tornado-322 pulsed device was calculated for an argon plasma by numerically solving a set of zero-dimensional time-dependent differential ionization balance equations for ions in all charge states with allowance for cross-field plasma diffusion, ionization, photorecombination, dielectronic recombination, and charge exchange with neutral atoms. It is shown that it is possible to achieve the DICS with a maximum at $Ar^{16+}$ at a plasma density of $2 \times 10^{13}$ cm$^{-3}$. The extracted ion current in this case can attain 1 A.

Thus, the ECR MCI source based on the Tornado confinement system is a very promising and easily available source, which can be created in the nearest future.

## ACKNOWLEDGMENTS

We thank S.V. Golubev and M.D. Tokman for fruitful discussions.

## REFERENCES


1. G. V. Skornyakov, Zh. Tekh. Fiz. **32**, 261 (1962) [Sov. Phys. Tech. Phys. **7**, 187 (1962)]; Zh. Tekh. Fiz. **32**, 777 (1962) [Sov. Phys. Tech. Phys. **7**, 571 (1963)]; J. Nucl. Energy C **8**, 561 (1966).
2. B. P. Peregood and B. Lehnert, Nucl. Instrum. Methods **180**, 357 (1981).
3. K. V. Abramova, A. V. Voronin, K. G. Hellblom, *et al.*, Trans. Fusion Technol. **35**, 263 (1999).
4. K. B. Abramova, A. V. Voronin, M. L. Lev, *et al.*, Zh. Tekh. Fiz. **67** (1), 30 (1997) [Tech. Phys. **42**, 25 (1997)].
5. G. A. Galechyan and B. P. Peregud, Zh. Tekh. Fiz. **39**, 1696 (1969) [Sov. Phys. Tech. Phys. **14**, 1272 (1969)].
6. K. B. Abramova, A. V. Voronin, G. A. Galechyan, and M. L. Lev, Zh. Tekh. Fiz. **67** (2), 12 (1997) [Tech. Phys. **42**, 134 (1997)].
7. A. N. Kozyrev and B. P. Peregud, Zh. Tekh. Fiz. **44**, 743 (1974) [Sov. Phys. Tech. Phys. **19**, 468 (1974)].
8. V. P. Pastukhov, Nucl. Fusion **14**, 235 (1974).
9. G. S. Voronov, At. Data Nucl. Data Tables **65** (1), 1 (1997).
10. J. M. Shull and M. van Steenberg, Astrophys. J., Suppl. Ser. **48**, 95 (1982).
11. P. Mazzotta, G. Mazzitelli, S. Colafrancesco, and N. Vittorio, Astron. Astrophys., Suppl. Ser. **133**, 403 (1998).
12. A. Muller and E. Salzborn, Phys. Lett. A **62**, 391 (1977).
13. A. L. Goldenberg and A. G. Litvak, Phys. Plasmas **2**, 2562 (1995).
14. A. Kitagawa, M. Muramatsu, M. Sekiguchi, *et al.*, Rev. Sci. Instrum. **71**, 1061 (2000).
15. K. B. Abramova, A. N. Smirnov, A. V. Voronin, and V. G. Zorin, Rev. Sci. Instrum. **71**, 921 (2000).


*Translated by N. Larionova*

*Technical Physics, Vol. 46, No. 10, 2001, pp. 1322–1325. Translated from Zhurnal Tekhnicheskoĭ Fiziki, Vol. 71, No. 10, 2001, pp. 120–122.*


**BRIEF COMMUNICATIONS**

# Surface Ionization of Products from Monomolecular Disintegration of Multimolecular Complexes

**G. Ya. Lavrent'ev**

*Ioffe Physicotechnical Institute, Russian Academy of Sciences, Politekhnicheskaya ul. 26, St. Petersburg, 194021 Russia*

Received October 2, 2000

**Abstract**—Mechanisms behind the narrow bell-shaped temperature dependences of the fluxes of ions and molecules being desorbed from the surface at low emitter temperatures have not been discovered so far. A model is suggested that allows the consideration of the narrow low-temperature peaks of various nature (associated ion peaks, dimer peaks, and those appearing under nonequilibrium surface ionization) from the unified viewpoint. It is believed that multimolecular complexes form on the surface and then disintegrate into fragments by the mechanism of monomolecular reactions with subsequent ionization of the fragments on the emitter surface.


Upon studying surface ionization, the temperature dependences of the desorbed ion current are usually used to determine the ionization potentials $V$ of atoms [1] and polyatomic particles [2]. In the latter case, either the initial portions of the curves or the peak current values are taken into consideration.

In [3, 4], the phenomenological description of reaction product ionization taking place on the surface during the monomolecular disintegration of polyatomic particles has been reported. This approach has made it possible to account for the bell-shaped temperature dependences of the polyatomic ion current $j(T)$ at high temperatures (1300–2000 K) and determine the ionization potentials, energy of activation of surface disintegration, the number of effective degrees of freedom, ion–surface interaction potentials [5], etc. However, along with the relatively broad high-temperature $j(T)$ peaks (with a half-width $\Delta j$ = 600–800 K), there exist extremely narrow $j(T)$ peaks ($\Delta j$ = 100–200 K) at low temperatures. The latter are observed, for example, in the case of associated ions [6] and ionized dimers [7]. Similar narrow temperature curves of the ion current have been obtained by the author in studying the nonequilibrium surface ionization of the products of acetone peroxide exothermic disintegration. Analysis of these peaks according to [3, 4] has failed, since the calculated number of degrees of freedom exceeded the actually available by one order of magnitude. In this work, an attempt to analyze the narrow temperature dependences of the polyatomic ion current in terms of the concept of multimolecular complexes and monomolecular disintegration is undertaken.

In [3, 4], the theory of monomolecular reaction in the gaseous phase was applied to the heterogeneous disintegration of polyatomic molecules with their subsequent ionization by the surface ionization mechanism. The justification of this theory was based on the principle of detailed balancing. In the gaseous phase, molecules are activated by collisions, whereas at the surface, molecules being adsorbed become excited when striking surface atoms. The lifetime of active molecules on the surface is negligible compared with the time of their de-activation, since the activation of an adsorbed molecule takes place only when the oscillation amplitudes of surface atoms are large, which is statistically of a low probability. Medium-amplitude atomic oscillations on the surface cause neither activation nor de-activation of the adsorbed molecules. For the rapid disintegration of the molecules, the experimental bell-shaped temperature dependences are described in terms of the statistical theory of monomolecular reactions, which gives the following expression for the rate constant [8]:

$$k_m = F\left[\frac{E}{kT}\right]^{s-1}\exp\left(-\frac{E}{kT}\right). \quad (1)$$

Here, $F$ = const, $E$ is the activation energy of the reaction (surface reaction in our case), and $s$ is the total number of vibrational degrees of freedom of a molecule (for polyatomic molecules, $s = 3n - 6$). The parameter $s$ is used when $kT \gg h\nu$, where $\nu$ is the oscillation frequency of the molecule. In the opposite case, i.e., $kT \ll h\nu$ (all our experiments fall into this range), the effective number of degrees of freedom $b$ [8] is taken instead of $s$. Usually, $b = (1/4 - 1/3)s$ [3, 4]. Then,

$$k_m = D\left[\frac{E}{kT}\right]^{b}\exp\left(-\frac{E}{kT}\right). \quad (2)$$

The rate constant $k_m$ is proportional to the number of activated adsorbed molecules that disintegrate into fragments ionizing on the surface. An expression for the current $j(T)$ of ions being desorbed from the surface

can be obtained by multiplying $k_m$ by the degree of surface ionization $\alpha$ ($\alpha \ll 1$) [4].

This expression will be given later. Note only that the preexponential in the expression for $j(T)$ is the same as in (2). As follows from (2), it is the preexponential that governs the descending branch (trailing edge) of the bell-shaped curves $k_m(T)$ and $j(T)$ is the same as in (2). As follows from (2), it is the pr; hence, it defines the half-width. As was already mentioned, the preexponential in (2) cannot describe the narrow temperature dependences. The parameter $b$ is proportional to the number of degrees of freedom for a disintegrating molecule or its fragment; hence, it is invariable for a given object. Consequently, the base of the power function in the preexponential must have a temperature dependence stronger than $1/kT$ to describe the narrow peaks in the temperature curves. Trimolecular reactions offer such an example. It is known [9] that they feature a negative temperature coefficient. The disintegration of a trimolecular complex is qualitatively explained within the theory of activated complex.

Let us assume that surface molecules form molecular complexes of two, three, four, etc. molecules at relatively low temperatures. This is a typical behavior of both atomic and molecular gases on the surface [10, 11]. The formation of multimolecular complexes on the surface may go in parallel with the dissociation, substitution, and association of the constituent molecules; in other words, the forming complex may be activated. Let us find the temperature dependence of the preexponential of the rate constant for some reaction (dissociation or disintegration) of this complex. Following the same line of reasoning as in [9], where the expression for the rate constant of a trimolecular reaction (hence, for the disintegration of a trimolecular complex) was derived, we write the general expression for the disintegration of a multimolecular complex $A_N \rightleftharpoons A_1 + \ldots + A_N$, relying on the concepts of the theory of activated complex:

$$k_N = \frac{kTQ^{\#}_{1,2\ldots N}}{hQ^N_A} e^{-\frac{E}{kT}}$$

$$= \frac{g^{\#}\frac{kT}{h}\left(\frac{2\pi\mu^{\#}kT}{h^3}\right)^{\frac{3}{2}}\frac{8\pi^2(8\pi^3 I^{\#}_x I^{\#}_y I^{\#}_z)^{\frac{1}{2}}(kT)^{\frac{3}{2}}}{\sigma^{\#}h^3}\prod_{i=1}^{3Nn-7}\left[1-\exp\left(-\frac{h\nu^{\#}_i}{kT}\right)\right]^{-1}}{g^N_A\left(\frac{2\pi m_A kT}{h^3}\right)^{\frac{3}{2}N}\left[\frac{8\pi^2(8\pi^3 I_x I_y I_z)^{\frac{1}{2}}(kT)^{\frac{3}{2}}}{\sigma_A h^3}\right]^N\left[\prod_{i=1}^{3n-6}\left[1-\exp\left(-\frac{h\nu_i}{kT}\right)\right]^{-1}\right]^N} e^{-\frac{E}{kT}}, \quad (3)$$

where $\mu^{\#}$ is the reduced mass; $m_A$ is the mass of molecule $A$; $N$ is the number of molecules in complex $A_N$; $n$ is the number of atoms in molecule $A$; $I^{\#}_x$, $I^{\#}_y$, $I^{\#}_z$, $I_x$, $I_y$, and $I_z$ are the principal moments of inertia of the activated complex (#) and its constituent molecules, respectively; $Q^{\#}$ and $Q_A$ are the statistical sums; $\sigma^{\#}$ and $\sigma_A$ are the symmetry factors; $\nu^{\#}$ and $\nu_i$ are the oscillation frequencies; and $g^{\#}$ and $g_A$ are the electron multiplicities.

The upper limit of the product in the numerator takes into account that one oscillation of the complex $A_N$ passes to the reaction coordinate. Equation (3) is written for the transition gas-phase complex without considering the specific features of a multimolecular complex on the surface. In particular, it ignores the fact that the surface gas may be two-dimensional, some orientation of the molecules may limit their rotation on the surface, etc. However, such detailing is yet premature.

Let us separate out factors in Eq. (3) that depend and do not depend on temperature (the product of the latter is designated by $G$). Then, Eq. (3) can be written as

$$k_N = G\frac{kT}{(kT)^{3(N-1)}}\frac{\prod_{i=1}^{3Nn-7}\left[1-\exp\left(\frac{h\nu^{\#}}{kT}\right)\right]^{-1}}{\left(\prod_{i=1}^{3n-6}\left[1-\exp\left(-\frac{h\nu_i}{kT}\right)\right]^{-1}\right)^N} e^{-\frac{E}{kT}}.$$

The temperature dependence of $k_N$ is specified by the second factor. Bearing in mind that we are dealing with the low-temperature range, we omit the ratio of the vibrational components, since

$$\left(1-e^{-\frac{h\nu}{kT}}\right) \approx 1$$

if $h\nu^{\#} \gg kT$ and $h\nu_i \gg kT$,

and obtain the simple qualitative result:

$$k_N \approx G\left(\frac{1}{kT}\right)^{3N-4} e^{-\frac{E}{kT}}. \quad (4)$$

Now consider the monomolecular disintegration of

a multimolecular complex. For the monomolecular disintegration of molecules or fragments of a multimolecular complex, the temperature dependence of the monomolecular reaction rate constant $k_m$ [see (2)] becomes stronger because of the temperature dependence of $k_N$ (4). Physically, the multimolecular complex has a significant binding energy (because of its many bonds), which can be statistically redistributed in favor of some fragment, causing, first, the disintegration of the multimolecular complex ($k_N$) and, second, the monomolecular disintegration of this fragment ($k_m$). Thus, since the processes in the multimolecular complex are primary, the preexponential of its rate constant (which has its own temperature dependence) will enter the power function of the preexponential of the monomolecular reaction rate constant $k_m$ as the base. Then, for the rate constant of the monomolecular disintegration of the multimolecular complex, we obtain

$$k_{m,N} \approx C\left[\left(\frac{1}{kT}\right)^{3N-4}\right]^b e^{-\frac{E}{kT}}. \tag{5}$$

Now, taking into account subsequent ionization (that is, multiplying (5) and (2) by the degree of surface ionization $\alpha$), we come to the dependences of the ion current on temperature and electric field:

$$j_N(T, F) \approx egA\left(\frac{1}{kT}\right)^{(3N-4)b} \times \exp\frac{e(\varphi + \sqrt{eF} - V) - E}{kT} \tag{6}$$

for the ions desorbed from the multimolecular complex and

$$j(T, F) = egB\left(\frac{E}{kT}\right)^b \exp\frac{e(\varphi + \sqrt{eF} - V) - E}{kT} \tag{7}$$

for one-molecule disintegration. Here, $g$ is the particle flux onto the surface, $A$ and $B$ are constants, $E$ is the energy of surface disintegration activation, $e$ is the charge of an electron, $e\varphi$ is the work function on the surface, $F$ is the field strength, and $kT$ is the surface temperature.

As follows from (6), for a multimolecular complex consisting, for example, of five molecules, the exponent of the preexponential increases by one order of magnitude compared with that in (7); hence, the trailing edge of the bell-shaped temperature curve is extremely steep and the half-width of the curve $j_N(T, F)$ is very small.

Formulas (6) and (7) describe the bell-shaped temperature curves for the ion current. By equating the first- and second-order derivatives of $j(T)$ and $j_N(T)$ with respect to $1/kT$ to zero, we determine the values of the temperature $T_m$ that corresponds to the peaks in the curves, and the values of $T_1$ and $T_2$ at which the curves $j(T)$ and $j_N(T)$ have inflections. Eventually, we have from (7) [3]

$$bkT_m = e(V - \varphi - \sqrt{eF} + E), \tag{8}$$

$$b = (T_m/T_1 - 1)^{-2}. \tag{9}$$

The dependence $b(F)$ found experimentally and Eq. (7) allow the value of $E$ to be found from current values for two fields [3].

Designating $(3N - 4)b = b^*$ in (6), we arrive at

$$b^* = (T_m/T_1 - 1)^{-2}. \tag{10}$$

The value of $b$ is determined using (10) and the preexponential exponent in (6):

$$b = \frac{b^*}{3N - 4}. \tag{11}$$

The ionization potential is given by Eq. (8) as before, because this equation involves the value of $T_m$ at the maximal current ion, not the width of the curve $j_N(T)$. With $b$ determined from (11), the ionization potential cannot be uniquely found from (8), since $N$ is not defined independently. Yet, we can find the order of $N$ and $V$, because the spread of the ionization potentials for polyatomic molecules of certain types is 1 to 2 eV.

At $N = 1$ and in view of (10) and (11), Eq. (6) passes to initial equation (7) up to the constant factor ($E^b$). Indeed, the exponent of the preexponential in (6) becomes negative at $N = 1$. However, the value of $b$ determined from (11) at $N = 1$ is $b = -b^*$, since $b^*$ is positive, as follows from (10). For Eqs. (6) and (11) to be used independently for all $N$, we separate out the numerical factor $E^{(3N-4)}$ from the constant $C$ in (6), insert it in the base of the preexponential in (6), and write the absolute value of the exponent. In so doing, Eq. (6) at $N = 1$ will be identical to Eq. (7). Eventually, for Eqs. (6) and (10), we will have, respectively,

$$j_N(T, F) \cong e\nu D\left(\frac{E}{kT}\right)^{|3N-4|b} \times \exp\frac{e(\varphi + \sqrt{eF} - V) - E}{kT}, \tag{12}$$

$$b = \frac{b^*}{|3N - 4|}. \tag{13}$$

Taking account of the above-mentioned specifics of the transition complex on the surface will change the coefficient before $N$ in Eqs. (12) and (13), leaving the structure of the equations unchanged.

To conclude, our model makes it possible to consider the narrow low-temperature peaks of ions of various nature (associated ion peaks, dimer peaks, and those appearing under nonequilibrium surface ionization) from the unified viewpoint. It is believed that multimolecular complexes form on the surface and then disintegrate into fragments by the mechanism of mono-

molecular reactions with subsequent ionization of the fragments on the emitter surface.

## ACKNOWLEDGMENTS

The author thanks N.D. Potekhina and N.M. Blashenkov for the support and valuable discussions.

## REFERENCES

1. É. Ya. Zandberg and N. I. Ionov, *Surface Ionization* (Nauka, Moscow, 1969).
2. É. Ya. Zandberg and U. Kh. Rasulev, Usp. Khim. **51**, 1425 (1982).
3. N. M. Blashenkov, N. I. Ionov, and G. Ya. Lavrent'ev, Pis'ma Zh. Tekh. Fiz. **13**, 392 (1987) [Sov. Tech. Phys. Lett. **13**, 160 (1987)].
4. N. M. Blashenkov, N. I. Ionov, and G. Ya. Lavrent'ev, Teor. Éksp. Khim**. 24** (1), 62 (1988).
5. N. M. Blashenkov and G. Ya. Lavrent'ev, Zh. Tekh. Fiz. **61** (1), 155 (1991) [Sov. Phys. Tech. Phys. **36**, 93 (1991)].
6. É. Ya. Zandberg and U. Kh. Rasulev, Dokl. Akad. Nauk SSSR **187**, 777 (1969) [Sov. Phys. Dokl. **14**, 769 (1970)].
7. N. I. Ionov and M. A. Mittsev, Zh. Tekh. Fiz. **35**, 1863 (1965) [Sov. Phys. Tech. Phys. **10**, 1436 (1966)].
8. V. N. Kondrat'ev and E. E. Nikitin, *Kinetics and Mechanism of Gas-Phase Reactions* (Nauka, Moscow, 1975).
9. G. M. Panchenkov and V. P. Lebedev, *Chemical Kinetics and Catalysis* (Khimiya, Moscow, 1985).
10. E. W. Muller, Ergeb. Exakten. Naturwiss. **27**, 290 (1953).
11. T. T. Tsong, Surf. Sci. Rep. **8**, 127 (1988).

*Translated by V. Isaakyan*

*Technical Physics, Vol. 46, No. 10, 2001, pp. 1326–1330. Translated from Zhurnal Tekhnicheskoĭ Fiziki, Vol. 71, No. 10, 2001, pp. 123–127.*


**BRIEF COMMUNICATIONS**

# Transformation of a Plane Wave by a Periodically Time Modulated Dielectric Medium

**N. I. Slipchenko, L. N. Shul'ga, and O. N. Rybin**

*Kharkov Technical University of Radioelectronics, Kharkov, 61726 Ukraine*

Received October 30, 2000

**Abstract**—The problem of the transformation of a plane monochromatic wave by a finite-duration sequence of periodic rectangular pulses of the dielectric permittivity and magnetic permeability is solved exactly with integral equations. The expressions for the transformed component of the electric field at any point in space at an arbitrary time are derived and analyzed. © *2001 MAIK "Nauka/Interperiodica".*

## INTRODUCTION

In the theory of wave processes, an important place is occupied by the study of the parametric modulation of media. Thus, of particular interest is the investigation of the transformation of electromagnetic waves in a medium whose parameters are periodically modulated in time. This problem has been extensively discussed in the specialized literature (see, e.g., [1–3]). In a certain spectral region, the changes in the electric and magnetic properties of a medium, caused by the changes in its dielectric permittivity and magnetic permeability, can be regarded as being jumplike [4]. This fact motivates theoretical interest in the problem of the transformation of electromagnetic waves in a medium modulated in time by a periodic sequence of rectangular pulses of the dielectric permittivity and magnetic permeability.

It should be noted that, according to the analysis of [1–3] and some other papers, analytic studies of the transformation of waves by periodically time modulated media are usually carried out only approximately under a number of simplifying assumptions. Harfoush and Taflove [5] carried out an approximate analytic investigation of the transformation of a plane wave by a medium that occupies a half-space and whose conductivity is harmonically modulated in time. However, their analysis was based on the methods of perturbation theory and was thereby restricted to small modulation depths. In addition, they considered the idealized case in which the parameters of the medium were modulated over an infinite time interval. In this context, it is of interest to investigate the transformation of electromagnetic waves by media whose physical parameters change periodically over a finite time interval.

In this study, we obtain an exact solution to the problem of the transformation of a monochromatic electromagnetic wave in an unbounded medium modulated in time by a finite-duration sequence of periodic rectangular pulses of the dielectric permittivity and magnetic permeability. We assume that the repetition rate of the pulses as well as their amplitude and duration are all arbitrary and that the pulses of the dielectric permittivity and magnetic permeability have the same duration.

We derive and analyze exact expressions for the transformed component of the electric field at any point in space at an arbitrary time.

## AN ELECTRIC FIELD IN A PERIODIC STEPWISE-MODULATED MEDIUM

We assume that, at the instant $t_0 = 0$, the parameters of an unbounded medium start to vary in time according to an arbitrary law. In [6], it was shown that the evolution of the electromagnetic field in such a medium is described by the integral Volterra equation of the second kind:

$$E(t, x) = F(t, x) + \int_0^t dt' \int_{-\infty}^{\infty} dx' K(t, t', x, x') E(t', x'), \quad t > 0, \tag{1}$$

where $E(x, t)$ is the electric component of the electromagnetic field, $K(t, t', x, x')$ is the kernel of the integral equation, and $F(t, x)$ is the free term. The integral equation (1) can be solved by the resolvent method [7] as follows:

$$E(t, x) = F(t, x) + \int_0^t dt' \int_{-\infty}^{\infty} dx' R(t, t', x, x') F(t', x'), \quad t > 0, \tag{2}$$

where $R(t, t', x, x')$ is the resolvent of Eq. (1).

If, at the instant $t_0 = 0$, the dielectric permittivity and magnetic permeability change in a jumplike manner, then the kernel and resolvent of Eq. (1) can be expressed in difference form:

$$K(t, t', x, x') = [1 - m^2]\delta(t - t')\delta(x - x')$$

1063-7842/01/4610-1326$21.00 

$$-\frac{1-a^2m^2}{2a^2m^2}\frac{\partial}{\partial t}\delta(v_0(t-t')-|x-x'|),$$

$$R(t,t',x,x') = \left[1-\frac{1}{m^2}\right]\delta(t-t')\delta(x-x') \tag{3}$$

$$-\frac{1-a^2m^2}{2}\frac{\partial}{\partial t}\delta(v_1(t-t')-|x-x'|),$$

where $m = \sqrt{\mu_0/\mu_1}$, $a = \sqrt{\varepsilon_0/\varepsilon_1}$, $v_1 = c/\sqrt{\varepsilon_1\mu_1}$, $\varepsilon_0$ and $\mu_0$ are the dielectric permittivity and magnetic permeability of an unperturbed medium (for $t < 0$), $\varepsilon_1$ and $\mu_1$ are the dielectric permittivity and magnetic permeability of a perturbed medium (for $t > 0$), $c$ is the speed of light in free space, and $\delta(t)$ is the Dirac delta function.

Let the dielectric permittivity and magnetic permeability of a medium change according to the law

$$\varepsilon(t) = \varepsilon_0 + (\varepsilon_1-\varepsilon_0)\sum_{k=1}^{N}\{\Theta(t-(k-1)T) - \Theta(t-\tau_1-(k-1)T)\},$$

$$\mu(t) = \mu_0 + (\mu_1-\mu_0)\sum_{k=1}^{N}\{\Theta(t-(k-1)T) - \Theta(t-\tau_1-(k-1)T)\}, \tag{4}$$

where $\tau_1$ is the duration of each pulse, $\tau_2$ is the repetition rate of the pulses, and $T = \tau_1 + \tau_2$ is the modulation period of the parameters of the medium.

We can show that, for any time interval during which the parameters of the medium remain constant, the electric field is described by the formulas

$$E_n(t,x) = F_n(t,x) + \int_{t_{n-1}}^{t} dt' \int_{-\infty}^{\infty} dx' R_n(t,t',x,x')F_n(t',x'),$$

$$F_n(t,x) = E_0(t,x) + \sum_{i=1}^{n-1}\int_{t_{i-1}}^{t_i} dt' \int_{-\infty}^{\infty} dx' K_i(t,t',x,x')E_i(t',x'), \tag{5}$$

where $E_0(t, x)$ is the initial electric field and $R_n(t, t', x, x')$ and $K_n(t, t', x, x')$ are the resolvent and kernel of the integral equation (1). The structure of the resolvent and kernel remains the same regardless of the number $n$ of the jump in the parameters of the medium.

Based on the last assertion and the structure of formulas (3), we can readily deduce the kernel and resolvent for an arbitrary time interval during which the parameters of the medium remain constant. Thus, for the time intervals $(n-1)T < t < \tau_1 + nT$ ($n = 1, \ldots, N$), over which the dielectric permittivity and magnetic permeability take on new values, the kernel and resolvent are described by formulas (4), whereas, for the time intervals

$$\tau_1 + (n-1)T < t < nT, \quad n = 1, \ldots, N;$$

over which the parameters of the medium take on their initial values (in what follows, we will call these time intervals the "rest intervals"), the kernel and resolvent are equal to zero:

$$K_n(t,t',x,x') = 0 = R_n(t,t',x,x'). \tag{6}$$

## TRANSFORMATION OF A PLANE WAVE BY THE PERIODIC STEPWISE MODULATION OF AN UNBOUNDED MEDIUM

Let $E_0(t, x)$ be the electric field of a plane monochromatic wave of unit amplitude, $E_0(t, x) = e^{i(\omega t - kx)}$, where $k = \omega/v_0$. We insert $E_0(t, x)$ into formulas (5) to determine the transformed electric field for the time interval after the first jump in the parameters of the system:

$$E(t,x) = C_1^+ e^{i(am\omega t - kx)} + C_1^- e^{-i(am\omega t + kx)}, \quad 0 < t < \tau_1. \tag{7}$$

Here,

$$C_1^{\pm} = \mp\frac{1-am}{2}am;$$

$$E(t,x) = A_1 e^{i(\omega t - kx)} + B_1 e^{-i(\omega t + kx)}, \quad \tau_1 < t < T, \tag{8}$$

where

$$A_1 = \frac{1-a^2m^2}{4am}e^{-i\omega\tau_1}\left\{\frac{1+am}{1-am}e^{iam\omega\tau_1} - \frac{1-1m}{1+am}e^{-iam\omega\tau_1}\right\},$$

$$B_1 = -\frac{1-a^2m^2}{2iam}e^{i\omega\tau_1}\sin(am\omega\tau_1).$$

Substituting expressions (4) and (6)–(8) into formulas (5) and using mathematical induction, we arrive at the following recurrence relations for the evolution of the electric field over each time interval after the second jump in the parameters of the medium ($n = 2, \ldots, N$):

$$E(t,x) = (C_n^+ + D_n^+)e^{i(am\omega t - kx)} + (C_n^- + D_n^-)e^{-i(am\omega t + kx)}, \quad (n-1)T < t < \tau_1 + (n-1)T. \tag{9}$$

Here,

$$C_n^{\pm} = \frac{1\mp am}{2}amB_{n-1}e^{\pm i(n-1)(1\mp am)\omega T},$$

$$D_n^{\pm} = \frac{1\mp am}{2}amB_{n-1}e^{\pm(n-1)(1\pm am)\omega T};$$

$$E(t,x) = A_n e^{i(\omega t - kx)} + B_n e^{-i(\omega t + kx)}, \quad \tau_1 + (n-1)T < t < nT, \tag{10}$$

where

$$A_n = \frac{1-a^2m^2}{4am}e^{i\omega\tau_1}\Bigg\{A_{n-1}\times\left(\frac{1+am}{1-am}e^{iam\omega\tau_1}-\frac{1-am}{1+am}e^{-iam\omega\tau_1}\right)+2iB_{n-1}e^{-2i\omega(n-1)T}\sin(am\omega\tau_1)\Bigg\},$$

$$B_n = -\frac{1-a^2m^2}{4am}e^{i\omega\tau_1}\Bigg\{B_{n-1}\times\left(\frac{1-am}{1+am}e^{iam\omega\tau_1}-\frac{1+am}{1-am}e^{-iam\omega\tau_1}\right)+2iA_{n-1}e^{-2i\omega(n-1)T}\sin(am\omega\tau_1)\Bigg\}.$$

From formulas (7)–(10), we can see that, because of the modulation of the parameters of an unbounded medium, the originally monochromatic wave splits into a forward monochromatic wave and a backward monochromatic wave. The wavenumbers of the new waves coincide in absolute value with the wavenumber of the original wave, and their amplitudes and frequencies are piecewise constant functions of time.

Now, we consider the electric field at the end the sequence of $N$ modulating pulses as a function of the number $n$ of pulses. To do this, we must analyze the expressions for the coefficients $A_n$ and $B_n$. We rewrite these expressions as a system of two recurrence relations:

$$\begin{aligned}A_{n+1} &= e^{-int_2}(fA_n - e^{-2int_2}h^*B_n),\\ B_{n+1} &= e^{int_2}(-he^{2int_2}A_n + f^*B_n),\quad n = 1,\ldots,N.\end{aligned}\tag{11}$$

Here, we introduced the parameters

$$f = \frac{e^{-i(t_1-t_2)}}{2am}\{2q\cos(amt_1) + i(1+a^2m^2)a\sin(amt_1)\},$$

$$h = \frac{1-a^2m^2}{2iam}e^{i(t_1-t_2)}\sin(am\tau_1).$$

which are independent of the number of the period.

We also introduce a new notation for the amplitudes, $a_n = A_ne^{int_2}$ and $b_n = B_ne^{-int_2}$, and represent expressions (7)–(10) in matrix form:

$$\begin{pmatrix}a_{n+1}\\ b_{n+1}\end{pmatrix} = R\begin{pmatrix}a_n\\ b_n\end{pmatrix},\quad a_1 = f,\quad b_1 = -h,\tag{12}$$

where

$$R = \begin{pmatrix} f & -h^*\\ -h & f^*\end{pmatrix}.$$

Using mathematical induction puts the matrix recurrence relation (12) in the form

$$\begin{pmatrix}a_{n+1}\\ b_{n+1}\end{pmatrix} = R^n\begin{pmatrix}a_1\\ b_1\end{pmatrix}.\tag{13}$$

We raise the matrix to a power $n$ to obtain [8]

$$R^n = U_{n-1}(\mathrm{Re}(f))R - U_{n-2}(\mathrm{Re}(f))I,$$

where $U_n(x)$ is the $n$th order Chebyshev polynomial of the second kind and $I$ denotes the unit matrix.

The components of the matrix relation (13) give the following expressions for the amplitudes of the forward and backward waves over the time interval after the $(n+1)$th jump in the parameters of the medium:

$$\begin{aligned}A_{n+1} &= e^{-(n+1)/it_2}\{(f^2+|h|^2)U_{n-1}(\mathrm{Re}(f)) - U_{n-2}(\mathrm{Re}(f))f\},\\ B_{n+1} &= -he^{-(n+1)/it_2}\{(f^2+f^*)U_{n-1}(\mathrm{Re}(f)) - U_{n-2}(\mathrm{Re}(f))\}.\end{aligned}\tag{14}$$

The amplitudes of the forward and backward waves were estimated numerically for the values of $a$ and $m$ such that $\varepsilon \approx 1$ and $m \approx 1$. Our computations showed that the periodic stepwise modulation of the dielectric permittivity and magnetic permeability of the medium may lead to a situation in which the amplitudes of the forward and backward waves exceed in absolute value the amplitude of the original wave at the expense of the time variation of the dielectric permittivity (Figs. 1, 2) and/or magnetic (Figs. 3, 4) permeability.

By examining the ratios $a_{n+1}/a_n$ and $b_{n+1}/b_n$ as functions of the number $n$ of pulses, we can reveal an important feature of the behavior of the amplitudes of the forward and backward waves from pulse to pulse. We carry out the corresponding manipulations with the matrix relation (13) to see that the ratios have the form

$$\begin{aligned}\frac{a_{n+1}}{a_n} &= f - \frac{h^*}{F_n},\\ \frac{b_{n+1}}{b_n} &= f^* - hF_n,\end{aligned}\tag{15}$$

where $F_n = a_n/b_n$.

We assume that the amplitude of the backward wave is nonzero (in other words, we exclude from consideration the trapping of the backward wave). In this case, we can divide the first of equalities (1) by the second

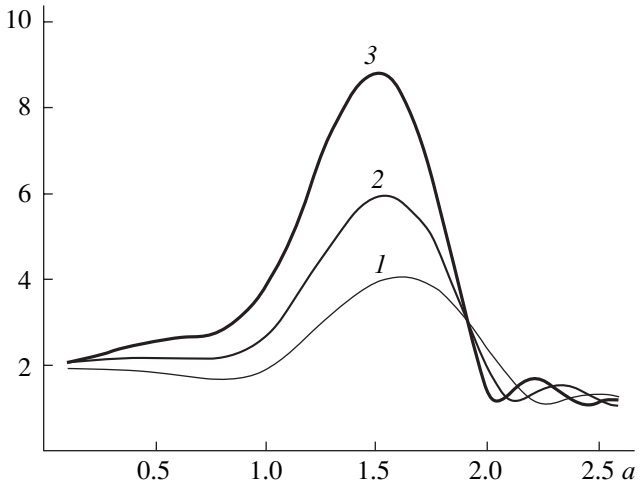


**Fig. 1.** Absolute value of the amplitude $A_n$ of the forward wave as a function of the relative change $a$ in the dielectric permittivity for $m = 1.1$, $t_1 = 1$, and $t_2 = 5$ and for different numbers of pulses perturbing the parameters of the medium: $n = (1)$ 3, $(2)$ 4, and $(3)$ 5.

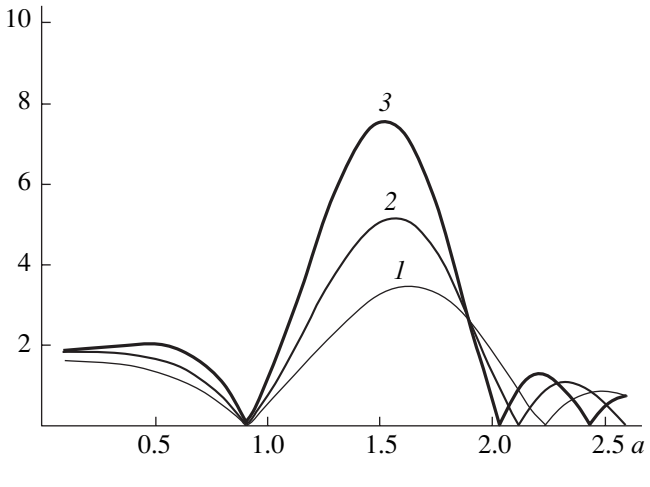


**Fig. 2.** Absolute value of the amplitude $B_n$ of the backward wave as a function of the relative change $a$ in the dielectric permittivity for $m = 1.1$, $t_1 = 1$, and $t_2 = 5$. Curves *1*, *2*, and *3* refer to the same numbers of perturbing pulses as in Fig. 1.

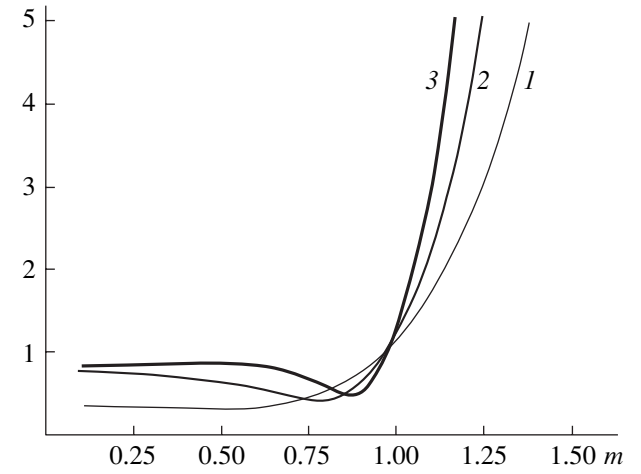


**Fig. 3.** Absolute value of the amplitude $A_n$ of the forward wave as a function of the relative change $m$ in the magnetic permeability for $a = 0.85$, $t_1 = 1$, and $t_2 = 5$ and for different numbers of pulses perturbing the parameters of the medium: $n = (1)$ 3, $(2)$ 4, and $(3)$ 5.

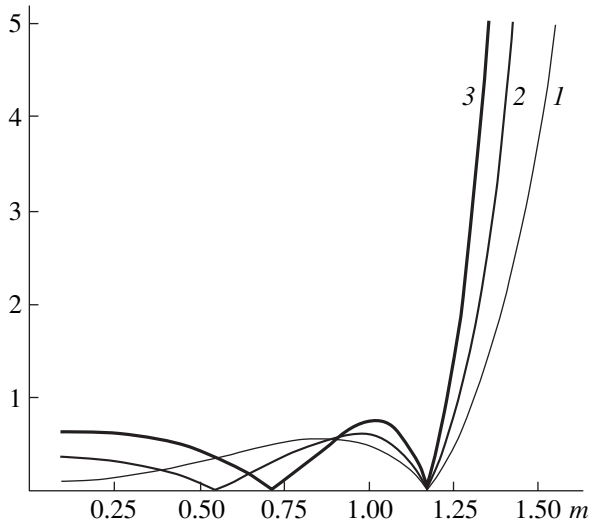


**Fig. 4.** Absolute value of the amplitude $B_n$ of the backward wave as a function of the relative change $m$ in the magnetic permeability for $a = 0.85$, $t_1 = 1$, and $t_2 = 5$. Curves *1*, *2*, and *3* refer to the same numbers of perturbing pulses as in Fig. 3.

one to arrive at the following recurrence relation for $F_n$:

$$F_{n+1} = \frac{-h^* + fF_n}{f^* - hF_n}. \qquad (16)$$

Let us analyze relation (16). For the first period, the ratio has the form

$$F_1 = \frac{a_1}{b_1} = -\frac{f}{h}$$

$$= \frac{2q\cot(am\tau_1) + i(1 + a^2m^2)}{i(1 - a^2m^2)} e^{-2i(\tau_1 - T)}.$$

The square of the absolute value of this ratio is equal to

$$|F_1|^2 = \frac{4a^2m^2\cot^2(am\tau_1) + (1 + a^2m^2)^2}{(1 - a^2m^2)^2}. \qquad (17)$$

Since $4a^2m^2\cot^2(am\tau_1) > -4a^2m^2$, we have $|F_n| > 1$. According to the theory of conformal transformations [9], the linear-fractional function (16) maps the exterior of a unit circle onto itself. Consequently, if $|F_1| > 1$, then a fortiori $|F_n| > 1$. This indicates that the amplitude of

the forward wave is always larger in absolute value than the amplitude of the backward wave.

## CONCLUSION

We have considered the transformation of a plane monochromatic electromagnetic wave by a finite-duration periodic stepwise modulation of the dielectric permittivity and magnetic permeability of an unbounded medium. We have shown that, at any point on the positive time axis, the transformed electric field is the sum of the electric fields of the forward and backward monochromatic waves, whose wave numbers coincide in absolute value with the wave number of the original wave and whose amplitudes and frequencies are piecewise constant functions of time. For the rest intervals, there is a certain range of parameter values of the medium and a certain range of frequencies of the original wave in which the amplitude of the forward wave is larger in absolute value than the amplitude of the backward wave. Our numerical calculations show that, over the rest intervals, the amplitudes of the forward and backward waves can exceed in absolute value the amplitude of the original wave.

## REFERENCES

1. L. B. Felsen and N. Marcuvitz, *Radiation and Scattering of Waves* (Prentice-Hall, Englewood Cliffs, 1973; Mir, Moscow, 1978).
2. S. I. Averkov and V. P. Boldin, Izv. Vyssh. Uchebn. Zaved., Radiofiz. **23**, 1060 (1980).
3. V. V. Borisov, *Transient Electromagnetic Waves* (Leningr. Gos. Univ., Leningrad, 1987).
4. B. M. Bolotovskiĭ, V. A. Davydov, and V. E. Rok, Usp. Fiz. Nauk **126**, 311 (1978).
5. F. A. Harfoush and A. Taflove, IEEE Trans. Antennas Propag. **39**, 898 (1991).
6. A. G. Nerukh and N. A. Khizhnyak, *Modern Problems of Transient Macroscopic Electrodynamics* (NPO Test-Radio, Khar'kov, 1991).
7. V. S. Vladimirov, *Equations of Mathematical Physics* (Nauka, Moscow, 1976; Marcel Dekker, New York, 1971).
8. M. Born and E. Wolf, *Principles of Optics* (Pergamon, Oxford, 1964; Nauka, Moscow, 1973).
9. M. A. Lavrent'ev and B. V. Shabat, *Methods of the Theory of Functions of a Complex Variable* (Nauka, Moscow, 1973).

*Translated by O. Khadin*

*Technical Physics, Vol. 46, No. 10, 2001, pp. 1331–1334. Translated from Zhurnal Tekhnicheskoĭ Fiziki, Vol. 71, No. 10, 2001, pp. 128–130.*


**BRIEF COMMUNICATIONS**

# Characteristic Features of the Development of Two-Stream Instability of Electron Beams in the Presence of Spatially Localized Perturbations

**A. E. Dubinov**

*All-Russia Research Institute of Experimental Physics, Russian Federal Nuclear Center, Sarov, Nizhni Novgorod oblast, 607188 Russia*

*e-mail: dubinov@ntc.vniief.ru*

Received December 13, 2000

**Abstract**—A study is made of the evolution of a spatially localized perturbation in the form of a Gaussian packet during two-stream instability in a plasma. It is shown that, on the whole, the moving perturbation is decelerated and its shape is distorted; moreover, the higher the group velocity of the packet, the higher the deceleration rate. © *2001 MAIK "Nauka/Interperiodica".*

The multistream (in particular, two-stream) instabilities of parallel electron beams in a vacuum and in plasma are a striking example illustrating the instability of nonequilibrium electron distribution. In the simplest cases, the dispersion relation describing the linear stage of the multistream instability can be solved and analyzed exactly. This analysis is given in many textbooks and monographs on plasma physics (see, e.g., [1, 2] for two-stream instability and [3] for multistream instability). A fairly comprehensive review of the literature on two-stream instability can be found in [4].

However, multistream (in particular, two-stream) instabilities are of interest not only from a methodological point of view. Thus, Fedorchenko *et al.* [5] experimentally investigated the excitation of high-frequency oscillations during multistream instability of a system of parallel electron beams. Additionally, in microwave devices such as vircators, reflex klystrons, and Barkhausen–Kurtz oscillators with a decelerating field, two-stream instability can develop in colliding beams (for vircators, the possible onset of two-stream instability was pointed out in [6]).

The linear stage of the two-stream instability is usually analyzed by linearizing the basic equations under the assumption that the initial perturbations of the system depend on the coordinate and time as $\propto \exp[i(kz - \omega t)]$. In other words, the initial perturbation is assumed to be distributed uniformly over the interval from $-\infty$ to $+\infty$, which corresponds to a system of infinitely long beams and, generally speaking, to the infinitely high energy of the perturbation.

In this context, it is of interest to study how two-stream instability develops when the initial perturbation is localized in space. As a matter of fact, the idea of investigating the characteristic features of the development of various instabilities in the case of spatially localized perturbations is not new (see, e.g., [7, 8]). However, from a methodological standpoint, it is somewhat difficult to analyze such perturbations by expanding them in harmonic waves [7], because the energy of a localized perturbation is finite (this is evidenced by the convergence of the corresponding integral), while each harmonic component of the perturbation has infinite energy. That is why, in my opinion, the simplest and most illustrative way of studying the instability of spatially localized perturbations is that which does not involve the Fourier analysis of the perturbations. As will be shown below, this approach provides a fairly simple analytical examination of two-stream instability.

We start with the traditional equations [3]

$$\frac{\partial n_\alpha}{\partial t} + \nabla \cdot n_\alpha \mathbf{v}_\alpha = 0, \tag{1}$$

$$\frac{\partial \mathbf{v}_\alpha}{\partial t} + (\mathbf{v}_\alpha \cdot \nabla)\mathbf{v}_\alpha = \frac{e}{m}\mathbf{E}, \tag{2}$$

$$\nabla \cdot \mathbf{E} = 4\pi e\left(\sum_\alpha m n_\alpha - N_i\right), \tag{3}$$

where $n_\alpha$ and $\mathbf{v}_\alpha$ are the density and velocity of the $\alpha$th electron beam, $e$ and $m$ are the charge and mass of an electron, and $\mathbf{E}$ is the electric field.

Equation (1) is the continuity equation for an electron beam, Eq. (2) is the equation of motion, and Eq. (3) is Gauss's law. For simplicity, we assume that parallel electron beams propagate against the background of immobile ions with density $N_i$, which serve merely to provide the charge and current neutralization of the unperturbed electron beams.

1063-7842/01/4610-1331$21.00 

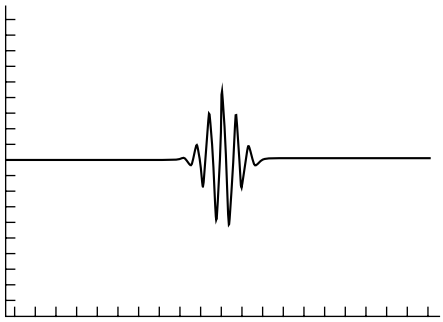

**Fig. 1.** Instantaneous shape of a perturbation in the form of a Gaussian packet.

We direct the $z$-axis along the propagation direction of the beams and assume that the system is uniform in transverse directions. In this case, Eqs. (1)–(3) constitute a set of one-dimensional equations for the densities and the projections of the velocity and electric field onto the $z$-axis. We represent the unknowns in the equations as

$$n_\alpha = N_\alpha + \tilde{n}_\alpha \exp[i(kz - \omega t)] \exp[-\chi^2 (z - V_g t)^2], \quad (4)$$

$$v_\alpha = V_\alpha + \tilde{v}_\alpha \exp[i(kz - \omega t)] \exp[-\chi^2 (z - V_g t)^2], \quad (5)$$

$$E = \tilde{E} \exp[i(kz - \omega t)] \exp[-\chi^2 (z - V_g t)^2]. \quad (6)$$

We can see that the perturbation is spatially localized and is described by a harmonically modulated Gaussian function with the parameters $\chi$ (which has units of inverse length and determines the spatial width of the perturbation) and $V_g$ (which is the group velocity of the perturbation). In the theory of wavelets, the function describing the perturbation coincides (to within a normalizing factor, which is unimportant for our purposes here) with the Gabor function [8]; in [7], this function is referred to as a Gaussian packet. The plot of this function is shown in Fig. 1.

In what follows, we assume that the perturbation amplitudes in representations (4)–(6) are small and omit the tilde from the perturbed quantities. We substitute representations (4)–(6) into the basic equations and, to the first order in the small perturbation amplitudes, obtain

$$n_\alpha [2\chi^2 (z - V_g t) V_g - i\omega] + (N_\alpha v_\alpha + n_\alpha V_\alpha) \times [-2\chi^2 (z - V_g t) + ik] = 0, \quad (7)$$

$$v_\alpha [2\chi^2 (z - V_g t) V_g - i\omega] \times v_\alpha V_\alpha [-2\chi^2 (z - V_g t) + ik] = \frac{e}{m} E, \quad (8)$$

$$E[-2\chi^2 (z - V_g t) + ik] = \sum_\alpha 4\pi e n_\alpha. \quad (9)$$

Solving Eqs. (7) and (8) with respect to $v_\alpha$ and $n_\alpha$ yields

$$v_\alpha = \frac{e}{m} \frac{E}{2\chi^2 (z - V_g t)(V_g - V_\alpha) + i(kV_\alpha - \omega)}, \quad (10)$$

$$n_\alpha = -\frac{e}{m} \frac{N_\alpha E[-2\chi^2 (z - V_g t) + ik]}{[2\chi^2 (z - V_g t)(V_g - V_\alpha) + i(kV_\alpha - \omega)]^2}. \quad (11)$$

We insert these expressions for $v_\alpha$ and $n_\alpha$ into Eq. (9) to arrive at the desired dispersion relation

$$1 = -\sum_\alpha \frac{\omega_{p\alpha}^2}{[2\chi^2 (z - V_g t)(V_g - V_\alpha) + i(kV_\alpha - \omega)]^2}, \quad (12)$$

where $\omega_{p\alpha} = (4\pi e^2 N_\alpha / m)^{1/2}$ is the Langmuir frequency of the $\alpha$th beam.

Now, we proceed to an analysis of the dispersion relation (12). First, note that, when deriving this dispersion relation, we failed to completely eliminate the dependence on the coordinate and time. However, this circumstance is usually associated with the expansion of functions in a series of the basic localized functions—wavelets [8, 9]—and makes it possible to analyze the processes in the $\{z, t\}$ and $\{k, \omega\}$ spaces simultaneously.

Note also that, for unlocalized perturbations ($\chi \longrightarrow 0$), the dispersion relation (12) passes over to the familiar dispersion relation for harmonic perturbations.

In the case of two parallel beams with arbitrary unperturbed densities and velocities, Eq. (12) contains many parameters, so that its analysis, although straightforward, is very lengthy. Here, we examine only the particular case of two counterpropagating identical beams with the same values of $\omega_{p\alpha} = \omega_p$ and $V_\alpha = V$. For such beams, the two-stream instability of a traditional harmonic perturbation is absolute in nature. We investigate the onset of the instability at different characteristics $C = z - V_g t = \text{const}$ of the perturbation envelope. In this case, the dispersion relation has the form

$$1 = -\frac{\omega_p^2}{[2\chi^2 (z - V_g t)(V_g - V) + i(kV - \omega)]^2} - \frac{\omega_p^2}{[2\chi^2 (z - V_g t)(V_g + V) - i(kV + \omega)]^2}. \quad (13)$$

We can readily see that, at the top of the envelope ($C = 0$), the instability develops in the same way as in the case of a harmonic perturbation. However, at the other parts of the envelope, the instability growth rates can differ substantially from those in the case of a har-

monic perturbation. Since Eq. (13) is a quartic equation in the variable $\omega$, we are dealing with the four roots

$$\omega_{1,2,3,4} = 2iCV_g \pm\sqrt{k^2V^2 + \omega_p^2 - 4\chi^2C^2V^2 + 4iC\chi^2kV \pm D}, \quad (14)$$

where

$$D = \sqrt{\omega_p^4 + 4\omega_p^2k^2V^2 - 16C^2\chi^4\omega_p^2V^2 + 16iC\chi^2\omega_p^2kV^2}.$$

In expression (14) and below, the first root is identified by the plus signs in front of and under the square root, the second, by the minus and plus signs, the third, by the plus and minus signs, and the fourth, by the minus signs. The imaginary parts of the roots, $\mathrm{Im}(\omega_{1,2,3,4})$, calculated as functions of the position $C$ on the envelope of the perturbation under the natural assumption $k^2 \gg \chi^2$ are illustrated graphically in Fig. 2.

Figure 2a refers to a nonpropagating ($V_g = 0$) perturbation with a certain value of $k$. At the top of the envelope, the second and third roots vanish, $\omega_{2,3} = 0$, while the first and fourth roots $\omega_{1,4}$ undergo a jump equal to the doubled instability growth rate for a harmonic perturbation. The growth rates increase with distance from the top, because the evolving perturbation acquires the nature of a uniform harmonic perturbation, so that the effective width of the envelope of the evolving perturbation increases (this effect is known as the spreading of a Gaussian packet).

For a perturbation with a low group velocity ($0 < V_g < V$), the dependence of $\mathrm{Im}(\omega_{1,2,3,4})$ on $C$ is somewhat different from that in the previous case. From Fig. 2b, we can see that the leading edge of the perturbation grows slower than the trailing edge. As a result, first, the centroid of the perturbation is displaced toward the trailing edge, indicating the deceleration of the perturbation; and, second, the leading edge of the perturbation becomes flatter than the trailing edge.

The leading edge of a perturbation with a sufficiently high group velocity ($V_g > V$) can even decay, while its trailing edge can grow at a very high rate (Fig. 2c). If the two beams under consideration are in an electrodynamic system of the carcinotron type, in which case we have $V_g < -|V| < 0 < V$ (Fig. 2d) and the characteristics $C$ are positive at the trailing edge of the perturbation, then the perturbation is also decelerated and its shape is deformed.

Although the above features of the evolution of a spatially localized perturbation were revealed in the linear approximation, they cannot be established in terms of a harmonic perturbation. These features can be described by expanding a spatially localized perturbation in harmonic waves, but this way is far more lengthy because it involves the calculation of integrals like the Duhamel's convolution.

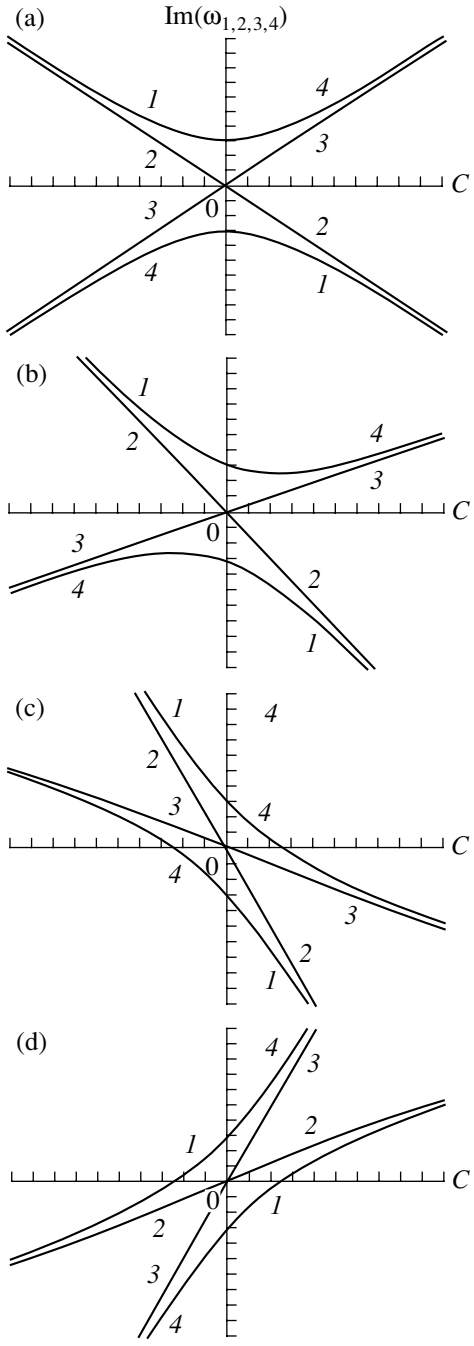


**Fig. 2.** Imaginary parts of the roots calculated for (a) $V_g = 0$, (b) $0 < V_g < V$, (c) $V_g > V$, and (d) $V_g < -|V| < 0 < V$.

## ACKNOWLEDGMENTS

I am grateful to A.A. Rukhadze for consultations on some problems associated with multistream instabilities.

## REFERENCES


1. N. A. Krall and A. W. Trivelpiece, *Principles of Plasma Physics* (Academic, New York, 1973; Mir, Moscow, 1975).
2. P. C. Clemmow and J. P. Dougherty, *Electrodynamics of Particles and Plasmas* (Addison-Wesley, Reading, 1990; Mir, Moscow, 1996).
3. T. H. Stix, *The Theory of Plasma Waves* (McGraw-Hill, New York, 1962; Atomizdat, Moscow, 1965).
4. R. J. Briggs, in *Advances in Plasma Physics*, Ed. by A. Simon and W. Thompson (Wiley, New York, 1971; Mir, Moscow, 1974), Vol. 4.
5. V. D. Fedorchenko, Yu. P. Mazalov, A. S. Bakaĭ, and B. N. Rutkevich, Zh. Éksp. Teor. Fiz. **65**, 2225 (1973) [Sov. Phys. JETP **38**, 1111 (1973)].
6. A. E. Dubnov, Radiotekh. Élektron. (Moscow) **45**, 875 (2000).
7. A. B. Mikhailovskii, *Theory of Plasma Instabilities* (Atomizdat, Moscow, 1971; Consultants Bureau, New York, 1974), Vol. 1.
8. S. K. Zhdanov and B. A. Trubnikov, *Quasi-Gaseous Unstable Media* (Nauka, Moscow, 1991).
9. N. M. Astaf'eva, Usp. Fiz. Nauk **166**, 1145 (1996) [Phys. Usp. **39**, 1085 (1996)].


*Translated by O. Khadin*

*Technical Physics, Vol. 46, No. 10, 2001, pp. 1335–1338. Translated from Zhurnal Tekhnicheskoĭ Fiziki, Vol. 71, No. 10, 2001, pp. 131–134.*


**BRIEF COMMUNICATIONS**

# On the Thermodynamics of Contact Interaction in an Atomic Force Microscope

**S. Sh. Rekhviashvili**

*Research Institute of Applied Mathematics and Automation, Kabardino–Balkar Scientific Center, Russian Academy of Sciences, Nal'chik, 360000 Russia*

Received December 18, 2000

**Abstract**—Contact interaction in an atomic force microscope is considered in terms of the thermodynamic approach. It is shown that hysteresis observed when a sample is probed in the vertical direction is due to the surface energy–work thermodynamic cycle. The force of sample–tip interaction is calculated for the case when the tip is a paraboloid of revolution. Fluctuations of the basic thermodynamic parameters are found. The role of electrocapillary forces is considered. A new method of spectroscopy in the lateral force mode is suggested.


## INTRODUCTION

Interest in the physics and chemistry of microcontacts has greatly quickened in the past few years. In particular, much attention is given to such surface phenomena as adhesion, wetting, friction, and adsorption. New domains of science, namely, electrochemistry, tribology, optics, and lithography of microcontacts, have appeared. To a great extent, this is due to the advent of new-generation multimode scanning probe microscopes (SPMs).

It is the aim of this work to thermodynamically describe a number of typical processes occurring in the SPM probe–sample system. Note at once that we use methods of equilibrium thermodynamics, which, generally speaking, apply to infinitely slow (reversible) processes. Actually, however, the irreversibility of the processes taking place in this system may be so high that such a description will cause considerable errors. Yet, the thermodynamic approach appears to be sufficiently informative, since it allows researchers, first, to find general relations between various contact properties and, second, to study different equilibrium states of the system. Specifically, with this approach, the run of the process can be elucidated.

## THERMODYNAMIC CYCLE IN THE PROBE–SAMPLE SYSTEM

Under atmospheric conditions, the sample under study is always covered by a thin layer of adsorbed moisture [1–3]. The tip of an atomic force microscope (AFM) "adheres" to the sample due to capillary forces, causing force hysteresis when the sample is probed in the vertical direction (Fig. 1). The distance from the surface at which the probe adheres to the surface is 10–50 nm. In a vacuum, the hysteresis is usually weak or even absent. If the interaction is hydrophilic, the capillary force holds the tip in continuous contact with the surface and varies insignificantly during scanning, because the tip–sample distance remains practically constant. If the interaction is hydrophobic, the tip must penetrate through the adsorbate to image the surface. Generally, the specific energy of adhesion is estimated from the well-known expression $U_a = \sigma(1 - \cos\theta)$, where $\sigma$ is the surface tension of a liquid film and $\theta$ is the wetting angle.

Let an adsorbed water film exist between the tip and the surface (Fig. 2). The internal energy of the isolated film is given by

$$dU = TdS - pdV + \sigma d\omega - Fdz, \qquad (1)$$

where $T$ is temperature, $S$ is entropy, $p$ is pressure, $V$ is volume, $\sigma$ is the surface tension of the film, $\omega$ is surface area, $F$ is the elastic force due to liquid film deformation, and $z$ is the deformation.

If the pressure and temperature are constant,

$$dG = d(U - TS + pV) = \sigma d\omega - Fdz, \qquad (2)$$

where $G$ is the Gibbs thermodynamic potential.

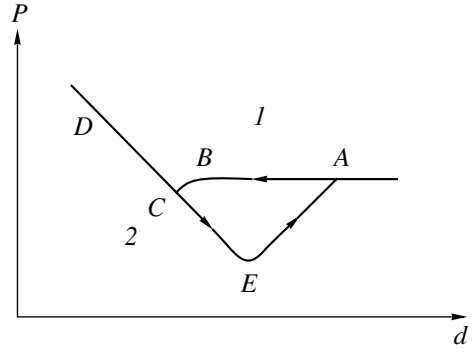


**Fig. 1.** Interaction force vs. distance when the tip (*1*) approaches and (*2*) moves away from the sample.

1063-7842/01/4610-1335$21.00 © 2001 MAIK "Nauka/Interperiodica"

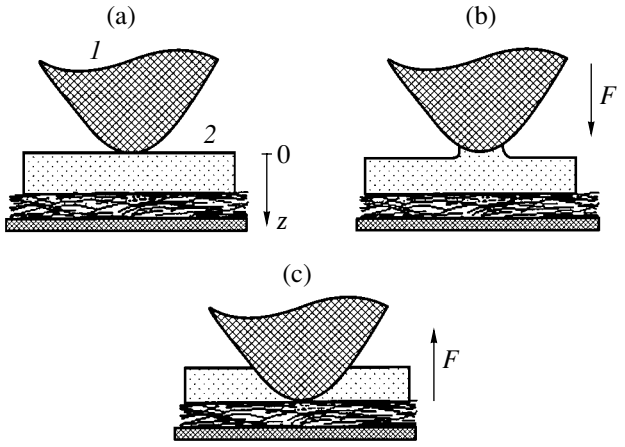


**Fig. 2.** Schematic representation of the contact in an AFM. (a) Initial instant of the contact, (b) meniscus formation, and (c) dipping of the tip into the liquid film. Arrows indicate the coordinate axis and the direction of the force. (*1*) Probe and (*2*) film.

Under thermodynamic equilibrium, $dG = 0$ and formula (2) can be recast as

$$\sigma d\omega = Fdz. \tag{3}$$

Expression (3) is the condition of a thermodynamic cycle when the work of the AFM probe is converted to the surface energy of the film and vice versa. In the state diagram (Fig. 1), the cycle is shown by the closed curve.

Consider this phenomenon in greater detail. At the initial stage, the probe approaches the surface. Once it touches the film (point *B* in Fig. 1), its tip becomes partially wetted and the additional force component due to hydrophilic attraction arises (Fig. 2b). This force can do a small mechanic work, drawing the probe into the contact region (portion *BC*). As the pressing force increases further, the probe touches the surface (Fig. 2c; portion *CD* in Fig. 1).[1] Then, as the probe moves away from the surface, the AFM scanning system does work to break the contact (portion *CE*). As the probe–surface distance grows, the probe completely detaches from the surface (portion *EA*) and the system returns to its initial state. The area enclosed by the curve *ABCE* in Fig. 1 is obviously the work of this cycle:

$$W = \int\limits_{A \to C} Fdz - \int\limits_{C \to A} Fdz.$$

Let us assume that the interaction is hydrophobic ($\theta = \pi/2$, $U_a = \sigma$). Then, if the probe is displaced by *dz*, the contact surface area is changed by $d\omega$. For a parabolic tip, the interaction forces and the contact stiffness are given by

$$F = \sigma\frac{d\omega}{dz} = 2\pi\sigma\sqrt{R^2 + 2zR}, \tag{4a}$$

$$K = \frac{dF}{dz} = 2\pi\sigma\sqrt{\frac{R}{R + 2z}}, \tag{4b}$$

where *R* is the radius of curvature of the tip.

Several consequences following from formulas (4a) and (4b) are worthy to note. The adhesion (detachment) forces become equal to $F(0) = 2\pi R\sigma$, which coincides with the result in [4]. The associated contact stiffness is $K(0) = 2\pi\sigma$. For $H_2O$ ($T = 300$ K, $\sigma = 0.07$ J/m$^2$) and $R = 20$ nm, we have $F(0) = 8.8$ nN and $K(0) = 0.44$ N/m. These data are typical of most experiments [1–3]. Knowing the detachment force and the contact stiffness, one can determine the critical displacement amplitude of the cantilever:

$$\varepsilon_0 = \frac{R}{n + 1}, \tag{5}$$

where *n* shows by how many times the cantilever stiffness differs from the contact stiffness ($n = K_c/K(0)$, where $K_c$ is the cantilever stiffness). Note that for soft cantilevers and hard contacts, $n \longrightarrow 0$; that is, $\varepsilon_0 \longrightarrow R$. In this case, expression (5) is conveniently used to find the radius of curvature of the tip.

Finally, it should be noted that other thermodynamic cycles related, for example, to heat exchange, adsorption, etc. may proceed in the probe–sample system. To make certain of it, it will suffice to change the pressure or temperature when the force curves in the AFM cell are measured. The measured curves will have a more complex shape.

## FLUCTUATIONS OF BASIC THERMODYNAMIC PARAMETERS

In the best AFM designs, the force resolution attains 1 pN and the distance resolution is 1 pm (in the vertical direction). It is believed that the resolution is adversely affected by electrical noise, mechanical drift, seismic vibrations, and thermal fluctuation of the cantilever [5, 6]. We will show that the resolution is also basically limited by fluctuations of interaction force, displacement, contact area, and surface tension.

Let us write the expression for the minimal mechanical work that is done by the AFM probe interacting with the liquid film:

$$W_{\min} = \Delta G - \sigma\Delta\omega + F\Delta z$$

[1] For solid surfaces, the slope of this portion depends on the cantilever stiffness.

$$= \frac{1}{2}\left[\frac{\partial^2 G}{\partial \omega^2}(\Delta\omega)^2 + 2\frac{\partial^2 G}{\partial \omega \partial z}\Delta\omega\Delta z + \frac{\partial^2 G}{\partial z^2}(\Delta z)^2\right]$$
$$= \frac{1}{2}\left[\Delta\omega\Delta\left(\frac{\partial G}{\partial \omega}\right)_z + \Delta z\Delta\left(\frac{\partial G}{\partial z}\right)_\omega\right] \quad (6)$$
$$= \frac{1}{2}[\Delta\omega\Delta\sigma - \Delta F\Delta z].$$

The probability that the system is in the appropriate thermodynamic state is found from expression (6) and Gibbs distribution

$$f \sim \exp\left(-\frac{W_{\min}}{kT}\right). \quad (7)$$

With (7), one can calculate the fluctuations of all parameters of interest. Consider two basic cases.

(1) Independent variables are $\Delta z$ and $\Delta\sigma$. In terms of these variables, the total differentials of the contact surface area and interaction force have the form

$$\Delta\omega = \left(\frac{\partial\omega}{\partial z}\right)\Delta z + \left(\frac{\partial\omega}{\partial\sigma}\right)\Delta\sigma,$$
$$\Delta F = \left(\frac{\partial F}{\partial z}\right)\Delta z + \left(\frac{\partial F}{\partial\sigma}\right)\Delta\sigma.$$

Substituting these expressions into formula (6) and making straightforward rearrangements, we obtain the expression for the minimal work:

$$W_{\min} = \frac{1}{2}\left[\left(\frac{\partial\omega}{\partial\sigma}\right)(\Delta\sigma)^2 - \left(\frac{\partial F}{\partial z}\right)(\Delta z)^2\right]. \quad (8)$$

With regard for (7) and (8), the final expression for the thermodynamic state probability is

$$f \sim \exp\left(-\frac{(\Delta\sigma)^2}{2kT}\left(\frac{\partial\omega}{\partial\sigma}\right)\right)\exp\left(\frac{(\Delta z)^2}{2kT}\left(\frac{\partial F}{\partial z}\right)\right). \quad (9)$$

From (9), it follows that the variables selected are statistically independent; that is, the equality $\langle\Delta\sigma, \Delta z\rangle = 0$ holds. Comparing the expression obtained with the normal distribution $f \sim \exp(-x^2/2\langle x^2\rangle)$, we find the fluctuations of the surface tension and displacement:

$$\langle(\Delta\sigma)^2\rangle = -kT\left(\frac{\partial\sigma}{\partial\omega}\right)_z, \quad (10a)$$

$$\langle(\Delta z)^2\rangle = kT\left(\frac{\partial z}{\partial F}\right)_\sigma. \quad (10b)$$

Since the fluctuations are positive, the minus sign in (10a) means that $\partial\sigma/\partial\omega < 0$.

(2) Independent variables are $\Delta\omega$ and $\Delta F$, which also are statistically independent; that is $\langle\Delta\omega, \Delta F\rangle = 0$. Following the above line of reasoning, we come to the following expressions for the fluctuations of the contact surface area and interaction force:

$$\langle(\Delta\omega)^2\rangle = -kT\left(\frac{\partial\omega}{\partial\sigma}\right)_F, \quad (11a)$$

$$\langle(\Delta F)^2\rangle = kT\left(\frac{\partial F}{\partial z}\right)_\omega. \quad (11b)$$

Now we perform numerical estimations, considering the detachment of the cantilever. From expressions (4a), (4b), (10b), and (11b) at $z = 0$, the rms deviations of the displacement and force are

$$\langle\Delta z\rangle = \sqrt{\frac{kT}{2\pi\sigma}}, \quad \langle\Delta F\rangle = \sqrt{2\pi\sigma kT}. \quad (12a), (12b)$$

For $H_2O$ at $T = 300$ K, $\langle\Delta z\rangle = 0.1$ nm and $\langle\Delta F\rangle = 0.043$ nN. The values are consistent with experimental data obtained in [7].

From (12a) and (12b), it follows that the rms deviations of the displacement and force do not depend on the probe size at $z = 0$ (on the film surface). It was shown above that the detachment force varies as the radius of curvature $R$. Therefore, the effect of the fluctuations will be enhanced for ultrasharp ($R < 10$ nm) tips.

## ELECTROCAPILLARITY

It is well known that the surface tension of an electrolyte severely depends on the applied voltage and the concentration of charged ions [8]. Let there exist a potential difference between the tip and the sample. Then, the expression for the Gibbs potential takes the form

$$dG = \sigma d\omega - Fdz - Qd\varphi,$$

where $Q$ is the total charge of the ions and $\varphi$ is the potential difference.

From the condition of thermodynamic equilibrium, we find the detachment force

$$F(0) = \left(\sigma\frac{d\omega}{dz} - QE\right)\Big|_{z=0} = 2\pi R\left(\sigma - \frac{C\varphi^2}{2}\right), \quad (13)$$

where $E$ is the field strength and $C$ is the capacitance per unit area of the contact.

Note that formula (13) can also be obtained if the solution of the Lippmann equation [8] is substituted for the surface tension in expression (4a).

From (13), it follows that the surface tension is maximal if the voltage across the electrodes is zero. If the potential difference is $\varphi = \sqrt{2\sigma/C}$, the detachment force vanishes. Thus, electrocapillary phenomena and, hence, adsorption can be studied with an AFM.

## SPECTROSCOPY IN THE LATERAL-FORCE MODE

The lateral-force mode of atomic force microscopy (this mode is also called scanning frictional microscopy [9]) is used for high-resolution studies of solids, specifically, of their tribological properties. In this mode, the cantilever moves over the surface with a constant velocity $v_0$ and its torsion due to shear forces is measured. We suggest a new method of spectroscopy that measures the total scanning energy (or the specific scanning energy, i.e., the energy per image area). Obviously, this parameter must distinctly correlate with thermodynamic parameters, such as surface energy, heat capacity, heat of sublimation, heat of fusion, etc.

When imaging, the cantilever spends energy that is expressed through the frictional loss power as

$$U = \int_0^{T_0} P\,dt, \quad P = \lim_{\Delta \to 0} \frac{\Delta U}{\Delta T} = v_0 f_{\parallel},$$

where $T_0$ is the scanning time; $F_{\parallel}$ is the shear force; $\Delta U = \Delta Q + \sum_k \Delta W_k$ is a change in the internal energy of the probe–sample system within a time $\Delta t$; $\Delta Q$ is a heat increment; and $\Delta W_k$ are the contributions to the energy of interaction due to interatomic (for example, Van der Waals or magnetodipole) interactions, changes in the volume and shape of contacting bodies, phase transitions (melting or sublimation), chemical reactions, and wear. If the temperature of the system remains constant during scanning, $\Delta U$ obviously equals the change in the free energy.

In experiments, this spectroscopic method is accomplished by repeatedly scanning the same surface area at various normal loads. To exclude the effect of surface inclination, imaging must be carried out in two, normal- and lateral-force, modes. Such investigations are easy to perform with commercial multimode microscopes from the NT-MDT company (Russia) [10].

## CONCLUSION

In this work, the thermodynamic analysis is applied to processes taking place in the AFM probe–sample system for the first time. It is assumed that an adsorbed water film exists between the hydrophobic tip and the sample. Expressions for the interaction force, contact stiffness, and fluctuations of the basic parameters are obtained. The method for determining the thermodynamic characteristics in the AFM lateral-force mode is suggested.

Another important issue omitted in the article is thermodynamics of magnetic force microscopy (MFM). The basic difficulties in describing the interaction in MFM are associated with the fact that the magnetic field may cause substantial distortions in the true distribution of magnetic forces over the sample surface. In general, when the cantilever with a magnetization $J$ moves in a magnetic field $H$, the area of the magnetomechanical hysteresis loop is given by $W = \oint_z F\,dz \oint_H J\,dH$.

## REFERENCES

1. M. Radmacher *et al.*, Biophys. J. **66**, 2159 (1994).
2. D. R. Baselt and J. D. Baldeschwieler, J. Appl. Phys. **76**, 33 (1994).
3. K. O. van der Werf *et al.*, Langmuir **10**, 1195 (1994).
4. B. V. Deryagin, N. V. Churaev, and V. M. Muller, *Surface Forces* (Nauka, Moscow, 1985).
5. A. I. Oliva *et al.*, Rev. Sci. Instrum. **63**, 3326 (1992); **66**, 3196 (1995).
6. Hans-Jurgen Butt and Manfred Jaschke, Nanotechnology **6** (1), 1 (1995).
7. J. P. Cleveland, T. E. Schaffer, and P. K. Hansma, Phys. Rev. B **52**, 8692 (1995).
8. A. W. Adamson, *The Physical Chemistry of Surfaces* (Wiley, New York, 1976; Mir, Moscow, 1979).
9. G. V. Dedkov, Usp. Fiz. Nauk **170**, 585 (2000).
10. V. A. Bykov *et al.*, in *Proceedings of the All-Russia Conference "Microprobing-99," Nizhni Novgorod, 1999*, p. 327.

*Translated by V. Isaakyan*

*Technical Physics, Vol. 46, No. 10, 2001, pp. 1339–1340. Translated from Zhurnal Tekhnicheskoĭ Fiziki, Vol. 71, No. 10, 2001, pp. 135–136.*


**BRIEF COMMUNICATIONS**

# A Static Model for Completely Polarized Ceramics

**M. G. Minchina and O. I. Yankovskiĭ**

Received January 9, 2001

**Abstract**—A model for completely polarized ceramics kept under a longitudinal compression stress σ has been advanced. The model is built upon the condition of the complete and partial stability of the domain polar **c** axes with due regard to the nonuniform distribution of the axes after 90° and 180° domain switches. By using this model, the ceramics piezoelectric coefficient $d_{33}$, its dependence on the longitudinal compression stress σ, and the relative numbers of 90° and 180° domain switches induced by the action of the stress σ were determined. *© 2001 MAIK "Nauka/Interperiodica".*

## 1. A CERAMICS MODEL

We consider polarized ferroelectric ceramics of the $\infty^*m$ point symmetry group with single-domain crystalline grains, whose polar **c** axes are aligned with the allowed directions of the spontaneous polarization vector $\mathbf{P}_s$ that are closest to the direction of a polarizing **E** field [1]. Let a unit sphere be taken as the geometric static image of the polarized ceramics and let the sphere surface be covered with the ends of the polar **c** axes of the domain ranged in their density, which lead out of the center of this sphere. Piezoelectric ceramics can be treated as a system of *N*-numbered single-domain crystalline grains polarized to saturation. Then, in the case of completely polarized ceramics, all the polar **c** axes of the domain are distributed in the upper part of the orientation sphere within a solid angle $2\pi(1 - \cos\theta)$ around the path of the **E** vector [2]. Taking into account all the possible 90° and 180° domain switches, the domains with polar axes making an angle $\theta = 54°44'$ with the path of the polarizing **E** vector will be farthest from the field [1–4]. Considering the geometric constraint on the angles $\gamma_c$, $\gamma_a$, and $\psi$ [2],

$$\cos\gamma_a = \sin\gamma_c\cos\psi. \quad (1)$$

The conditions for the 90° and 180° switches of the domain polar axes were found from that of the **c** axes complete and partial stability about the path of the polarizing **E** vector.

The condition

$$\cos\gamma_c - \cos\gamma_a \geq 0 \quad (2)$$

is satisfied for the complete stability zone of the polar **c** axes.

Substituting Eq. (1) into Eq. (2) gives

$$\cos\gamma_c - \sin\gamma_c\cos\psi \geq 0 \quad (3)$$

analyzing inequality (3), we find that the complete stability zone of the **c** axes is located in the region

$$0° \leq \gamma_c \leq 45°. \quad (4)$$

In the initial state, the **a** axes of all the crystal grains with the given angles $\gamma_c$ show a uniform circular distribution, and the **a** axes nearest to the **E** field are grouped in a quadrant of this circle with $\psi$ ranging between –45° and 45°. Within the complete stability zone of the **c** axes, the **a** axes are closest to the polarizing **E**-field direction ($\psi = 0$). In the case of completely polarized ceramics, the partial stability zone of the **c** axes implies a region where, in fulfillment of inequality (2), crystal-grain **a** axes are most distant from the polarizing **E**-field direction ($\psi = 45°$). The partial stability zone of the polar **c**-axes extends over a range

$$45° \leq \gamma_c \leq 54°44', \quad (5)$$

for which, after all the possible domain switches [5], the **c**-axis density is

$$\rho_c'' = (3N/2\pi)((1 - |4\arccos(\cot\gamma_c)|)/\pi). \quad (6)$$

The piezoelectric coefficient $d_{33}^{\text{theor}}$ was calculated by the integration over the orientation sphere taking into account the probability density of the **c** axes and by averaging over all crystal grains (or domains). For instance, in the case of disk-shaped ceramics, it was done by the formula

$$d_{33}^{\text{theor}} = 1/N \int_{\theta=0°}^{45°}\int_{\varphi=0°}^{2\pi} d_{33}(\theta)3N/2\pi\sin\theta d\theta d\varphi + 1/N \int_{\theta=45°}^{54°44'}\int_{\varphi=0°}^{2\pi} d_{33}(\theta)(3N/2\pi) \times (1 - |4\arccos(\cot\gamma_c)|/\pi)\sin\theta d\theta d\varphi, \quad (7)$$

where

$$d_{33}(\theta) = (d_{15} + d_{31})\cos\theta\sin^2\theta + d_{33}\cos^3\theta \quad (8)$$

and $\theta$ is the angle between the $Z$ and $Z'$ axes.

1063-7842/01/4610-1339$21.00 © 2001 MAIK "Nauka/Interperiodica"

## 2. THE CERAMICS MODEL SUBJECTED TO A LONGITUDINAL COMPRESSION STRESS σ

Consider a piezoceramic plate in a principal crystal-physics *XYZ* coordinate system, where the polarization vector **P** is aligned with the *OZ* axis. Let us impose a uniaxial mechanical stress σ to the plate. The polar **c** axes show a preferred orientation, arranged on the upper part of an orientation sphere within a solid angle θ. With due regard for all the possible 90° and 180° domain switches of the polar **c** axes, they show a nonuniform distribution in the complete and partial stability zones. In the case of the stress $\sigma_{33}$ applied to the ceramics, the complete stability condition for the *c* axes can be written as

$$\cos\gamma_c - \cos\gamma_a \geq \sigma_c/\sigma, \tag{9}$$

where $\gamma_c$ is the angle between the **E**-field vector and the domain **c** axis; $\gamma_a$ is the angle between the **a** axis nearest to the **E**-field vector and this vector; $\sigma_c$ is the coercive stress; σ is the applied stress; and

$$0 \leq \gamma_c \leq (\arccos(\sigma_c/\sigma)(\sqrt{2}/2)) - 45°. \tag{10}$$

Inequality (10) yields the angular boundaries of the complete stability zone of the polar **c** axes when the longitudinal stress σ is applied to the ceramics. The condition for partial stability of the polar **c** axes, when the **a** axes are most distant from the path of the polarizing **E** field (φ = 45°), has the form

$$\cos\gamma_c - (\sqrt{2}/2)\sin\gamma_c \geq \sigma_c/\sigma. \tag{11}$$

Equation (11) can be brought into the form

$$45° \leq \gamma_c \leq 54.733° - \arcsin((\sigma_c/\sigma)(\sqrt{2}/\sqrt{3})). \tag{12}$$

Under the action of the longitudinal stress σ, the piezoelectric coefficient $d_{33}$ changed by a value of $\Delta d_{33}^T$, which was computed by integrating over the orientation sphere of the polar **c** axes and averaging the piezoelectric constants $d'_{33}$, $d'_{31}$, and $d'_{15}$ over all the crystal grains with the formula:

$$\begin{aligned}\Delta d_{33}^T = 1/N \int_{\varphi=0°}^{2\pi} \int_{\theta=0°}^{\arccos((\sqrt{2}/2)(\sigma_c/\sigma)45°)} & d_{33}(\theta)(3N/2\pi) \\ & \times \sin\theta d\theta d\varphi \\ + 1/N \int_{\varphi=0°}^{2\pi} \int_{\theta=0°}^{54°44' - \arccos(\sqrt{2}/\sqrt{3})(\sigma_c/\sigma)} & d_{33}(\theta)(3N/2\pi) \\ & \times \{1 - 4\arccos[\cot\theta + \sigma_c/(\sigma\sin\theta)]/\pi\}\sin\theta d\theta d\varphi.\end{aligned} \tag{13}$$

We separated the contributions from the 90° and 180° domain switches by formula (8) (for instance, in the case of the complete stability zone of the **c** axes, the **c**-axis density is equal to $\rho^{90°} = N/\pi$ and $\rho^{180°} = N/2\pi$ for the 90° and 180° switches, respectively). Then, the relative numbers of the 90° and 180° domain switches ($A^{90°}$ and $A^{180°}$, in percent) induced by the stress σ were obtained for a given σ [6]. In the final form, the formula for the piezoelectric coefficient $d_3^T$ of a ceramic plate exposed to a stress σ is written as

$$d_{33}^T = d_{33} - \Delta d_{33}^T, \tag{14}$$

where the piezoelectric coefficient $d_{33}$ is obtained from (8).

## CONCLUSIONS

(1) A static model for completely polarized ceramics has been advanced. It is based on the condition of complete and partial stability of the **c** axes with due regard for their nonuniform distribution after 90° and 180° domain switches.

(2) A static model was considered for completely polarized ceramics exposed to a longitudinal compression stress σ.

(3) On the basis of this model for ceramics, the piezoelectric coefficient $d_{33}$ was calculated, and its behavior as a function of the longitudinal compression stress σ, as well as the stress-induced relative numbers of the 90° and 180° domain switches, were determined.

## REFERENCES

1. B. Jaffe, W. R. Cook, and H. Jaffe, *Piezoelectric Ceramics* (Academic, New York, 1971; Mir, Moscow, 1974).
2. *Polarization Piezoelectric Ceramics*, Ed. by E. G. Fesenko (Rost. Gos. Univ., Rostov-on-Don, 1962).
3. S. V. Bogdanov, B. M. Vul, and A. M. Timonin, Izv. Akad. Nauk SSSR, Ser. Fiz. **21**, 374 (1957).
4. L. A. Shuvalov, Kristallografiya **2**, 119 (1957) [Sov. Phys. Crystallogr. **2**, 115 (1957)].
5. M. G. Minchina and V. P. Dudkevich, Zh. Tekh. Fiz. **68** (7), 75 (1998) [Tech. Phys. **43**, 814 (1998)].
6. M. G. Minchina and O. I. Yankovskiĭ, Zh. Tekh. Fiz. **69** (6), 46 (1999) [Tech. Phys. **44**, 650 (1999)].

*Translated by B. Malyukov*

*Technical Physics, Vol. 46, No. 10, 2001, pp. 1341–1344. Translated from Zhurnal Tekhnicheskoĭ Fiziki, Vol. 71, No. 10, 2001, pp. 137–140.*


**BRIEF COMMUNICATIONS**

# A 1-kW/cm$^2$ Flash KrCl Excimer Lamp

**M. V. Erofeev, M. I. Lomaev, É. A. Sosnin, V. F. Tarasenko, and D. V. Shitz**

*Institute of High-Current Electronics, Siberian Division, Russian Academy of Sciences, Akademicheskiĭ pr. 4, Tomsk, 634055 Russia*

*e-mail: badik@loi.hcei.tsc.ru*

Received January 18, 2001

**Abstract**—The amplitude–time characteristics of the emission from a one-barrier flash KrCl excimer lamp and conditions for the maximum luminosity in the UV spectrum range are reported. The best result is achieved for a Ne : Kr : $Cl_2$ = 50 : 1 : 1 (torr) mixture. When the lamp is excited by the combined Fitch circuit, the pulse half-height duration 107 ns and the power density $E(0,0)$ = 1.1 kW/cm$^2$ are attained. © *2001 MAIK "Nauka/Interperiodica".*

## INTRODUCTION

Interest in UV lamps excited by a pulse discharge in inert gases, halogens, and their mixtures has quickened in recent years [1–9]. It is believed that the lamps emit in the wavelength range shorter than 250 nm, and their power density (luminosity) is as high as tens of kilowatts per square centimeter; therefore, they seem to be promising for microelectronics technology. In this work, the amplitude–time characteristics of the emission from one-barrier flash KrCl excimer lamps and conditions for the maximum luminosity in the UV spectrum range are reported.

## EXPERIMENTAL

The design of the excimer lamp emitter is shown in Fig. 1. The discharge is ignited in the gap between inner high-voltage electrode *1* and an insulating barrier (a ceramic with $\varepsilon \approx 1000$) made as a tube with an inner diameter of 7.8 cm. From the outside, the ceramic tube is covered by an electrode that is grounded during operation. The inner electrode was made of a stainless steel wire that has the shape of a rod or a helix with different pitch and diameter. The discharge gap can be varied between 2.6 and 3.6 cm. The emission was extracted through a 1-cm-thick quartz window with a transmission coefficient of 80% at the wavelength 200 nm. At the exit from the lamp, the beam diameter was 8 cm and then linearly increased with distance from the exit window. The discharge type depended on the high-voltage electrode configuration and the value of the product *pd*. Under the optimal (in terms of maximum output power) conditions, an initially multiple-spark discharge transforms into a discharge consisting of many cones with their bases at the ceramic wall of the lamp. Although the discharge is inhomogeneous, the illuminance $E(x, r)$ at the exit from the lamp smoothly varies along the radius $r$ and has a bell-shaped distribution. The axial illuminance $E$ vs. distance $x$ from the exit window is shown in Fig. 2.

Two circuits to feed the lamp were used (Fig. 3): the Fitch voltage-doubling circuit and sometimes a circuit

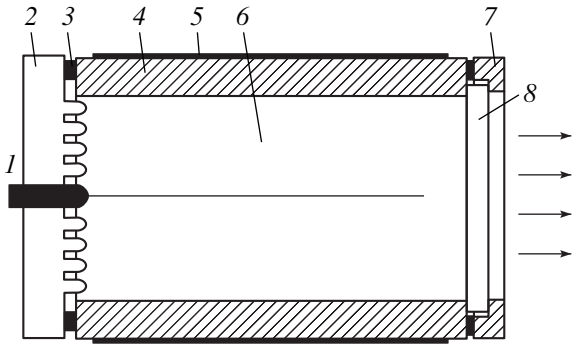


**Fig. 1.** Design of the KrCl flash lamp. *1*, inner (high-voltage) electrode; *2*, insulator; *3*, seal; *4*, ceramic tube; *5*, outer electrode; *6*, working volume of excilamp; *7*, flange; and *8*, quartz exit window. Arrows indicate the direction of emission. Light grey regions show the typical form of the discharge.

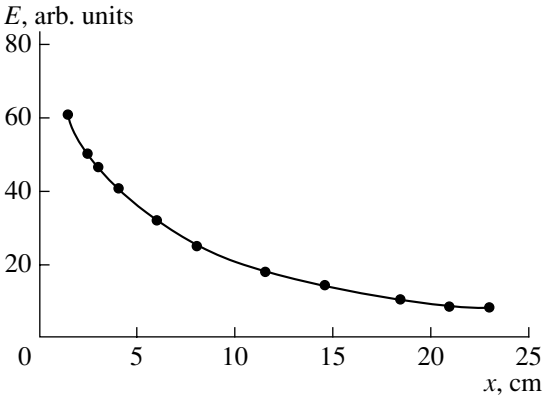


**Fig. 2.** Axial illuminance $E$ vs. distance from the exit window.

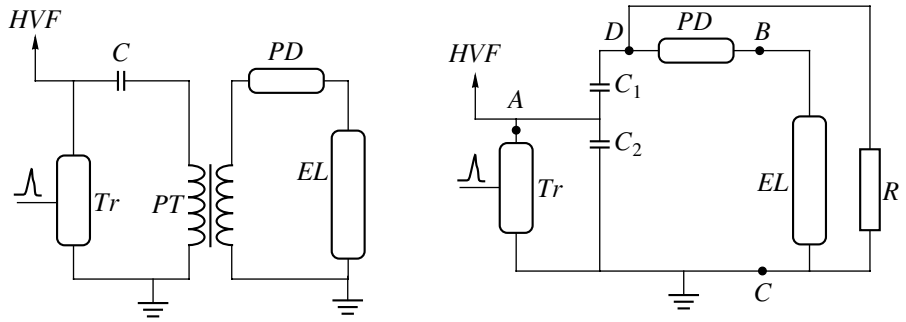


**Fig. 3.** Feed circuits for the KrCl flash excilamp: *HVF*, high-voltage feed; *PD*, peaker (industrial switch); *R*, discharge resistor; $C$–$C_2$, storage capacitors; *Tr*, thyratron; *EL*, excilamp; and *PT*, pulse transformer. The Fitch circuit is on the right, and the circuit with the pulse transformer, on the left.

with a pulse transformer (with a transformation ratio of 2 to 3). The capacitors $C$, $C_1$, and $C_2$ were fed by a controllable high-voltage (to 25 kV) feed source (*HVF* in Fig. 3). The Fitch circuit (on the right) included a KVI-3 storage capacitor battery ($C_1$ and $C_2$) with an impact capacitance of ≈2.2 nF, a discharge resistor $R$, a TGI-1000/25 thyratron (*Tr*), a feed circuit, a thyratron-triggering generator, and a peaker *PD* (RU-26 or RU-47 industrial switch). The total inductance of the capacitor battery wires and the excilamp is made as low as possible in order to cut the leading edge of the voltage pulse at the peaker. A choke is inserted at the point *A* in the capacitor discharge circuit. The choke can also be connected parallel to the lamp (between points *B* and *C*).

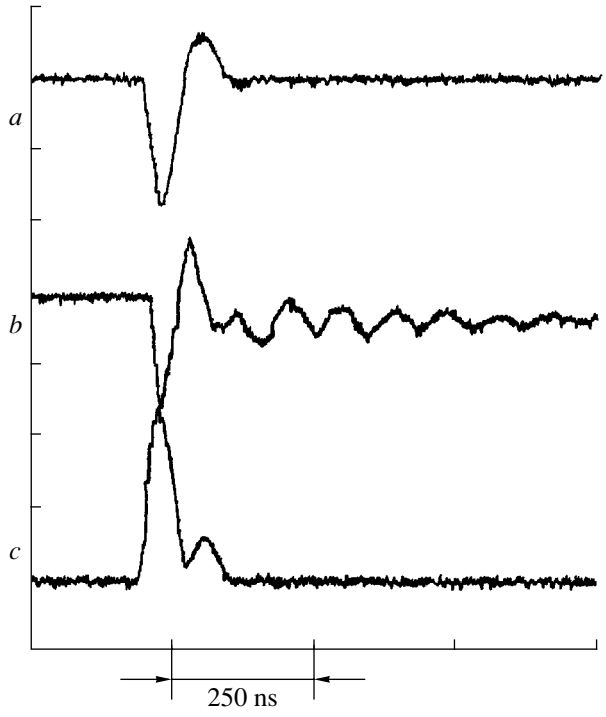


**Fig. 4.** Typical waveforms of the (*a*) current, (*b*) voltage, and (*c*) light pulses. The Fitch circuit; discharge-initiating voltage 20 kV.

Our circuit includes the same components as the Fitch circuit plus a high-voltage pulse transformer (*PT*).

In addition, we used a combined Fitch circuit, where the pulse transformer was connected after the peaker *PD* in the conventional Fitch circuit in order to increase the high-voltage amplitude at the excilamp.

The current and voltage values were measured with a resistive shunt and a capacitive voltage divider (with a voltage ratio of $5 \times 10^3$). The signals from the shunt and the divider were applied to a TDS-220 double-beam storage oscilloscope. The flash power in a given wavelength range was determined with an FÉK-22 SPU vacuum photodiode with a known spectral sensitivity in the visible and UV ranges. The signal from the photodiode was applied to a pulse voltmeter or an oscilloscope. The spectral composition of the emission was monitored with calibrated light filters.

The working mixtures were prepared directly in the lamp by successively delivering a halogen ($Cl_2$ or HCl), an inert gas (Xe or Kr), and a buffer gas (Ne or He).

## RESULTS AND DISCUSSION

In the optimal mixtures, the percentage of the emission with $\lambda < 260$ nm exceeded 90%, which is typical of KrCl excilamps.

In the experiments, we were confronted with the question as to which of the feed circuits is best suited to obtaining stable and high-power emission pulses. It turned out that the output flash power is the highest when the voltage applied to the barrier is as high as possible (which is provided by using the modified Fitch circuit).

Figure 4 shows the waveforms of the (a) voltage, (b) current, and (c) light pulses that illustrate the operation of the conventional Fitch circuit. It is seen that the base widths of the current and emission pulses coincide.

In a number of the experiments, the emission power of the excilamp was unstable. The basic reason for the instability was the time spread in the lamp breakdowns relative to the instant the voltage at the Fitch circuit out-

put was maximal (at point *D*). The spread in the flash power of the lamp may be as high as 50%. However, one can reduce the instability to 10%, using the *PD* and varying the pressure of the gas mixture.

The insertion of sharpening capacitors (85–400 pF) parallel to the lamp did not increase the pulse voltage. This is because of the self-capacitance of an excilamp.

The discharge type in the lamp depended on the high-voltage electrode diameter and also on the partial pressures of the mixture components. The dependence on the Kr and halogen pressures is strong, while the dependence on the buffer gas (helium or neon) pressure is much weaker.

Under similar conditions for mixture excitation (similar values of $U_0$, $C_1$, and $C_2$), the emission intensity is the highest when Ne is used as a buffer gas. This is explained by the fact that the conductivity of a neon-containing plasma is higher than that of a helium-containing plasma, as in KrCl and XeCl excimer lasers.

As the $Cl_2$ partial pressure is increased to 2 torr or higher, the quenching process KrCl* + $Cl_2$ $\longrightarrow$ Kr + Cl + $Cl_2$ causes the emission yield to drop. Moreover, when the chlorine concentration increases, a volume discharge becomes difficult to initiate.

Figure 5 shows the dependence of the flash illuminance from the KrCl lamp on the pressure of Ne introduced into the chamber during operation. In the $Cl_2$-containing mixtures, the output power increases only if a small amount of Ne is added, while in the mixtures with HCl, Ne additions up to a pressure of 1 atm slowly raise the output power.

Figure 6 demonstrates the output power density of the KrCl excimer lamp vs. the number of flashes in the Kr : $Cl_2$ = 50 : 1 mixture at various pressures. As follows from this figure, the lifetime of the mixtures can be increased by raising the $Cl_2$ concentration; in this case, however, the discharge becomes more inhomogeneous and the emission yield drops. The lifetime of the KrCl lamp can be increased further by making the working mixture in the chamber slowly flow, by using special coatings applied on the inner surface of the lamp to decrease the halogen loss due to the heterogeneous reactions, and/or by expanding the buffer volume of the lamp [4, 5].

The best result was achieved in the case of the Ne : Kr : $Cl_2$ = 50 : 1 : 1 (torr) mixture when it was excited with the combined circuit at the impact capacitance $C_1$ = 2.2 nF and $U_0$ = 23 kV. With such parameters, the pulse half-height duration 107 ns and the pulse power density $E(0,0)$ = 1.1 kW/cm$^2$ were attained.

The total power radiated into the solid angle $4\pi$ was estimated at 400 kW. With an energy of 2.32 J stored in the storage capacitor and with regard for the fact that only one third of the total energy is spent to excite the gas mixture, the efficiency of the KrCl lamp is estimated at 5% (relative to the power radiated into the solid angle $4\pi$).

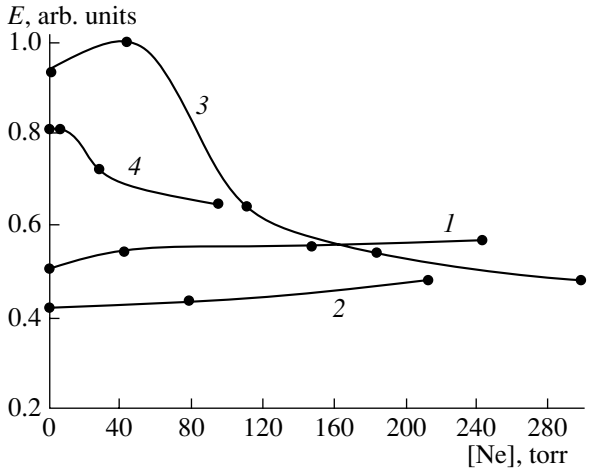


**Fig. 5.** Illuminance from the KrCl flash lamp vs. pressure of buffer Ne introduced into the lamp during operation. Fitch circuit, $U_0$ = 23 kV, $C_1 + C_2$ = 8.8 nF. Kr : HCl = (*1*) 50 : 1 (153 torr) and (*2*) 20 : 1 (63 torr); Kr : $Cl_2$ = (*3*) 40 : 1 (121.5 torr) and (*4*) 80 : 1 (123 torr).

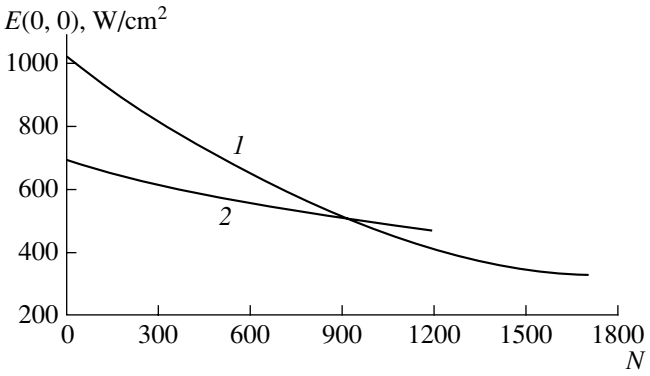


**Fig. 6.** Power density of the KrCl excilamp emission vs. the number of flashes in the binary mixture Kr : $Cl_2$ = 50 : 1 at a pressure of (*1*) 105 and (*2*) 153 torr. Fitch circuit, $U_0$ = 26 kV, $C_1 + C_2$ = 8.8 nF.

To conclude, we note that the general problem of obtaining a high pulse power of spontaneous emission from gas mixtures containing a heavy inert gas and a halogen (Kr + $Cl_2$ or HCl in our case) is split into two partial problems: to provide a high output of the emission from a discharge plasma and to provide the maximal efficiency of extracting the output from the working volume (emitter). It seems that the efficiency of the KrCl lamp obtained in this work can be improved by further optimizing the feed circuit and the lamp design (for example, by using special optical elements: mirrors, lenses, etc.).

## ACKNOWLEDGMENTS

This work was supported by the Alameda Applied Sciences Corporation (contract no. US-7(99)) and by the International Research Center (project no. 1270).

## REFERENCES

1. G. V. Rulev and V. B. Saenko, Pis'ma Zh. Tekh. Fiz. **19** (21), 53 (1993) [Tech. Phys. Lett. **19**, 687 (1993)].
2. V. F. Tarasenko, M. I. Lomaev, A. N. Panchenko, *et al.*, Proc. SPIE **3349**, 732 (1998).
3. V. S. Skakun, A. V. Krivonosenko, M. I. Lomaev, *et al.*, Opt. Atmos. Okeana **13**, 309 (2000).
4. A. M. Boĭchenko, V. S. Skakun, É. A. Sosnin, *et al.*, Kvantovaya Élektron. (Moscow) **23**, 344 (1996).
5. A. M. Boĭchenko, V. F. Tarasenko, E. A. Fomin, *et al.*, Kvantovaya Élektron. (Moscow) **20**, 7 (1993).
6. L. M. Vasilyak, S. V. Kostyuchenko, A. V. Krasnochub, *et al.*, Teplofiz. Vys. Temp. **33**, 826 (1995).
7. S. Bollanti, G. Clementi, P. Di Lazzaro, *et al.*, IEEE Trans. Plasma Sci. **27**, 211 (1999).
8. V. V. Ivanov, K. S. Klopovskii, Yu. A. Mankelevich, *et al.*, Laser Phys. **6**, 654 (1996).
9. T. V. Gavrilova and V. P. Aver'yanov, Opt. Zh., No. 9, 55 (1995) [J. Opt. Technol. **62**, 619 (1995)].

*Translated by V. Isaakyan*

*Technical Physics, Vol. 46, No. 10, 2001, pp. 1345–1346. Translated from Zhurnal Tekhnicheskoĭ Fiziki, Vol. 71, No. 10, 2001, pp. 141–142.*


**BRIEF COMMUNICATIONS**

# The Possibility of Detecting Gravitational Waves from a Shift in the Resonance Frequency of an Optical Resonator

**G. G. Karapetyan**

*Yerevan Physics Institute, Yerevan, 375036 Armenia*

*e-mail: gkarap@crdlx5.yerphi.am*

Received May 3, 2000; in final form, January 29, 2001

**Abstract**—Under the action of the gravitational wave, the length of an optical resonator and, therefore, its resonance frequency change. In conventional resonators, this frequency shift is too small to be detected. We propose a method that provides a very high resonance frequency-versus-resonator length slope. As a result, a gravitational wave with an intensity of $10^{-21}$ can shift the resonance frequency by more than 10 kHz, which can easily be detected. © *2001 MAIK "Nauka/Interperiodica".*

Facilities for detecting gravitational waves (GWs) that are presently under development [1–4] rely on the laser interferometry. They expect to measure a small phase shift between two laser beams propagating in the two orthogonal arms of the interferometer. This phase shift occurs, because the arm lengths of the interferometer experience oscillations under the action of the GW at the GW frequency with one arm becoming longer and the other becoming shorter. As follows from realistic theoretical estimates, near the Earth, the intensity $h$ of the GWs emitted by certain astrophysical objects is on the order of $10^{-21}$, which is expected to produce the relative change of $|\Delta L/L| = h/2 \sim 10^{-21}$ in the interferometer arm length $L$. Since the modern laser interferometry is capable of measuring absolute displacements of up to $10^{-16}$ cm, detection of the GWs requires a sufficiently long $L$. For example, the most ambitious LIGO project uses 4-km-long interferometer arms [4].

Another possibility of detecting GWs relies on the use of an optical resonator. As is known, the resonance frequency $f_0$ of an optical resonator is determined from the condition that its length $L$ measures an integer number of half-wavelengths or, in other words, the phase advance through the optical resonator equals an integer number of $\pi$:

$$2\pi f_0 L/c = m\pi, \tag{1}$$

where $c$ is the velocity of light and $m$ is an integer.

The length of the optical resonator and, consequently, its resonance frequency slightly change under the action of the GW. As follows from condition (1), the shift $\delta f$ in the resonance frequency of the optical resonator is proportional to the change in its length:

$$\delta f = f_0|\Delta L/L| = f_0 h/2. \tag{2}$$

At $f_0 = 3 \times 10^{14}$ Hz and $h \sim 10^{-21}$, Eq. (2) predicts $\delta f \sim 10^{-7}$ Hz, i.e., in a conventional resonator, the shift in the resonance frequency due to the action of the GW is prohibitively small and it cannot be detected in practice.

This paper proposes a new method, which produces a much stronger relation between the change in the length of the optic resonator and the shift in the resonance frequency that is provided by Eq. (2). This method, referred to as the than *phase shift method*, was developed in order to significantly improve the characteristics of optical gyroscopes [5]. It consists of placing a special phase shifter into the optical resonator. In this case, the resonance frequency $f_1$ complies with the requirement

$$2\pi f_1 L/c + \varphi(f_1) = m\pi, \tag{3}$$

instead of condition (1). Here, $\varphi(f)$ is the phase-versus-frequency response of the phase shifter, which describes the phase advance through the phase shifter at the frequency $f$.

Assuming that $\Delta L$ and $\Delta f$ in (3) are small and expanding $\varphi(f)$ into power series about $f_1$, we obtain the following quadratic equation relating $\Delta L$ and $\Delta f$:

$$\varphi''\Delta f^2 + 2[\varphi' + 2\pi(L + \Delta L)/c]\Delta f + 4\pi f_1 \Delta L/c = 0, \tag{4}$$

where $\varphi'$ and $\varphi''$ are the first derivative (the slope of the phase response) and second derivative of the phase with respect to frequency at the point $f_1$ of the unperturbed resonance.

The analysis of solutions to Eq. (4) have shown that, when the phase shifter's frequency–response slope is

$$\varphi' = -2\pi L/c, \tag{5}$$

the shift in the resonance frequency is proportional to the square root of $\Delta L$ within the relative error of $\sim|\Delta L/L|^{1/2}$:

$$\Delta f \approx \pm(-4\pi f_1 \Delta L/c\varphi'')^{1/2}. \quad (6)$$

Hence, when $\Delta L$ and $\varphi''$ have different signs, a small change in the length of the optical resonator with a phase shifter causes its resonance frequency to split into two frequencies: $f_1 \pm \Delta f$. When $\Delta L$ and $\varphi''$ have the same signs, formula (6) gives imaginary values for $\Delta f$ which means that the resonator does not support resonance oscillations. To estimate the frequency shift from formula (6), one should know the value of $\varphi''$, which may differ in a wide range for different phase shifters. For a crude estimate, one may assume that $\varphi'' \sim \varphi'/f_1 \sim L/cf_1$. As a result, we obtain

$$\Delta f \sim f_1|\Delta L/L|^{1/2} \sim f_1 h^{1/2} \sim 10 \text{ kHz}, \quad (7)$$

which is much greater than the frequency shift (2) of the conventional resonator. Therefore, a small change in the length of the optical resonator with a phase shifter whose slope complies with Eq. (5) creates (when $\Delta L\varphi'' < 0$) two resonances separated by $2\Delta f$. This frequency difference can be used to find the change in the resonator length from (6) and, therefore, the GW intensity. Note that Eq. (6) also remains valid when condition (5) is slightly violated until the second term in Eq. (4) becomes equal to the first one in the order of smallness. This occurs when $\varphi'$ changes by $\sim|\Delta L/L|^{1/2}/c$. Hence, condition (5) may be satisfied within the relative error of $\sim|\Delta L/L|^{1/2}$ and the property $\Delta f/f_1 \sim |\Delta L/L|^{1/2}$ will still be valid.

The main problem in implementing the method proposed above is the development of a phase shifter with the negative frequency-response slope complying with condition (5) in a certain small frequency range. In optics, such phase shifters may be developed based on media with anomalous dispersion, in which the wave number and, hence, the phase advance through the phase shifter decrease with increasing frequency. In a usual dielectric, the anomalous dispersion is accompanied by strong absorption and is almost unused in practice. Therefore, one should study active (amplifying) media, in which the anomalous dispersion is observed at the frequencies near the amplification line [6], or periodic structures, which are also known [7] to be capable of exhibiting low-loss anomalous dispersion.

Thus, we proposed a method, which significantly improves the sensitivity of the optical resonator's resonance frequency to change in its length. The method is intended for the use in gravitational-wave detectors. It can also be used in various optical sensors based on the measurement of the shift in the resonance frequency of the optical resonator. For example, laser gyroscopes use Sagnac's effect [8]: rotation of a ring optical resonator causes a small relativistic change in its optical length. The resultant small frequency change is used to calculate the rate of rotation. Our estimates [5] show that this method provides an orders-of-magnitude increase in the sensitivity of the gyroscope such that it becomes possible to measure angular velocities lower than $10^{-9}$ deg/h. Therefore, a more accurate experimental verification of certain fundamental physical principles and geophysical hypotheses becomes feasible (see [9] for details).

## ACKNOWLEDGMENTS

This work was supported by the INTAS, project no. 97-30748.

## REFERENCES

1. A. Abramovici *et al.*, Science **256**, 325 (1992).
2. C. Bradaschia *et al.*, Nucl. Instrum. Methods Phys. Res. A **289**, 518 (1990).
3. V. B. Braginskiĭ, Usp. Fiz. Nauk **170**, 743 (2000).
4. J. Dietrich, Eng. Sci. **61** (2), 8 (1998).
5. G. G. Karapetyan, Izv. Akad. Nauk Resp. Arm., Tekh. **53**, 412 (2000).
6. A. M. Steinberg and R. Y. Chiao, Phys. Rev. A **49**, 2071 (1994).
7. R. A. Silin and V. P. Sazonov, *Retarding Systems* (Sov. Radio, Moscow, 1966).
8. S. I. Bychkov, D. P. Luk'yanov, and A. I. Bakalyar, *Laser Gyroscope* (Nauka, Moscow, 1975).
9. G. E. Stedman, Rep. Prog. Phys. **60**, 615 (1997).

*Translated by A. Khzmalyan*